A lush Arabia beckoned ancient humans *p. 994*

Where China spends its R&D money *p. 1006*

Houses and their inhabitants share microbes *p. 1048*

Science

$10
29 AUGUST 2014
sciencemag.org

AAAS

How far are these stars?

Precise interferometry settles the question for the Pleiades

pp. 1001 & 1029

CONTENTS

29 AUGUST 2014 • VOLUME 345 • ISSUE 6200

1000 & 1074
Genetic changes involved in domestication

NEWS

IN BRIEF

986 Roundup of the week's news

IN DEPTH

988 ANIMAL WELFARE ACCREDITATION CALLED INTO QUESTION
PETA study finds violations more often in approved labs *By D. Grimm*

989 GENOMES REVEAL START OF EBOLA OUTBREAK
Viral sequences demonstrate how the disease spread in Sierra Leone
By G. Vogel
▸ *SCIENCE* EXPRESS REPORT BY S. K. GIRE *ET AL.*

990 AS VOLCANO RUMBLES, SCIENTISTS PLAN FOR AVIATION ALERTS
Ash sensors ready to deploy on ground, planes *By C. Gramling*

991 A CHOCOLATE HABIT IN ANCIENT NORTH AMERICA
Residues on pottery suggest close ties between Mesoamerica and cultures to the north *By M. Bawaya*

992 WHY NULL RESULTS RARELY SEE THE LIGHT OF DAY
"File drawer" study proposes registry for unpublished social science data
By J. Mervis
▸ *SCIENCE* EXPRESS REPORT BY A. FRANCO *ET AL.*

993 SUPERNOVA BREAKS THE MOLD
A massive explosion in a nearby galaxy both confirms and confounds astronomers' expectations *By D. Clery*

FEATURE

994 IN SEARCH OF GREEN ARABIA
Reseachers are scouring the now-barren Arabian Peninsula to uncover its hidden role in ancient human migration
By A. Lawler

INSIGHTS

PERSPECTIVES

998 GLIMPSING GLASS STRUCTURE UNDER PRESSURE
Nuclear magnetic resonance spectroscopy of a glass under pressure adds to our understanding of network structure *By R. E. Youngman*
▸ REPORT P. 1027

1000 ON THE ORIGIN OF PETER RABBIT
Domestication of rabbits led to changes across the genome, particularly in regions related to brain development
By K. E. Lohmueller
▸ REPORT P. 1074

1001 ONE GOOD COSMIC MEASURE
Radio-wave interferometry provides an accurate measurement of cosmic distances *By L. Girardi*
▸ REPORT P. 1029

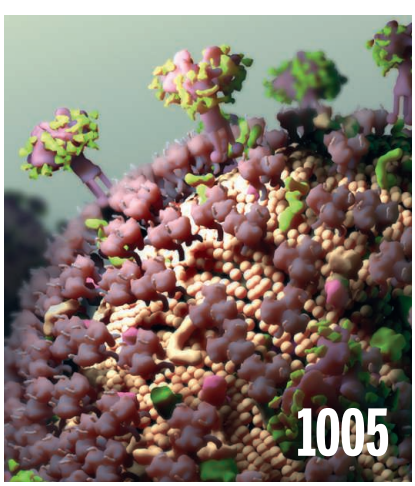

1002 MANY MODES OF MOTILITY
Cells use a piston-driven mechanism, among others, to migrate
By D. W. DeSimone and A. R. Horwitz
▸ REPORT P. 1062

1004 STORIES OF ARCTIC COLONIZATION
Genetic data elucidate the population history of the North American Arctic
By R. W. Park
▸ RESEARCH ARTICLE P. 1020

1005 REKINDLED HIV INFECTION
What does the "Mississippi baby" tell us about curing HIV-1 infection?
By J. D. Siliciano and R. F. Siliciano

1006 DEMYSTIFYING CENTRAL GOVERNMENT R&D SPENDING IN CHINA
Should funding focus on scientific research? *By Y. Sun and C. Cao*

BOOKS *ET AL.*

1009 AMERICAN PLAINS BISON
By J. A. Bailey, reviewed by J. A. DeWoody

LETTERS

1010 IS IT TIME TO DESTROY THE SMALLPOX VIRUS?
By I. Arita and D. Francis

1010 GENE DRIVES RAISE DUAL-USE CONCERNS
By D. Gurwitz

1010 RESPONSE
By K. A. Oye and K. M. Esvelt

1011 TECHNICAL COMMENT ABSTRACTS

RESEARCH

IN BRIEF

1016 From *Science* and other journals

RESEARCH ARTICLES

1020 ARCTIC GENETICS
The genetic prehistory of the New World Arctic *M. Raghavan* et al.
RESEARCH ARTICLE SUMMARY; FOR FULL TEXT: dx.doi.org/10.1126/science.1255832
▸ PERSPECTIVE P. 1004

Published by AAAS

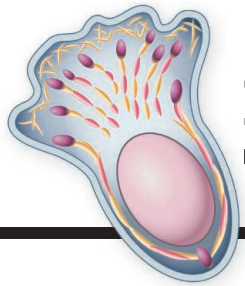

1002 & 1062

Different mechanisms for cell movement

1004 & 1020

Paleo-Eskimo population expansion

1021 ION CHANNEL STRUCTURE
X-ray structures of AMPA receptor–cone snail toxin complexes illuminate activation mechanism *L. Chen* et al.
▸ REPORT P. 1070

REPORTS

1027 GLASS STRUCTURE
Observation of the transition state for pressure-induced $BO_3 \rightarrow BO_4$ conversion in glass *T. Edwards* et al.
▸ PERSPECTIVE P. 998

1029 STELLAR DISTANCES
A VLBI resolution of the Pleiades distance controversy *C. Melis* et al.
▸ PERSPECTIVE P. 1001

1032 CIRCUMSTELLAR DISKS
Large impacts around a solar-analog star in the era of terrestrial planet formation *H. Y. A. Meng* et al.

1035 SUPERFLUIDITY
A mixture of Bose and Fermi superfluids *I. Ferrier-Barbut* et al.

1038 EARTHQUAKE DYNAMICS
Strength of stick-slip and creeping subduction megathrusts from heat flow observations *X. Gao and K. Wang*

1041 CONSERVATION ECONOMICS
Using ecological thresholds to evaluate the costs and benefits of set-asides in a biodiversity hotspot *C. Banks-Leite* et al.

1045 PALEOCEANOGRAPHY
Holocene history of ENSO variance and asymmetry in the eastern tropical Pacific *M. Carré* et al.

1048 HUMAN MICROBIOTA
Longitudinal analysis of microbial interaction between humans and the indoor environment *S. Lax* et al.
▸ PODCAST

1052 MICROBIAL METABOLISM
Growth of nitrite-oxidizing bacteria by aerobic hydrogen oxidation *H. Koch* et al.

1054 MEMORY ENHANCEMENT
Targeted enhancement of cortical-hippocampal brain networks and associative memory *J. X. Wang* et al.

1058 GERMINAL CENTERS
Dynamic signaling by T follicular helper cells during germinal center B cell selection *Z. Shulman* et al.

1062 CELL MIGRATION IN 3D
Generation of compartmentalized pressure by a nuclear piston governs cell motility in a 3D matrix *R. J. Petrie* et al.
▸ PERSPECTIVE P. 1002

1065 CHROMATIN REGULATION
Histone H3 lysine-to-methionine mutants as a paradigm to study chromatin signaling *H.-M. Herz* et al.

1070 ION CHANNEL STRUCTURE
Structure of an agonist-bound ionotropic glutamate receptor *M. V. Yelshanskaya* et al.
▸ RESEARCH ARTICLE P. 1021

1074 EVOLUTIONARY GENOMICS
Rabbit genome analysis reveals a polygenic basis for phenotypic change during domestication *M. Carneiro* et al.
▸ PERSPECTIVE P. 1000

DEPARTMENTS

985 EDITORIAL
Australia needs a strategy
By Ian Chubb

1090 WORKING LIFE
Having it all
By Jyoti Mishra

ON THE COVER

The Pleiades, also known as the Seven Sisters, is a cluster of stars easily seen in fall and winter that is critical for our understanding of stars throughout the universe. For decades, there has been considerable debate over the distance from our solar system to the Pleiades. Very long baseline radio interferometry now provides a "gold standard" distance measurement. See pages 1001 and 1029. *Photo: Roberto Colombari/astrobin.com/users/rob77*

Science Staff 982
AAAS News & Notes 1012
New Products 1080
Science Careers 1081

SCIENCE (ISSN 0036-8075) is published weekly on Friday, except the last week in December, by the American Association for the Advancement of Science, 1200 New York Avenue, NW, Washington, DC 20005. Periodicals mail postage (publication No. 484460) paid at Washington, DC, and additional mailing offices.

Copyright © 2014 by the American Association for the Advancement of Science. The title SCIENCE is a registered trademark of the AAAS.

Domestic individual membership and subscription (51 issues): $153 ($74 allocated to subscription). Domestic institutional subscription (51 issues): $1282; Foreign postage extra: Mexico, Caribbean (surface mail) $55; other countries (air assist delivery) $85. First class, airmail, student, and emeritus rates on request. Canadian rates with GST available upon request, GST #1254 88122. Publications Mail Agreement Number 1069624. **Printed in the U.S.A.**
Change of address: Allow 4 weeks, giving old and new addresses and 8-digit account number. **Postmaster:** Send change of address to AAAS, P.O. Box 96178, Washington, DC 20090–6178. **Single-copy sales:** $10.00 current issue, $15.00 back issue prepaid includes surface postage; bulk rates on request.

Authorization to photocopy material for internal or personal use under circumstances not falling within the fair use provisions of the Copyright Act is granted by AAAS to libraries and other users registered with the Copyright Clearance Center (CCC) Transactional Reporting Service, provided that $30.00 per article is paid directly to CCC, 222 Rosewood Drive, Danvers, MA 01923. The identification code for *Science* is 0036-8075. *Science* is indexed in the *Reader's Guide to Periodical Literature* and in several specialized indexes.

PHOTO: (TOP RIGHT) UNIVERSITY OF ABERDEEN. COPYRIGHT AND COURTESY OF QANIRTUUQ, INC.; (RIGHT) NASA/JPL-CALTECH/R. HURT (IPAC)

Published by AAAS

EDITORIAL

Australia needs a strategy

Australians are constantly told that our economy is '"in transition."' We need to move up the global value chain, build knowledge-based industries, prepare for the Asian Century, and be the "food bowl of the world." These are grand ambitions that we share with many other nations, in our region and beyond. The question for all of us is: How?

I am not one of those who think that good things will happen just because we expect them to, in Australia or anywhere else. I think we need to organize, evaluate, and cohere; to make sure that we align our efforts and investments with our national interests, focus on areas that are of particular importance or where there is a particular need, and build to a scale that will make a difference both to ourselves and to a changing world. It is the knowledge that science will offer, and the sensible application of that knowledge to agreed-on goals, that will build stronger national economies and societies.

As Australia's Chief Scientist, my role is to advise the federal government on matters of science policy and advocate a better understanding of science in industry and the community. Like the rest of Australia's scientific community, I was disappointed by cuts in our recent federal budget. My real concern, however, is the lack of a strategy that would help us maximize the value of the science resources we do have.

This is not a new problem. It is one that has been allowed to persist for decades. Our support for science is the victim of short-term, on-again, off-again, thinking, terminating programs rather than giving them sustained support. We seem reluctant to identify national priorities and make sure we fund them appropriately—areas where we have the advantage, or need, or capacity to grow to scale or to take new products to the global market. This puts us at odds with an emerging global consensus.

This week, science advisory delegations from around the world convene in Auckland, New Zealand, to discuss the importance and challenges of providing policy-relevant science advice to governments. Policy-makers globally have recognized the obvious point: Science isn't like a toothbrush. You can't buy it when you get there if you forgot to pack one. To build both capacity and capability, we need strategic investment supported by good planning and long-term commitment.

"If we are serious in our wish for a fair and prosperous Australia, in a better and happier world, then we will look to science to sustain us."

It troubles me that Australia remains the only country among the members of the Organisation for Economic Co-operation and Development (OECD) without a science or technology strategy. The consequences are and will be felt in our performance, in a world more reliant than ever before on science and science-trained people.

We often claim to "punch above our weight," but in reality our research effort could and ought to be better. School participation in science and mathematics, particularly at senior levels, has fallen, when the trend should be heading the other way. The level of collaboration between our researchers and our businesses is one of the poorest in the OECD.

If we are serious in our wish for a fair and prosperous Australia, in a better and happier world, then we will look to science to sustain us. And we will need to be strategic. We will get the future we earn.

– Ian Chubb

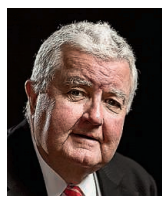

Ian Chubb is Australia's Chief Scientist. E-mail: chief.scientist@chiefscientist.gov.au

CREDITS: (INSET) VLADGRIN/ISTOCKPHOTO; (RIGHT) STEFAN POSTLES

Downloaded from www.sciencemag.org on August 29, 2014

10.1126/science.1259741

Published by AAAS

NEWS

> "We owe wine country in part to earthquakes."
>
> **Ross Stein**, a geophysicist at the U.S. Geological Survey. The terrain of Napa Valley, California, was shaped by faults. A 6.0 temblor struck there on 24 August.

IN BRIEF

A space parasol unfurls

A sunshield like this will protect the telescope (not pictured).

The most sensitive space observatory ever planned will need powerful protection from the sun. The instruments on the James Webb Space Telescope must be kept at or below –233°C in order to detect infrared radiation from distant sources. The solution is a nearly 20-meter-long parasol made from five polymer membranes that will reflect all but a millionth of the sun's heat. A test unit was successfully unfurled for the first time in mid-July in Redondo Beach, California, and is now being disassembled and inspected. The telescope, a collaboration between NASA, the European Space Agency, and the Canadian Space Agency, is targeted for a 2018 launch.

AROUND THE WORLD

Iranian science minister ousted

TEHRAN | An effort to breathe new life into Iranian universities is at a crossroads after the nation's parliament last week ousted science minister Reza Faraji-Dana. "His downfall is a sad day for science in Iran," says a scientist at the Sharif University of Technology in Tehran who asked to remain anonymous because of the uncertain political climate. Strengthening the higher education system has been a priority for Iranian President Hassan Rouhani. Faraji-Dana, an electrical engineer, had worked to create conditions for a freer atmosphere on Iranian campuses, an effort that apparently alienated the conservative parliament. One of his accomplishments during his 9 months as minister, says the Sharif researcher, was to implement a more open and transparent mechanism for appointing university chancellors based on talent rather than political persuasion. http://scim.ag/sciminIran

China blocks studies of GMOs

BEIJING | China's Ministry of Agriculture decided not to renew biosafety certificates that allowed research groups to grow two strains of genetically modified (GM) rice and one variety of GM corn. The

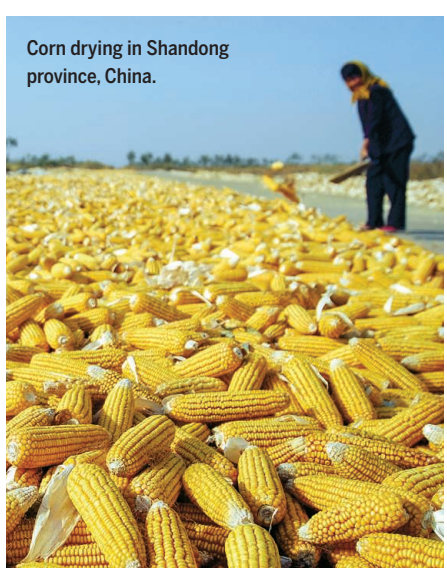

Corn drying in Shandong province, China.

PHOTOS: (LEFT TO RIGHT) CHRIS GUNN/NASA; © IMAGINECHINA/CORBIS

Downloaded from www.sciencemag.org on August 29, 2014

Published by AAAS

Ice buckets make a splash in research fundraising

What do rap star Eminem, actor Tom Cruise, and Massachusetts Institute of Technology (MIT) President L. Rafael Reif have in common? All have been swept up in the social media explosion known as the Ice Bucket Challenge, in which people, famous and unknown, drench themselves in ice water to raise awareness of amyotrophic lateral sclerosis (ALS) and money for research and patient care. Since going viral in July, the challenge has raised $88.5 million for the national ALS Association, which typically devotes about 25% of its revenue to research grants. The unexpected response has generated a debate among some about the appropriateness of public relations gimmicks to drive charitable donations for funding science. The chatter, however, didn't prevent Reif, an engineer, from enlisting MIT students to design a contraption rigged to dump a bucket of icy water on his head. Reif (left) had been called out by Harvard University President Drew Faust, who also took the challenge last week, surrounded by Harvard stem cell scientists working on ALS.

permits, granted with much fanfare in 2009, expired on 17 August. Whether this represents a change in policy regarding agricultural biotechnology is not clear. Public opposition to GM crops has grown in the intervening 5 years. But the government is still supporting work on corn carrying a gene from the *Bacillus thuringiensis* (Bt) bacterium that enhances pest resistance. One researcher told *Science* that GM corn faces less opposition because it is primarily used for animal feed. http://scim.ag/ChinaGM

Biggest bat catcher unveiled

PAPE, LATVIA | German and Latvian biologists took a giant first step toward understanding the mysteries of bat migration last week, setting up a 15-meter-high funnel-shaped net to waylay flying mammals traveling across Europe. With this first-of-its-kind net, they expect to catch up to 1000 animals a night for tagging and releasing, United Press International reported on 18 August. Researchers hope that by setting up the net along a narrow, bat-rich strip of land between the Baltic Sea and a neighboring lake, they will be able to gather an unprecedented amount of data about the animals' flight paths, hibernation areas, and metabolism.

NEWSMAKERS

Three Q's

This month, math and science teacher **Amanda Curtis**, 34, became the Democratic nominee for U.S. Senate from her home state. The novice member of Montana's part-time state legislature stepped onto the national stage when the expected nominee, interim Senator John Walsh, dropped out after charges of plagiarism in his master's thesis.

Q: What's harder, teaching or lawmaking?
A: I'd say teaching. There's no more pressure than to say, "You get these kids for 56 minutes a day, if they show up at all, and you're required to meet these standards. Of course, you also need to catch them up from the past 3 years' work. And we don't really like you very much."

Q: Did you always like math?
A: No, I really struggled in high school. And the first college course I took was a remedial math course. [But at Montana Tech] a professor laid out the beautiful picture that is calculus, and all of a sudden I understood it. It just clicked for me.

Q: Does that help you as a teacher?
A: I tell my students, if I can do it, you can do it. That's been my message about math, and that's my message about politics. http://scim.ag/CurtisSen

BY THE NUMBERS

9780

Kilometers of illegal off-road tracks near the Arizona border with Mexico, according to a study in *Land Degradation & Development*. Smugglers' vehicles could harm the threatened flat-tailed horned lizard.

8:30 a.m.

Earliest time that middle and high school should begin, according to a new policy statement by the American Academy of Pediatrics. Sleep-wake cycles shift up to 2 hours later during puberty.

PHOTOS: (TOP TO BOTTOM) BRIELLE DOMINGS/MIT ALUMNI ASSOCIATION AND SLICE OF MIT BLOG; THE STATE OF MONTANA/WIKIMEDIA COMMONS

Published by AAAS

IN DEPTH

A USDA inspector examines ferrets in a research lab.

SCIENTIFIC COMMUNITY

Animal welfare accreditation called into question

PETA study finds violations more often in approved labs

By **David Grimm**

The international gold standard of laboratory animal care may have lost a bit of its luster. Labs accredited by the United States' only independent certifier of research animal welfare violate national animal welfare guidelines more frequently than do unaccredited facilities, a study conducted by an animal rights organization has found. As both the National Institutes of Health (NIH) and the Department of Defense (DOD) waive certain inspection requirements for labs vetted by the Association for Assessment and Accreditation of Laboratory Animal Care (AAALAC) International, the findings may force a rethink of how lab animal welfare is overseen in the United States and other countries.

"Funders, journal editors, and the general public should be reevaluating whether AAALAC accreditation is a meaningful distinction," says the study's lead author, Justin Goodman, the director of the Laboratory Investigations Department at People for the Ethical Treatment of Animals (PETA). But AAALAC's executive director, Christian Newcomer, disputes that conclusion, saying the report is based on biased data collected by the U.S. Department of Agriculture (USDA). Still, he adds, "I can guarantee this study will generate discussion within AAALAC. It won't be discounted just because it was conducted by PETA."

AAALAC was founded in 1965 by leading scientists and veterinarians who wanted to provide rigorous independent oversight to the burgeoning use of lab animals. The United States was about to pass the Animal Welfare Act (AWA), which regulates the use of animals in research, but AAALAC's creators felt it could be more nimble and knowledgeable than the USDA inspectors tasked with enforcing the minimal standards of the AWA, Newcomer says.

Today, more than 900 institutions in 38 countries have earned AAALAC accreditation, including the top 100 NIH-funded labs and all major pharmaceutical companies. Although accreditation is voluntary, many granting agencies, including DOD, require it. Labs are subject to triennial inspections and must pay a yearly fee ranging from $2600 to more than $9000, depending on their size. "We have chosen to meet standards that go above and beyond the animal research regulations required by law," reads a poster sold by AAALAC to accredited labs.

But PETA's Goodman notes that AAALAC keeps all its inspections confidential. "There's a lot of stock being put into this seal of approval, but what it actually means in terms of animal welfare has been unknown."

So Goodman and colleagues turned to the yearly on-site inspection reports USDA conducts at every government-funded lab that does animal research. In all, the researchers analyzed the 2010 and 2011 records from 823 facilities, 315 of which were AAALAC-accredited and 508 of which were not. On average, when controlling for the number of animals, accredited facilities were cited with 2.13 violations of animal welfare guidelines, or about one per year, whereas unaccredited facilities were cited for 1.56 violations, or about 0.75 per year, the team will report next month in the *Journal of Applied Animal Welfare Science*.

"AAALAC accreditation has become more of a PR tool than a meaningful oversight mechanism," Goodman says. He speculates that accredited facilities have become less vigilant about animal welfare. At the very least, he says, "you certainly can't say that animals are better off in these facilities."

But in an e-mail to *Science*, NIH's Office of Laboratory Animal Welfare says the study's implications are unclear. One complication is that Goodman's team was unable to ascertain just how each violation affected animal welfare. USDA has historically issued violations for everything from failing to anesthetize 50 goats during invasive surgeries to simple errors in paperwork. NIH also notes that AAALAC accreditation is just one of the many criteria it uses to evaluate an institution's animal program. "For these reasons," it writes, "it is difficult to concur with the authors' conclusion."

Newcomer says the USDA data on which the study is based are flawed. Whereas uncertified labs tend to be smaller operations, performing simpler tasks such as using rabbits to create antibodies, AAALAC labs tend to be large and complex operations performing cutting-edge animal research, he contends. "These complex environments are disorienting to the USDA," he says, and that makes the agency's inspectors more likely to find violations. (A USDA spokesman responds: "Our inspectors are trained professionals with the knowledge and capacity to inspect regulated research facilities.")

"It's a really interesting report, and I applaud the effort to take a look at these data," says Larry Carbone, the associate director of the Laboratory Animal Resource Center at the University of California, San Francisco. But Carbone, who authored a book on the history of the AWA, agrees with NIH that the implications for animal welfare are murky. He also notes that in his experience, AAALAC inspections tend to be more rigorous than USDA inspections. Nevertheless, Carbone says, "If I were AAALAC, I would put together a task force to figure out if there really is a problem with their accreditation process. If there is, they should figure out a way to fix it." ■

PHOTO: R. ANSON EAGLIN/USDA APHIS

Downloaded from www.sciencemag.org on August 29, 2014

Published by AAAS

INFECTIOUS DISEASE

Genomes reveal start of Ebola outbreak

Viral sequences demonstrate how the disease spread in Sierra Leone

By **Gretchen Vogel**

When the young woman arrived at the Kenema Government Hospital in Sierra Leone in late May, she had high fever and had just miscarried. The hospital suspected she had contracted Lassa fever, because the viral disease is endemic in the region and often causes miscarriages. But Ebola virus disease, another hemorrhagic fever illness, had been spreading in neighboring Guinea for months, so when she began bleeding profusely, staff tested her for that virus as well. The results were positive, making her the first confirmed case of Ebola in Sierra Leone.

Volunteers in protective gear bury a victim of Ebola in Kenema.

PHOTO: MOHAMMED ELSHAMY/ANADOLU AGENCY/GETTY IMAGES

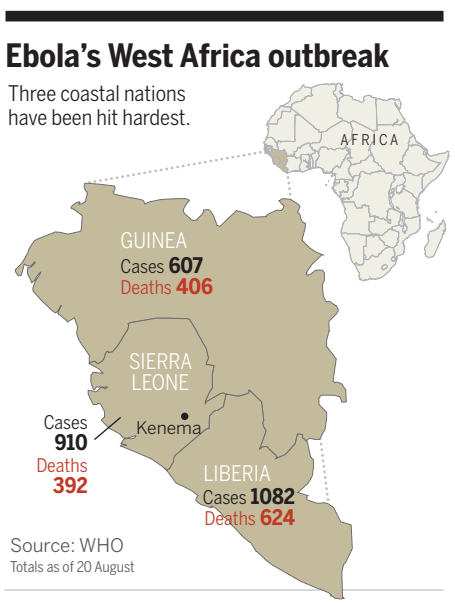

The young woman, who eventually recovered, is now at the heart of a tragic but potentially important research tale. In a paper online this week in *Science* (http://scim.ag/sgire), a collaboration led by Stephen Gire and Pardis Sabeti of Harvard University and the Broad Institute in Cambridge, Massachusetts, report sequencing and analyzing the genomes of Ebola virus samples from 78 people in Sierra Leone who were diagnosed with Ebola between late May and mid-June, including the young woman who came to Kenema's hospital. The 99 complete sequences—some patients were sampled more than once—provide insights into how the virus is changing during the outbreak, which could help improve current diagnostic tests and, in the long term, guide researchers working on vaccines and treatments.

The study, however, also highlights the unrelenting toll the outbreak has taken on health workers on the front lines. More than 50 co-authors from four countries helped collect and analyze the viral sequences. Five of them contracted Ebola virus disease themselves and died.

That first diagnosed case in Sierra Leone infected no one at the hospital, says Robert Garry, a virologist at Tulane University in New Orleans, Louisiana, who works with the Kenema hospital's Lassa fever research center and is also a co-author on the paper. But a team from the ministry of health was immediately dispatched to the woman's home village to find out where and how she had been infected. They learned that she had attended the recent funeral of a traditional healer—an herbalist—who had been treating Ebola patients from across the nearby border with Guinea.

The team found 13 more people who were infected, all women who had attended the burial. It was those mourners who largely sparked Sierra Leone's outbreak, which has sickened more than 900 and killed more than 390 people. Blood samples from 12 of those mourners and other infected people have allowed Gire, Sabeti, and their colleagues to track how the virus changed as it spread. "It is the first time that the real evolution of the Ebola virus can be observed in humans," says Sylvain Baize of the Institut Pasteur in Lyon, France, who sequenced some of the first Ebola virus samples from patients in Guinea, where the current outbreak originated, but who was not involved in this project.

The genomic data also shed new light on how the virus—officially called EBOV—ended up in West Africa. EBOV, one of five ebolaviruses known to infect humans, has caused at least 12 outbreaks in Central Africa and Gabon since 1976. Until this year, though, it had never been identified in West Africa.

Some researchers theorized, based on early sequencing data, that EBOV had circulated for decades, undetected, in animals in the region. But the new analysis, strengthened by the unprecedented number of genomes, supports another theory: that the virus spread, via animal hosts, from Central Africa within the last decade. Researchers aren't sure which animal to blame, but fruit bats are their leading suspects (*Science*, 11 April, p. 140). At least one fruit bat species known to carry ebolavirus has a population range that stretches from Central Africa across to Guinea.

Gire, Sabeti, and their colleagues found that in the current outbreak the virus's genome is changing fairly quickly, including in regions that are key for the accuracy of the PCR-based diagnostic tests. It will be important to keep track of such changes, Gire says, so that tests can be updated if necessary. Vaccines and antibody-based treatments—such

Downloaded from www.sciencemag.org on August 29, 2014

Published by AAAS

as the ZMapp drug that was used in a handful of patients—could also be affected by the kinds of changes the researchers identified. (Sabeti says ZMapp researchers contacted her about the new sequences her group had posted online.)

The analysis reveals that the outbreak in Sierra Leone was sparked by at least two distinct viruses, introduced from Guinea at about the same time. It is unclear whether the herbalist was infected with both variants, or whether perhaps another funeral attendee was independently infected. One Ebola virus lineage disappears from patient samples taken later in the outbreak, while a third lineage appears. That lineage—tied to a nurse who was traveling to reach a hospital but died along the way—seems to have originated when one of the lineages present at the funeral gained a new mutation. This third lineage was spread, Garry says, via a truck driver who transported the nurse, as well as others who cared for her in the town where she died.

Further studies of the differences between the various Ebola lineages might link such mutations to the virus's behavior—how lethal it is, and how easily it spreads, for example. "The paper shows the unrealized potential of what these methods could do," says Roman Biek, who studies the evolution and ecology of infectious diseases at the University of Glasgow in the United Kingdom.

Missing from the sequencing analysis are Ebola samples from people infected in Liberia and Guinea. Stephan Günther of the Bernhard Nocht Institute for Tropical Medicine in Hamburg, Germany, says he has samples from Guinea in his lab, waiting to be sequenced once he and colleagues can find the time. (This week Günther was in Nigeria, tracing contacts of an Ebola patient there, who was infected by a traveler from Liberia.) Researchers in Liberia have also collected samples, but are focused on attempting to slow the epidemic there, where it is spreading in the densely populated capital and shows no signs of slowing down. (Congo is also on high alert as Ebola has popped up in a remote region in the northwest of the country. As *Science* went to press, it was not clear which ebolavirus is causing that outbreak.)

Sabeti, who with her colleagues posted the virus sequences in a public database as soon as they were generated, says she hopes this work and the tragedy that befell her coauthors and other health care workers will inspire other researchers to make their data public quickly, in both this outbreak and future epidemics. "We've got to crowdsource the epidemic," she says. "The more information you get into hands of people who can help, the more likely you are to come up with a solution." ■

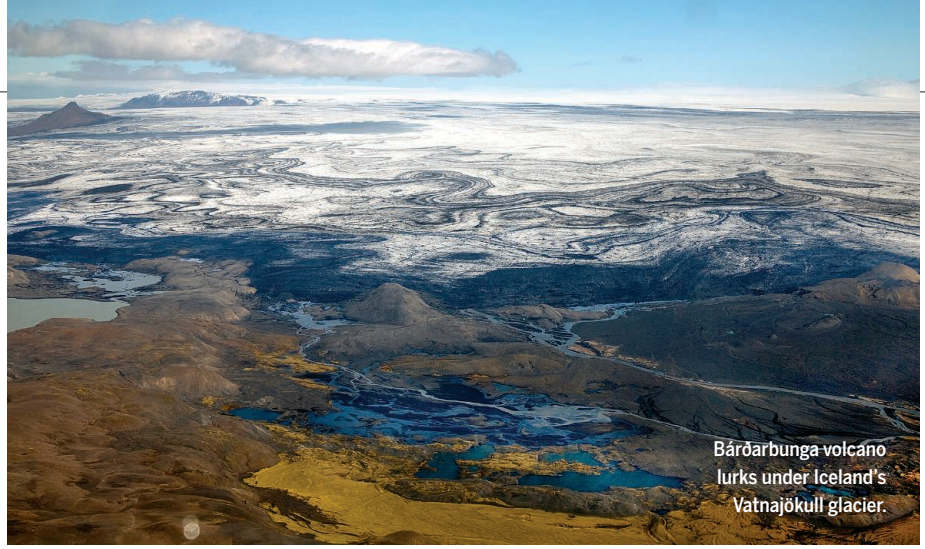

Bárðarbunga volcano lurks under Iceland's Vatnajökull glacier.

PHOTO: © EGGERT NORÐDAHL/DEMOTIX/CORBIS

ICELAND

As volcano rumbles, scientists plan for aviation alerts

Ash sensors ready to deploy on ground, planes

By **Carolyn Gramling**

After 2 weeks of seismic grumbling, Iceland's Bárðarbunga volcano was holding scientists—and the aviation industry—in suspense this week. Buried beneath the island's giant Vatnajökull glacier, under 100 to 400 meters of ice, the volcano had yet to erupt as *Science* went to press. But scientists at the Icelandic Meteorological Office (IMO) in Reykjavík, seasoned by back-to-back eruptions at Eyjafjallajökull in 2010 and Grímsvötn in 2011 that produced large ash clouds and caused costly air traffic snarls over northern Europe, are better prepared than before to monitor ash and assess its threat to aircraft.

"One of the criticisms of the 2010 incident was that there were a lot of model forecasts," but few observations, says Fred Prata, an atmospheric scientist at Nicarnica Aviation in Kjeller, Norway. Airlines thought flights were disrupted unnecessarily and "were a bit critical of the scientists," Prata says.

In August 2011, at the urging of Iceland's government, IMO began devoting more resources to volcano hazards. IMO and the University of Iceland are leading a European Union–funded research program, FUTUREVOLC, that has brought new monitoring capabilities. "We have installed new seismic stations, [and] an experimental type of new water chemistry that … can look for chlorine, fluorine, sulfur, and other species indicative of volcanic activity," says IMO atmospheric volcanologist Melissa Pfeffer. If there's an explosive eruption, "we have a lot more instrumentation that will go into the field."

In July, as part of FUTUREVOLC, Prata's team delivered three ground-based infrared cameras to Iceland that can detect silicate particles in volcanic ash. Prata and Nicarnica also tested a plane-mounted sensor, the Airborne Volcanic Object Imaging Detector (AVOID) last October: The team released a tonne of ash, scooped from a deposit in Iceland, over France's Bay of Biscay and flew an Airbus airplane fitted with AVOID behind the cloud. The sensor, which uses multispectral cameras to distinguish silicate from ice particles, detected the ash from 60 kilometers away. If Bárðarbunga erupts, Prata says, the team could deploy another AVOID unit in 36 to 72 hours. They are also gearing up to equip partnering airline easyJet with removable ash sensors for future eruptions.

At press time, alarm over Bárðarbunga was subsiding. IMO scientists briefly raised the aviation alert to red on 23 August, when they saw seismic tremors—small, continuous earthquakes thought to be generated when lava encounters ice—followed by rapid seismic swarms. They interpreted this as a likely eruption under the ice—but testing and reconnaissance revealed no meltwater surges, cracks in the ice, or telltale gases, Pfeffer says.

Most current seismic activity is at the tip of a magma intrusion, or dyke, extending tens of kilometers north from the caldera, beyond the edge of the glacier. If magma reaches the surface there, less water interaction would mean a less explosive eruption, Pfeffer says. But the magma could still erupt beneath the glacier. Scientists are standing by. ■

Published by AAAS

ARCHAEOLOGY

A chocolate habit in ancient North America

Residues on pottery suggest close ties between Mesoamerica and cultures to the north

By **Michael Bawaya**

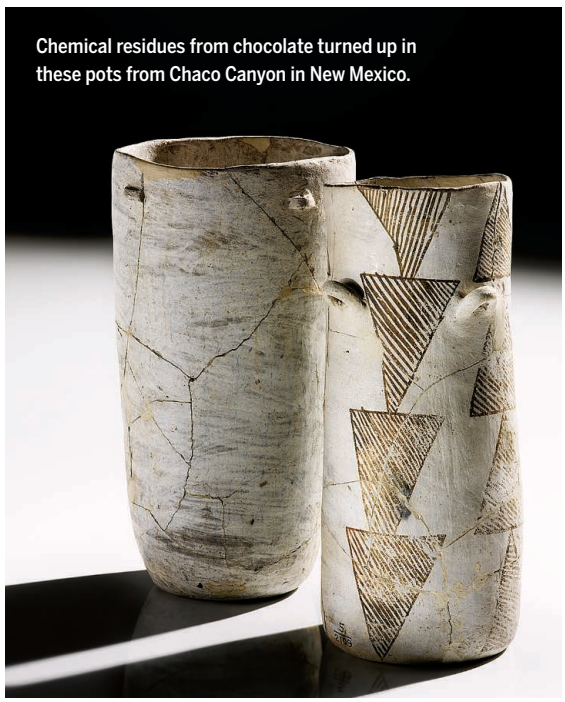

Chemical residues from chocolate turned up in these pots from Chaco Canyon in New Mexico.

PHOTO: NATIONAL MUSEUM OF THE AMERICAN INDIAN, SMITHSONIAN INSTITUTION [052109.000 (RIGHT) 052116.000 (LEFT)]. PHOTO BY WALTER LARRIMORE

For centuries, elite people in ancient Mesoamerica drank a foaming beverage made from the ground beans of the tropical *Theobroma cacao* tree. Served in cylindrical jars and spouted pitchers, this was a chocolate drink steeped in ritual. Priests prepared the beverage in religious ceremonies, and in their great cities in present-day Mexico and Central America the Maya honored the cacao god Ek Chuah.

North America had its great prehistoric cities, too—for example, ancient Cahokia near St. Louis, Missouri, or Chaco Canyon in New Mexico—but for years most archaeologists assumed little contact between the cultures. Chocolate may change that picture, with the recent discovery of subtle residues of it in pots from Cahokia. Added to similar evidence from the Southeast and Southwest, the findings suggest regular trade in cacao—and movements of the people who imbued it with significance—between ancient Mesoamericans and their northern neighbors, says Dorothy Washburn, an archaeologist at the University of Pennsylvania Museum of Archaeology and Anthropology and co-author of a new paper, published online last month. But the new work also reveals the complexities of such residue analysis, she says.

"The separation of archaeology north and south of the border is a political reality but a historical fiction," says archaeologist Stephen Lekson of the University of Colorado, Boulder, who has long argued for contact between the cultures. "If we needed a final nail, cacao shows us that ancient civilizations north of the border were deeply and significantly connected to the civilizations of Mesoamerica."

Though some Mesoamerican artifacts have turned up in the Southwest, the evidence for contact between these two centers of pre-Columbian culture is scant. Many archaeologists believed that few interactions took place across the thousands of kilometers of desert and mountains dividing them. Then, in 2009, researchers reported cacao residue on sherds of cylinder jars from Chaco Canyon. A few years later, Washburn and her husband William, who was then a chemist at Bristol-Myers Squibb, reported that they had detected theobromine, a telltale alkaloid biomarker in *T. cacao*, in about 50 vessels from great house pueblos in Chaco Canyon and from Los Muertos, a Hohokam site in southern Arizona. But many archaeologists, skeptical that consumption of this elite beverage was so prevalent, assumed that the jars were contaminated.

In their new paper, in the *Journal of Archaeological Science*, the Washburns and their colleagues report finding some contamination in the 123 vessels they analyzed, from sites in the Southwest, Southeast, and Midwest dating from 900 to 1400 C.E. They rinsed the ancient ceramics and analyzed the solution for three alkaloids from *T. cacao*—theobromine, caffeine, and theophylline. As controls, they tested pots from times and places where prehistoric cacao usage was extremely unlikely and also sampled dust from the museum shelves where the vessels were stored.

Most vessels had at least a low level of theobromine, which the Washburns attribute to airborne contamination: People today consume so much chocolate and coffee (which contains the same alkaloids) that traces of this molecule are everywhere. Thus, theobromine's mere presence or absence in a pot is not conclusive, Dorothy Washburn says.

But the team found that roughly one-third of the vessels, including 17 from the Southeast and Midwest—and none of the controls—contained significantly higher levels of theobromine, which they attribute to ancient cacao.

The team also studied regional plant databases to make sure that no nearby plants contained theobromine. One Southeastern holly, *Ilex vomitoria*, does, and it was brewed in a tea by ancient people. But cacao has a different alkaloid signature than *I. vomitoria*, with more theobromine than caffeine, so the team says that pots with that higher ratio must have held chocolate.

Added to other lines of evidence for contact, such as Mesoamerican-style platform mounds near Cahokia and ball courts in the Southwest, the cacao residues show robust interaction and a transfer of "ritual concepts" between peoples, Washburn argues.

Some researchers find the new evidence impressive. "It's an important paper," says Steve Wolverton, an archaeologist at the University of North Texas, Denton, who specializes in applying analytical chemistry to archaeology. He noted that there's still a chance that an unknown plant containing theobromine left its mark on the ceramics. But he considers contact between the regions plausible.

Others are doubtful. There are just too many vessels with purported cacao, says archaeologist Timothy Pauketat of the University of Illinois, Urbana-Champaign. The drink is thought to have been reserved for the privileged, yet most of the North American vessels said to have cacao residue come from the hinterlands of Cahokia. He doesn't rule out contact, however: "I will not be surprised if we do find chocolate in a few pots from, say, Cahokia, at some point in the future," he says. But for now, "we have not one bean."

Washburn and Lekson acknowledge that the Mesoamerican palaces were a long way from the grand structures of Chaco and Cahokia. But in their view, ancient Americans could and did travel those distances. Says Lekson: "Before colonial wars, it was all one continent." ■

Michael Bawaya is the editor of American Archaeology.

Downloaded from www.sciencemag.org on August 29, 2014

Published by AAAS

RESEARCH TRANSPARENCY

Why null results rarely see the light of day

"File drawer" study proposes registry for unpublished social science data

By **Jeffrey Mervis**

Researchers have put numbers on the "file drawer" phenomenon, in which scientists abandon results that they believe journals are unlikely to publish.

In a study published online this week in *Science* (http://scim.ag/AFranco), a team at Stanford University in Palo Alto, California, traced the publication outcomes of 221 survey-based experiments funded by the National Science Foundation. Nearly two-thirds of the social science experiments that produced null results, those that did not support a hypothesis, were simply filed away. In contrast, researchers wrote up 96% of the studies with statistically strong results (see graph).

Such practices can skew the literature and lead to wasteful duplication, the authors argue. Their remedy: Deposit all data and study designs into public registries. But while most scientists agree that a registry would be valuable, some worry that it would become burdensome and could even introduce new biases. "I wouldn't want to take all the unpublished findings and give them the same prominence as those containing strong results," says political scientist Gary King of Harvard University.

The question of what to do with null results—when researchers fail to see an effect that should be detectable—has long been hotly debated among those conducting medical trials, where the results can have a big impact on lives and corporate bottom lines. More recently, the debate has spread to the social and behavioral sciences, which also have the potential to sway public and social policy. There were little hard data, however, on how often or why null results were squelched. "Yes, it's true that null results are not as exciting," King says. "But I suspect another reason they are rarely published is that there are many, many ways to produce null results by messing up. So they are much harder to interpret."

In the new study, Stanford political economist Neil Malhotra and two of his graduate students examined every study since 2002 that was funded by a competitive grants program called TESS (Time-sharing Experiments for the Social Sciences). TESS allows scientists to order up Internet-based surveys of a representative sample of U.S. adults to test a particular hypothesis (for example, whether voters tend to favor legislators who boast of bringing federal dollars to their districts over those who tout a focus on policy matters).

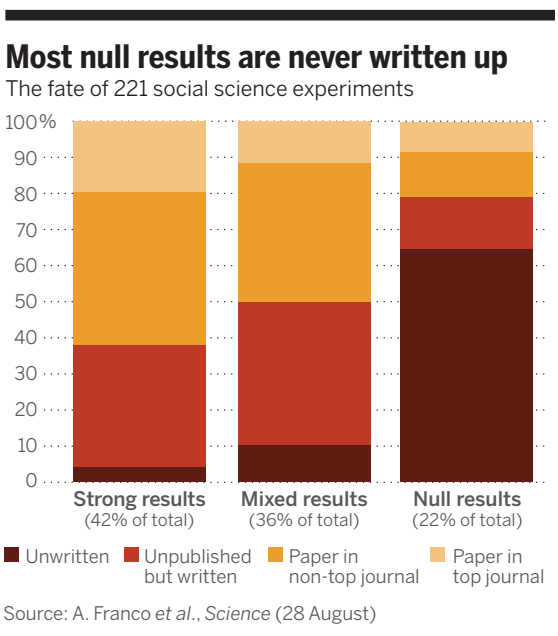

Malhotra's team tracked down working papers from most of the experiments that weren't published, and for the rest asked grantees what had happened to their results. In their e-mailed responses, some scientists cited deeper problems with a study or more pressing matters—but many also believed that journals just wouldn't be interested. "The unfortunate reality of the publishing world are that null effects do not tell a clear story," said one scientist. Said another, "Never published, definitely disappointed to not see any major effects."

Their answers suggest to Malhotra that rescuing findings from the file drawer will require a shift in expectations. "What needs to change is the culture—the author's belief about what will happen if the research is written up," he says.

Not unexpectedly, the statistical strength of the findings made a huge difference in whether they were ever published. Overall, 42% of the experiments produced statistically significant results. Of those, 62% were ultimately published, compared with 21% of the null results. However, the Stanford team was surprised that researchers didn't even write up 65% of the experiments that yielded a null finding.

Scientists not involved in the study praise its "clever" design. "It's a very important paper" that "starts to put numbers on things we want to understand," says economist Edward Miguel of the University of California, Berkeley.

He and others note that the bias against null studies can waste time and money when researchers devise new studies replicating strategies already found to be ineffective. Worse, if researchers publish significant results from similar experiments in the future, they could look stronger than they should because the earlier null studies are ignored. Even more troubling to Malhotra was the fact that two scientists whose initial studies "didn't work out" went on to publish results based on a smaller sample. "The non-TESS version of the same study, in which we used a student sample, did yield fruit," noted one investigator.

A registry for data generated by all experiments would address these problems, the authors argue. They say it should also include a "preanalysis" plan, that is, a detailed description of what the scientist hopes to achieve and how the data will be analyzed. Such plans would help deter researchers from tweaking their analyses after the data are collected in search of more publishable results.

Some researchers are wary. Requiring a preanalysis plan, for instance, could breed resentment, says James Coan, a social psychologist at the University of Virginia in Charlottesville. "It's part of a scientist's job to be canny enough" to do the most appropriate statistical analyses, he says. "The implicit message is that scientists are not to be trusted with those decisions."

Miguel, a member of the recently formed Berkeley Initiative for Transparency in the Social Sciences, is one of many who say a registry should be encouraged, but not imposed. "We want the community to adopt good norms, and then promote them," he says. "That's certainly the most attractive outcome." ■

Downloaded from www.sciencemag.org on August 29, 2014

Published by AAAS

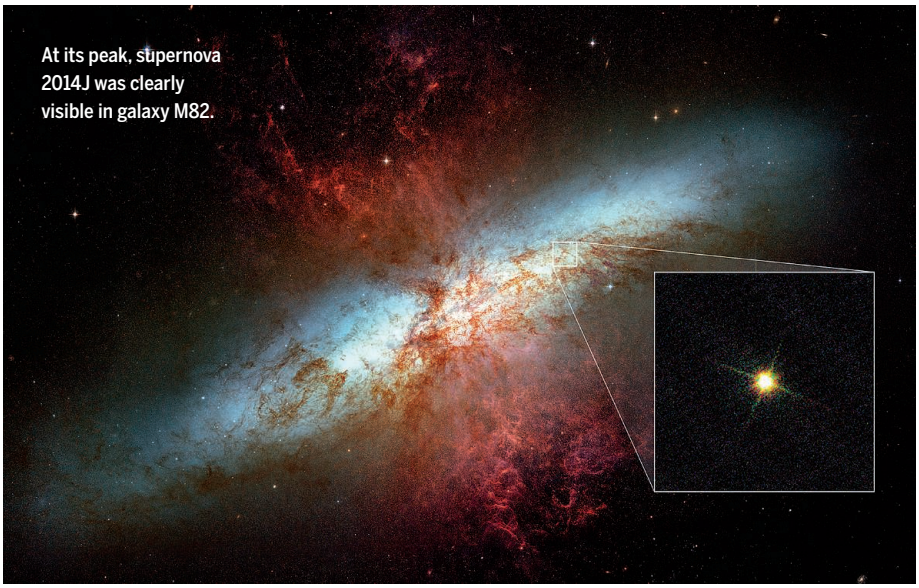

At its peak, supernova 2014J was clearly visible in galaxy M82.

CREDITS: (NEW SUPERNOVA IMAGE) NASA, ESA, A. GOOBAR (STOCKHOLM UNIVERSITY), AND HUBBLE HERITAGE; (IMAGE OF MESSIER 82) NASA, ESA, AND THE HUBBLE HERITAGE TEAM (STSCI/AURA). ACKNOWLEDGMENT: J. GALLAGHER (UNIVERSITY OF WISCONSIN), M. MOUNTAIN (STSCI), AND P. PUXLEY (NSF)

ASTRONOMY

Supernova breaks the mold

A massive explosion in a nearby galaxy both confirms and confounds astronomers' expectations

By **Daniel Clery**

In January, while teaching undergraduates to use a telescope at the University of London Observatory, astronomer Steve Fossey noticed an unusually bright star in the nearby galaxy M82. It was the discovery of a lifetime—the first type Ia supernova in 42 years close enough to Earth to be studied at a whole range of wavelengths. Since then, observations by other astronomers have confirmed the reigning theory for this kind of supernova: that it is a cataclysmic nuclear explosion. But they have also challenged the common assumption that every type Ia is the same.

The implications of that challenge are far-reaching. By comparing the apparent brightness of type Ia supernovae with their supposedly uniform intrinsic brightness, astronomers use them as "standard candles" to measure distances as much as halfway across the universe. Those measurements have enabled them to pin down how fast the universe is expanding—and to detect signs that cosmic expansion is accelerating. But because such blasts are so rare, no one had studied them closely enough to prove that they all occur in the same way, every time.

This week in *Nature*, a team led by Eugene Churazov of the Max Planck Institute for Astrophysics in Garching, Germany, reports that the big picture, at least, appears to be in order. Gamma rays that Churazov and colleagues spotted in observations from Europe's INTEGRAL space telescope confirm that the blast, now dubbed SN 2014J, was powered by the fusion of carbon atoms. "It's a thermonuclear explosion beyond doubt," Churazov says.

The gamma rays are byproducts of a runaway fusion reaction in a white dwarf star. In the classic scenario for the origin of a type Ia, a white dwarf—the glowing ember of a star about as massive as our sun—starts off in a close binary orbit with another, younger star. As the dwarf's gravity strips material from its companion, its mass increases. When it reaches about 1.4 solar masses, the dwarf's carbon-rich core becomes hot and dense enough to ignite, blowing the star apart.

During this violent final act, carbon quickly fuses into heavier nuclei, which in turn fuse into others until they reach nickel-56—the end of the line for fusion. Within a couple of weeks, the nickel decays into cobalt-56, emitting gamma rays, and over the next few months the cobalt decays into stable iron-56, emitting more gammas. Initially, debris from the blast absorbs the gamma rays and re-emits them as light. But after about a month the material becomes diffuse enough for gammas to escape.

Churazov and colleagues measured the rays emitted between 50 and 100 days after the blast. The counts mesh with theory, providing conclusive evidence, the team says, of the supernova's thermonuclear nature. They are also consistent with the classic companion-star mechanism for triggering the blast, which would yield supernovae of consistent brightness.

But other INTEGRAL data are at odds with the classic scenario. A team led by Roland Diehl of the Max Planck Institute for Extraterrestrial Physics in Garching detected nickel-56 decay about 20 days after the blast—much sooner than expected, they reported online in *Science* on 31 July. "This was surprising. It means somehow [some of the nickel-56] was on the outside so the gamma rays could get out," Diehl says.

Diehl says their results favor a scenario in which helium from the companion star accumulates in a ring around the dwarf's equator. The helium ring ignites, fusing helium into carbon and then nickel-56 (the early signal). It also sparks carbon fusion inside the white dwarf, producing a supernova. The new result "shows something like this exists—it's real in nature," Diehl says.

Challenges have also come from observations at other wavelengths. In the classic scenario, some material sucked from the companion star would escape, creating a cloud of gas around the binary pair. The supernova's fireball would hit the gas, producing detectable radio waves and x-rays. But astronomers using an array of European radio telescopes drew a blank. "We saw nothing, down to our instrument's finest sensitivity," says Miguel Pérez-Torres of the Institute of Astrophysics of Andalusia in Granada, Spain. A U.S. team using NASA's Swift and Chandra x-ray satellites also came away empty-handed. Both teams, reporting in *The Astrophysical Journal*, say their results indicate the classic companion star model could not have triggered this blast. They suggest an alternative in which two white dwarfs merge, busting the mass limit and going thermonuclear.

If an alternative mechanism is at work in type Ias, "that may be blurring the distances" astronomers have inferred, says Robert Kirshner of the Harvard-Smithsonian Center for Astrophysics in Cambridge, Massachusetts, a member of the U.S. x-ray team. Helium-triggered fusion could ignite a white dwarf before it reaches the critical threshold of 1.4 solar masses, resulting in a dimmer blast. Merging black holes could exceed the critical mass limit, resulting in a type Ia look-alike with a higher luminosity. Standard candles, Diehl says, may be "anything but standard."

Whatever the trigger, Kirshner is happy at least to have confirmed the thermonuclear nature of the blast. "It's a story we've been telling a long time," he says. "I'm glad to see it's true." ■

Downloaded from www.sciencemag.org on August 29, 2014

Published by AAAS

In search of Green Arabia

Researchers are scouring the now-barren Arabian Peninsula to uncover its hidden role in ancient human migration

By **Andrew Lawler**

In 2001, archaeologist Michael Petraglia was picking through boxes in a museum storeroom in Riyadh, the dusty capital of Saudi Arabia. Petraglia, who had been coaxed by Saudi colleagues to examine the country's prehistory on a Fulbright scholarship, was stunned to find huge numbers of stone tools crafted by ancient hunter-gatherers and apparently tens or even hundreds of thousands of years old.

Like most researchers interested in human origins, Petraglia had dismissed the Arabian Peninsula as a place of marginal interest. Conventional wisdom held that humans settled this inhospitable environment only a few thousand years ago, when domesticated animals like goats and camels made it habitable. "Arabia was thought of as empty," he says.

Intrigued by the tools, he set out to explore the harsh landscape. Walking the sand dunes, the lanky American-born scientist spotted the outlines of long, dry lakes—and littering their vanished shores, he saw innumerable gray and brown triangular pieces of rock expertly knapped by human hands. Today, these deserts are home only to hardy Bedouin nomads and the occasional crew drilling for oil. In the distant past, however, large numbers of our ancestors apparently found this land a congenial home. "I was blown away," recalls Petraglia, now a professor at the University of Oxford in the United Kingdom. "There were artifacts everywhere—it was astounding."

Michael Petraglia in his element, near the oasis of Tayma in Saudi Arabia.

The finds had particular relevance for him. Many researchers contend that modern humans did not expand beyond their African homeland until 55,000 years or so ago, moving quickly eastward around the Indian Ocean to reach Australia within 10,000 years. But even before he spotted those artifacts in the desert, Petraglia had suspected that humans left their home continent tens of thousands of years earlier and wandered slowly eastward, deep into Asia. An ancient Arabia that welcomed modern humans with lakes and greenery fitted neatly into these ideas: "I understood immediately that it was a steppingstone toward South Asia," he says.

Busy with excavations in India, where he found stone tools amid 74,000-year-old volcanic ash—evidence, he says, that our ancestors reached India by that date—Petraglia waited a decade before he returned to Saudi Arabia. His black hair now shading to gray, he is no longer a lone researcher on a brief scholarship. Armed with a $3.3 million grant from the European Research Council (ERC) and backed by a Saudi prince, Petraglia oversees an effort involving a dozen institutions

PHOTOS: RICHARD JENNINGS/UNIVERSITY OF OXFORD (2)

Downloaded from www.sciencemag.org on August 29, 2014

Published by AAAS

Archaeologists dig near ancient Lake Mundafan in the Rub al Khali desert.

and some 50 researchers from around the world who are fanning out across the kingdom to uncover Arabia's role in human dispersal out of Africa.

"Climate is at the heart of this," says Petraglia, who organized a meeting in Oxford in April to discuss new Arabian finds. The human artifacts, though abundant, are mostly undated and difficult to link to specific cultures. But his group and others canvassing neighboring Oman and the United Arab Emirates have amassed evidence that during the crucial time when human ancestors may have left Africa, the Arabian Peninsula was, at least at intervals, temptingly wet and green.

Petraglia's group is using satellite data to map ancient lakes and river systems, then traversing the vast region to confirm their findings on the ground. All told, they have pinpointed more than a thousand ancient lakes that were filled with water off and on during the past few hundred thousand years, along with hundreds of artifact-filled sites. In the past 3 years, his team and others dated a handful of these sites, the earliest of them to 125,000 and 211,000 years ago. What's still missing are bones of the people who left the artifacts, which could reveal who the peninsula's ancient inhabitants were—modern humans or extinct human relatives.

Already, though, Petraglia is convinced that rather than skirting Arabia, modern humans on their way from Africa into the wider world may have colonized it, hopping from lake to lake across the peninsula in pursuit of game and useful plants—a slow, meandering dispersal rather than the rapid march commonly envisioned. In time, he is likely to have the bones that could confirm this scenario—or contradict it.

"With all the activity in Arabia these days, Petraglia's team is going to find a human fossil eventually," says archaeologist John Shea of Stony Brook University in New York. "It is just a matter of time."

ACCORDING TO A SAYING of the Prophet Muhammad, Judgment Day will not come "until the land of the Arabs returns to its state of lush pasture and abundant rivers." The notion that the sand dunes and bare mountains of Arabia were once verdant has long demanded a leap of faith. The region includes the Rub al Khali, Arabic for "the Empty Quarter," the planet's largest sand desert, a Texas-sized wilderness where temperatures soar above 50°C and rain averages fewer than 30 millimeters annually.

Yet even today, Arabia's landscape is not entirely dry or sandy. In the extreme southern province of Dhofar in Oman, for example, more than 200 millimeters of rain green the hills most summers, when the annual Indian Ocean monsoon grazes the Omani coast. And climate models suggest that during the intervals between ice ages, this greening spreads across the peninsula. According to the models, the monsoon system then slips northward, drenching what is now desert for a few thousand years or more before resuming its more typical southerly course.

The most pronounced period of wet and warm weather in the past few hundred thousand years took place about 125,000 years ago, during the height of the last interglacial. Less dramatic monsoon shifts came about 80,000 and 55,000 years ago. "When the water pump is on, brown Arabia turns green," explains geoarchaeologist Adrian Parker of Oxford Brookes University in the United Kingdom, who's involved in the project.

Other geologic clues, such as paleolakes, mineral deposits in caves, and alluvial fans, support the paleoclimate models, pointing to moist periods of varying length, says Richard Jennings, a University of Oxford archaeologist and climate expert who recently spent 4 months gathering field data. During the wet spells, lakes filled up, rivers ran, and a savannalike environment resembling that of today's East Africa dominated Arabia. "There could be tens of thousands of former lakes and wetlands" in Arabia during the wet periods, says Paul Breeze of King's College London, a hydrologist who has already identified 1300 paleolake and wetland sites in just 10% of the peninsula.

Members of a Petraglia expedition recently explored one dry lakebed near the town of Jubbah, about 350 kilometers north of Riyadh in the Kentucky-sized Nefud Desert that lies between Jordan and central Arabia. "Jubbah was a huge lake, thick with reeds and full of mollusk beds," during wet periods, says University of Oxford archaeologist Ash Parton. Given the botanical and faunal remains, the lake "may have been a long-term oasis"—a refuge for plants, animals, and humans even during dry eras, he says. Another paleolake called Mundafan, deep in the forbidding Empty Quarter, was once surrounded by

Making the desert bloom

Researchers are working to further detail Arabia's ancient rivers and lakes.

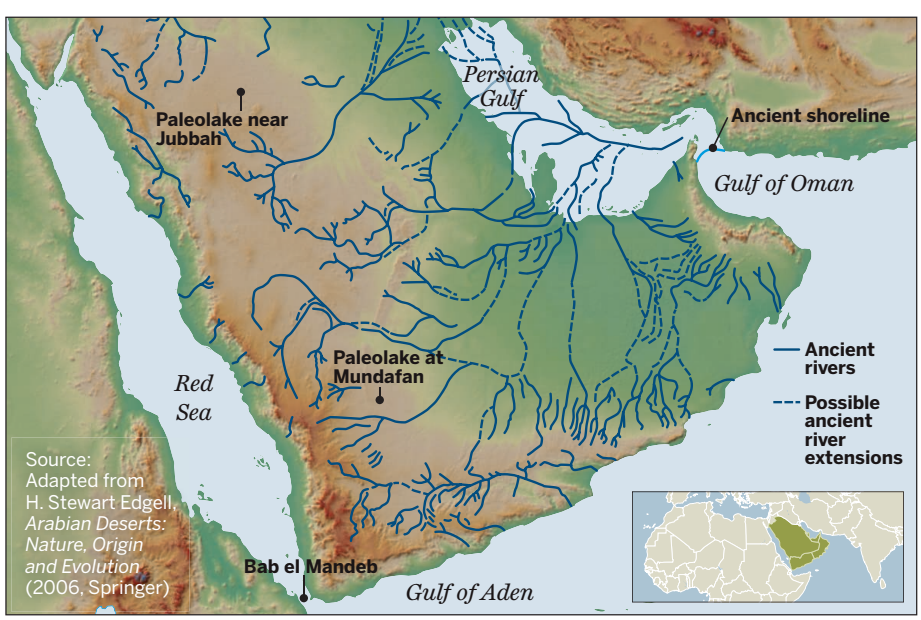

Published by AAAS

grasslands, as shown by studies of microscopic plant remains called phytoliths.

Breeze's team is also mapping a river system, now largely hidden by dunes or shrunk to seasonal wadis, which once flowed north out of the Yemeni highlands, across central Arabia, and into a broad river valley that today is the shallow Persian Gulf. Another system included a river, 2 meters deep, 20 meters wide, and flanked by grasses and palms, that gushed out of the mountains of Oman and traveled 400 kilometers across what is now barren land, according to phytolith and sedimentology work in the United Arab Emirates by Oxford Brookes' Parker.

Discoveries of ancient animal bones provide additional confirmation that during the past half-million years, Arabia periodically was wet enough to draw fauna from Africa and other parts of Asia. Last October, a team led by the University of Oxford's Christopher Stimpson found bones of a panther and elephant in a 325,000-year-old fossil field near the oasis town of Tayma in the Nefud.

How African animals crossed into Arabia—whether across the Sinai Peninsula at one end of the Red Sea or over the Bab el Mandeb strait separating Djibouti from Yemen at the other end (see map, p. 995)—is a matter of debate. Today the southern passage (the name is Arabic for "gateway of anguish" because of its treacherous currents) is 30 kilometers wide. It would have been wider during warmer and wetter eras, although an island chain north of the strait may have made the crossing possible. Baboons, ostrich, mongoose, leopard, cheetah, and genet likely took this route, says geographer Nick Drake of King's College London.

Modern humans appear to have taken the northern route, into the Sinai Peninsula, during the crucial wet period 125,000 years ago. Human bones—the oldest with modern traits found outside Africa—have been excavated from two Israeli caves, and dated to as long ago as 120,000 years (*Science*, 13 May 2005, p. 965). Scientists have long assumed that these early wayfarers died out before spreading deeper into Asia, in part because the terrain between what is now Israel and Iran was hostile desert. "This model is so entrenched," says Petraglia, with a note of impatience. "It was difficult to publish anything to the contrary."

But if Arabia was an appealing route rather than a barrier, he says, then these early modern humans could have tracked familiar game and plants across a welcoming savanna dotted with lakes and crisscrossed with rivers, ultimately crossing into the Indian subcontinent. Arriving in time to experience the fall of ash from the Indonesian volcano of Toba 74,000 years ago, India's early moderns crafted tools resembling those in Africa, he argues. And if Arabia was indeed a steppingstone for eastward-journeying modern humans, its sands must hold stones and bones recording their passage.

Freshwater snails (*top*) and lake sediments show a wetter environment for ancient Arabia.

Ancient people in Arabia left behind tools like this stone point, 7 centimeters high, from paleolake Mundafan.

EARLIER WAVES OF HOMININS certainly left their mark. The University of Oxford's Huw Groucutt recalls his astonishment on stumbling upon one of the largest collections of tools he had ever seen, on the second day of a 2010 survey in the Jubbah region. The stones lay spread out by the thousands across the barren landscape, seemingly as undisturbed as when they were dropped by their ancient users.

Jubbah is no anomaly. Groucutt and others are finding hundreds of sites littered with many thousands of tools. Though few are dated, their styles suggest that substantial populations of archaic hominins made Arabia their home well before modern humans came out of Africa. Along one ancient riverbed in the Nefud, for example, archaeologists found 3000 artifacts on the surface identified as Acheulean, a type of tool first used as early as 1.8 million years ago and linked to *Homo erectus*.

Most of the Arabian artifacts appear more recent, typical of the Middle Paleolithic—a period from about 200,000 years ago until 45,000 years ago, when modern humans might have been spreading across the peninsula. These carefully prepared cores or cobbles were used to produce predictably shaped flakes for cutting and scraping. These are the kind of artifacts Petraglia saw in the Riyadh storerooms—but their precise ages are unknown. Tools can be dated only if they've been dug from dated strata, and the Riyadh artifacts, like thousands of others, were simply picked up from the ground. "Until 2011, there wasn't a single dated [stone] tool in all of Arabia," Petraglia says.

In the past 4 years, however, archaeologists have found a handful of buried artifacts that could be dated using optically stimulated luminescence, which reveals how long an object has been buried. One of the most important finds came from near a cave shelter in the United Arab Emirates called Jebel Faya, some 2000 kilometers east of the African coast. There, a team from the University of Tübingen in Germany led by Hans-Peter Uerpmann found tool assemblages that they dated to 125,000 years ago (*Science*, 28 January 2011, p. 453). The same year, archaeologist Jeffrey Rose and colleagues pinpointed another buried site on the Dhofar coast to about 100,000 years ago. And Petraglia's team has dated objects from five sites near Jubbah to as early as 211,000 years old, with most clustering between 90,000 and 74,000 years ago.

Researchers are now gleaning dates from about 20 other sites in Arabia, and more datable sites are likely to be uncovered soon. Three-quarters of the paleolakes

PHOTOS: (TOP TO BOTTOM) IAN CARTWRIGHT/SCHOOL OF ARCHAEOLOGY, UNIVERSITY OF OXFORD; RICHARD JENNINGS/UNIVERSITY OF OXFORD (2)

Published by AAAS

Even today the southern edge of Arabia turns green when grazed by the monsoon (*top*, in Oman), but most of the peninsula stays dry year-round.

PHOTOS: (TOP TO BOTTOM) RANDOLPH CAGUINTUAN/REUTERS; ADRIAN G. PARKER/OXFORD BROOKES UNIVERSITY

that Breeze surveyed were rimmed with Middle Paleolithic tools.

THE RELATIVELY RECENT dates of these artifacts suggest that modern humans could have been the toolmakers, and the style of the tools is right, too, say Petraglia, Uerpmann, and Rose. They argue that the Arabian Middle Paleolithic tools bear striking resemblance to those made in Northeast Africa between 125,000 and 70,000 years ago.

That idea got a shot of support from an 8 August paper published online in the *Journal of Human Evolution* by Eleanor Scerri of the University of Bordeaux in France and colleagues including Groucutt. The team analyzed artifacts from Jubbah and from Northeast Africa and concluded that although the materials differ, the methods of producing cores and flakes are similar. But Scerri says that some Arabian tools look distinct from those of Africa, with regional flavors that suggest diverse populations or even different types of hominins.

Other researchers say that until archaeologists find the bones of the toolmakers, their identity will remain wide open. Chris Stringer, a paleontologist at London's Natural History Museum, suggests they could have been Neandertals, who survived in Europe until about 40,000 years ago. Although Neandertal remains have not been found south of Iraqi Kurdistan, more than 1500 kilometers north of Riyadh, the new climate data make it conceivable that our extinct cousins, too, were drawn to a green Arabia, Stringer says. "Why not?"

Stony Brook University's Shea adds that the recently discovered Denisovans, archaic humans apparently once widespread in Asia, could also have fashioned the tools after reaching Arabia from the east. "Nobody knows who or what was running around South Asia back then," he says. "Why nobody thinks populations could disperse into Arabia from South Asia is a mystery to me."

A few skeptics adamantly reject the idea of an ancient Arabia bustling with modern humans. To archaeologist Paul Mellars of the University of Cambridge in the United Kingdom, it is inconceivable that modern humans successfully sojourned outside Africa before 55,000 years or so ago. Even then, he says, they did not meander through the Arabian Peninsula but hugged the coast in a quick sprint to Southeast Asia and Australia. "Colonizing the deserts in Arabia would be a suicidal act," he says. "You can say Green Arabia, but it was only green for brief periods." He suggests that any Arabian forays by modern humans were short and ineffectual.

Petraglia admits that the picture remains murky. Until he or others can bring home the bones, "Arabia is a complete unknown when it comes to species," he says. Meanwhile, he says, a slew of peer-reviewed papers will be published in the next year or two as teams work in the field and lab, sharpening the picture of the ancient green place that might have hosted modern humans.

At the Oxford meeting, Prince Sultan bin Salman, a former shuttle astronaut, pledged to create a Green Arabia Institute devoted to research on climate and the early occupation of Saudi Arabia, a sign that research is likely to continue far beyond the ERC grant that ends in 2017. Petraglia himself will be back on the Arabian sands in November. "I can't wait to get back out there," he says. "It's a gold mine. Without Arabia, we can't tell an accurate story of human migration." ■

Published by AAAS

INSIGHTS

Genetics of rabbit domestication *p. 1000*

Tackling viral rebound to cure HIV infection *p. 1005*

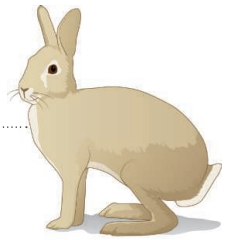

PERSPECTIVES

AMORPHOUS MATERIALS

Glimpsing glass structure under pressure

Nuclear magnetic resonance spectroscopy of a glass under pressure adds to our understanding of network structure

By **Randall E. Youngman**

Archaeologists suggest that the earliest known use of glass, natural obsidian, dates to the Stone Age, with extensive "modern" utilization as early as ~12,500 BCE (*1*). The first historical appearance of synthetic glass is around ~5000 BCE, where it was used as a glaze on clay and stone beads (*2*). Today, glass has broad uses in technology, architecture, packaging, and art. Throughout the technological (and artistic) advances in inorganic glasses, temperature has remained the single most important variable, controlling glass formation and playing a critical role in the short-range atomic structure of these disordered solids. On page 1027 of this issue, Edwards *et al.* (*3*) present findings on glass structure where pressure is the extrinsic variable. Using a novel nuclear magnetic resonance (NMR) methodology, they measured the boron-11 NMR spectrum of a borosilicate glass as a function of pressure in situ, in contrast to the more common postcompression analyses of glass. Their findings, augmented with ab initio calculations, demonstrate deformation of planar BO_3 triangles, a key feature in boron-containing glasses, that leads to their eventual conversion to fourfold coordinated boron.

Glass, given its widespread use, is a surprisingly complex material. Melt together sand, limestone, and soda ash, cool to room temperature, and you obtain soda-lime silicate glass—the most widely used glass in history. One of the attractive features of an inorganic glass-forming system (e.g., soda-lime silicates or alkali borosilicates) is that it can be melted with a variety of inorganic compounds (e.g., to add color or to generate specific optical or physical properties)

Ancient glass art. A portrait of King Amenhotep II, Egypt (1426 to 1400 BCE) measures 4 cm high, 2.9 cm wide, and 3.4 cm deep.

PHOTO: COLLECTION OF THE CORNING MUSEUM OF GLASS, CORNING, NY. PURCHASED IN PART WITH FUNDS FROM THE MUSEUM ENDOWMENT FUND

Published by AAAS

and, with sufficiently rapid cooling, force the molten liquid to solidify without crystallization. The critical cooling rate necessary for glass formation depends on composition (*4*), and understanding glass-forming tendencies for various inorganic systems has been critical in the development of glasses for optics, automotive, and architectural uses, as well as the recent application of glass in liquid-crystal display panels and as protective covers in consumer electronics.

However, the process of cooling the melt into glass is much more complicated, especially when other components are included. For example, glasses containing boron oxide (e.g., borosilicates), which is typically added as a flux, have short-range atomic structures that are influenced by the cooling rate, and thus the temperature, at which the melt solidified (*5*). The study of structure-property relations has emerged as an important field in tandem with the development of methods to characterize glass structure. One of the more mature and arguably most powerful techniques for glass structure determination is NMR (*6*). Given the importance of boron, silicon, aluminum, and other elements in glasses used in various technologies, NMR is particularly well suited for study of glass network structure and the effect of both temperature and pressure.

The first of these variables, temperature, can be studied either directly by measuring NMR and other spectroscopic data as a function of temperature, sometimes exceeding the glass transition temperature (where viscosity is 10^{12} Pa·s), or indirectly through examination of glasses having experienced different cooling rates (e.g., thermal history) (*7*). For both practical applications and fundamental understanding, the temperature sensitivity of glass structure and related glass properties continues to captivate researchers. Glass scientists, and especially geochemists interested in silicates, have gained useful understanding of the temperature dependence of glass and melt structures. In turn, these findings have resulted in powerful new approaches to optimize properties of glass. Glass artists anneal their finished work to eliminate thermal stresses and increase their durability. Glass manufacturers might anneal glass for the same reason, but they also seek to leverage the structure-property relations in their materials to reduce warp, compaction, and other detrimental physical changes that often accompany the heating and cooling cycles that reset the thermal history of a glass.

A classic example of glass under pressure. Understanding glass structure and dynamics as a function of temperature, pressure, or both is critical in development of glasses for high-technology applications and for advances in the geophysics of volcanology and magmas.

Pressure is another variable in materials processing that has gained considerable traction in the glass science community. As with temperature, the primary drivers of research into glasses and high pressure are geoscientists, constantly seeking a better understanding of volcanology and magmatic processes (*8*, *9*) (see the figure). In glass science, pressure effects on structure and properties are generally studied on glasses after application of pressure (i.e., postcompression) (*10*). Recently, the development of high-temperature and high-pressure apparatuses has opened up research into glasses cooled from moderate to high temperatures while under pressure (*11*). These types of experiments continue to provide new insight into glass attributes, but only after application of pressure, where it must be assumed that pressure had a lasting impact on the material. The simultaneous combination of pressure and temperature is unfortunately limited to somewhat modest pressures (less than 1 GPa), at least when working with samples of sufficient size for most property and structural characterization.

The work of Edwards *et al.* uncovers the mechanism of the conversion of threefold BO_3 into fourfold BO_4 that had previously been studied at ambient conditions as a function of cooling rate, or in glasses after being subjected to high pressure. This glimpse into glass structure while under pressure may signify the start of a new approach to understanding inorganic glasses, even those that we have "understood" for centuries. Long-standing limitations in understanding the effect of pressure on glass structure make the work of Edwards *et al.* that much more remarkable in that these researchers have devised a combined experimental and computational approach to study the boron environment of a borosilicate glass while maintaining the application of pressure. These types of experiments now begin to unveil the mechanisms of how liquids and glasses respond to pressure. They hold great promise for understanding natural glasses and liquids, but also may generate considerable interest in leveraging pressure in the commercial glass industry. Work is already under way to investigate the effect of pressure on key glass attributes (*12*), but mechanistic understanding of the type described by Edwards *et al.* is an exciting and necessary contribution to understanding an ancient material. ■

Science and Technology Division, Corning Inc., Corning, NY 14831, USA. E-mail: youngmanre@corning.com

REFERENCES

1. A. M. Pollard, C. Heron, *Archaeological Chemistry* (Royal Society of Chemistry, Cambridge, 2008).
2. K. Cummings, *A History of Glassforming* (A & C Black, London, 2002).
3. T. Edwards, T. Endo, J. Walton, S. Sen, *Science* **345**, 1027 (2014).
4. P. I. K. Onorato, D. R. Uhlmann, *J. Non-Cryst. Solids* **22**, 367 (1976).
5. J. F. Stebbins, S. E. Ellsworth, *J. Am. Ceram. Soc.* **79**, 2247 (1996).
6. H. Eckert, *Prog. Nucl. Magn. Reson. Spectrosc.* **24**, 159 (1992).
7. F. Angeli *et al.*, *Phys. Rev. B* **85**, 054110 (2012).
8. S. Webb, *Rev. Geophys.* **35**, 191 (1997).
9. G. Calas, G. S. Henderson, J. F. Stebbins, *Elements* **2**, 265 (2006).
10. S. K. Lee *et al.*, *J. Phys. Chem. C* **116**, 2183 (2011).
11. M. M. Smedskjaer *et al.*, *Sci. Rep.* **4**, 10.1038/srep03770 (2014).
12. M. N. Svenson *et al.*, *ACS Appl. Mater. Interfaces* **6**, 10436 (2014).

10.1126/science.1258785

PHOTO: U.S. GEOLOGICAL SURVEY

Published by AAAS

EVOLUTION

On the origin of Peter Rabbit

Domestication of rabbits led to changes across the genome, particularly in regions related to brain development

By **Kirk E. Lohmueller**

Which genetic changes occur when animals are domesticated, or selectively bred in order to increase the frequency of characteristics that humans find desirable? Studies aiming to address this question can not only reveal the biological basis of important phenotypes, but also provide a glimpse into the mechanisms of rapid evolutionary change. On page 1074 of this issue, Carneiro *et al.* (*1*) report a population genomic study of rabbit domestication that shows that there is no single "domestication gene." Rather, many genetic variants across the genome have been affected by natural selection throughout domestication. Further, these variants tend to be in regulatory regions located in genes related to brain development.

Advances in genomic technology have allowed researchers to compare the genomes of wild and domesticated populations in search of genetic changes associated with domestication. Recent studies on domesticated chickens (*2*), pigs (*3*), and dogs (*4*) have found candidate regions for selective sweeps—or areas of the genome where natural selection has increased a favorable allele to high frequency—associated with domestication. However, they did not assess the broader evolutionary questions regarding the type of genomic changes and mechanism of selection involved.

Rabbits provide a potentially powerful system to study the genetics of animal domestication. Historical records and previous genetic work (*5*) suggest that rabbits were domesticated from a single wild population in Southern France about 1400 years ago. The domestication process for rabbits thus appears to have been simpler than that for other species, which have either undergone multiple independent domestication events (*6*) or experienced extensive back-crossing with wild populations (*7*, *8*). Further, non-domesticated descendants of the ancestral rabbit population are readily available, providing a control group that may not be available for other species.

Department of Ecology and Evolutionary Biology, Interdepartmental Program in Bioinformatics, University of California, Los Angeles, CA 90095, USA. E-mail: klohmueller@ucla.edu

To search for the genetic changes associated with rabbit domestication, Carneiro *et al.* performed whole-genome sequencing of six breeds of domestic rabbits, wild rabbits in Southern France (descendants of the same putative ancestral population as the domesticated rabbits), and wild rabbits from the Iberian Peninsula. This sequencing strategy allows for relatively unbiased estimates of allele frequencies at variable sites across the genome.

The authors then searched for signatures of selection in domestic rabbits using two statistical methods. First, they looked for regions of the genome that have large differences in allele frequency between domestic and wild rabbits and that also show reduced genetic variation. Both patterns are signatures of selective sweeps (*9*). A major strength of the study is that the authors attempt to control for population history by assessing the probability of these patterns under models of population history that do not include selection. No individual region of the genome had patterns of variation so unexpected that they could not be explained by population history alone. However, the authors found roughly twice as many unusual regions in the data as expected under models with only population history, suggesting that population history, without natural selection, cannot explain the genome-wide patterns of variation. Second, the authors used a model-based test for selection (*10*) and found 78 regions that were significantly unusual under their demographic model, even after accounting for the number of statistical tests performed. Taken together, these results provide strong evidence for selection at many loci throughout the genome.

Carneiro *et al.* then examined the types of functional changes that may underlie these sweeps. Those variants showing the largest differences in frequency between wild and domesticated rabbits tend to be located more often than expected by chance at conserved noncoding regions, untranslated regions, and codings regions. Variants showing less extreme differences in allele frequency between wild and domestic rabbits were still enriched in untranslated regions and conserved noncoding regions. However, the enrichment in coding regions disappeared. These results suggest that domestication involved shifts in allele frequency at many loci across the genome and that these variants may be regulatory, rather than coding.

Finally, Carneiro *et al.* examined how the variants showing the largest differences in allele frequency between wild and domestic

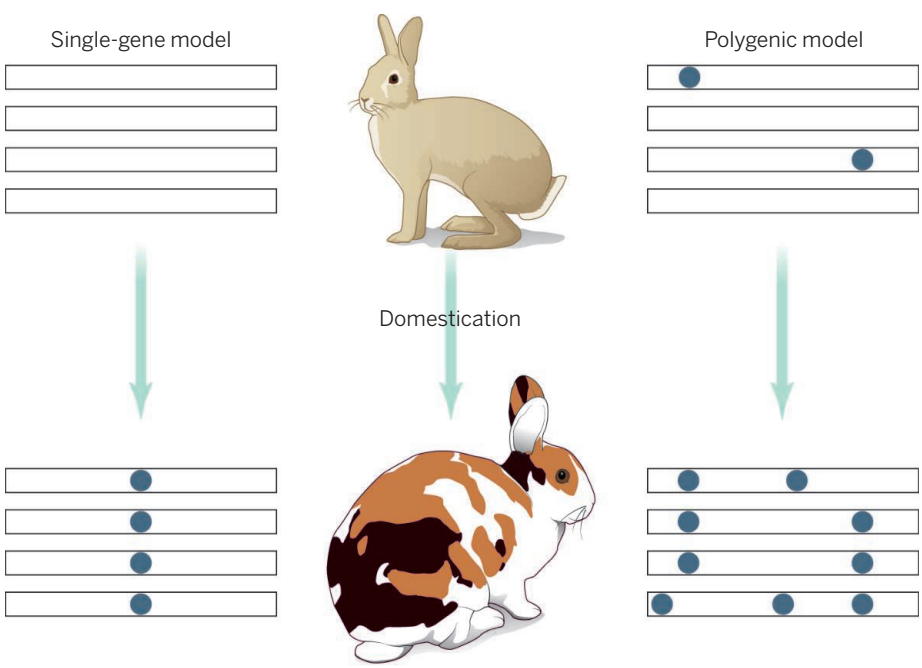

Two models of the genetic basis of domestication. In the single-gene model, a single mutation increases in frequency as a result of positive selection and is carried by all the domesticated animals. In the polygenic model, domestication occurs by changes at many genetic variants, each of which has an individually small effect. Carneiro *et al.* favor the polygenic model for rabbit domestication.

ILLUSTRATION: P. HUEY/*SCIENCE*

Published by AAAS

rabbits cluster into biologically functional categories. The categories showing the most significant enrichment of differentiated variants were related to nervous system development. Additionally, the differentiated variants preferentially occurred in genes that, when disrupted in mice, give rise to defects in the nervous system. These results suggest that selection during domestication may have affected genes relating to specific behaviors, perhaps those allowing the animals to better interact with humans.

The study of Carneiro *et al.* adds to the growing literature suggesting the importance of polygenic adaptation as an evolutionary process (see the figure) (*11*, *12*). In addition to there being many putatively selected variants, rabbits show other patterns often associated with the polygenic model. For example, at least some of the selection occurred on genetic variation that already existed in the population, rather than on new mutations. Second, many of the putatively selected variants are not carried by all of the domesticated rabbits. These findings do not rule out the occurrence of classic selective sweeps, in which the selected allele becomes fixed in the population. Indeed, Carneiro *et al.* also found evidence of such sweeps. Rather, the results suggest that both mechanisms are likely occurring.

It is tempting to compare the genomic properties of selection during domestication in rabbits to that in other species, such as dogs, pigs, horses, and chickens. However, such a comparison is fraught with complications at the present time. The genomic studies in the different taxa use very different designs and statistical methods. A proper comparison of the key attributes of selection during domestication awaits systematic genome resequencing across the multiple taxa, combined with application of the same statistical methods to the data. Such comparative population genomic analyses promise to reveal general insights into the domestication process and how rapid evolution under strong selection operates across genomes. ■

REFERENCES

1. M. Carneiro *et al.*, *Science* **345**, 1074 (2014).
2. C.-J. Rubin *et al.*, *Nature* **464**, 587 (2010).
3. C.-J. Rubin *et al.*, *Proc. Natl. Acad. Sci. U.S.A.* **109**, 19529 (2012).
4. B. M. vonHoldt *et al.*, *Nature* **464**, 898 (2010).
5. M. Carneiro *et al.*, *Mol. Biol. Evol.* **28**, 1801 (2011).
6. G. Larson *et al.*, *Science* **307**, 1618 (2005).
7. A. H. Freedman *et al.*, *PLOS Genet.* **10**, e1004016 (2014).
8. V. Warmuth *et al.*, *Proc. Natl. Acad. Sci. U.S.A.* **109**, 8202 (2012).
9. P. C. Sabeti *et al.*, *Science* **312**, 1614 (2006).
10. R. Nielsen *et al.*, *Genome Res.* **15**, 1566 (2005).
11. J. K. Pritchard, J. K. Pickrell, G. Coop, *Curr. Biol.* **20**, R208 (2010).
12. P. W. Messer, D. A. Petrov, *Trends Ecol. Evol.* **28**, 659 (2013).

10.1126/science.1258775

Taking a measure. A view of the Taurus constellation, including two stellar clusters whose distances were provided by the Hipparcos satellite. The Pleiades (top right) and the Hyades (bottom center, slightly to the right of the bright red star Aldebaran). Only the Pleiades distance has been controversial, raising the possibility that hydrogen-burning stars in the Hyades and Pleiades could be intrinsically very different in their fundamental properties.

ASTRONOMY

One good cosmic measure

Radio-wave interferometry provides an accurate measurement of cosmic distances

By **Léo Girardi**

As Earth orbits around the Sun, nearby stars are seen to move against the background of more distant stars and galaxies. The angular amplitude of this motion is called parallax and provides a direct, trigonometric measurement of the stellar distances as compared to the size of Earth's orbit. A great achievement of the European Space Agency's satellite Hipparcos (*1*) was the measurement of parallaxes of over 100,000 stars simultaneously, making it widely recognized as having provided accurate distances to thousands of normal stars and to a few star clusters. Since the first release of the Hipparcos results in 1997, however, it was noted that the distance obtained for the Pleiades star cluster was abnormal (see the figure). Its hydrogen-burning stars, when compared with stars of similar effective temperature in other well-measured clusters like the Hyades, appeared to be systematically too faint, were the Hipparcos-derived distances adopted. The effect implied either that the Hipparcos distances were too short or that Pleiades hydrogen-burning stars had some very peculiar property, such as an extremely high fraction of helium in their interiors (*2*). On page 1029 of this issue, Melis *et al.* (*3*) present new observations of stars in the Pleiades cluster, demonstrating that the Hipparcos-derived distances were indeed off by 10%. Their radio-wave interferometry approach thus demonstrates a precise and accurate method to determine stellar distances.

For the Pleiades cluster, Melis *et al.* point decisively to a distance of 136 parsecs, which is essentially the same distance expected by the stellar physicists under the assumption that hydrogen-burning stars share the same intrinsic properties, independently of the clusters where they are born. Melis *et al.* applied a completely independent technique, using very large baseline interferometry at radio wavelengths to measure the angles between five Pleiades stars and a background quasar. Even if skepticism about the Hipparcos distance to the Pleiades has somewhat prevailed among the stellar-modeling community, now it should be more widely apparent that the problem is not in understanding what weird stellar physics could be going on in the Pleiades hydrogen-burning stars. The problem is understanding what went wrong with the Hipparcos measurements.

Hipparcos used a simple, if revolutionary, approach whereby the entire sky was continuously scanned over 3 years. Using two slits separated by 58°, there were multiple measurements for each star of its position with respect to those of widely separated stars; their best-fit positions, angular velocities, and parallaxes could be derived by performing a global optimization of the astrometric solution. However, a careful examination of

CREDITS: TILL CREDNER AND SVEN KOHLE, WWW.ALLTHESKY.COM

Published by AAAS

the Hipparcos raw data by van Leeuwen (*4*) led to identification and correction of many artifacts and systematics in the derivation of parallaxes, but, surprisingly, the apparently too-short distance to the Pleiades did not change. Even more surprisingly, evidence of two other clusters with "anomalous" hydrogen-burning stars was found.

Hipparcos has contributed decisively to a more solid distance scale to normal and nearby stars, but it was still not enough to establish a solid scale for extragalactic studies; for instance, it did not provide accurate parallaxes to Cepheids, the stellar pulsators that constitute the basic tool to measure distances to galaxies up to several megaparsecs away. This was among the strong scientific cases made for the recently launched satellite Gaia (*5*). In Gaia, the concept of global astrometric solutions pioneered in Hipparcos will be brought to extreme limits, with a huge forward leap in terms of targeted accuracy and number of observed stars. The astronomy community holds great expectations for Gaia, if not for drawing a detailed map of our sector of the Milky Way galaxy, at least for providing robust distances to an appreciable number of Cepheids. But the case of the Pleiades indicates that, under circumstances we still do not understand, the method of global astrometric solutions to be used by Gaia might fail.

> ***"... understanding what went wrong between Hipparcos and the Pleiades will be crucial."***

In addition, it is as yet unclear whether similar errors could be randomly affecting field stars, far away in space from the Pleiades. It has been suspected that the failure is the manifestation of widespread spatially correlated errors in Hipparcos (*6*), but this suspicion has not been translated into a solid quantitative explanation or correction to the previously derived parallaxes (*4*). It is also striking that, considering the impressive effort being put in the simulation of the Gaia astrometry (*7*), no simulations seem to have predicted or explained the Hipparcos output for the Pleiades.

It may well be that Gaia data itself will reveal the solution to the Hipparcos puzzle in a couple of years, either telling us clearly where these putative correlated errors are or favoring the solution that apparently accommodates all distance measurements: namely, that the Pleiades have an elongated spatial distribution, with the bright stars observed by Hipparcos being much closer than its faint stars (*8*). Indeed, the faint stars are those now being measured at larger distances and correspond to the hydrogen-burning stars that are usually compared to stars in the Hyades and other clusters. This kind of solution, however, sounds very unlikely and still requires some unidentified physics taking place in the brightest Pleiades stars.

At the very least, we have to agree with Melis *et al.* that targeted observations using independent methods are necessary for a cross check of the parallaxes provided by the global astrometric solutions, which hardly give the average astronomer a chance for a detailed check of the methods and results. Unfortunately, high-resolution radio observations such as those used by Melis *et al.* represent a substantial observational effort, involving a network of 13 radio telescopes distributed around the globe and covering a time span of 1.5 years. Such efforts are too demanding to be considered as a systematic check of Gaia parallaxes. Moreover, they can only be applied to cool stars or to those rare compact stellar objects that emit in radio wavelengths. At optical wavelengths, hope of improving parallax measurements comes from a scanning technique being developed by the Space Telescope Science Institute team to measure distances to individual Cepheids (*9*), but its promise is limited by the constraints on the Hubble Space Telescope observing time. It is not even guaranteed that Hubble will keep working long enough for an appreciable number of parallaxes to be determined.

Because systematic checks of Gaia distances will not be possible, understanding what went wrong between Hipparcos and the Pleiades will be crucial. Bringing closure to the issue would increase our confidence in the results of Gaia enormously and hopefully would prevent a new "Pleiades controversy" from happening a few years from now. ■

REFERENCES

1. The Hipparcos and Tycho Catalogues (ESA Publications Division, 1997 Series, Noordwijk, Netherlands, ESA SP Series, vol. no.: 1200, 1997).
2. M. H. Pinsonneault *et al.*, *Astrophys. J.* **504**, 170 (1998).
3. C. Melis *et al.*, *Science* **345**, 1029 (2014).
4. F. van Leeuwen, *Hipparcos, the New Reduction of the Raw Data*, Astrophysics and Space Science Library, Vol. 350 (Springer, Berlin, 2007)
5. M. A. C. Perryman *et al.*, *Astron. Astrophys.* **369**, 339 (2001).
6. V. K. Narayanan, A. Gould, *Astrophys. J.* **523**, 328 (1999).
7. L. Lindegren *et al.*, *Astron. Astrophys.* **538**, A78 (2012).
8. D. Stello, P. E. Nissen, *Astron. Astrophys.* **374**, 105 (2001).
9. A. G. Riess, S. Casertano, J. Anderson, J. MacKenty, A. V. Filippenko, *Astrophys. J.* **785**, 161 (2014).

Istituto Nazionale di Astrofisica (INAF), Osservatorio Astronomico di Padova, Padova I-35122, Italy. E-mail: leo.girardi@oapd.inaf.it

10.1126/science.1258425

CELL BIOLOGY

Many modes of motility

Cells use a piston-driven mechanism, among others, to migrate

By **Douglas W. DeSimone** *and* **A. Rick Horwitz**

Directed cell migration in multicellular organisms is essential to fundamental processes including embryogenesis, defense from infection, and tissue repair and regeneration. It is also key in cancer progression as metastatic cells disseminate throughout the body. Much research has focused on cells migrating on two-dimensional (2D) extracellular matrices (ECMs) because such experimental systems are easily accessible and observable. However, recent studies of cell motility in 3D environments are challenging the ubiquity and generality of 2D-based models. On page 1062 of this issue, Petrie *et al.* (*1*) propose that in a constrained 3D space, a cell can use its nucleus as a piston to polarize internal pressure and create protrusions that facilitate movement.

Studies of cell motility on 2D ECMs have produced a detailed outline of some basic migration mechanisms, including the formation of lamellipodia arising from actin nucleation and polymerization at the cell front, adhesion-mediated traction, actomyosin contractility, and integrated signals orchestrated by adhesion and Rho guanosine triphosphatases (*2*). Recent studies of migration in situ have revealed other potential migration modes, depending on the cell type and the physical environments through which the cells migrate (*3*–*5*). The mechanisms that drive and control these alternative modes can vary dramatically and appear to repurpose elements of a canonical migration machinery. To elucidate these new mechanisms, attention has turned to experimental conditions that more closely resemble the 3D environments encountered in vivo. From this, many cellular responses have emerged reflecting the ECM molecular composition, the density and orientation of fibrillar elements (e.g., collagen), and the bulk and local stiffness (*6*). For example, incorporating cells into engineered 3D ECMs or decellularized, cell-derived matrix can promote nonlamellipodial migration. Such modes include blebbing and the formation

Published by AAAS

of blunt-ended cylindrical extensions called lobopodia (*7*). In the blebbing mode, some components common to the lamellipodial migration machinery are reorganized; in both cases, myosin II drives movement.

Petrie *et al.* investigated how lobopodia form and mediate the migration of human primary fibroblasts in 3D matrix environments. Cells forming lobopodia displayed numerous short-lived membrane blebs along their lateral surface. Blebbing is thought to occur where the underlying actin-rich cortex is weak, and thus more susceptible to "ballooning out" in response to an actomyosin-driven increase in intracellular pressure. In some cell types, this blebbing behavior is sufficient to promote cell migration (*8*). However, Petrie *et al.* considered side blebs as indicative of an increase in hydrostatic pressure required to generate the lobopodial protrusion. The authors compared the intracellular hydrostatic pressures generated by cells forming lamellipodia or lobopodia in 2D or 3D matrices, respectively. Intracellular pressures were substantially higher in lobopodial cells. Moreover, intracellular pressure in the forward compartment—defined by the presence of lobopodia and side blebs—was greater than that in the trailing compartment (2400 Pa versus 900 Pa). The border of these two compartments was defined by the nucleus, which suggests that this organelle might act as a "plug" and maintain a pressure differential. Lobopodial behavior, overall morphology, maintenance of pressure differences between the two compartments, and periodic movement of the nucleus all required actomyosin contractility. The latter suggests the remarkable possibility that the nucleus is pulled forward like a piston to pressurize the forward compartment and initiate blebbing and lobopodia formation (see the figure).

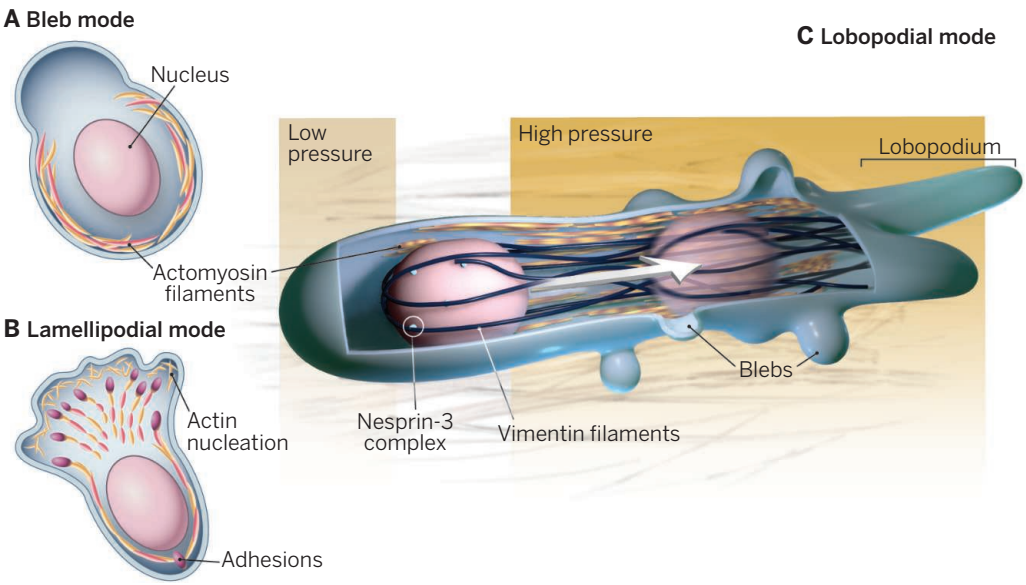

Cell migration, three ways. (**A**) In the bleb mode, contractile actomyosin filaments increase intracellular hydrostatic pressure to push the membrane out through areas of weakness. (**B**) The lamellipodial mode is driven by actin polymerization and adhesion at the front and by actomyosin contraction and de-adhesion at the rear. (**C**) The lobopodial mode is observed in a constrained 3D matrix environment. The nucleus compartmentalizes the cell and is pulled forward by actomyosin filaments, which act through vimentin filaments and nucleus-associated nesprin-3 to create high pressure at the front. This leads to the formation of a protrusion (lobopodium).

How might contractility of the actomyosin cytoskeleton drive the nuclear piston? Petrie *et al.* noted that vimentin filaments and myosin IIA are polarized to the anterior of lobopodial cells. The authors propose that actomyosin contractility acts through vimentin to pull the nucleus forward. A key player in this process is likely nesprin-3, a nuclear membrane protein presumed to link the nucleoskeleton to the vimentin and actin cytoskeletons (*9*, *10*). Indeed, reducing nesprin-3 expression decreased the migration velocity and overall intracellular pressure, thus converting lobopodial to lamellipodial protrusions. This conversion was also seen when constituents of the RhoA signaling pathway, which modulates actomyosin activity, were inhibited.

Other mechanisms have been proposed to account for lamellipodial-independent modes of cell migration in constrained 3D environments. Tumor cell migration in highly confined microfluidic channels is reported to require neither actin polymerization at the leading edge nor myosin II–dependent contractility (*11*). Here, the proposed model is that motility arises from a polarized distribution of ion channels and aquaporins, which controls water permeation and cell volume. When and where such highly constrained environments exist in vivo and promote this mode of migration remains to be established; however, the mechanism appears very different from the pressure-driven formation of blebs and lobopodial protrusions, which requires myosin II.

It is clear that many cells have an arsenal of potential mechanisms for motility at their disposal and use it to adapt to the complex physical and chemical environments that they encounter in vivo. Petrie *et al.* show that the plasticity of an individual fibroblast, as it switches from actin-driven broad lamellipodial protrusion to a nuclear piston lobopodial-driven mode of migration, depends on differences in ECM architecture. As new migration mechanisms are revealed, many questions arise about the role of cell adhesion, the generation of cell polarity, the role of actin polymerization, and the integration of corresponding cellular behaviors. A major question concerns when and where these kinds of migration are used.

The various modes of cell movement have implications for engineering synthetic matrices to promote tissue regeneration and for developing strategies to inhibit metastatic cell migration. But just when we thought we were beginning to understand cell migration, we may only be recognizing one limb and a few branches of what is turning out to be a very large tree. ■

Department of Cell Biology, University of Virginia School of Medicine, Charlottesville, VA 22903, USA. E-mail:desimone@virginia.edu; horwitz@virginia.edu

ILLUSTRATION: V. ALTOUNIAN/*SCIENCE*

REFERENCES

1. R. J. Petrie, H. Koo, K. M. Yamada, *Science* **345**, 1062 (2014).
2. A. J. Ridley *et al.*, *Science* **302**, 1704 (2003).
3. P. Friedl, S. Alexander, *Cell* **147**, 992 (2011).
4. P. Friedl, K. Wolf, *J. Cell Biol.* **188**, 11 (2010).
5. S. Nourshargh, P. L. Hordijk, M. Sixt, *Nat. Rev. Mol. Cell Biol.* **11**, 366 (2010).
6. K. E. Kubow, S. K. Conrad, A. R. Horwitz, *Curr. Biol.* **23**, 1607 (2013).
7. R. J. Petrie, N. Gavara, R. S. Chadwick, K. M. Yamada, *J. Cell Biol.* **197**, 439 (2012).
8. E. K. Paluch, E. Raz, *Curr. Opin. Cell Biol.* **25**, 582 (2013).
9. M. L. Lombardi *et al.*, *J. Biol. Chem.* **286**, 26743 (2011).
10. K. Wilhelmsen *et al.*, *J. Cell Biol.* **171**, 799 (2005).
11. K. M. Stroka *et al.*, *Cell* **157**, 611 (2014).

10.1126/science.1259176

Published by AAAS

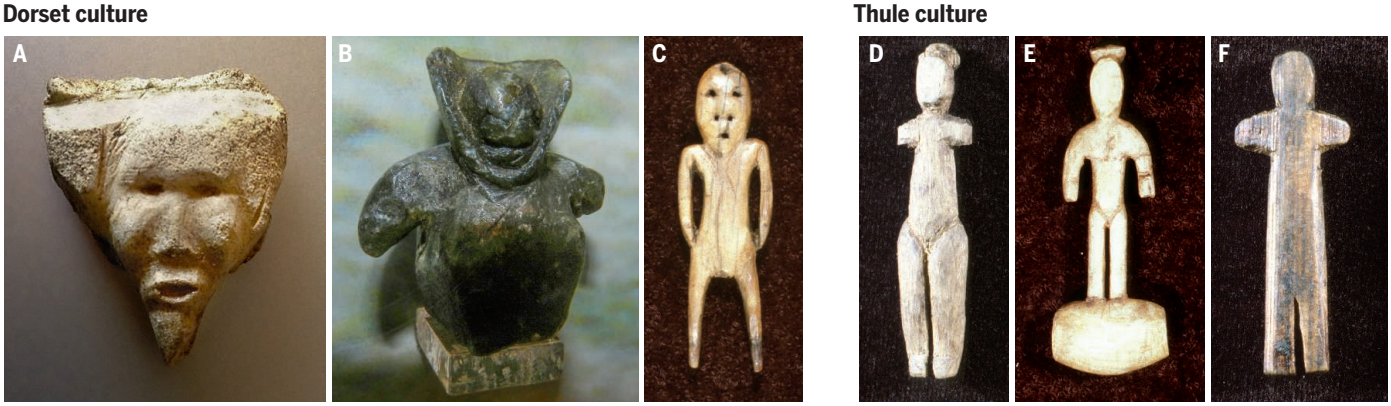

Arctic cultures. Figurines made by the Dorset people show facial features and the high-collared parkas that they wore. The Thule, who eventually replaced the Dorset, made figurines with flat, featureless faces; the arms are often just suggested by protruberances. Raghavan *et al*.'s data suggest that the two cultures did not mix genetically, possibly because the Dorset died out before the Thule arrived. The figurines were found on Bathurst Island (**A**), Shuldham Island (**B**), and Devon Island (**C** to **F**).

ANTHROPOLOGY

Stories of Arctic colonization

Genetic data elucidate the population history of the North American Arctic

By **Robert W. Park**

In the winter of 1902 to 1903, the last original inhabitants of two islands at the north end of Canada's Hudson Bay perished from a disease introduced by whalers. Called Sadlermiut by the Aivilingmiut Inuit who occupied the adjacent mainland coast, they appear to have actively avoided interaction with any people outside their own society. According to the Aivilingmiut, the Sadlermiut had spoken a strange dialect; were bad at vital Inuit skills such as making skin clothing, constructing igloos, and tending oil lamps; were uncleanly; and did not observe standard Inuit taboos. They also made sharp stone tools by flaking chert, whereas all other Inuit groups in the Canadian Arctic and Greenland made sharp stone tools mainly by grinding slate (*1*). Who were these mysterious people (*2*, *3*)? On page 1020 of this issue, Raghavan *et al.* (*4*) report genetic data that shed light on this and other questions about the population history of the North American Arctic.

At the time of the Sadlermiut's demise, nothing was known about the Dorset culture that inhabited much of the Canadian Arctic between 3000 and 1000 years ago. This culture was the last of the Paleo-Eskimo cultures who first colonized Arctic Canada and Greenland from Alaska ~4500 years ago. All Paleo-Eskimo cultures made flaked stone tools, and their artifact styles were very different from those of their Inuit successors (see the figure). By the 1960s, it had become apparent that the Paleo-Eskimos had been replaced throughout their territories ~1000 years ago by the Alaskan Thule culture, who made stone tools by grinding slate and were, researchers concluded, the direct ancestors of the Inuit.

What happened to the people of the Dorset culture? Did they join Thule societies and abandon their own cultural traditions, as most researchers concluded, or did they die out? And given the apparent uniqueness of the Sadlermiut among the Inuit populations of Arctic Canada and Greenland, could they have been a relict Dorset population?

Until recently, these questions could only be addressed through comparisons of technologies and artifact styles. Raghavan *et al.* now report genetic data that elucidate the population history of the North American Arctic and that explain what happened when the Thule replaced the Dorset, and how the Sadlermiut fit into that transition. They are not the first to carry out genetic analyses in this vast and remote region (*5*), but the scope and sophistication of the work provides a valuable new line of evidence to understand Arctic population history.

The study of prehistoric population histories—whether by analyzing technologies and styles or by using genetic data—relies heavily on precise dating, especially radiocarbon dating. However, some factors render this technique less reliable in the Arctic than elsewhere (*6*, *7*). For example, many species hunted by Arctic cultures are sea mammals, which, due to the marine reservoir effect, produce radiocarbon dates older by decades or centuries than their actual age. The reservoir effect varies geographically, and the Arctic's many migratory species are therefore especially difficult to date. The problem is further compounded when human remains are dated, because the contribution of the reservoir effect to their inferred age depends on the proportion of marine mammals in their diet and on the migratory history of each species consumed.

These problems are relevant because the radiocarbon dating, stylistic and technological analyses, and Raghavan *et al.*'s genetic analyses sometimes disagree. For example, Savelle and Dyke recently proposed a second Paleo-Eskimo migration into Canada ~2800 years ago based on apparent hiatuses in radiocarbon dates and on differences in architectural and artifact styles between the early Paleo-Eskimo Pre-Dorset and the Dorset cultures (*8*). Raghavan *et al.*'s finding of genetic continuity from Pre-Dorset to Dorset refutes that theory.

Another theory that Raghavan *et al.* refute is the idea that the Sadlermiut were descendants of a relict Dorset population. Genetically, the Sadlermiut only show evidence of Inuit ancestry, and their cultural differences from other Inuit seem to have been the result of their isolation. The real mystery is therefore why the Dorset disappeared so completely around a thousand years ago after they and their Paleo-Eskimo ancestors had survived successfully in the Eastern Arctic for around 3500 years.

Dorset and Thule radiocarbon dates appear to show that the last Paleo-Eskimos coexisted with their successors for up to two centuries. The absence of archaeological evidence for cultural exchanges has led some

Anthropology Department, University of Waterloo, 200 University Avenue W, Waterloo, Ontario N2L 3G1, Canada. E-mail: robert.park@uwaterloo.ca

PHOTOS: B: TIM RAST, COURTESY THE ROOMS CORPORATION OF NEWFOUNDLAND AND LABRADOR, PROVINCIAL MUSEUM DIVISION; ALL OTHERS, ROBERT W. PARK

Published by AAAS

researchers to propose that they actively avoided each other (*9*, *10*). However, there is no evidence that the Late Dorset changed their traditional camping locations, as would be expected had they been trying to avoid the Thule. It is hard to imagine a cultural barrier so impermeable that the complete reproductive isolation documented by Raghavan *et al.* could have been maintained between these small and scattered hunter-gatherer populations. Maybe the absence of Paleo-Eskimo haplotypes among the Thule and their descendants is indirect evidence that the Dorset had died out before the Thule arrived, and that the apparently overlapping radiocarbon dates are erroneous.

Just over a thousand years ago, the arrival of Norse Vikings in the North American Arctic completed the expansion of humanity around Earth's circumference. Sutherland has argued that there was extensive interaction, including trade, between the Dorset and the Norse Vikings in Baffin Island (*11*, *12*). Yet, the lack of evidence for intermarriage documented by Raghavan *et al.* is almost impossible to explain if such interactions took place. The problem may lie in the radiocarbon dating, and the Dorset may have died out before the Norse arrived. In this and other cases, Raghavan *et al.*'s findings are likely to influence models of prehistoric migrations and cultural contacts in the North American Arctic for some time to come. ■

REFERENCES

1. T. Mathiassen, *Archaeology of the Central Eskimos: Descriptive Part* (Gyldendalske Boghandel, Nordisk Forlag, Copenhagen, 1927).
2. H. B. Collins, *Natl. Geogr. Mag.* **110**, 669 (1956).
3. S. D. M. Rowley, in *Threads of Arctic Prehistory: Papers in Honour of William E. Taylor, Jr*, D. A. Morrison, J. Pilon, Eds. (Canadian Museum of Civilization, Archaeological Survey of Canada, Hull, 1994), pp. 361–384.
4. M. Raghavan *et al.*, *Science* **345**, 1255832 (2014); 10.1126/science.1255832.
5. M. G. Hayes, J. B. Coltrain, D. H. O'Rourke, in *Contributions to the Study of the Dorset Palaeo-Eskimos*, P. D. Sutherland, Ed. (Canadian Museum of Civilization, Archaeological Survey of Canada, Hull, 2005), pp. 11–32.
6. R. McGhee, J. A. Tuck, in *Eastern Arctic Prehistory: Paleoeskimo Problems*, M. S. Maxwell, Ed. (Society for American Archaeology, Washington, DC, 1976), pp. 6–14.
7. H. Tauber, in *Radiocarbon Dating*, R. Berger, H. Suess, Eds. (Univ. of California Press, Los Angeles, CA, 1979), pp. 447–452.
8. J. M. Savelle, A. S. Dyke, *Am. Antiq.* **79**, 249 (2014).
9. R. McGhee, in *Fifty Years of Arctic Research: Anthropological Studies from Greenland to Siberia*, R. Gilberg, H. C. Gulløv, Eds. (Department of Ethnography, National Museum of Denmark, Copenhagen, 1997), pp. 209–213.
10. T. M. Friesen, in *Identities and Cultural Contacts in the Arctic*, M. Appelt, J. Berglund, H. C. Gulløv, Eds. (The Danish National Museum and Danish Polar Center, Copenhagen, 2000), pp. 206–220.
11. P. D. Sutherland, in *Identities and Cultural Contacts in the Arctic*, M. Appelt, J. Berglund, H. C. Gulløv, Eds. (The Danish National Museum and Danish Polar Center, Copenhagen, 2000), pp. 159–169.
12. P. D. Sutherland, in *The Northern World AD 900-1400*, H. D. G. Maschner, O. K. Mason, R. McGhee, Eds. (Univ. of Utah Press, Salt Lake City, 2009), pp. 279–299.

10.1126/science.1258607

AIDS/HIV

Rekindled HIV infection

What does the "Mississippi baby" tell us about curing HIV-1 infection?

By **Janet D. Siliciano**[1] *and* **Robert F. Siliciano**[1,2]

Palpable disappointment accompanied the news last month of a child (the "Mississippi baby") who was thought to be cured of HIV-1 infection by early antiretroviral treatment, but suddenly had detectable virus in the blood 2 years after the treatment was stopped. This setback followed the report of similar delayed viral rebounds 3 to 8 months after antiretroviral treatment was ended in two HIV-1–infected adults who had received bone marrow transplants (*1*). These findings have been viewed as a blow to HIV-1 eradication efforts. Although disappointing, the late rebounds are of enormous scientific importance. They reaffirm the concept that HIV-1 can persist by establishing latent infection and point to this challenge as the major hurdle in achieving a cure for HIV-1 infection.

The Mississippi baby was born to an HIV-1–infected mother who had no prenatal antiviral treatment. The infant tested positive for virus in the blood and was started on antiretroviral therapy 30 hours after delivery (*2*). The amount of virus in the blood (viremia) fell rapidly to below the limit of detection. At 18 months, treatment was stopped (against medical advice), but subsequent testing failed to reveal a rebound in viremia, which normally occurs 2 weeks after treatment interruption. There was widespread excitement that early therapy prevented the establishment of stable viral reservoirs in this infant. However, viremia suddenly rebounded 27 months after treatment interruption.

The two HIV-1–infected adults were given bone marrow transplants for other conditions while on antiretroviral therapy. The antiretroviral drugs protected donor cells from infection while host immune cells, including infected cells, were largely eliminated by chemotherapy and graft-versus-host disease (in which immune cells in the grafted tissue attack the host's immune cells) (*1*). Antiretroviral therapy was eventually stopped, and initially there was no viral rebound, raising hopes for cure. However, both patients later experienced sudden and dramatic rebounds in viremia.

The major barrier to cure is a small but extremely stable pool of resting memory $CD4^+$ T cells that carry an integrated but transcriptionally silent viral genome (*3*–*6*). Upon cellular activation, these latent proviruses are transcribed and replication-competent virus is released. Strategies for curing HIV-1 infection involve early antiretroviral therapy to prevent the establishment of a reservoir of latently infected cells, and a "shock and kill" approach (in which latency is reversed so the infected cells can be eliminated) (*7*). Due to the associated risks, bone marrow transplantation is only a curative strategy in patients requiring a transplant for other conditions.

The recent cases of delayed rebound suggest that even a small number of latently

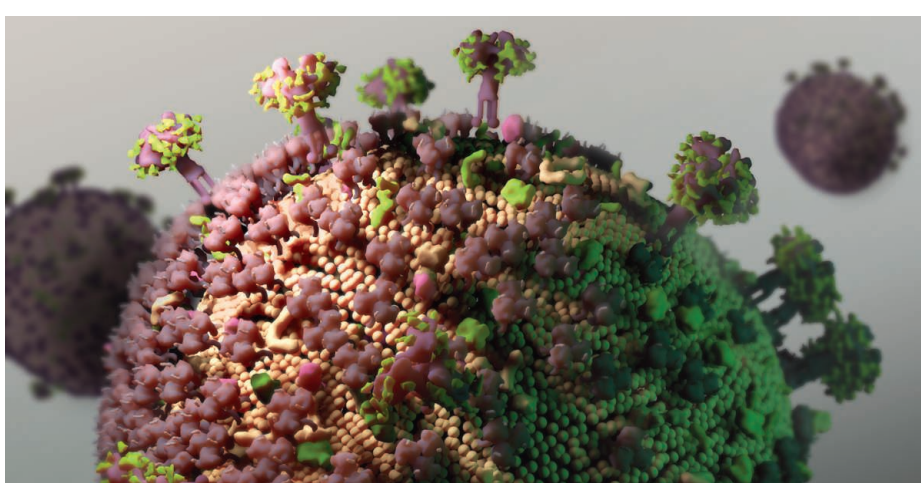

Silent reservoir. HIV-1 may establish a latent infection in T cells that is unaffected by antiretroviral therapy. The virus may rebound later.

ILLUSTRATION: V. ALTOUNIAN/*SCIENCE*

Published by AAAS

infected cells established in early infection or persisting after transplantation may be sufficient to rekindle viral replication. But there has been some promising news too. Established simian immunodeficiency virus infection in nonhuman primates was cleared by vaccine-induced T cell responses (*8*). There is also evidence that a histone deacetylase inhibitor can perturb the latent HIV-1 reservoir in humans, potentially making the infected cells vulnerable to immune clearance (*9*). In addition, the well-known "Berlin patient"—an HIV-1–infected adult who developed leukemia—remains virus-free after being off of antiretroviral therapy for 5 years. This patient received a bone marrow transplant from a donor who did not express C-C chemokine receptor type 5, a co-receptor for HIV-1 (and was therefore resistant to commonly transmitted forms of HIV-1) (*10*).

> ***"The rebound cases also provide insight into the likely outcome of cure strategies."***

There has been lingering concern that HIV-1 persistence in patients who are on antiretroviral therapy might be due in part to low amounts of viral replication, occurring perhaps in an anatomical site with low drug concentrations (*11*). If persistent replication were occurring in these patients during therapy, rebound should have occurred rapidly after treatment interruption, particularly because HIV-1–specific immune responses were absent or diminished (*1*, *2*). The finding that viremia can remain undetected with the most sensitive assays for months to years in patients off therapy before a dramatic and sudden rebound to high concentrations (>2,000,000 copies/ml in the transplant patients) can only be explained by the persistence of a latent form of HIV-1. It is not clear where the rebound virus came from in the Mississippi baby or in the two adults, but the latent reservoir in resting memory $CD4^+$ T cells is present in every patient and persists indefinitely even in patients on suppressive antiretroviral therapy (*12*).

The recent cases illustrate a major challenge: measuring the latent reservoir. This reservoir was initially defined using a quantitative viral outgrowth assay (QVOA), which measures the frequency of resting $CD4^+$ T cells that produce replication-competent virus after the T cells are activated. Typical values are ~1 per 10^6 resting $CD4^+$ T cells. Measurement of HIV-1 DNA by polymerase chain reaction (which amplifies a targeted DNA sequence) gives higher frequencies for infected cells because both replication-competent and defective viral genomes are detected (*13*, *14*). Before rebound, the QVOA was negative in the recent cases, and HIV-1 DNA was at or below the limit of detection. Thus, viral rebound occurred even though the best available assays for persistent HIV-1 were negative. The problem is not assay sensitivity. Both the QVOA and polymerase chain reaction can detect a single latently infected cell. The limitation is the size of the tissue sample tested. Even large blood or tissue samples may be devoid of such cells although they persist elsewhere in the patient.

The rebound cases also provide insight into the likely outcome of cure strategies. For example, if treatments that produce multilog reductions in the latent reservoir can be found, patients may interrupt therapy and remain aviremic for months to years, during which time assays for viral persistence would be negative (because of sample size). However, rebound could occur in a sudden and unpredictable fashion at late time points after interruption (*15*). Although the time to rebound will increase with reservoir reduction, enormous patient-to-patient variation in time to rebound can be expected because of the stochastic nature of the reactivation of latently infected cells. Thus, frequent monitoring of viremia over long periods of time would be needed. However, patients can only be considered safe from rebound if all latently infected cells are eliminated. It is much more likely that we will be able to achieve partial reductions, allowing a prolonged but uncertain interval off therapy—something that many patients would welcome. It is not too soon to begin planning for how to monitor this type of cure scenario. ■

[1]Department of Medicine, Johns Hopkins University School of Medicine, Baltimore, MD, USA. [2]Howard Hughes Medical Institute, Baltimore, MD, USA. E-mail: rsiliciano@jhmi.edu

REFERENCES

1. T. J. Henrich *et al.*, *Ann. Intern. Med.* 10.7326/M14-1027 (2014).
2. D. Persaud *et al.*, *N. Engl. J. Med.* **369**, 1828 (2013).
3. T. W. Chun *et al.*, *Nature* **387**, 183 (1997).
4. D. Finzi *et al.*, *Science* **278**, 1295 (1997).
5. J. K. Wong *et al.*, *Science* **278**, 1291 (1997).
6. T. W. Chun *et al.*, *Proc. Natl. Acad. Sci. U.S.A.* **94**, 13193 (1997).
7. D. D. Richman *et al.*, *Science* **323**, 1304 (2009).
8. S. G. Hansen *et al.*, *Nature* **502**, 100 (2013).
9. N. M. Archin *et al.*, *Nature* **487**, 482 (2012).
10. G. Hütter *et al.*, *N. Engl. J. Med.* **360**, 692 (2009).
11. C. V. Fletcher *et al.*, *Proc. Natl. Acad. Sci. U.S.A.* **111**, 2307 (2014).
12. J. D. Siliciano *et al.*, *Nat. Med.* **9**, 727 (2003).
13. S. Eriksson *et al.*, *PLOS Pathog.* **9**, e1003174 (2013).
14. Y. C. Ho *et al.*, *Cell* **155**, 540 (2013).
15. A. L. Hill, D. I. Rosenbloom, F. Fu, M. A. Nowak, R. F. Siliciano, *Proc. Natl. Acad. Sci. U.S.A.* 10.1073/pnas.1406663111 (2014).

10.1126/science.1259452

RESEARCH FUNDING

Demystifying central government R&D spending in China

Should funding focus on scientific research?

By **Yutao Sun**[1,2] *and* **Cong Cao**[2]*

China has become a powerhouse in research and development (R&D) spending. In 2012, its gross domestic expenditure on R&D (GERD) topped yuan renminbi (RMB) 1 trillion ($163 billion in current dollars). Measured by purchasing power parity, China's GERD reached $294 billion, behind the United States' $454 billion and the European Union's $341 billion but ahead of Japan's $152 billion (*1*). China's GERD as a percentage of gross domestic product (GERD/GDP) reached 1.98%; it more than tripled since 1995, surpassing the 28 member states of EU, which together managed 1.96% (*1*, *2*).

POLICY

China's recent requirement that central government agencies release their departmental annual reports (DARs) indicates that the nation is catching up to international norms in disclosing the government's expenditure, including its R&D expenditure profile, emphasizing not only aggregate statistics but also the structure of, and government's contribution to, the expenditure. Taking advantage of this disclosure, we disaggregate and analyze China's central R&D expenditure [see supplementary materials (SM)], to opening the "black box" of China's government R&D expenditure (fig. S1). We pinpoint the roles of agencies with missions in R&D in China's national innovation system. The analysis also promotes transparency through normalizing China's R&D expenditure statistics as a whole.

APPROPRIATION AND EXPENDITURE. Rather than aligning with international norms in reporting R&D expenditure, the Chinese government embeds R&D expen-

Downloaded from www.sciencemag.org on August 29, 2014

Published by AAAS

diture in the broader science and technology (S&T) expenditure statistics. We analyze the R&D expenditure as present in the 2011 DARs of the 71 central government agencies, totaling 73.73 billion RMB, accounting for 8.5% of GERD (868.7 billion RMB), or 39.2% of government's contribution to GERD. We draw R&D data from the central government S&T expenditure including expenditure on basic–applied–development research and Mega-Engineering Programs (MEPs) initiated under the Medium and Long-Term Plan for the Development of Science and Technology (MLP) in 2006 (*3*). Certain items of S&T expenditure (e.g., S&T affair management) are not categorized as R&D expenditure according to the *Frascati Manual* (*4*) and thus are excluded. We examine expenditure on the natural sciences and engineering technology, although the *Frascati Manual* also includes social sciences research.

The role of the Ministry of Science and Technology (MOST) in managing R&D budgeting has diminished (fig. S2). MOST and other S&T mission agencies go through the same budgeting process and get appropriations from the Ministry of Finance (MOF). Other mission agencies have started to compete for government appropriations, especially through the Knowledge Innovation Program at the Chinese Academy of Sciences (CAS) and MEPs. Government agencies also obtain part of their research spending from other sources, including other central agencies, local government, or enterprises (see the table).

There are several mechanisms through which government agencies allocate R&D expenditure. First is competitive, peer-reviewed, investigator-initiated research, such as the general program at the National Natural Science Foundation of China (NSFC), which mainly supports exploratory research. The second is competitive, peer-reviewed, mission-oriented research aimed at meeting S&T challenges related to the nation's economic and social development, such as some MEPs. The third is mission-oriented contract research; defense-related research falls into this category. The fourth is for operation of R&D organizations such as the fund that supports the state key laboratories or the establishment of new R&D institutes.

PHOTO: THINKSTOCK/GETTYIMAGES

[1]Dalian University of Technology, Dalian 116024, China. [2]University of Nottingham, Nottingham NG8 1BB, UK. *Corresponding author. cong.cao@nottingham.ac.uk

KEY R&D MISSION AGENCIES. With more than 10 billion RMB each, MOST, CAS, and NSFC combined for more than 70% of central R&D spending across all 71 agencies in 2011.

MOST. Despite no longer managing China's overall civilian S&T budget, MOST still received the most S&T revenues from the central government. Its budget is mainly earmarked for National S&T Programs (NSTPs) with most of its R&D expenditure on the State Basic R&D Program (the 973 Program) including Mega-Science Programs (MSPs), also under MLP; the State High-Tech R&D Program (the 863 Program); and the National Key Technologies R&D Program, which altogether accounted for about 90% of the total NSTPs. Other NSTPs are not funded by MOST, whose role in MEPs is also limited.

CAS. In 2011, slightly more than half of its S&T spending came from the central appropriation, which was then channeled to its research institutes. CAS obtained most of the other revenues from research funds, ranging from NSTPs and foreign R&D tasks to cooperative projects with universities, enterprises, and local governments. Most such revenues were spent on basic and applied research.

Ministry of Industry and Information Technology (*MOIIT*). MOIIT emerged as a super-ministry, along with the National Development and Reform Commission (NDRC), during the 2008 government reform. A merger of several agencies, MOIIT controls vast amounts of public resources and is important in China's industrial R&D. It spent most of the government revenue on applied research and MEPs.

NDRC. NDRC is probably most important in formulation and implementation of S&T policies. In 2011, it funded only 290 million RMB of S&T activities, of which 25.25% was from the central government, much less than the S&T spending that MOST received from the central government. Rather than a major funder of S&T activities, NDRC seems to participate as a major S&T policy-maker, via economic regulations and strategic distribution of huge financial resources that are not included in its budget but are distributed under its discretion. Presumably, part of the extra-budgetary fund could be used for S&T-related and high-tech industrialization projects. We found no documents that reflect how money was spent on such projects.

Slightly less than half (45.25%) of the central government R&D spending in 2011 is not accounted for, likely spent at the eight defense-related agencies that have not disclosed DARs. By comparison, more than half of the U.S. government R&D expenditure is defense-related (*1*).

BASIC, APPLIED, AND MEGA RESEARCH. *Basic research.* China's top four government agencies in terms of basic research funding were NSFC, CAS, MOST, and Ministry of Education (MOE). NSFC has a portfolio of funding instruments that addresses different segments of the research community. MOST manages the 973 Program and MSPs as part of its NSTP portfolio. CAS receives central government revenue for intramural research and competes for extramural funding from NSFC, MOST, and other sources. MOE plays a key role in basic research through its 75 directly affiliated universities.

Applied research. In 2011, four agencies—MOST, CAS, Ministry of Agriculture (MOA), and MOIIT—were major agencies of applied research funds. More than 70% of central spending on applied research was not accounted for, presumably defense-related research at agencies that have not disclosed DARs.

Mega-engineering programs. In 2011, the top four agencies involved in MEPs were MOIIT, Ministry of Health (MOH), CAS, and MOA. Impacts of MEPs on China's R&D budget are significant. In 2010, central government spending on MEPs equaled funds for NSFC, the 973 Program, and the 863 Program combined. MEPs have affected the distribution of central government's R&D appropriation with more funds going to the S&T mission agencies than to MOST.

The large amount of money appropriated to MEPs has been spent in a rush, especially toward the end of the 11th Five-Year Plan (FYP) period (2006–2010) in 2010. China's S&T budget tends to be implemented according to the FYP. NSTPs and NSFC programs have been introduced

Published by AAAS

China's major central agencies by S&T/R&D expenditure from central appropriation in 2011 (billion RMB)

AGENCIES	S&T EXPENDITURE	R&D EXPENDITURE				
		BASIC	APPLIED	DEVELOPMENT	MEPs	TOTAL
MOST	27.67	4.69	8.86	7.76	0.013	21.33
CAS	18.95	8.3	7.46	0.25	0.425	16.44
NSFC	14.66	14.66				14.66
MOIIT	6.21	0.16	1.74	0.025	4.2	6.13
MOE	3.88	3.13	0.44	0.12	0.03	3.72
MOA	3.25	0.22	1.97	0.004	0.42	2.61
MOH	2.47	0.06	0.606	0.001	1.56	2.22
NDRC	0.073		0.062	0.004	0.001	0.068
71 agencies	88.349	31.568	26.796	8.29	7.076	73.731
Nondisclosed agencies	105.865					60.937*
Central government	194.214	29.426	97.988			134.668*

*These figures are estimated (see SM).
[Source: Department Annual Reports on Financial Budgets and Final Accounts (DARs) at central agencies and central government level (*5*)]

China's major central agencies by S&T/R&D expenditure from central appropriation in 2011 (billion RMB). See SM for data and details.

for many years, so budget management has been institutionalized. The relatively new MEPs have been led, organized, and implemented by different government agencies and launched at different times. Budgets have to be spent within the FYP in which a program starts. Quality control in the selection of the projects might have been compromised.

A NEED FOR FURTHER REFORMS. China has decentralized distribution of its central R&D spending through a series of reforms. MOST is no longer in charge of government R&D budgeting and allocation of total civilian R&D spending. A decentralized and diversified funding system could be advantageous but presents new challenges. The lack of top-level design, unified planning, effective coordination, and transparency in budgeting and spending has led to overlap between NSTPs under the administration of different ministries, or even within the same ministry, and a rush to spend funds in programs such as MEPs (*5*).

Further reform of China's R&D budgeting and reporting process to align it with international norms and to make S&T mission agencies accountable seems urgent. China's government should switch its reporting from S&T expenditure to R&D expenditure, as well as place the government R&D expenditure in the national R&D expenditure statistics. It is a key step to bringing transparency to government R&D funding and helping reduce corruption, as well as harmonizing with international norms.

China may want to consider restructuring MOST by dividing its functions into two parts. One would be an elevated Office of S&T Policy under the State Council focusing on top-level design, unified planning, interagency coordination, and R&D budgeting, in addition to its responsibility for the existing functions of S&T strategy and policy formulation (*5*). The other becomes an independent Office of National S&T Programs, managing and monitoring all department budgets related to NSTPs, including mission-oriented research. The remaining functions of MOST can be redistributed to other agencies.

China has witnessed a sharp decline in the amount of money spent on basic and applied research in the past two decades. In 2011, expenditure for basic and applied research was 4.7% and 11.8% of GERD, respectively. Comparatively, in 2009, those expenditures were 19% and 17.8% in the United States and 12.5% and 22.3% in Japan (*1*, *6*). Combined basic and applied (scientific) research averaged more than 35% of GERD in developed countries and newly industrialized economies (*7*). The low share of scientific research expenditure has negatively affected China's innovation capability and may jeopardize China's ambition to become an innovation-oriented nation (*8*, *9*). Shrinking of applied research is a serious problem, because applied research links basic and development research.

Other countries have experienced decreased shares of scientific research funds coming from government (*10*). The Chinese case is extraordinary. Although most of China's central R&D spending is on scientific research, predominately applied research, GERD has been shifting downstream from applied research to development research (table S2). This may be attributed to China's evolving innovation policy that emphasizes development over scientific research (*11*). The government also devotes far less of its funding to scientific research compared with countries that show similar GERD/GDP (table S3). Government's overall contribution to GERD in 2011 was only 21.7%, with 77.9% coming from enterprises. Government should increase its contribution to 30% of GERD by 2020, an average share of Organization for Economic Cooperation and Development (OECD) countries (*1*), with much from the central government.

Increased central government R&D expenditure could be put into existing organizations or administered by new institutions. As MEPs have seemingly failed to effectively use the new money through existing organizations, specific policy action could include upgrading the medical science department of NSFC to a National Institute of Health (NIH) directly under the MOH to fund scientific research in population and health. This follows the U.S. model of NIH and propagates the better practice of NSFC in research funding management. The Chinese scientific community also has long been campaigning for such an establishment. ■

REFERENCES AND NOTES

1. OECD, Main Science and Technology Indicators: Issue 1 (OECD Press, Paris, 2014); www.oecd.org/sti/msti.htm.
2. R. Van Noorden, *Nature* **505**, 144 (2014).
3. C. Cao, R. P. Suttmeier, D. F. Simon, *Phys. Today* **59**, 38 (2006).
4. OECD, *Frascati Manual* (OECD Press, Paris, 2002).
5. C. Cao, N. Li, X. Li, L. Liu, *Science* **341**, 460 (2013).
6. NSF, Science and Engineering Indicators; www.nsf.gov/statistics/seind12/.
7. MOST, *China Science and Technology Indicators 2010* [in Chinese] (Scientific and Technical Documentation Press, Beijing, 2011).
8. D. Breznitz, M. Murphree, *Run of the Red Queen: Government, Innovation, Globalization, and Economic Growth in China* (Yale Univ. Press, New Haven, 2010).
9. K. Bound *et al.*, *China's Absorptive State: Research, Innovation, and the Prospect for China–UK Collaboration* (NESTA, London, 2014); www.nesta.org.uk/sites/default/files/chinas_absorptive_state_0.pdf.
10. P. Stephan, *How Economics Shapes Science* (Harvard Univ. Press, Cambridge, 2012).
11. F. Liu, D. F. Simon, Y. Sun, C. Cao, *Res. Policy* **40**, 917 (2011).

ACKNOWLEDGMENTS

The authors thank R. P. Suttmeier, D. F. Simon, and three anonymous reviewers for comments. Partial support came from the EU 7th Framework Programme–Marie Curie International Incoming Fellowship (302303/911303), the National Natural Science Foundation of China (71203020), and the U.S. NSF (SES–1115319).

SUPPLEMENTARY MATERIALS

www.sciencemag.org/content/345/6200/1006/suppl/DC1

10.1126/science.1253479

Published by AAAS

BOOKS *et al.*

WILDLIFE MANAGEMENT

Heirloom genomes and bison conservation

By **J. Andrew DeWoody**

I acquired *American Plains Bison* at a recent conservation meeting, where an acquaintance gave me a copy immediately before our funding deliberations. I was skeptical, partly because I presumed my colleague was about to lobby for a particular cause, but my interest was piqued by the dual themes of conservation genetics and evolution.

James A. Bailey, who was at Colorado State University, wrote this book "to describe some details of the breadth and depth of wildness in American plains bison, and to show how bison wildness is threatened by creeping domestication." He does not write for scientists (though I found the book interesting and informative), but for laypersons in an effort to forge a wild bison constituency. It is a sobering assessment of bison biology today. Bailey's thesis is that most bison advocates undervalue wildness to the detriment of bison and our sense of free will.

Early on, it becomes apparent that this book will not be a dusty academic treatise that only looks backward: Bailey quickly makes his foray into contemporary issues and notes that today, only two bison herds in the contiguous United States live in the presence of any nonhuman predators. How can we expect bison to continue a natural journey when we have removed predators as evolutionary drivers?

The book then proceeds to provide the obligatory summary of how humans devastated bison populations. Bailey does so in depressingly successful fashion, replete with photos and shameful anecdotes of our ancestors' exploits.

Bailey drives home the point that the maintenance of bison in small pens is a travesty. Our society should instead retain elements of bison wildness by challenging them in a natural manner. This means with competitors, predators (wolves, bears, and humans), pathogens, and the environment itself. Wild plains bison evolved historically in the presence of pathogens and predators,

The reviewer is at the Department of Forestry and Natural Resources and the Department of Biological Sciences at Purdue University. E-mail: dewoody@purdue.edu

American Plains Bison Rewilding an Icon
James A. Bailey
Farcountry, 2013. 258 pp.

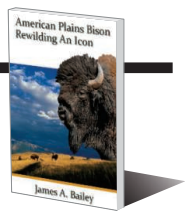

and they remain the best means to control population sizes.

Bailey convincingly argues that traits necessary for the survival of wild animals are ill-adapted for captivity and vice versa. Animal production (i.e., farming or ranching) is insufficient to maintain the historical and biological integrity of wild animals. Many attributes of wild bison populations (e.g., dominance hierarchies) simply do not exist in most captive populations because artificial breeding schemes selectively avoid them. As a conservationist and hunter myself, I agree with this sentiment and particularly like his admonition that hunters and biologists must avoid artificial selection (e.g., for horn size) to the extent possible.

Bailey analyzes the 44 largest conservation herds of plains bison in the United States by considering a number of factors related to "wildness," including range size, supplemental feeding, the presence of natural predators, sex ratio, and disease management (lack thereof being most consistent with wildness). The results are a bit disheartening: only two herds (Yellowstone and Utah's Henry Mountains) stand out as justifiably "wild."

In the remaining herds, inbreeding, hybridization, and artificial selection (domestication) reduce the wildness of native bison and diminish their capacity to provide natural ecosystem services that are crucial to many other plains species. A variety of other species are described (e.g., prairie chickens and Arkansas darters) that could benefit from the establishment of large bison herds.

Bailey then switches gears, from esoteric discussions about why we should conserve wild bison to how we actually do so. The vast majority of states have no recovery plan for bison, and their regulatory status impedes conservation in most Western states because bison are not managed like most wildlife species. Bailey does not wave his hands and say "Let's rewild bison everywhere," but he provides detailed suggestions about where and how to conserve wild bison. The practical problems that are apt to confound bison rewilding are clearly recognized, including the uncertainties of global warming, the (incomprehensible) fact that many states do not legally recognize bison as wildlife, and the tendency to relegate bison to poor-quality lands because they will be easiest (and cheapest) to acquire. He argues that an objective review of bison status under the Endangered Species Act would at least identify them as threatened and recognizes that it might take a century or more to widely restore wild plains bison in the United States.

Bailey's musings about nature resonated deeply, in large part because of the author's intuitive understanding of wildness. He writes that "Wildness is the most unique and irreplaceable characteristic of wildlife. … In a world where humans increasingly restrict their own freedom by crowding and monotonizing their environment, wild bison should be retained, at least as a symbol of what we have sacrificed in domesticating and civilizing ourselves."

The plight of the bison should strike a chord with Bailey's intended general audience, but ecologists, evolutionary biologists, and wildlife managers will find this book an effective primer on practical conservation biology. It should be required reading for all wildlife students; I know it will be for mine.

10.1126/science.1256422

CREDIT: GETTY IMAGES/ISTOCKPHOTO

Downloaded from www.sciencemag.org on August 29, 2014

Published by AAAS

LETTERS

Edited by **Jennifer Sills**

Is it time to destroy the smallpox virus?

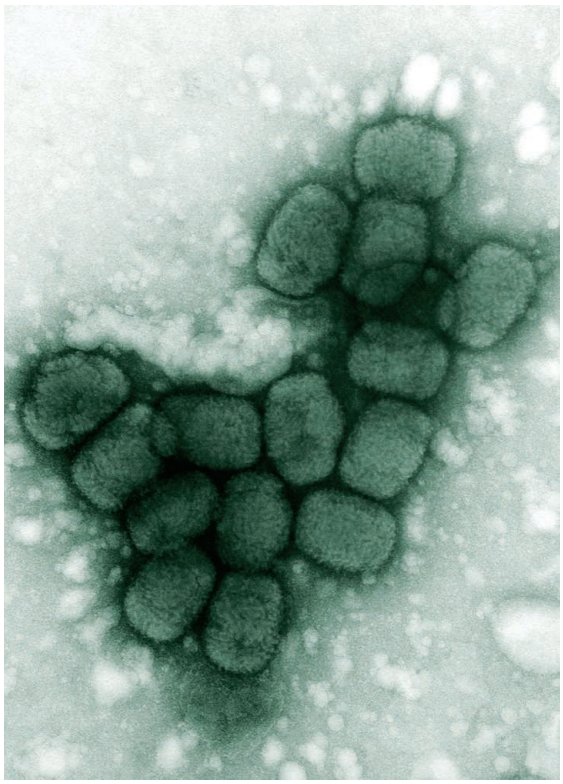

THE LAST CASES of smallpox occurred more than 37 years ago. Should we now destroy the variola virus samples that remain in the two World Health Organization (WHO)–designated smallpox laboratories, located in the United States (Centers for Disease Control and Prevention) and Russia (Koltsobo, Siberia)? In May, the 67th World Health Assembly in Geneva decided that the previously agreed-upon decision to destroy the smallpox virus stocks would, once again, be postponed for an additional 3 years until the 70th World Health Assembly in 2017. We support the decision not to destroy the virus.

Although true eradication and protection from bioterrorist smallpox attacks will only be assured once the causative agent is eliminated from all laboratories, there is no way to guarantee that all stocks have been destroyed. During the last search for residual variola, all nations collaborated and responded to a special WHO letter addressed to the heads of health service of each country. Sixteen smallpox isolates were reported (*1*). Given these results, more stocks likely exist in unknown places. The recent discovery of variola in old specimens at the National Institutes of Health (NIH) in Bethesda, Maryland, highlights this risk (*2*–*4*). Furthermore, from the late 1980s to the early 1990s, the former USSR biowarfare laboratory produced huge amounts of variola virus. Much like the recent NIH situation, it would not be surprising to find that, in some dark corner of this or a similar facility, viable tubes of variola virus were still resting comfortably.

The destruction of official government stocks could serve to increase, rather than decrease, risk in the event that adversarial groups gain access to the virus. Moreover, synthesis of smallpox virus could be accomplished by a well-trained laboratory technician. Lack of access to the original strain could also impede research should a new strain emerge.

Given the likely continuing need to have viable variola virus to conduct required research, the security and the political threats in today's world, and historical efforts to use variola as a biologic weapon, we support the establishment of a secure system to maintain live smallpox virus under the supervision of the United Nations. We recommend that the WHO establish a special commission to implement this system.

Isao Arita*[1] *and Donald Francis*[2]*

[1]Director Emeritus, National Hospital Organization, Kumamoto Medical Center, Kumamoto 861–8068, Japan. [2]Executive Director, Global Solutions for Infectious Diseases, South San Francisco, CA 94080, USA.

*Corresponding author. E-mail: dfrancis@gsid.org

REFERENCES

1. D. A. Henderson, I. Arita, *Biosecur. Bioterror.* **12**, 117 (2014).
2. CDC Media Statement on Newly Discovered Smallpox Specimens (2014); www.cdc.gov/media/releases/2014/s0708-nih.html.
3. S. Reardon, *Sci. Am.* (2014); www.scientificamerican.com/article/vials-of-smallpox-virus-found-unsecured-at-nih/.
4. J. Kaiser, *Science Insider* (2014); http://news.sciencemag.org/health/2014/07/six-vials-smallpox-discovered-u-s-lab.

Gene drives raise dual-use concerns

THERE IS NO doubt that clear regulations are required before gene drives can be released into the environment, as K. A. Oye *et al.* point out in their Policy Forum "Regulating gene drives" (8 August, p. 626; published online 17 July). However, they do not address a more pressing concern. Regulations are effective only for legitimate organizations and nations, whereas gene drive technologies can, in the wrong hands, potentially be used for malicious purposes. For example, just as gene drives can make mosquitoes unfit for hosting and spreading the malaria parasite, they could conceivably be designed with gene drives carrying cargo for delivering lethal bacteria toxins to humans. Other scary scenarios, such as targeted attacks on major crop plants, could also be envisaged.

Fortunately, learning how to insert a gene drive into the germline and optimize its function will have to be done anew for each species, and may be far trickier in organisms with larger genomes (*1*). It is therefore timely to call upon the scientific research community to prevent the disclosure of exact instructions on making specific gene drives in scientific manuscripts or patent applications. Just as the exact technical instructions for making nuclear weapons remain classified 70 years after the Manhattan Project—as they rightfully should—the gene drive methodological details do not belong in the scientific literature.

David Gurwitz

Department of Human Molecular Genetics and Biochemistry, Sackler Faculty of Medicine, and Sagol School of Neuroscience, Tel Aviv University, Tel Aviv, 69978, Israel.
E-mail: gurwitz@post.tau.ac.il

REFERENCE

1. K. M. Esvelt, A. L. Smidler, F. Catteruccia, G. M. Church, *eLife* 10.7554/eLife.03401 (2014); published online 17 July 2014.

Response

WE RESPECT GURWITZ'S concern over potential misuse of gene drives but disagree with his proposal to restrict information access. Treating information related to gene drives as classified would be technically ineffective and politically counterproductive.

Gene drives incorporate CRISPR genome editing machinery such that editing occurs anew in each organism that inherits a copy (*1*). Building standard gene drives in a new species will involve adapting the widely available CRISPR technology to that species. At best, classifying information would force agents intent on misuse to adapt CRISPR on their own. This is unlikely to impede any agent able to overcome the formidable challenge of introducing entirely new traits intended for misuse.

Even if withholding information on CRISPR adaptation or gene drives did

PHOTO: DR. FRED MURPHY/CDC

Downloaded from www.sciencemag.org on August 29, 2014

Published by AAAS

impede attempts at misuse, it could also backfire by delaying the construction of time-sensitive reversal and immunization drives useful for defense. Classifying details would also fuel suspicion, retard development of technological safeguards, and vitiate informed debate on risks. Given that the vast majority of species will not represent biosecurity threats, acting as if the risk of misuse outweighs the benefits of transparency would be shortsighted.

The analogy to classifying instructions on making nuclear weapons does not hold. Classification in the nuclear domain differentiates between methods needed to develop weapons, which cannot be defended against, and methods used in nuclear power and medicine (*2*). By contrast, classifying information required to build gene drives cannot target potential misuses without also impeding development of defenses, as well as environmental, health, agricultural, and safety applications of CRISPR technology.

We encourage scientists to consider the possibility of eventual misuse and to consult with biosecurity experts before initiating development of gene drives in a new species, but suggest that banning release of technical information would reduce rather than enhance biosecurity.

Kenneth A. Oye[1] and Kevin M. Esvelt[2]

[1]Center for International Studies, Massachusetts Institute of Technology, Cambridge, MA 02139, USA. [2]Wyss Institute for Biologically Inspired Engineering, Harvard Medical School, Boston, MA 02115, USA.

*Corresponding author. E-mail: oye@mit.edu

REFERENCES

1. K. M. Esvelt, A. L. Smidler, F. Catteruccia, G. M. Church, *eLife* 10.7554/eLife.03401 (2014).
2. J. B. Tucker, Ed., *Innovation, Dual Use, and Security: Managing the Risks of Emerging Biological and Chemical Technologies* (MIT Press, Cambridge, MA, 2012).

TECHNICAL COMMENT ABSTRACTS

Comment on "The hologenomic basis of speciation: Gut bacteria cause hybrid lethality in the genus *Nasonia*"

James Angus Chandler and Michael Turelli

■ Brucker and Bordenstein (Reports, 9 August 2013, p. 667) claim that adaptive codivergence of gut bacteria with hosts contributes to hybrid lethality. Yet, they provide no evidence for coadaptation of bacteria and *Nasonia* hosts. Their data on hybrid viability suggest that bacteria contribute to inviability only because intrinsic hybrid dysfunction increases susceptibility to free-living bacteria. Hologenomic speciation remains testable speculation without experimental support.

Full text at http://dx.doi.org/10.1126/science.1251997

Response to Comment on "The hologenomic basis of speciation: Gut bacteria cause hybrid lethality in the genus *Nasonia*"

Robert M. Brucker and Seth R. Bordenstein

■ Chandler and Turelli postulate that intrinsic hybrid dysfunction underscores hybrid lethality in *Nasonia*. Although it is a suitable conception for examining hybrid incompatibilities, their account of the evidence is factually inaccurate and leaves out the evolutionary process for why lethality became conditional on nuclear-microbe interactions. Hybrid incompatibilities in the context of phylosymbiosis are resolved by hologenomic principles and exemplify this emerging postmodern synthesis.

Full text at http://dx.doi.org/10.1126/science.1256708

George De Boer and Jo Ellen Roseman of Project 2061, which is named for the return of Halley's Comet, a nod to the program's long-term focus.

Before the Common Core, There Was *Science for All Americans*

The landmark AAAS book continues to influence education reform 25 years after it defined the concept of science literacy.

By **Kathy Wren**

Many of the debates swirling around states' adoption of the Common Core State Standards and the Next Generation Science Standards have a distinctly 21st-century feel. But at the heart of these efforts lies an ambitious AAAS book published 25 years ago that was the first to articulate what the next generation should know and be able to do in science, mathematics, and technology.

Today, education experts agree that *Science for All Americans*—a 3-year collaboration among hundreds of scientists, mathematicians, and other scholars—has had a significant impact on science education reform, by helping to define the concept of science literacy and lay the groundwork for national education standards in science, technology, engineering, and mathematics (STEM).

More than 40 states and the District of Columbia have now adopted the Common Core standards for math and English, and 12 states plus the District have adopted the Next Generation Science Standards. A nationwide consensus on whether these standards will significantly improve STEM education remains elusive, but many educators and other STEM experts nonetheless embrace the idea of a set of shared goals to guide the teaching of all U.S. students. Such a vision was initially laid out in 1989, when AAAS' Project 2061 published *Science for All Americans*.

"It's often forgotten, but it's this book that got it all going and just pervades everything else," said George De Boer, deputy director of Project 2061.

Science for All Americans was the first major publication from Project 2061, then a fledgling program headed by James Rutherford, former assistant director of the National Science Foundation and assistant secretary of education at the U.S. Department of Education. At the time, federal enthusiasm for improving STEM education, which had spiked after the Soviet Union's launch of the Sputnik satellite, had waned. And Rutherford felt he had seen too many education reform efforts fail to achieve a lasting impact.

"That's when it occurred to me that what was wrong with our whole approach was that it was too short term," Rutherford said. "We're a big, complicated country. It's going to take time to turn things around. I decided we needed to have some kind of statement saying, 'Here are the understandings and skills of science that we'd like all people to have.' "

In the last two decades, the National Research Council and other organizations have also developed STEM education standards. But, it was *Science for All Americans* that first marked a clear departure from the previous era, according to Jo Ellen Roseman, director of Project 2061.

PHOTO: CARLA SCHAFFER/AAAS

Downloaded from www.sciencemag.org on August 29, 2014

Published by AAAS

"The post-Sputnik science education reform was really about preparing the next generation of scientists," she said. *"Science for All Americans* took a new position on science literacy, which was that everyone needs some level of science knowledge and habits of mind so that when reading about a scientific report in the newspaper, for example, one would think about it in a more critical way."

To launch the project, Rutherford and his associate director, Andrew "Chick" Ahlgren, convened panels of scientists, mathematicians, engineers, physicians, philosophers, historians, and educators, and tasked them with identifying the most important STEM concepts for students to master by the time they graduated high school.

These discussions formed the basis for *Science for All Americans,* which emphasized the interdependence of STEM fields, the importance of key concepts and principles of science, the diversity and unity of the natural world, and the need to use scientific knowledge and ways of thinking to benefit the individual and society.

The book was followed 4 years later by the AAAS report *Benchmarks for Science Literacy,* which specifies how students should progress toward these goals as they move through successive grade levels.

"What James Rutherford and Chick Algren did was pare things down and focus the content on the really big ideas. The second thing they did was use language that was very clear and not overly technical," said Rodger Bybee, a writing team leader for the Next Generation Science Standards. "Those are the types of things that we also tried to do in the new standards."

"I especially liked the theme in *Science for All Americans* that less detail and rote memorization is better,'" said Gil Omenn, who was a member of the initial Project 2061 council and is now a professor of internal medicine, human genetics, and public health at the University of Michigan and the director of the UM Center for Computational Medicine & Bioinformatics. Omenn, who also served as AAAS president, noted that Project 2061 continued in this direction with a series of textbook evaluations that helped publishers reduce jargon and introduce terms more meaningfully.

Today, Project 2061 is helping teachers implement the Next Generation Science Standards through workshops that offer tools, resources, and strategies based on *Science for All Americans, Benchmarks for Science Literacy,* and the related *Atlas of Science Literacy.* ■

PHOTO: EARL LANE/AAAS

Brain Signaling May Be Next Target of Autism Treatment

In a break with tradition, researchers look to reverse the disorder's neurological causes.

By **Earl Lane**

Experts agree that early behavioral intervention is the preferred first line of treatment for autism, but some speakers at a recent Capitol Hill briefing suggested that drugs that affect brain signaling may be among future therapies.

The traditional view has been that drug treatments cannot change or cure autism's underlying neurological disorder, said Diane Chugani, professor of pediatrics at Wayne State University and director of the Translational Imaging Laboratory at Children's Hospital of Michigan in Detroit. However, animal studies suggest that there may be ways to reverse neurological deficits associated with autism-related disorders such as Rett syndrome and tuberous sclerosis complex, she said, and there could be common neurochemical features associated with many genes implicated in autism.

More public awareness and better diagnoses may partly explain the recent increase in autism cases, said Catherine Lord.

Chugani and other scientists discussed advances in the diagnosis and treatment of autism spectrum disorder (ASD) at a well-attended 17 July briefing, which drew about 50 congressional staffers and members of the public. The briefing was hosted by AAAS through the support of the Dana Foundation in conjunction with Rep. Chaka Fattah (D-Pa.).

Future ASD drugs might target the neurochemical messengers that are released at the brain's synapses, the small gaps at the ends of neighboring neurons where signals are transmitted from one cell to another. Chugani has done positron emission tomography (PET) studies of serotonin synthesis in children with autism and has found differences in developmental changes in serotonin synthesis in the brains of young autistic children compared to nonautistic children. Based upon these results, she and her colleagues conducted a clinical trial on a drug called buspirone that mimics serotonin in young autistic children, and are pursuing further testing on its effects.

The emerging understanding of how genetic variability affects the synapses and communication among brain cells should prove to be "a rich source of new drug treatments for ASD," Chugani said. She predicted that genetic testing, use of biomarkers in the blood, and brain imaging methods will help clinicians determine which treatments are most appropriate for individuals with autism at different stages of their development. "I think we are on the threshold of some very interesting results," Chugani said.

Catherine Lord, director of the Center for Autism and the Developing Brain at New York-Presbyterian Hospital, Weill Cornell Medical College and Columbia University Medical Center, was more guarded in her outlook. "We don't have any biological markers," she said. "We have a lively, interesting, wonderful background of neuroscience that is moving forward, but it has basically had no practical result, I would say, in the last 20 years."

Chugani said that early use of intensive behavioral therapy remains the current standard of care and must be made available to all children with autism spectrum disorders. There remains a need for faster, more effective screening of children, according to Lord, and active, early involvement by parents is essential. "We can do a very good job" of diagnosis, she said, but it requires time and input from both the parents and skilled clinicians. ■

Published by AAAS

AAAS Annual Election: Preliminary Announcement

The 2014 AAAS election of general and section officers is scheduled to begin in October. All members will receive a ballot for election of the president-elect, members of the Board of Directors, and members of the Committee on Nominations. Members registered in sections will receive ballots for elections for each section (up to three) they are enrolled in.

Candidates for section elections are listed below. Candidates for the general election will appear in the September issue of News & Notes. Additional names may be placed in nomination for any office by petition submitted to the Chief Executive Officer no later than 24 September 2014. Petitions nominating candidates for president-elect, members of the Board, or members of the Committee on Nominations must bear the signatures of at least 100 members of the association. Petitions nominating candidates for any section office must bear the signatures of at least 50 members of the section. A petition to place an additional name in nomination for any office must be accompanied by the nominee's curriculum vitae and statement of acceptance of nomination. Biographical information for the following candidates will be enclosed with the ballots sent to members. ■

SECTION ELECTIONS

Agriculture, Food, and Renewable Resources

Chair Elect: Steven C. Huber, Univ. of Illinois at Urbana-Champaign; Harry J. Klee, Univ. of Florida

Member-at-Large of the Section Committee: Blake C. Meyers, Univ. of Delaware; Johanna Schmitt, Univ. of California, Davis

Electorate Nominating Committee: Lisa Durso, USDA-ARS; Peggy Ozias-Akins, Univ. of Georgia; Amanda D. Rodewald, Cornell Univ.; Roger Philip Wise, USDA-ARS/Iowa State Univ.

Council Delegate: Jim Giovannoni, USDA-ARS/Cornell Univ.; Neelima Roy Sinha, Univ. of California, Davis

Anthropology

Chair Elect: Steven R. Leigh, Univ. of Colorado Boulder; Dennis H. O'Rourke, Univ. of Utah

Member-at-Large of the Section Committee: Joanna E. Lambert, Univ. of Texas at San Antonio; Dawnie Wolfe Steadman, Univ. of Tennessee, Knoxville

Electorate Nominating Committee: Yolanda T. Moses, Univ. of California, Riverside; Peter Neal Peregrine, Lawrence Univ.; J. Josh Snodgrass, Univ. of Oregon; Anne C. Stone, Arizona State Univ.

Astronomy

Chair Elect: Joan Centrella, NASA Goddard Space Flight Center; Debra Meloy Elmegreen, Vassar College

Member-at-Large of the Section Committee: James M. Cordes, Cornell Univ.; Henry C. Ferguson, Space Telescope Science Institute

Electorate Nominating Committee: Harriet L. Dinerstein, Univ. of Texas at Austin; Steven M. Kahn, Stanford Univ.; Nancy A. Levenson, Gemini Observatory; Sylvain Veilleux, Univ. of Maryland, College Park

Atmospheric and Hydrospheric Sciences

Chair Elect: Jack A. Kaye, NASA; Don Wuebbles, Univ. of Illinois at Urbana-Champaign

Member-at-Large of the Section Committee: Carol Arnosti, Univ. of North Carolina at Chapel Hill; Ronald C. Cohen, Univ. of California, Berkeley/Lawrence Berkeley National Laboratory

Electorate Nominating Committee: Chris E. Forest, Pennsylvania State Univ.; Alexander Pszenny, NASA; James M. Russell, Brown Univ.; Howard Joe Witte, Adnet Systems, Inc./NASA

Biological Sciences

Chair Elect: Pamela C. Ronald, Univ. of California, Davis; Venkatesan Sundaresan, Univ. of California, Davis

Member-at-Large of the Section Committee: Sarah M. (Sally) Assmann, Pennsylvania State Univ.; Craig S. Pikaard, Indiana Univ.

Electorate Nominating Committee: David A. Baum, Univ. of Wisconsin-Madison; Evan E. Eichler, Univ. of Washington; N. Louise Glass, Univ. of California, Berkeley; Kenneth Keegstra, Michigan State Univ./DOE Plant Research Laboratory

Chemistry

Chair Elect: Carol J. Burns, Los Alamos National Laboratory; Peter C. Ford, Univ. of California, Santa Barbara

Member-at-Large of the Section Committee: Seth M. Cohen, Univ. of California, San Diego; Michael P. Doyle, Univ. of Maryland, College Park

Electorate Nominating Committee: Joanna Aizenberg, Harvard Univ.; Stephanie L. Brock, Wayne State Univ.; William R. Montfort, Univ. of Arizona; Martin Moskovits, Univ. of California, Santa Barbara

Dentistry and Oral Health Sciences

Chair Elect: Jacques E. Nör, Univ. of Michigan; Susan Reisine, Univ. of Connecticut

Member-at-Large of the Section Committee: Matthew P. Hoffman, National Institute of Dental and Craniofacial Research/NIH; Stefan Ruhl, Univ. of Buffalo SUNY

Electorate Nominating Committee: Rena N. D'Souza, Univ. of Utah; Laurie K. McCauley, Univ. of Michigan; James E. Melvin, National Institute of Dental and Craniofacial Research/NIH; Michael L. Paine, Univ. of Southern California

Education

Chair Elect: Deborah Allen, Univ. of Delaware; Cathy Middlecamp, Univ. of Wisconsin-Madison

Member-at-Large of the Section Committee: Tammy M. Long, Michigan State Univ.; Catherine Milne, New York Univ.

Electorate Nominating Committee: Adam P. Fagen, Genetics Society of America; Claire A. Hemingway, National Science Foundation; M. Patricia Morse, Northeastern Univ.; James J. Smith, Michigan State Univ.

Engineering

Chair Elect: Michael D. Amiridis, Univ. of South Carolina; Larry V. McIntire, Georgia Tech

Member-at-Large of the Section Committee: Jeffrey J. Chalmers, Ohio State Univ.; Lance Collins, Cornell Univ.

Electorate Nominating Committee: Panos J. Antsaklis, Univ. of Notre Dame; Carol K. Hall, North Carolina State Univ.; Umit S. Ozkan, Ohio State Univ.; H. Vincent Poor, Princeton Univ.; Ramamoorthy Ramesh, Oak Ridge National Laboratory; Rebecca Richards-Kortum, Rice Univ.

Council Delegate: Mark A. Barteau, Univ. of Michigan; Stuart L. Cooper, Ohio State Univ.; Debasish (Deba) Dutta, Purdue Univ.; Molly Sandra Shoichet, Univ. of Toronto (Canada)

General Interest in Science and Engineering

Chair Elect: Bruce V. Lewenstein, Cornell Univ.; Cristine Russell, Harvard Univ.

Member-at-Large of the Section Committee: Andy Boyles, Highlights for Children, Inc.; David F. Salisbury, Vanderbilt Univ.

Electorate Nominating Committee: Beryl Lieff Benderly, Science Careers/Prism Magazine; Sharon Dunwoody, Univ. of Wisconsin-Madison; A'ndrea Elyse Messer, Pennsylvania State Univ.; Ginger Pinholster, AAAS

Geology and Geography

Chair Elect: Kevin P. Furlong, Pennsylvania State Univ.; Philip D. Gingerich, Univ. of Michigan

Member-at-Large of the Section Committee: Paul H. Glaser, Univ. of Minnesota; Arthur I. Zygielbaum, Univ. of Nebraska-Lincoln

Published by AAAS

Electorate Nominating Committee: Mary L. Droser, Univ. of California, Riverside; John Harrington Jr., Kansas State Univ.; Jean-Bernard H. Minster, Univ. of California, San Diego; Sarah L. Shafer, U.S. Geological Survey

History and Philosophy of Science

Chair Elect: Janet Browne, Harvard Univ.; additional candidate to be announced

Member-at-Large of the Section Committee: Hanne Andersen, Aarhus Univ. (Denmark); Janet D. Stemwedel, San Jose State Univ.

Electorate Nominating Committee: Robert (Jay) Malone, Univ. of Notre Dame/History of Science Society; Michael A. Osborne, Oregon State Univ.; Jason Robert, Arizona State Univ.; James Woodward, Univ. of Pittsburgh

Council Delegate: Frederick Grinnell, Univ. of Texas Southwestern Medical Center; Chris Young, Alverno College

Industrial Science and Technology

Chair Elect: Katharine Blodgett Gebbie, National Institute of Standards and Technology; William Tumas, National Renewable Energy Laboratory

Member-at-Large of the Section Committee: Sudarsanam Suresh Babu, Univ. of Tennessee at Knoxville; William D. Provine, DuPont

Electorate Nominating Committee: Hideaki Kasai, Osaka Univ. (Japan); Laura Privalle, Bayer CropScience; Proctor Reid, National Academy of Engineering; Kevin C. Reilly, Donald Danforth Plant Science Center; Fei-Yue Wang, Chinese Academy of Sciences/Beijing Engineering Research Center (China)

Council Delegates: Cammy R. Abernathy, Univ. of Florida; Frances M. Ross, IBM Research

Information, Computing, and Communication

Chair Elect: Joseph Halpern, Cornell Univ.; Jeannette Wing, Microsoft/Carnegie Mellon Univ.

Member-at-Large of the Section Committee: Nancy Amato, Texas A&M Univ.; Randy Howard Katz, Univ. of California, Berkeley

Electorate Nominating Committee: Jeffrey Dean, Google, Inc.; Peter Fox, Rensselaer Polytechnic Institute; Phokion G. Kolaitis, Univ. of California, Santa Cruz/IBM Almaden Research Center; Manuela M. Veloso, Carnegie Mellon Univ.

Linguistics and Language Science

Chair Elect: Jennifer Cole, Univ. of Illinois at Urbana-Champaign; Johanna Nichols, Univ. of California, Berkeley

Member-at-Large of the Section Committee: William J. Idsardi, Univ. of Maryland, College Park; Maria Polinsky, Harvard Univ.

Electorate Nominating Committee: Jonathan David Bobaljik, Univ. of Connecticut; Dan Jurafsky, Stanford Univ.; Angelika Kratzer, Univ. of Massachusetts Amherst; Nan Bernstein Ratner, Univ. of Maryland, College Park

Mathematics

Chair Elect: Eric M. Friedlander, Univ. of Southern California; William Yslas Vélez, Univ. of Arizona

Member-at-Large of the Section Committee: Luís M. A. Bettencourt, Santa Fe Institute; Jack Xin, Univ. of California, Irvine

Electorate Nominating Committee: L. Pamela (Pam) Cook, Univ. of Delaware; Lloyd E. Douglas, Independent Consultant; Joceline Lega, Univ. of Arizona; Philippe Tondeur, Univ. of Illinois at Urbana-Champaign

Medical Sciences

Chair Elect: Harry B. Greenberg, Stanford Univ. School of Medicine; Gregory A. Petsko, Weill Cornell Medical College/Cornell University

Member-at-Large of the Section Committee: Barbara J. McNeil, Brigham and Women's Hospital/Harvard Medical School; Anil K. Rustgi, Univ. of Pennsylvania Perelman School of Medicine

Electorate Nominating Committee: Nancy C. Andrews, Duke Univ.; Paul A. Insel, Univ. of California, San Diego; Mary E. Klotman, Duke University School of Medicine; JoAnn E. Manson, Brigham and Women's Hospital/Harvard Medical School

Council Delegate: Jeffrey S. Chamberlain, Univ. of Washington; Garrett A. FitzGerald, Univ. of Pennsylvania Perelman School of Medicine; Anna Di Gregorio, Weill Cornell Medical College; Charles M. Rice, Rockefeller Univ.; Andrew I. Schafer, Weill Cornell Medical College; Licia Selleri, Weill Cornell Medical College; Roy L. Silverstein, Medical College of Wisconsin; Dudley K. Strickland, Univ. of Maryland School of Medicine

Neuroscience

Chair Elect: Darwin K. Berg, Univ. of California, San Diego; Don W. Cleveland, Univ. of California, San Diego/Ludwig Institute for Cancer Research

Member-at-Large of the Section Committee: Gail D. Burd, Univ. of Arizona; Diane Lipscombe, Brown Univ.

Electorate Nominating Committee: Robert E. Burke, Columbia Univ.; Leslie C. Griffith, Brandeis Univ.; John Huguenard, Stanford Univ. School of Medicine; Lori L. Isom, Univ. of Michigan Medical School

Pharmaceutical Sciences

Chair Elect: Serrine S. Lau, Univ. of Arizona; Peter Wipf, Univ. of Pittsburgh

Member-at-Large of the Section Committee: Gunda I. Georg, Univ. of Minnesota; Swati Nagar, Temple Univ.

Electorate Nominating Committee: Jeffrey Aubé, Univ. of Kansas; Amy M. Barrios, Univ. of Utah; James C. Barrow, Johns Hopkins Univ. School of Medicine/Lieber Institute for Brain Development; Gary O. Rankin, Marshall Univ.

Physics

Chair Elect: Greg Boebinger, Florida State Univ./Univ. of Florida; Harrison B. Prosper, Florida State Univ.

Member-at-Large of the Section Committee: Lynn R. Cominsky, Sonoma State Univ.; Young-Kee Kim, Univ. of Chicago

Electorate Nominating Committee: Angel E. García, Rensselaer Polytechnic Institute; Gail G. Hanson, Univ. of California, Riverside; M. Cristina Marchetti, Syracuse Univ.; E. Ward Plummer, Louisiana State Univ.

Psychology

Chair Elect: John Gabrieli, Massachusetts Institute of Technology; Barbara Landau, Johns Hopkins Univ.

Member-at-Large of the Section Committee: Sian L. Beilock, Univ. of Chicago; Randi C. Martin, Rice Univ.

Electorate Nominating Committee: Susan A. Gelman, Univ. of Michigan; Dedre Gentner, Northwestern Univ.; Steven J. Luck, Univ. of California, Davis; Jeremy M. Wolfe, Brigham and Women's Hospital/Harvard Medical School

Council Delegate: David A. Rosenbaum, Pennsylvania State Univ.; Michael K. Tanenhaus, Univ. of Rochester

Social, Economic, and Political Sciences

Chair Elect: Ann Bostrom, Univ. of Washington; Henry E. Brady, Univ. of California, Berkeley

Member-at-Large of the Section Committee: Guillermina Jasso, New York Univ.; Walter R. Mebane, Univ. of Michigan

Electorate Nominating Committee: Mathew D. McCubbins, Duke Univ./Duke Law School; Melvin L. Oliver, Univ. of California, Santa Barbara; Stanley Presser, Univ. of Maryland, College Park; Gary Sandefur, Oklahoma State Univ.

Council Delegate: Thomas Dietz, Michigan State Univ.; Paula Stephan, Georgia State Univ.

Societal Impacts of Science and Engineering

Chair Elect: David Goldston, Natural Resources Defense Council; Jane Maienschein, Arizona State Univ.

Member-at-Large of the Section Committee: Kevin Finneran, National Academies; Anne Fitzpatrick, U.S. Department of Energy

Electorate Nominating Committee: Cathleen A. Campbell, CRDF Global; Edward G. Derrick, AAAS; Anne-Marie Carroll Mazza, National Academy of Sciences; Julia A. Moore, Pew Charitable Trusts

Statistics

Chair Elect: Nicholas P. Jewell, Univ. of California, Berkeley; Vijay Nair, Univ. of Michigan

Member-at-Large of the Section Committee: Raymond J. Carroll, Texas A&M Univ.; Charmaine Dean, Univ. of Western Ontario (Canada)

Electorate Nominating Committee: Chris Amos, Dartmouth College; Sastry G. Pantula, Oregon State Univ.; Simon Tavaré, Univ. of Cambridge (UK); Naisyin Wang, Univ. of Michigan

Published by AAAS

RESEARCH

Squeezing out changes in a borosilicate glass structure
Edwards et al., *p. 1027*

IN *SCIENCE* JOURNALS

Edited by **Melissa McCartney** *and* **Margaret Moerchen**

A Brazilian opossum in the Atlantic Forest

CONSERVATION ECONOMICS

Cost-effective conservation on private land

How affordable is biodiversity conservation in a fragmented landscape? Banks-Leite *et al.* asked this question for the biodiversity hotspot of the Brazilian Atlantic Forest. An annual investment of <10% of Brazil's agricultural subsidies could support effective ecological restoration on private lands. This would increase biodiversity in set-aside land to the same level observed in protected areas. The cost-effectiveness of this scheme suggests a path forward for conservation strategies in other similarly mixed landscapes, too. — AMS

Science, this issue p. 1041

HUMAN MICROBIOTA

Signature microbes follow you from house to house

Householders share more than habitation; they also share inhabitants. In a diverse sample of U.S. homes, Lax *et al.* found that people and animals sharing homes shared their microbial communities (microbiota) too, probably because of skin shedding and hand and foot contamination. When families moved, their microbiological "aura" followed. If one person left the home even for a few days, their contribution to the microbiome diminished. These findings have implications not only for household identity and composition, but also for indicators of the members' health and well-being. — CA

Science, this issue p. 1048

STELLAR DISTANCES

Distance score settled for Seven Sisters

Most of us have seen the Pleiades star cluster in the night sky, one of the few groups of physically related stars that are separately visible to the naked eye. In spite of its proximity to us, its distance has been disputed. Melis *et al.* settle the controversy with astrometric measurements from radio interferometry that reveal a distance of 136.2 parsecs (see the Perspective by Girardi). Other methods yielded similar values, but the trusted astrometry satellite Hipparcos measured only 120.2 parsecs. The new result alleviates the concern that astronomers would need to adjust their stellar evolution models to align with the Hipparcos distance. — MMM

Science, this issue p. 1029; see also p. 1001

EARTHQUAKE DYNAMICS

Strong yet creeping megathrust faults

Powerful faults in subduction zones, called "megathrust faults," produce the largest earthquakes on Earth. Gao and Wang use heat flow data to show that when the faults subduct jagged sea floor, they generate tamer earthquakes than do faults that subduct smooth sea floor. The rugged sea floor brings irregularities into the fault that cause it to deform slowly over time, which results in a comparatively higher fault strength and lower seismicity. The finding has a direct impact on assessing regional earthquake and tsunami hazards. — BG

Science, this issue p. 1038

EVOLUTIONARY GENOMICS

Rabbits softly swept to domestication

When people domesticate animals, they select for tameness and tolerance of humans. What else do they look for? To identify the selective pressures that led to rabbit domestication,

Downloaded from www.sciencemag.org on August 29, 2014

PHOTOS: (TOP TO BOTTOM) STUDIOCASPER/ISTOCK PHOTO; THOMAS PÜTTKER

Published by AAAS

Carneiro *et al.* sequenced a domestic rabbit genome and compared it to that of its wild brethren (see the Perspective by Lohmueller). Domestication did not involve a single gene changing, but rather many gene alleles changing in frequency between tame and domestic rabbits, known as a soft selective sweep. Many of these alleles have changes that may affect brain development, supporting the idea that tameness involves changes at multiple loci. — LMZ

Science, this issue p. 1074; see also p. 1000

IMMUNOLOGY

Cutting out a kinase for T cell survival

Sufficient numbers of T cells are required in the body to fight pathogens. To survive, T cells need to receive signals through both the T cell receptor and the interleukin-7 receptor. However, constant interleukin-7 receptor activation causes T cells to die, so the T cell receptor intermittently blocks the activity of the interleukin-7 receptor. Signaling through the interleukin-7 receptor requires the kinase Jak1. Katz *et al.* found that T cells contained very little Jak1 protein and that it was unstable. When researchers activated the T cell receptor, they generated increased amounts of microRNA. The microRNA prevented the T cells from producing new Jak1 protein and interfered with the ability of the interleukin-7 receptor to signal. — JFF

Sci. Signal. **7**, ra83 (2014).

CELL MIGRATION IN 3D

Push me, pull you, that's the way to move

Primary cells, derived directly from human tissue, exhibit different behaviors in shape and signaling within three-dimensional (3D) or 2D spaces. When the pressure within the cell increases, cells display limb-like bumps, which they use to move through their 3D environment. Petrie *et al.* now show that when the complex of actin and myosin contracts, it controls the pressure within cells and therefore the shape of those protruding structures (see the Perspective by DeSimone and Horwitz). The authors measured internal pressures in migrating mammalian cells. In the 3D matrix, those cells have higher pressure that differs between the front and back of the cell, which creates a piston effect. — SMH

Science, this issue p. 1062; see also p. 1002

PAIN

An enzyme offers a new path to pain control

Many people suffer from uncontrolled pain, and new drugs are needed. Zambelli *et al.* build on the fact that aldehydes—molecules that occur naturally in the body—can cause pain directly. Specifically, an enzyme that degrades aldehydes is a key regulator of pain. Mice with genetically inactive versions of the enzyme are extra sensitive to a painful stimulus. Conversely, revving up the enzyme with a drug reverses this effect. New drugs that modulate aldehyde levels could benefit patients, possibly without risk of addiction. These results may also explain the greater pain sensitivity in East Asians, many of whom carry a relevant mutation. — KLK

Sci. Transl. Med. **6**, 251ra119 (2014).

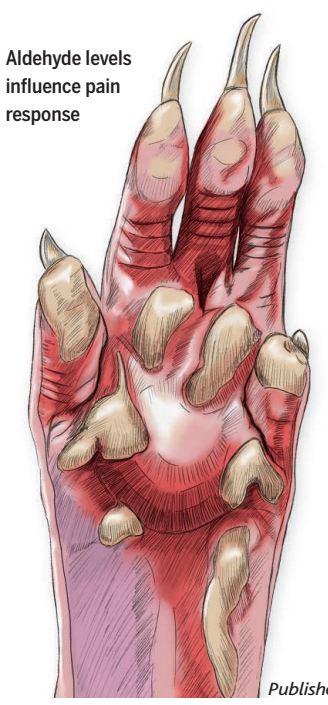

Aldehyde levels influence pain response

ILLUSTRATIONS: (TOP TO BOTTOM) BRYCE SMALL/STANFORD UNIVERSITY; V. ALTOUNIAN/*SCIENCE*

IN OTHER JOURNALS

Edited by **Melissa McCartney** *and* **Margaret Moerchen**

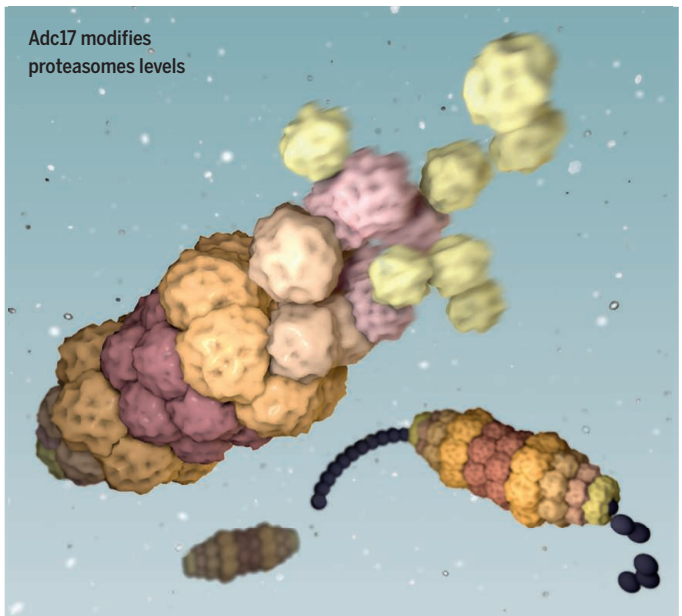

Adc17 modifies proteasomes levels

PROTEOSTASIS

Need proteasomes? Make some!

Cells need to clear out damaged proteins, or they age and become unhealthy. To do this, cells use tiny protein-destroying machines called proteasomes. Building these proteasomes is a complex process, and it's not clear how stressed cells can make sure the proteasome supply meets demand. Working with yeast cells, Hanssum *et al.* discovered a protein that helps cells assemble just enough proteasomes to fit their needs. In a process called chaperoning, the protein, which they called Adc17, helps pair two proteasomal proteins, Rpt6 and Rpt3, during proteasome assembly. — SMH

Mol. Cell 10.1016/j.molcel.2014.06.017 (2014).

HUMAN BEHAVIOR

Incentives work on economists, too!

Editors treasure prompt and informative referees. Chetty *et al.* show that modest psychological and economic nudges can speed up how rapidly referees return their reviews without degrading their quality. In a randomized experiment involving 1500 referees at the *Journal of Public Economics*, they offered some referees $100 for turning in their reviews by the 4-week deadline, whereas they told others, who had agreed to a 6-week deadline, that their delivery dates would be posted publicly. From a comparison across these groups and the non-incentivized controls, they conclude that 4 weeks is enough and that both social pressure and money work. — GJC

J. Econ. Perspect. **28**, 169 (2014).

PHYSICS

Eliminating the effects of the pesky bulk

A material's imperfections can greatly influence how well it conducts electricity. Theoretical physicists have, however, come up with the concept of topological insulators (TIs): materials that conduct only at their surface in a way that makes them

Published by AAAS

"immune" to certain kinds of disorder. The compounds that have been identified as TIs, such as Bi_2Se_3, fall short of this ideal because they conduct electricity both through the "immune" surface states and the bulk of the material, which is still affected by disorder. Brahlek *et al.* made thin samples of Bi_2Se_3, adding copper atoms in precise quantities. When the samples were thick enough and had just the right concentrations of copper, the authors found that the samples were conducting only at their surfaces. This work is a step forward toward making useful TI devices. — JS

Phys. Rev. Lett. **113**, 026801 (2014).

GEOPHYSICS

Making mantle melt analogs more accurate

Glasses, which can be thought of as "frozen" liquids, often are used as a proxy to study the properties of silicate melts in Earth's mantle. Glasses can be studied at temperatures and pressures lower than those found deep underground, which are impossible to achieve in the lab. Ghosh *et al.* conduct computational analyses to show that temperature is important in determining the properties of glass. Glass compressed at high temperature can change its structure and become denser than glass compressed at room temperature, making it a better analog for liquid melts generated deep in the mantle. — BG

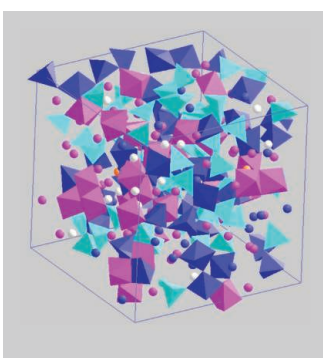

Hot-compressed glass structure

Am. Mineral. 10.2138/am.2014.4631 (2014).

INNATE IMMUNITY

Cleaving RNA dials down inflammation

The immune system detects viruses when viral nucleic acids bind protein receptors in immune cells. But what keeps these receptors from reacting to the host cells' own nucleic acids in the cytoplasm and causing unwanted inflammation? Eckard *et al*. examined the case of RIG-I–like receptors (RLRs), which bind to viral RNA. They found that host RNAs generated during cellular stress could induce an RLR-dependent inflammatory response. In normal cells, the protein SKIV2L, which is part of a large protein complex that chews up RNA, prevented such inflammation by degrading the RNAs. The authors observed an inflammatory response in two patients who had mutated versions of SKIV2L, suggesting that SKIV2L keeps inflammation in check in human cells, too. — KLM

Nat. Immunol. 10.1038/ni.2948 (2014).

SOCIAL SCIENCE

Moving from one novelty to the next

Life would be boring if things were always the same. Tria and colleagues explore whether novelties—discoveries of things new to us—are independent of each other or whether one novelty leads to another. They analyzed selected text, online music, Wikipedia, and a social tagging site and measured how the number of different elements grew with time. Although two of the data sets contained innovations (items new to everyone) and two contained novelties (items new to individual users), they all showed the same kinetics and probability distributions. Modeling analyses suggested that novelties are not independent of each other. As the authors state, each novelty "comes with a cloud of other potentially new ideas that are thematically adjacent to it and hence can be triggered by it." — BJ

Sci. Rep. 10.1038/srep05890 (2014).

The South American fur seal may have helped spread TB

INFECTIOUS DISEASE

Seals infected early Americans with TB

How did *Mycobacterium tuberculosis*, which causes tuberculosis (TB), first infect humans? Microbial DNA from 1000-year-old Peruvian mummies suggests that seals may have spread the disease to South American humans long before European settlers arrived. Bos ***et al***. used DNA sequencing to solve the mystery. After finding the TB bacteria's DNA in three of the mummies, the team determined that the bacterial genomes were closest in sequence to a TB strain that infects marine mammals, suggesting that the ancient humans got TB from eating seal or sea lion meat, the researchers say. — EP

Nature 10.1038/nature13591 (2014).

CATALYSIS

Interior design with nanoparticles

Catalysts made from metal nanoparticles (NPs) absorbed on oxide surfaces often are used in many industrial reactions and in automotive catalysts. These usually work best at high temperatures. High temperatures, however, promote surface diffusion and the subsequent formation of larger particles with less surface area, which become less active over time. Qiao *et al.* synthesized thermally stable NPs of palladium (Pd) and platinum within a hollow shell of microporous silica that allowed small molecules to enter and leave the interior. Polymer nanodots synthesized with the shell-bound metal ions formed NPs with average sizes under 2 nm and high thermal stability upon reduction and heating. The micropores also controlled catalytic product formation. Oxidative reduction of cyclohexene with trapped Pd NPs yielded almost pure benzene, versus a host of larger oxygenated rings for exposed Pd NPs. — PDS

J. Am. Chem. Soc. 10.1021/ja505903r (2014).

CREDITS: (LEFT TO RIGHT) D. B. GHOSH *ET AL. AMERICAN MINERALOGIST* **99** (JULY 2014) © MINERALOGICAL SOCIETY OF AMERICA; © INCAMERASTOCK/ALAMY

Published by AAAS

ALSO IN *SCIENCE* JOURNALS

Edited by **Melissa McCartney** *and* **Margaret Moerchen**

CIRCUMSTELLAR DISKS

A cosmic dust storm that came and went

Unseen planets may still kick up a lot of dust. While rocky exoplanets finish their growth, destructive collisions among them throw off clouds of fine debris that shine bright in the infrared. Meng *et al.* monitored the star ID8 with the *Spitzer* Space Telescope and observed a rapid thermal flareup and fadeout within only 2 years. This modulation is consistent with recent collisions among its orbiting protoplanets. Such dynamic variations in presumed planet-forming systems encourage more studies that exploit the real-time changes. – MMM

Science, this issue p. 1032

SUPERFLUIDITY

Making a superfluid lithium mixture

At some of the coldest temperatures achieved in the laboratory, researchers can coax dilute gases of atoms into becoming a superfluid, with the whole gas behaving as one entity. Bosonic atoms, which like to congregate in one state, achieve this willingly. Fermions, which effectively repel each other, require more persuasion. Ferrier-Barbut *et al.* made a superfluid mixture of two gases, one made up of bosons and one of fermions. They used two isotopes of lithium, fermionic ^{6}Li and bosonic ^{7}Li. When they made the mixture oscillate, the two components took turns feeding energy into each other. – JS

Science, this issue p. 1035

GLASS STRUCTURE

Catching changing boron coordination

Laboratory glassware and kitchen cookware alike are made of glass that contains different cations, including boron, sodium, and aluminum. Properties of glass depend on the number and location of oxygen atoms surrounding each cation. Edwards *et al.* combine nuclear magnetic resonance measurements with theoretical calculations to understand structural transformations in borosilicate glass (see the Perspective by Youngman). Boron atoms in planar threefold coordination move out of plane with increasing pressure to form trigonal pyramids. Identification of this type of transition state connects structural evolution with stress-induced processes in amorphous materials. In borosilicate glass, the transition leads to the formation of tetrahedral fourfold-coordinated boron that tunes glass properties for use in numerous applications. – BG

Science, this issue p. 1027; see also p. 998

HUMAN GENETICS

Arctic genetics comes in from the cold

Despite a well-characterized archaeological record, the genetics of the people who inhabit the Arctic have been unexplored. Raghavan *et al.* sequenced ancient and modern genomes of individuals from the North American Arctic (see the Perspective by Park). Analyses of these genomes indicate that the Arctic was colonized 6000 years ago by a migration separate from the one that gave rise to other Native American populations. Furthermore, the original paleo-inhabitants of the Arctic appear to have been completely replaced approximately 700 years ago. – LMZ

Science, this issue p. 1020; see also p. 1004

ION CHANNEL STRUCTURE

Activating a receptor to excite a neuron

Transmitting signals between nerve cells, occuring at structures known as synapses, is critical to processes such as learning and memory. Fast transmission occurs when glutamate is released from a presynaptic neuron and binds to ionotropic glutamate receptors (iGluRs) in the cell membrane of a postsynaptic neuron. The iGluR

Published by AAAS

contains an ion channel that is transiently opened, to activate the postsynaptic neuron, but then closes rapidly. Chen *et al.* and Yelshanskaya *et al.* report crystal structures in a range of conformations that together provide insight into how glutamate binding causes the channel to open and how other molecules that bind to the receptor modulate this. The information could aid in the design of drugs to treat cognitive impairment or seizure disorders – VV

Science, this issue p. 1021 and p. 1070

MEMORY ENHANCEMENT

Brain stimulation to improve human memory

The hippocampus is a crucial brain area for certain types of memory. Working with humans, Wang *et al.* found that a specific type of non-invasive brain stimulation improved memory tests and enhanced information flow between the hippocampus and a number of other brain regions. This increased connectivity was highly specific for the individual target areas selected for each participant. – PRS

Science, this issue p. 1054

CHROMATIN REGULATION

Chromatin mutations disrupt development

Histone proteins form the core packaging material for our genomic DNA, and covalent modifications to amino acid residues in their structure play an important role in the epigenetic control of gene expression. Herz *et al*. show that specific mutations in the residues that are normally modified to regulate expression cause severe disruption of normal development in the fruit fly. Similar mutations are known to be involved in a subtype of aggressive pediatric brain cancers. Insights into the epigenetic regulatory pathways disrupted by these mutations in *Drosophila* may suggest possible treatments for human cancers. – GR

Science, this issue p. 1062

GERMINAL CENTERS

T and B cells' intricate molecular dance

Generating high-affinity antibodies to fight infection is no easy task. To do so requires multiple steps, including T cells interacting with antibody-producing B cells in lymph nodes. These interactions select B cells expressing high-affinity antibodies for further proliferation, ensuring that the immune response generates high-affinity antibodies in large quantities. Shulman *et al*. use fluorescent live-cell imaging in mice to determine the molecular details of these interactions. They find that T cells engage B cells in short-lived mobile contacts during selection. These contacts cause T cells to flux calcium and produce proteins called cytokines, which probably drive B cells to proliferate and produce high-affinity antibodies. – KM

Science, this issue p. 1058

MICROBIAL METABOLISM

Oxidizing hydrogen in place of nitrite

Microorganisms are important drivers of Earth's nitrogen cycle. Many of the organisms responsible for mediating the reactions of one phase of nitrogen to another are thought to be ecologic specialists. Using a combination of genomic and experimental analyses, Koch *et al.* show that *Nitrospira moscoviensis*, a member of a widely distributed genus of nitrite-oxidizing bacteria, can oxidize hydrogen instead of nitrite to support growth when oxygen is present. Not only does this ecologic flexibility suggest a broader distribution of these organisms in natural settings, but they may be important in engineered environments as well. – NW

Science, this issue p. 1052

PALEOCEANOGRAPHY

El Niño shifted between the center and the East

El Niño has changed quite a bit over the past 10,000 years. During some periods it was less variable than now, and during others it shifted from its current locale toward the central Pacific. Carré *et al.* analyzed the shells of mollusks from Peru to construct a record of the El Niño–Southern Oscillation (ENSO) in the eastern Pacific over the Holocene period. They compared this record with other records from the rest of the Pacific to reveal how much the strength and frequency of El Niños changed and how their positions varied. – HJS

Science, this issue p. 1045

Published by AAAS

RESEARCH ARTICLE SUMMARY

ARCTIC GENETICS

The genetic prehistory of the New World Arctic

Maanasa Raghavan, Michael DeGiorgio, Anders Albrechtsen, Ida Moltke, Pontus Skoglund, Thorfinn S. Korneliussen, Bjarne Grønnow, Martin Appelt, Hans Christian Gulløv, T. Max Friesen, William Fitzhugh, Helena Malmström, Simon Rasmussen, Jesper Olsen, Linea Melchior, Benjamin T. Fuller, Simon M. Fahrni, Thomas Stafford Jr., Vaughan Grimes, M. A. Priscilla Renouf, Jerome Cybulski, Niels Lynnerup, Marta Mirazon Lahr, Kate Britton, Rick Knecht, Jette Arneborg, Mait Metspalu, Omar E. Cornejo, Anna-Sapfo Malaspinas, Yong Wang, Morten Rasmussen, Vibha Raghavan, Thomas V. O. Hansen, Elza Khusnutdinova, Tracey Pierre, Kirill Dneprovsky, Claus Andreasen, Hans Lange, M. Geoffrey Hayes, Joan Coltrain, Victor A. Spitsyn, Anders Götherström, Ludovic Orlando, Toomas Kivisild, Richard Villems, Michael H. Crawford, Finn C. Nielsen, Jørgen Dissing, Jan Heinemeier, Morten Meldgaard, Carlos Bustamante, Dennis H. O'Rourke, Mattias Jakobsson, M. Thomas P. Gilbert, Rasmus Nielsen, Eske Willerslev*

INTRODUCTION: Humans first peopled the North American Arctic (northern Alaska, Canada, and Greenland) around 6000 years ago, leaving behind a complex archaeological record that consisted of different cultural units and distinct ways of life, including the Early Paleo-Eskimos (Pre-Dorset/Saqqaq), the Late Paleo-Eskimos (Early Dorset, Middle Dorset, and Late Dorset), and the Thule cultures.

RATIONALE: We addressed the genetic origins and relationships of the various New World Arctic cultures to each other and to modern-day populations in the region. We obtained 26 genome-wide sequences and 169 mitochondrial DNA sequences from ancient human bone, teeth, and hair samples from Arctic Siberia, Alaska, Canada, and Greenland, and high-coverage genomes of two present-day Greenlandic Inuit, two Siberian Nivkhs, one Aleutian Islander, and two Athabascan Native Americans. Twenty-seven ancient samples were radiocarbon dated for accurate cultural assignment, of which 25 were corrected for marine reservoir effect to account for the dominant marine component in these individuals' diets.

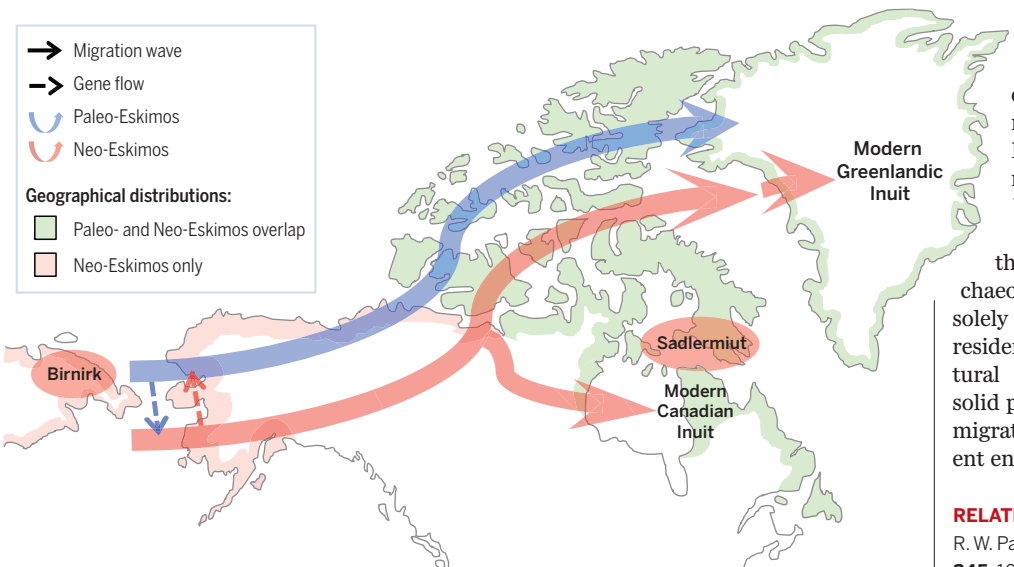

Genetic origins of Paleo-Eskimos and Neo-Eskimos. All Paleo-Eskimos represent a single migration pulse from Siberia into the Americas, independent of the Neo-Eskimo Thule people (ancestors of modern-day Inuit) and the related extinct Sadlermiut population. The Siberian Birnirk people were likely cultural and genetic ancestors of modern-day Inuit. We also show ancient admixture between the Paleo- and Neo-Eskimo lineages, occurring at least 4000 years ago.

RESULTS: Nuclear and mitochondrial DNA data unequivocally show that the Paleo-Eskimos are closer to each other than to any other present-day population. The Thule culture represents a distinct people that are genetic and cultural ancestors of modern-day Inuit. We additionally find the Siberian Birnirk culture (6th to 7th century CE) as likely cultural and genetic ancestors of the Thule. The extinct Sadlermiut people from the Hudson Bay region (15th to 19th century CE), considered to be Dorset remnants, are genetically closely related to Thule/Inuit, rather than the Paleo-Eskimos. Moreover, there is no evidence of matrilineal gene flow between Dorset or Thule groups with neighboring Norse (Vikings) populations settling in the Arctic around 1000 years ago. However, we do detect gene flow between the Paleo-Eskimo and Neo-Eskimo lineages, dating back to at least 4000 years.

ON OUR WEB SITE

Read the full article at http://dx.doi.org/10.1126/science.1255832

CONCLUSION: Our study has a number of important implications: Paleo-Eskimos likely represent a single migration pulse into the Americas from Siberia, separate from the ones giving rise to the Inuit and other Native Americans, including Athabascan speakers. Paleo-Eskimos, despite showing cultural differences across time and space, constituted a single population displaying genetic continuity for more than 4000 years. On the contrary, the Thule people, ancestors of contemporary Inuit, represent a population replacement of the Paleo-Eskimos that occurred less than 700 years ago. The long-term genetic continuity of the Paleo-Eskimo gene pool and lack of evidence of Native American admixture suggest that the Saqqaq and Dorset people were largely living in genetic isolation after entering the New World. Thus, the Paleo-Eskimo technological innovations and changes through time, as evident from the archaeological record, seem to have occurred solely by movement of ideas within a single resident population. This suggests that cultural similarities and differences are not solid proxies for population movements and migrations into new and dramatically different environments, as is often assumed. ■

RELATED ITEMS IN SCIENCE

R. W. Park, Stories of Arctic colonization. *Science* **345**, 1004–1005 (2014)

The list of author affiliations is available in the full article online.
*Corresponding author. E-mail: ewillerslev@snm.ku.dk
Cite this article as M. Raghavan *et al.*, *Science* **345**, 1255832 (2014). DOI: 10.1126/science.1255832

Published by AAAS

RESEARCH ARTICLE

ARCTIC GENETICS

The genetic prehistory of the New World Arctic

Maanasa Raghavan,[1] Michael DeGiorgio,[2] Anders Albrechtsen,[3]* Ida Moltke,[3,4]* Pontus Skoglund,[5,6]* Thorfinn S. Korneliussen,[1] Bjarne Grønnow,[7] Martin Appelt,[7] Hans Christian Gulløv,[7] T. Max Friesen,[8] William Fitzhugh,[9] Helena Malmström,[1,5] Simon Rasmussen,[10] Jesper Olsen,[11] Linea Melchior,[12] Benjamin T. Fuller,[13] Simon M. Fahrni,[13] Thomas Stafford Jr.,[1,11] Vaughan Grimes,[14,15] M. A. Priscilla Renouf,[14]† Jerome Cybulski,[16,17] Niels Lynnerup,[12] Marta Mirazon Lahr,[18] Kate Britton,[15,19] Rick Knecht,[19] Jette Arneborg,[20,21] Mait Metspalu,[22,23] Omar E. Cornejo,[24,25] Anna-Sapfo Malaspinas,[1] Yong Wang,[26,27] Morten Rasmussen,[1] Vibha Raghavan,[28] Thomas V. O. Hansen,[29] Elza Khusnutdinova,[30,31] Tracey Pierre,[1] Kirill Dneprovsky,[32] Claus Andreasen,[33] Hans Lange,[33] M. Geoffrey Hayes,[34,35,36] Joan Coltrain,[37] Victor A. Spitsyn,[38] Anders Götherström,[39] Ludovic Orlando,[1] Toomas Kivisild,[22,40] Richard Villems,[22,23] Michael H. Crawford,[41] Finn C. Nielsen,[29] Jørgen Dissing,[12] Jan Heinemeier,[11] Morten Meldgaard,[1] Carlos Bustamante,[24] Dennis H. O'Rourke,[37] Mattias Jakobsson,[5] M. Thomas P. Gilbert,[1] Rasmus Nielsen,[26] Eske Willerslev[1]‡

The New World Arctic, the last region of the Americas to be populated by humans, has a relatively well-researched archaeology, but an understanding of its genetic history is lacking. We present genome-wide sequence data from ancient and present-day humans from Greenland, Arctic Canada, Alaska, Aleutian Islands, and Siberia. We show that Paleo-Eskimos (~3000 BCE to 1300 CE) represent a migration pulse into the Americas independent of both Native American and Inuit expansions. Furthermore, the genetic continuity characterizing the Paleo-Eskimo period was interrupted by the arrival of a new population, representing the ancestors of present-day Inuit, with evidence of past gene flow between these lineages. Despite periodic abandonment of major Arctic regions, a single Paleo-Eskimo metapopulation likely survived in near-isolation for more than 4000 years, only to vanish around 700 years ago.

Humans first peopled the North American Arctic (northern Alaska, Canada, and Greenland) from the Bering Strait region beginning around 6000 years before the present (*1*), leaving behind a complex archaeological record [supplementary text S1 (*2*) and Fig. 1]. Over successive millennia, the pioneering Arctic cultures developed into distinct lifestyles and cultural stages grouped within two broad cultural traditions known as Paleo-Eskimo and Neo-Eskimo. Early Paleo-Eskimo people representing the Denbigh, Pre-Dorset, Independence I, and Saqqaq cultures (~3000 to 800 BCE) lived in tent camps and hunted caribou, musk ox, and seals with exquisitely flaked stone tools similar to those used by northeast Siberian Neolithic cultures (*3*–*6*). In northern Alaska, the Denbigh cultural groups were succeeded by the Paleo-Eskimo Choris and Norton cultures starting around 900 BCE, with the Norton material culture further developing into the Ipiutak culture around 200 CE (*6*, *7*). Simultaneously, during the cold period beginning around 800 BCE, innovations in housing and hunting technologies accompanied the formation of the Late Paleo-Eskimo or Dorset culture in eastern Arctic (eastern Canadian Arctic and Greenland), with population growth and more intensive use of marine mammals, including walrus (*8*, *9*). The Dorset culture is divided into three phases: (i) Early Dorset, ~800 BCE to 0 BCE/CE; (ii) Middle Dorset, ~0 BCE/CE to 600 to 800 CE; and (iii) Late Dorset ~600 to 800 CE to 1300 CE (*9*). The Paleo-Eskimo tradition in the eastern Arctic ended sometime between 1150 to 1350 CE, shortly after the sudden appearance of the Neo-Eskimo Thule whale-hunters from the Bering Strait region (*9*–*17*).

The Siberian Old Bering Sea culture is the earliest expression of the Neo-Eskimo tradition ~2200 years before the present, developing into the Punuk culture around the sixth century CE. Almost concurrently, the Old Bering Sea culture developed into the Birnirk culture in the northern parts of the Bering Strait region. Interactions between people of the Birnirk and Punuk cultures gave rise to the western Thule culture on both sides of the Bering Strait, with contribution from the Paleo-Eskimo Ipiutak culture in Alaska (*18*). By the early second millennium CE, western Thule cultural groups began their movement into the eastern North American Arctic (*14*, *19*). With the Thule culture came more effective means of transportation like dog sleds and large skin boats, complex tool kits like sinew-backed bows, and harpoon float gear for hunting large whales (*10*, *20*). Thule culture spread quickly throughout the eastern Arctic, rapidly replacing Dorset in most, if not all, regions. The decline of whaling during the latter part of the Little Ice Age (16th to 19th century CE) resulted in a readjustment to ice-edge hunting of walrus and breathing-hole

[1]Centre for GeoGenetics, Natural History Museum of Denmark, University of Copenhagen, Øster Voldgade 5–7, 1350 Copenhagen, Denmark. [2]Department of Biology, Pennsylvania State University, 502 Wartik Laboratory, University Park, PA 16802, USA. [3]Bioinformatics Centre, Department of Biology, University of Copenhagen, Ole Maaloes Vej 5, 2200 Copenhagen, Denmark. [4]Department of Human Genetics, University of Chicago, Chicago, IL 60637, USA. [5]Department of Evolutionary Biology, Uppsala University, Norbyvägen 18D, 75236 Uppsala, Sweden. [6]Department of Genetics, Harvard Medical School, Boston, MA 02115, USA. [7]Arctic Centre at the Ethnographic Collections (SILA), National Museum of Denmark, Frederiksholms Kanal 12, 1220 Copenhagen, Denmark. [8]Department of Anthropology, University of Toronto, Toronto, Ontario M5S 2S2, Canada. [9]Arctic Studies Center, Post Office Box 37012, Department of Anthropology, MRC 112, National Museum of Natural History, Smithsonian Institution, Washington, DC 20013–7012, USA. [10]Center for Biological Sequence Analysis, Department of Systems Biology, Technical University of Denmark, Kemitorvet, 2800 Kongens Lyngby, Denmark. [11]AMS 14C Dating Centre, Department of Physics and Astronomy, Aarhus University, Ny Munkegade 120, 8000 Aarhus C, Denmark. [12]Anthropological Laboratory, Institute of Forensic Medicine, Faculty of Health Sciences, University of Copenhagen, Frederik V's Vej 11, 2100 Copenhagen, Denmark. [13]Department of Earth System Science, University of California, Irvine, CA 92697, USA. [14]Department of Archaeology, Memorial University, Queen's College, 210 Prince Philip Drive, St. John's, Newfoundland, A1C 5S7, Canada. [15]Department of Human Evolution, Max Planck Institute for Evolutionary Anthropology, 04103 Leipzig, Germany. [16]Canadian Museum of History, 100 Rue Laurier, Gatineau, Quebec K1A 0M8, Canada. [17]Department of Anthropology, University of Western Ontario, 1151 Richmond Street North, London N6A 5C2, Canada. [18]Leverhulme Centre for Human Evolutionary Studies, Department of Archaeology and Anthropology, University of Cambridge, Cambridge CB2 1QH, UK. [19]Department of Archaeology, University of Aberdeen, St. Mary's Building, Elphinstone Road, Aberdeen AB24 3UF, Scotland, UK. [20]National Museum of Denmark, Frederiksholms kanal 12, 1220 Copenhagen, Denmark. [21]School of Geosciences, University of Edinburgh, Edinburgh EH8 9XP, UK. [22]Estonian Biocentre, Evolutionary Biology Group, Tartu 51010, Estonia. [23]Department of Evolutionary Biology, University of Tartu, Tartu 51010, Estonia. [24]Department of Genetics, School of Medicine, Stanford University, Stanford, CA 94305, USA. [25]School of Biological Sciences, Washington State University, Post Office Box 644236, Pullman, WA 99164, USA. [26]Department of Integrative Biology, University of California, Berkeley, CA 94720, USA. [27]Ancestry.com DNA LLC, San Francisco, CA 94107, USA. [28]Informatics and Bio-computing, Ontario Institute for Cancer Research, 661 University Avenue, Suite 510, Toronto, Ontario, M5G 0A3, Canada. [29]Center for Genomic Medicine, Rigshospitalet, University of Copenhagen, Blegdamsvej 9, 2100 Copenhagen, Denmark. [30]Institute of Biochemistry and Genetics, Ufa Scientific Center of Russian Academy of Sciences, Ufa, Russia. [31]Department of Genetics and Fundamental Medicine, Bashkir State University, Ufa, Bashkortostan 450074, Russia. [32]State Museum for Oriental Art, 12a, Nikitsky Boulevard, Moscow 119019, Russia. [33]Greenland National Museum and Archives, Post Office Box 145, 3900 Nuuk, Greenland. [34]Division of Endocrinology, Metabolism and Molecular Medicine, Department of Medicine, Northwestern University Feinberg School of Medicine, Chicago, IL 60611, USA. [35]Department of Anthropology, Weinberg College of Arts and Sciences, Northwestern University, Evanston, IL 60208, USA. [36]Center for Genetic Medicine, Northwestern University Feinberg School of Medicine, Chicago, IL 60611, USA. [37]Department of Anthropology, University of Utah, Salt Lake City, UT 84112, USA. [38]Research Centre for Medical Genetics of Russian Academy of Medical Sciences, 1 Moskvorechie, Moscow 115478, Russia. [39]Department of Archaeology and Classical Studies, Stockholm University, Stockholm, Sweden. [40]Department of Archaeology and Anthropology, University of Cambridge, Cambridge CB2 1QH, UK. [41]Laboratory of Biological Anthropology, University of Kansas, Lawrence, KS 66045, USA.
*These authors contributed equally to this work. †Deceased.
‡Corresponding author. E-mail: ewillerslev@snm.ku.dk

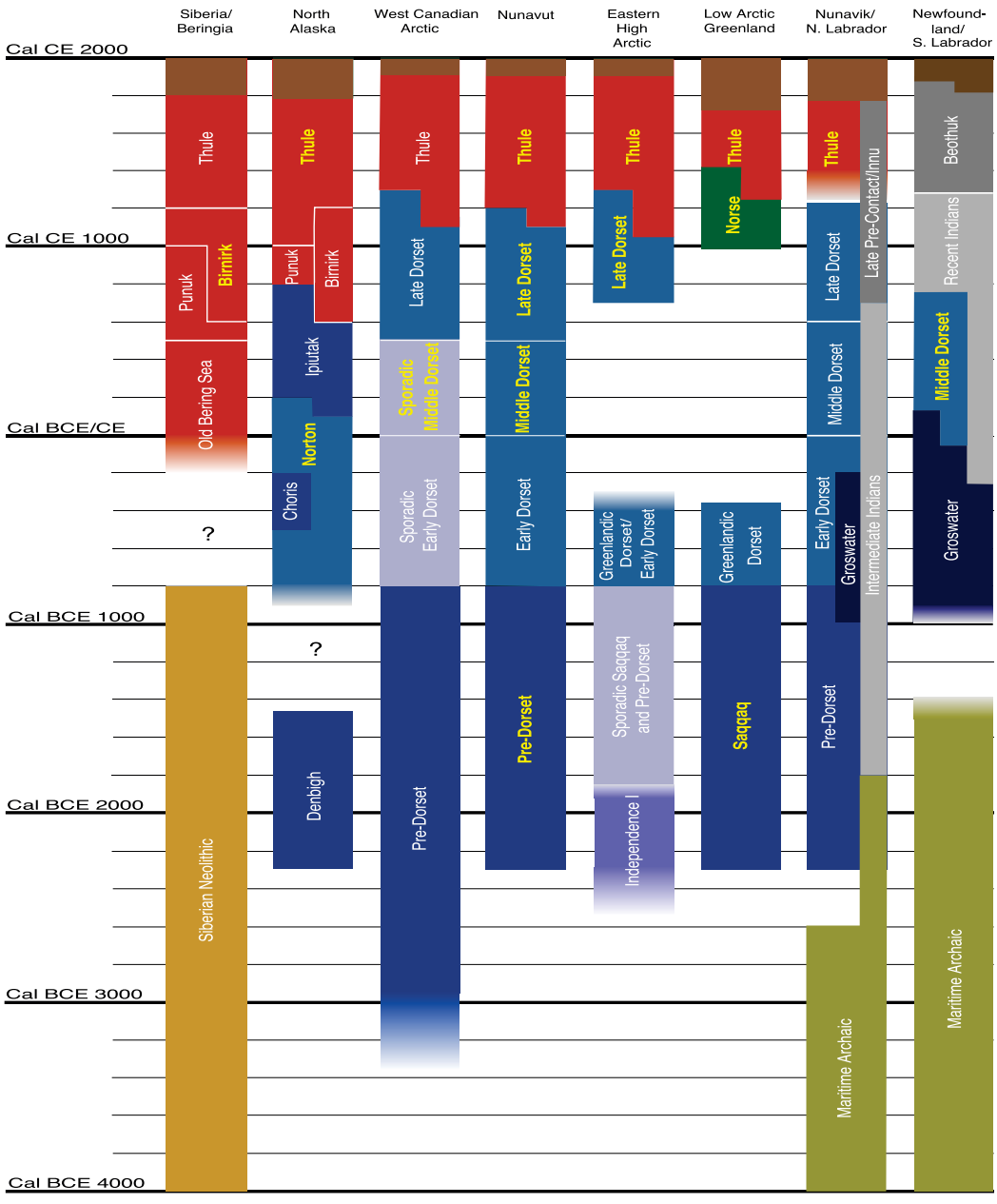

Fig. 1. Chronology of the prehistoric cultures in the New World Arctic and northeast Siberia. This framework is based on a combination of screened radiocarbon dates on associated terrestrial materials, typological studies, and contexts [e.g., (*6*, *9*, *37*, *40*, *83*–*85*)]. Fading colors symbolize uncertainties concerning the beginnings or ends of the archaeological cultures, owing to plateaus or wiggles in the radiocarbon calibration curve or lack of data. Defined archaeological phases within a culture are separated by a white line. Dark reddish-brown toward the top of the figure indicates historical times. Cultural contexts from which samples included in this study arise are highlighted in yellow.

hunting of seal, laying the foundation for modern Inuit cultures (*21*). Additionally, the Norse (Vikings) formed settlements in Greenland around 985 CE and occupied regions in southern Greenland for about 500 years, contemporaneous with both the Late Dorset and Thule, reaching Newfoundland and Labrador in eastern Canada around 1000 CE (*22*).

Continuities in chipped stone bifaces and blade and burin technology point to Paleo-Eskimo origins among Siberian Neolithic cultures (*6*, *10*, *23*, *24*). Genetic evidence suggests that the earliest eastern Arctic Paleo-Eskimo people represented an independent Siberian migration into the New World (*25*, *26*) (Fig. 2B, scenario 1). However, to date. we have been unable to identify the likely Siberian ancestral population. Some have argued for origins from an ill-defined 8000-year-old South Alaskan Eskimo-Aleut or Na Dene blade and burin complex (*27*), but this remains controversial. A recent genetic study provides evidence in support of the Early Paleo-Eskimos, specifically Saqqaq, sharing ancestry with Na Dene Native Americans (Fig. 2B, scenario 2), as part of a three-wave peopling model of the Americas consisting of (i) First Americans, (ii) Eskimo-Aleuts and, (iii) Saqqaq and Na Dene speakers (*28*). Alternative hypotheses on Dorset origins include the Aleutian Islanders (*29*) (Fig. 2B, scenario 3) and earlier theories of Amerindian cultures in eastern Canada and even further south (*30*–*33*) (Fig. 2B, scenario 4). Current views favor an in situ origin of Dorset from Canadian Pre-Dorset in northern Hudson Bay (*10*, *13*, *34*, *35*).

Additionally, whether the individual Early, Middle, and Late Dorset phases represent genetic continuity of the same peoples or not remains unresolved (Fig. 2A). The Dorset chronological sequence from the T1 site on Southampton Island, Igloolik, South Baffin, and Labrador in Canada provide evidence of cultural continuity through Early to Late Dorset (*20*, *30*, *36*), although regional differences and settlement discontinuities are also common (*37*–*41*). Notable regional discontinuities and occupation gaps also occur in Greenland (*9*). It is also debated whether abandoned areas were reoccupied by people from a different genetic background and whether this occurred from a Central Arctic ecological "core area" or regional "core areas" into which human populations retreated and restructured before expanding again into periodically refurbished marginal zones (*20*, *34*). The resolution of these controversies has been hindered by the limited

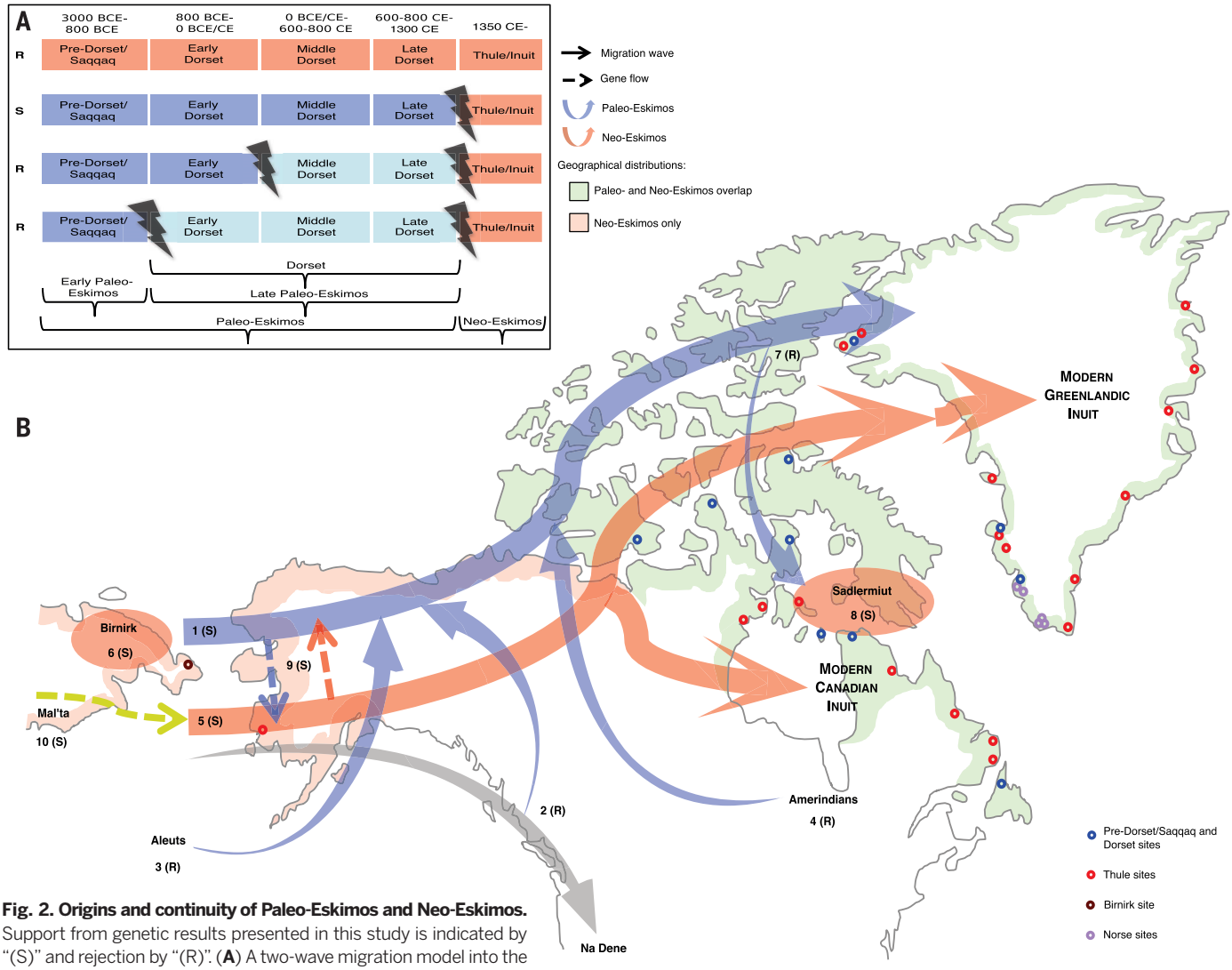

Fig. 2. Origins and continuity of Paleo-Eskimos and Neo-Eskimos. Support from genetic results presented in this study is indicated by "(S)" and rejection by "(R)". (**A**) A two-wave migration model into the New World Arctic, with continuity throughout the Paleo-Eskimo tradition, followed by the Neo-Eskimo migration, is supported. Black thunderbolt symbols represent genetic discontinuity. (**B**) This schematic summarizes the origins of Paleo- and Neo-Eskimos in the archaeological and genetic literature, including the present study, and their relationships with other ancient populations in the North American Arctic. See main text for details on the different scenarios represented by numbers 1 to 10 in the figure. For reference, we show the maximal geographical distribution of the Paleo-Eskimos and Neo-Eskimos in the New World Arctic and far-east Siberia (*9*). Additionally, plotted are Paleo-Eskimo (Pre-Dorset, Saqqaq, Dorset), Thule, Birnirk, and Norse sites from which samples in this study derive; for further information, see fig. S1 and table S1.

amount of Paleo-Eskimo human material, difficulties in assigning cultural affiliation of some finds (*41*), and dating uncertainties resulting from the strong marine component in the Arctic diet (*9*).

Samples and sequence data

We collected bone, teeth, and hair samples from the field and museums representing 169 ancient human remains from Arctic Siberia, Alaska, Canada, and Greenland (fig. S1 and table S1). These remains have been assigned to one of several ancient Arctic cultures on the basis of typological and/or stratigraphic evidence and, in some cases, radiocarbon dating (supplementary text S1). To circumvent drawing conclusions from single genomes (*42*), we generated mitochondrial DNA (mtDNA) data from 154 and low-coverage whole genome data sets from 26 of the ancient samples (up to 0.3× depth) (supplementary text S3 and tables S1 and S7). Despite colder temperatures in the Arctic, DNA survival in the ancient samples was surprisingly low, ranging from ~0 to 3.2% endogenous content based on the genome sequencing data (table S7). This low endogenous content may be explained by the remains being largely surface burials that suffered from fluctuating temperatures and humidity, and to subsequent storage conditions at museums.

We also sequenced two high-coverage genomes from present-day North American Native Americans belonging to the Na Dene family (the Dakelh of British Columbia, hereafter referred to as Athabascans) and unrelated, present-day Greenlandic Inuit (n = 2), Aleutian Islander (n = 1) and Siberian Nivkhs (n = 2) to average depths of 20 to 40× (supplementary text S3 and table S8). Only the Aleutian Islander showed evidence of recent European admixture and was masked for non–Native American ancestry tracts prior to analyses (supplementary text S5). Additionally, we radiocarbon dated 27 ancient samples and corrected 25 of the dates for marine reservoir effect to account for the dominant marine component in these individuals' diets (15 of these samples are represented in the ancient genomic data set) (supplementary text S2). This is critical in the accurate cultural assignment of these individuals, especially in cases where stratigraphic information is inconclusive or contentious (supplementary text S1).

Origins of Paleo-Eskimos

Diagnostic mtDNA coding region markers were targeted in the ancient samples to determine their mtDNA haplogroup (hg) affinities. Although hgs A, B, C, D, and X are the five founding mtDNA haplogroups in the Americas,

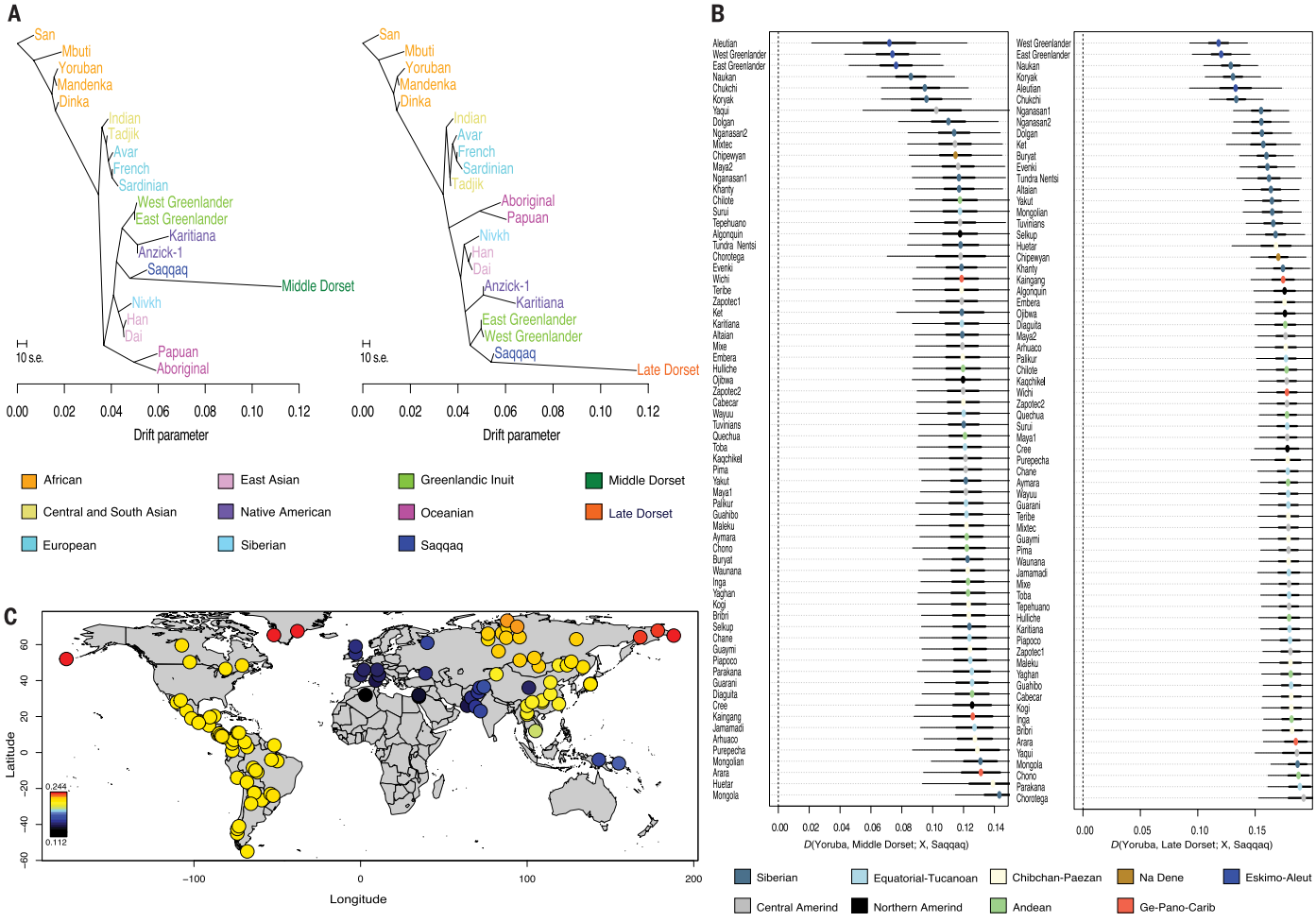

Fig. 3. Origins of Paleo-Eskimos and genetic continuity. (**A**) Sequencing data-based maximum likelihood trees constructed with *TreeMix* (*51*) with the high-coverage Saqqaq (*26*), Middle Dorset, and Late Dorset data sets, and 17 present-day and two ancient populations; for Greenlandic Inuit, see note in supplementary text S5. The scale bar represents 10 times the average standard error (s.e.) of the values in the covariance matrix. Residual matrices are shown in fig. S8, C and D. (**B**) SNP chip data-based *D*-statistic tests of the form *D*(Yoruba, Dorset; X, Saqqaq), where X represents present-day American and Siberian populations from (*28*) (colored centers represent populations divided by linguistic affiliation, see legend at bottom). Thick and thin lines represent 1 and 3 standard errors of the *D*-statistics, respectively. Middle and Late Dorset (left and right panels, respectively) are significantly (no overlap at 3 standard errors) closer to Saqqaq than to the sampled present-day populations. (**C**) Heat map of the SNP chip data-based statistic f_3(Yoruba; Saqqaq, X), where X represents present-day worldwide non-African populations from (*28*). The graded heat key (to the left of the image) represents the magnitude of the computed f_3-statistics.

previous studies have shown the near-absence of hgs B, C, and X in Paleo-Eskimos and Thule, as well as among present-day Inuit (*25*, *43*–*47*). We observe mtDNA hg D, specifically the lineage hg D2a, in both Early and Late Paleo-Eskimos, with the majority of the Pre-Dorset/Saqqaq and Middle Dorset samples further classified as hg D2a1 (supplementary text S4 and tables S1 and S9A). The absence of biological remains affiliated to the Early Dorset phase precludes genetic testing for this period. Hgs D2a and D2a1 are found in present-day Aleutian Islanders and Siberian Eskimos (*48*), who are genetically among the closest living populations to the previously sequenced Greenlandic Paleo-Eskimo (Saqqaq) individual that also belonged to hg D2a1 (hereafter, high-coverage Saqqaq) (*26*). The single Canadian Pre-Dorset sample (XIV-H:168, Rocky Point) was typed to hg D4e [referred to as hg D2 in (*48*)], which is ancestral to hg D2a, but lacks further phylogenetic resolution owing to the low-coverage nature of the shotgun data (supplementary text S4).

Maximum likelihood trees based on nuclear DNA variation place the Middle Dorset, Late Dorset, and the Canadian Pre-Dorset individuals as sister groups to the high-coverage Saqqaq individual (Fig. 3A and fig. S8, B to D), separately from contemporary Greenlandic Inuit or Native Americans [represented by the South American Karitiana (*49*) and the ancient Clovis Anzick-1 individual (*50*)]. Similar results were obtained when allowing for admixture between populations with *TreeMix* (*51*) (fig. S8, C and D). When the analysis was repeated and included the Aleutian Islander, which was masked for European ancestry over ~80% of its genome (supplementary text S5), the Middle Dorset and the Late Dorset individuals grouped with the high-coverage Saqqaq, as before (fig. S9).

Pairwise outgroup f_3-statistics (*52*, *53*) and *D*-statistics (*52*, *54*) confirm Early and Late Paleo-Eskimos as being significantly [no overlap at three standard errors for the single-nucleotide polymorphism (SNP) chip data and at 1 standard error for the sequencing data] closer to one another than to any of the sampled present-day populations, including those from the Americas and Siberia (Fig. 3B and fig. S10, A to D). Furthermore, admixture clustering profiles (*55*) of the high-coverage Saqqaq and a Dorset individual are near-identical (fig. S7), with both sharing components with present-day Siberian Chukchi and Greenlandic Inuit and, to a lesser extent, with other Siberians and East Asians (Han). We note that variations in *TreeMix* graph topologies occurred with the inclusion of the different ancient samples (supplementary text S5); however, the resulting conclusions from these trees are consistent with other analyses. Hence, evidence from mitochondrial as well as nuclear markers suggests that all Paleo-Eskimos, from both Canada and Greenland, represent a

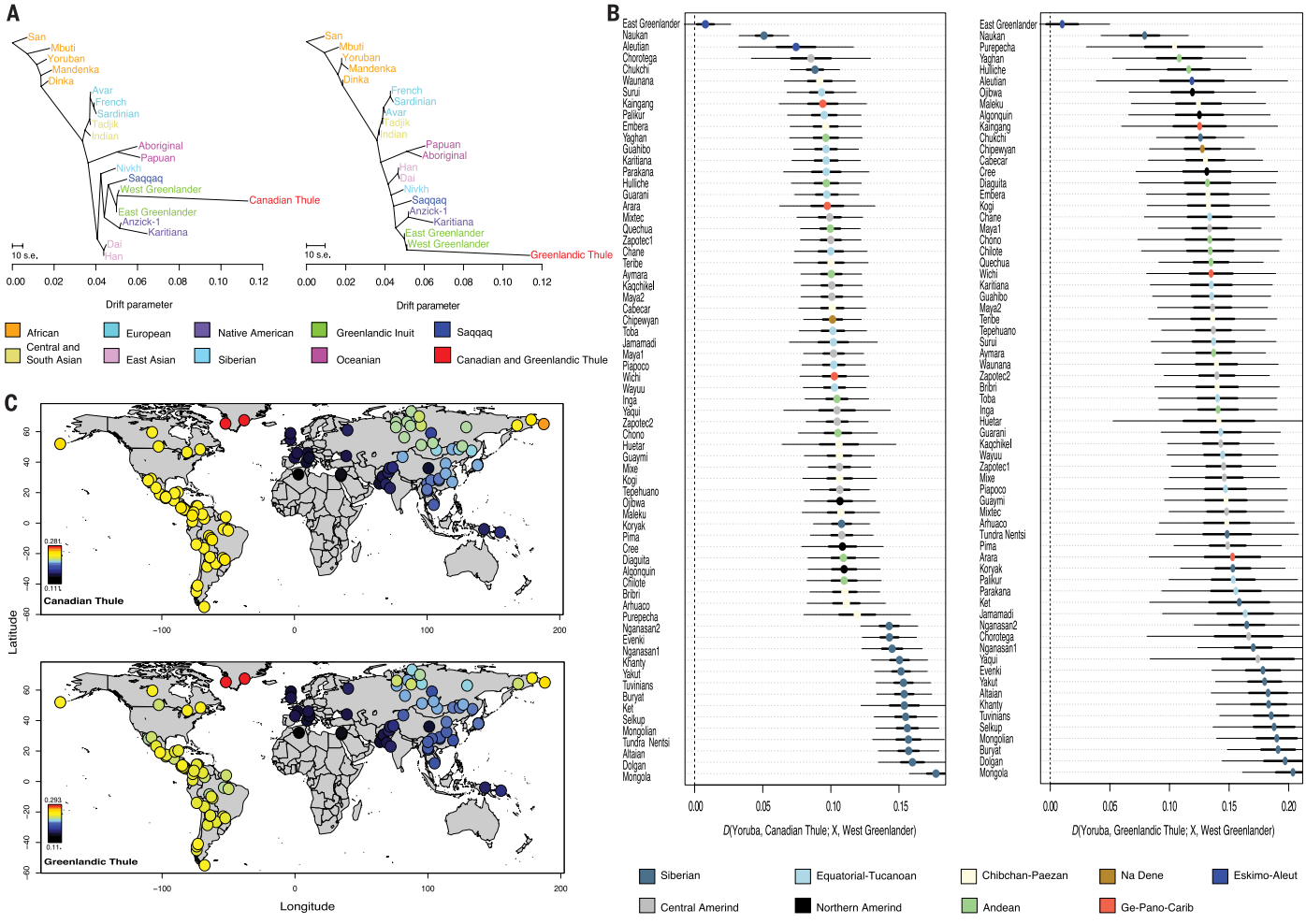

Fig. 4. Genetic affinities of the Neo-Eskimo Thule. (**A**) Sequencing data-based maximum likelihood trees constructed with *TreeMix* (*51*) with the high-coverage Saqqaq (*26*), Canadian Thule, and Greenlandic Thule data sets, and 17 present-day and 2 ancient populations. The scale bar represents 10 times the average standard error (s.e.) of the values in the covariance matrix. Residual matrices are shown in fig. S13, A and B. (**B**) SNP chip data-based *D*-statistic tests of the form *D*(Yoruba, Thule; X, West Greenlander), as in Fig. 3. Canadian and Greenlandic Thule (left and right panels, respectively) are significantly (no overlap at 3 standard errors) closer to present-day West Greenlandic Inuit than to other worldwide present-day populations. Similar results are observed with East Greenlandic Inuit in place of West Greenlandic Inuit (fig. S14C). (**C**) Heat maps of the SNP chip data-based statistic f_3(Yoruba; Thule, X), as in Fig. 3.

continuum of the same single ancestral population (Fig. 2, A and B, scenario 1). Present-day populations that are genetically closely related to the Paleo-Eskimos include the Greenlandic Inuit, Aleutian Islanders, and far-east Siberians (Fig. 3C and fig. S10E).

We additionally tested the claim that Saqqaq and Na Dene speakers were part of the same expansion into the Americas (*28*) by including present-day Athabascans, who represent distinct early branches of Native Americans (*50*), in the *TreeMix* (*51*) analysis. The maximum likelihood tree places the Athabascans as a sister clade to Karitiana and Anzick-1 (fig. S11A). Similarly, using SNP chip data from select Old and New World populations, masked for European admixture, we observe that the high-coverage Saqqaq individual forms a clade with the far-east Siberian Koryaks instead of with the Chipewyan, another Na Dene population (*28*) that groups with the South American Karitiana (fig. S11B). Outgroup f_3-statistics (*52*, *53*) and *D*-statistics (*52*, *54*) show that the high-coverage Saqqaq individual is closer to Greenlandic Inuit than to the Na Dene speakers (fig. S12, A to C). Furthermore, the lack of support for the Saqqaq being closer to the Athabascans than to Karitiana (fig. S12B) is incompatible with a scenario where Saqqaq and Na Dene speakers share a fraction of their ancestries through a secondary Asian stream (*28*). Overall, our results support the Paleo-Eskimo migration into the Americas as being separate from that of the Na Dene Native Americans.

Genetic affiliations of Neo-Eskimos

Greenlandic and Canadian Neo-Eskimo Thule, and present-day Greenlandic Inuit, form a clade in the maximum likelihood trees (Fig. 4A), even under admixture scenarios generated with *TreeMix* (*51*) (fig. S13, A and B). This supports genetic continuity over the last ~1000 years between these populations, which is also evident by the shared mtDNA haplogroups (hgs A2a, A2b, and D3a2a) between them (supplementary text S4 and tables S1 and S9A). Furthermore, outgroup f_3-statistics (*52*, *53*) and *D*-statistics (*52*, *54*) demonstrate that both Greenlandic and Canadian Thule are closer to present-day Inuit than to other sampled present-day populations or the high-coverage Saqqaq individual (Fig. 4, B and C, and fig. S14, A to C). These results are in agreement with the archaeological literature which suggests that present-day Greenlandic Inuit are direct descendants of the Thule (*9*, *56*–*58*) (Fig. 2B, scenario 5).

We additionally analyzed five ancient individuals dated to the 6th to 7th century CE and associated with the Siberian Birnirk culture, which is part of the Neo-Eskimo tradition and may be one of the cultural ancestors of the Thule (*59*–*61*). Evidence from both mitochondrial typing (hg A2a) (tables S1 and S9A) and nuclear markers (fig. S15, A to D) reveals that these individuals are genetically closely related to present-day Greenlandic

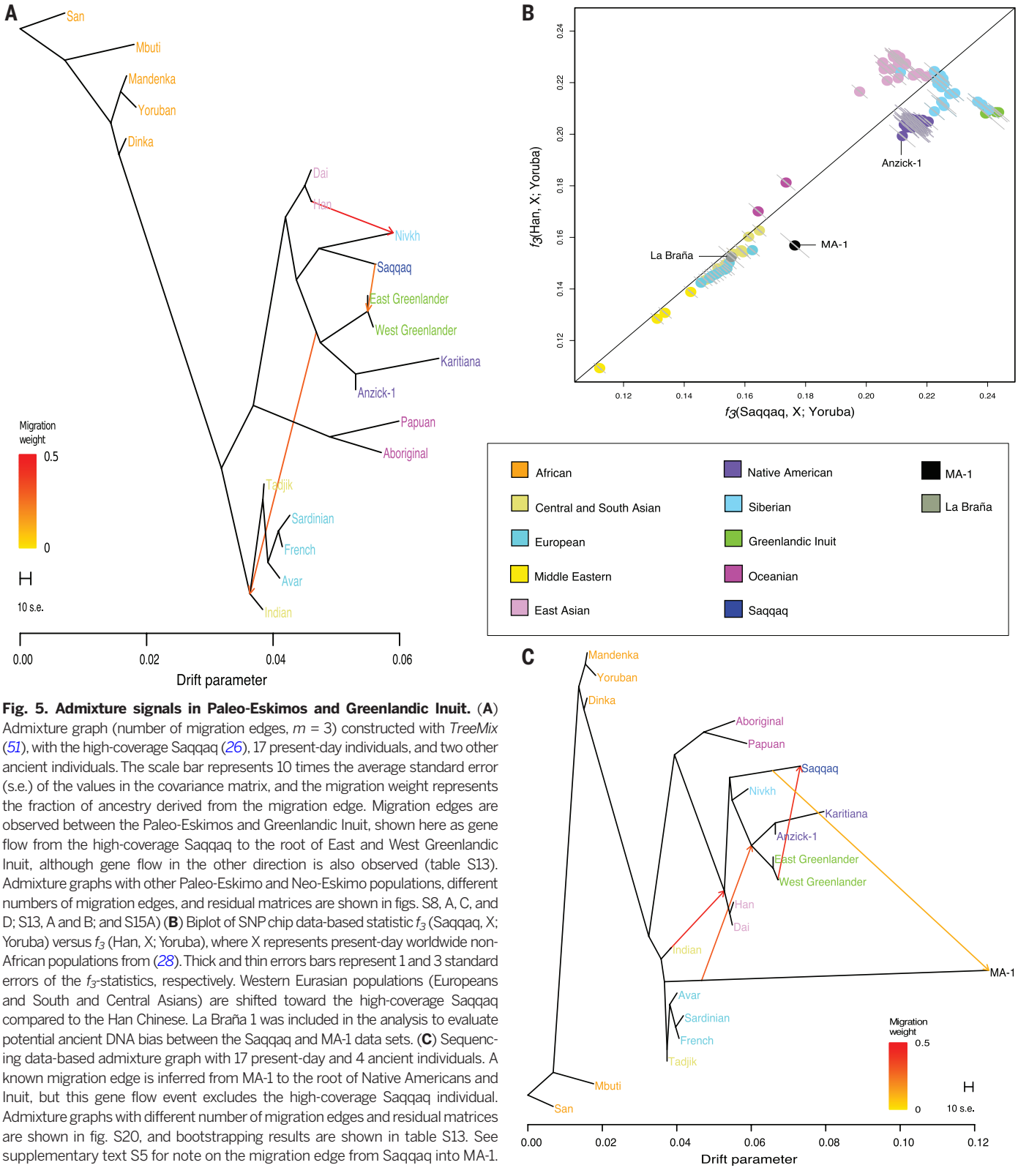

Fig. 5. Admixture signals in Paleo-Eskimos and Greenlandic Inuit. (**A**) Admixture graph (number of migration edges, m = 3) constructed with *TreeMix* (*51*), with the high-coverage Saqqaq (*26*), 17 present-day individuals, and two other ancient individuals. The scale bar represents 10 times the average standard error (s.e.) of the values in the covariance matrix, and the migration weight represents the fraction of ancestry derived from the migration edge. Migration edges are observed between the Paleo-Eskimos and Greenlandic Inuit, shown here as gene flow from the high-coverage Saqqaq to the root of East and West Greenlandic Inuit, although gene flow in the other direction is also observed (table S13). Admixture graphs with other Paleo-Eskimo and Neo-Eskimo populations, different numbers of migration edges, and residual matrices are shown in figs. S8, A, C, and D; S13, A and B; and S15A) (**B**) Biplot of SNP chip data-based statistic f_3 (Saqqaq, X; Yoruba) versus f_3 (Han, X; Yoruba), where X represents present-day worldwide non-African populations from (*28*). Thick and thin errors bars represent 1 and 3 standard errors of the f_3-statistics, respectively. Western Eurasian populations (Europeans and South and Central Asians) are shifted toward the high-coverage Saqqaq compared to the Han Chinese. La Braña 1 was included in the analysis to evaluate potential ancient DNA bias between the Saqqaq and MA-1 data sets. (**C**) Sequencing data-based admixture graph with 17 present-day and 4 ancient individuals. A known migration edge is inferred from MA-1 to the root of Native Americans and Inuit, but this gene flow event excludes the high-coverage Saqqaq individual. Admixture graphs with different number of migration edges and residual matrices are shown in fig. S20, and bootstrapping results are shown in table S13. See supplementary text S5 for note on the migration edge from Saqqaq into MA-1.

Inuit, providing the first genetic evidence of an Old World population that was not only a cultural precursor of the Thule, but also either closely related to or a component of the ancestral Inuit gene pool (Fig. 2B, scenario 6). We also reassessed claims that the Sadlermuit population from Southhampton Island in the Hudson Bay region are remnants of the Dorset Paleo-Eskimo people on the basis of cultural similarities and mtDNA markers (*33*, *46*, *62*) (Fig. 2B, scenario 7). We typed 10 Sadlermiut individuals, dating to the 14th to 19th century CE, to mtDNA hgs A2b and D3a2a (supplementary text S4 and tables S1 and S9A), which are characteristic of the Thule/Inuit. Also, from their nuclear genome sequences, two of these

individuals (Canadian Thule) form a clade with present-day Greenlandic Inuit and not the high-coverage Saqqaq individual (Fig. 4A and fig. S13A). This implies that the Sadlermiut were either genetically derived from or closely related to the Thule rather than the Paleo-Eskimos (Fig. 2B, scenario 8).

Additionally, whether the Norse admixed with neighboring Dorset or Thule groups remains debated, even though no anthropological evidence supporting such admixture has been found (*63*). To address this hypothesis, we tested 34 Norse individuals from southern Greenland, across the time span of their occupation in the region, for matrilineal admixture with neighboring Paleo- and Neo-Eskimo populations (supplementary text S1). We found no New World–specific mitochondrial markers in these Norse samples, especially the Arctic-specific hgs A and D, suggesting that no detectable matrilineal gene flow occurred from the Dorset or Thule into the sampled Greenlandic Norse (supplementary text S4 and table S9, B and C).

Admixture signals in Paleo- and Neo-Eskimos

We further investigated the observed genetic affinity between present-day Greenlandic Inuit and Paleo-Eskimos. *D*-statistics (*52*, *54*) and outgroup f_3-statistics (*52*, *53*) support the Paleo-Eskimos as being closer to Greenlandic Inuit than to other present-day New World populations (figs. S12A and S16, A and B), with the exception of the Aleutian Islanders, whose genetic proximity to the Inuit is evident in analyses from both sequencing data (fig. S9) and SNP chip data (*28*) and the Naukan who have been shown to possess Eskimo-Aleut ancestry as a result of back-migration of a related population (*28*). Maximum likelihood trees with migration edges inferred with *TreeMix* show evidence for admixture between Paleo-Eskimos and Greenlandic Inuit (Fig. 5A), mediated by the Neo-Eskimo groups that include the Canadian Thule, Greenlandic Thule, and Siberian Birnirk (figs. S8, A and C to D; S13, A and B; and S15A). In all the cases, this gene flow event is among the first few migration edges to be inferred by *TreeMix* (number of migration edges m = 1 to 4). Bootstrap support suggests that gene flow likely occurred in both directions between the Paleo- and Neo- Eskimo groups (table S13).

Although gene flow was also observed when the high-coverage Saqqaq individual was included, we sought to determine whether this was due to *TreeMix* being unable to distinguish between Saqqaq and Dorset as a result of their genetic similarity and if admixture might have actually occurred between Dorset and Neo-Eskimos. Therefore, we generated simulated data sets with varying levels of admixture (10 and 25%) between Dorset and Inuit in both directions, and determined whether a migration edge was observed in the *TreeMix* admixture graphs between the high-coverage Saqqaq individual and the Inuit in the absence of the Dorset (supplementary text S5). Simulated admixture from Dorset to Inuit was detected by the analysis in the form of gene flow between Saqqaq and Inuit, but the reverse—that is, from Inuit to Dorset through gene flow involving Saqqaq and Inuit—was less likely (fig. S17, A and B, and table S13). Because our data show support for gene flow from the various Neo-Eskimo groups, including present-day Inuit, into the high-coverage Saqqaq individual, it is likely that the admixture involving Saqqaq is not an artifact and occurred from the Neo-Eskimo lineage into Saqqaq. We cannot, however, exclude the possibility of gene flow from Paleo-Eskimos into Neo-Eskimos as well, or that subsequent gene flow did not occur between the later Dorset phases and the Neo-Eskimo lineage (table S13).

Because the observed admixture involves the 4000-year-old Saqqaq individual, it implies that the meeting and intermixing of Paleo-Eskimo and Neo-Eskimo ancestors predates the first archaeological observations of their coexistence in the eastern Arctic by ~3000 years or earlier, since Thule groups entered eastern Canada and Greenland, previously occupied by the Late Dorset, only in the 12th or 13th century CE. This also suggests that the admixture is more likely to have occurred either in the Old World before the entry of the Neo-Eskimos into the Americas, or in Beringia, but not further east in the New World, because no archaeological evidence of a parallel existence of Paleo- and Neo-Eskimos around 4000 years ago or earlier has been documented in this region (Fig. 2B, scenario 9).

We also investigated the level of genetic contribution from the ~24,000-year-old Siberian boy from Mal'ta (MA-1) (*53*) into Paleo-Eskimos and Greenlandic Inuit. Pairwise outgroup f_3-statistics (*52*, *53*) show that sampled western Eurasians and MA-1 are slightly closer to the high-coverage Saqqaq than to the Han Chinese (Fig. 5B and fig. S18). To confirm that this genetic affinity between Saqqaq and MA-1 was not due to ancient DNA bias, we also included the ~7000-year-old La Braña 1 sample from Spain (*64*) in our analysis and found that it clustered close to present-day Europeans, hence confirming that our results were not skewed by ancient DNA attraction (Fig. 5B). *TreeMix* infers gene flow from the high-coverage Saqqaq into MA-1 and vice versa, the latter admixture edge being consistent with (*65*), but with low support to substantiate this signal and the inferred direction (Fig. 5C, table S13, and supplementary text S5).

In contrast, gene flow from MA-1 into the root of the clade comprising Native American populations (Karitiana and Anzick-1) and including the Greenlandic Inuit is detected with high bootstrap support, in agreement with (*53*) (Fig. 2B, scenario 10; Fig. 5C; and table S13). Additionally, *D*-statistics (*52*) and outgroup f_3-statistics (*52*, *53*) based on SNP chip data show that MA-1 is significantly (no overlap at 3 standard errors) closer to the Chipewyan than to the high-coverage Saqqaq (fig. S19), which is compatible with other results presented in this study that also reject a single-wave model for Saqqaq and Na Dene speakers. Overall, although there is evidence of genetic affinity between MA-1 and Saqqaq, we cannot ascertain whether this is due to gene flow or shared ancestry between the two lineages. It is also possible that this affinity is a consequence of the aforementioned gene flow from Neo-Eskimos, who received MA-1 gene flow, into the Saqqaq lineage.

Discussion

We overcome the difficulties of studying the peopling of the Arctic by including an extensive collection of Paleo-Eskimo remains for both ancient DNA and radiocarbon analyses. We have shown that Paleo-Eskimos likely represent a single migration pulse into North America from Siberia; separate from the migration events giving rise to Native Americans and Inuit. However, while being genetically distinct from other New World populations, Paleo-Eskimos are still more closely related to these populations than to non–New World populations, which is in agreement with a single ancestral population giving rise to many subpopulations and possibly many migration pulses into the Americas, as suggested by the Beringian standstill model (*66*) and a three-stage colonization model (*67*). Moreover, although our data are in agreement with Reich *et al*. (*28*), we find no support for Saqqaq or the rest of the Paleo-Eskimo tradition being a part of one of the two waves of Native American ancestors entering the more southern regions of the Americas. Therefore, an additional Paleo-Eskimo migration wave should be added to the three-wave hypothesis in explaining the peopling of the Americas (*28*).

Furthermore, Paleo-Eskimo and Inuit peoples appear to have occupied the New World Arctic for more than 4000 years, with only a single population replacement (Thule) less than 700 years ago. In contrast with the dynamic responses of the Thule people to climate change (*21*, *68*, *69*), Siberian iron trade (*70*), and Norse contact (*16*), the 4000-year Paleo-Eskimo period presents a single tradition of continuous technological and social development, including geographical dislocations and periods of relative stability punctuated by episodes of rapid change (*20*). The long-term continuity of the Paleo-Eskimo population and its culture is especially striking given the climatic and ecological cycles over 4000 years—from warm hypsithermal to cold sub-boreal through the early medieval warm event, as well as changes in sea ice distribution and in animal population cycles and distribution (*13*). In light of this, Paleo-Eskimo survival must be due to remarkable resilience among dispersed local groups with the ability to shift their small population units to new areas when their homes became untenable, like the complete depopulation of Greenland and the abandonment of the Canadian High Arctic between ~1 to 700 CE (*9*). Such events argue for the reformulation of the original "core area" hypothesis to a network of regional "core areas" that served as demographic reservoirs for repopulating areas abandoned as a result of climate change, animal population crashes, or human overhunting.

This study also contributes to the long-standing debate about the Dorset-Thule transition. New

series of radiocarbon dates suggest temporal overlap between the Dorset and the Thule that lasted between 50 and 200 years, with geographical coexistence in some areas (*14*, *16*, *71*–*75*), whereas an earlier reassessment of the eastern Arctic radiocarbon dates suggested that Dorset had disappeared from the eastern Arctic more than 200 years prior to Thule entering the eastern Arctic and thus the two groups never met (*12*, *76*). Although we cannot preclude later gene flow between the Dorset and the Thule (that is, subsequent to the more ancient gene flow that occurred at least 4000 years ago), the contrasting genetic and cultural affinities of the Sadlermiut individuals present a conundrum. This culture that went extinct in 1903 CE from European disease has long been considered Thule-acculturated Dorset people, likely due to intermarriage (*33*, *77*, *78*); however, genetic evidence from this study suggests that they were Thule people who had somehow acquired Dorset stone technology (*12*, *79*). Hence, if the acculturation evident among the Sadlermiut was not a result of intermarriage, what social mechanisms resulted in genetic isolation but allowed for cultural exchange? Similar questions can be raised with regard to lack of Thule or Dorset matrilineal gene flow with the Greenlandic Norse (*75*).

Our study contrasts with previous population-level genetic studies, such as those focusing on the introduction of agriculture in Europe (Neolithization), which found that population movements instigated changes in culture and subsistence strategies (*65*, *80*–*82*). Paleo-Eskimo technological innovations seem to have occurred solely by the movement of ideas within a single resident population. Hence, our findings suggest that caution is required when using cultural similarities and differences as proxies for population movements and migrations into new and dramatically different environments.

Methods

DNA from 169 ancient human bone, teeth, and hair samples from Arctic Siberia, Alaska, Canada, and Greenland was extracted and targeted for haplogroup diagnostic mtDNA markers, while a subset of 26 samples was converted into Illumina libraries and sequenced, using standard laboratory procedures (supplementary text S3). Two present-day Greenlandic Inuit, two Nivkhs, one Aleutian Islander, and two Athabascans were genome sequenced with no objections from The National Committee on Health Research Ethics, Denmark (H-3-2012-FSP21) (supplementary text S2). Twenty-seven ancient samples were radiocarbon dated, of which 25 dates were corrected for marine reservoir offset (supplementary text S2). Mitochondrial DNA contamination estimates were computed as noted in supplementary text S4. Error rate analysis, DNA damage analysis, multidimensional scaling analysis on SNP chip and sequencing data, NGSadmix analysis, ABBA-BABA tests on sequencing data, *D*-statistics and f_3-statistics tests on SNP chip and sequencing data, *TreeMix* analysis on SNP chip and sequencing data, neighbor-joining analysis, and ancestry painting of the Aleutian genome were performed as described in supplementary text S5.

REFERENCES AND NOTES

1. R. K. Harritt, Paleo-Eskimo beginnings in North America: A new discovery at Kuzitrin Lake, Alaska. *Etud. Inuit* **22**, 61–81 (1998).
2. Supplementary materials are available on *Science* Online.
3. H. B. Collins, in *Prehistoric Cultural Relations Between the Arctic and Temperate Zones of North America*, J. M. Campbell, Ed. (Arctic Institute of North America, Montreal, 1962), pp. 126–139.
4. N. N. Dikov, *Early Cultures of Northeast Asia* (U.S. Department of the Interior, Shared Beringian Heritage Program, National Park Service, Anchorage, AK, 1979).
5. D. E. Dumond, *The Eskimos and Aleuts* (Thames and Hudson, London, 1977).
6. J. Dixon, *Arrows and Atl Atls: Guide to the Archaeology of Beringia* (National Park Service, Washington, DC, 2013).
7. S. L. Anderson, A. K. Freeburg, A high-resolution chronology for the Cape Krusenstern site complex, Northwest Alaska. *Arctic Anthropol.* **50**, 49–71 (2013).
8. M. S. Maxwell, in *Handbook of North American Indians: Vol. 5, Arctic*, W. C. Sturtevant, D. Damas, Eds. (Smithsonian Institution, Washington, DC, 1984). pp. 359–368.
9. B. Grønnow, M. Sørensen, in *Dynamics of Northern Societies*, J. Arneborg, B. Grønnow, Eds. (National Museum of Denmark, Copenhagen, 2006), pp. 59–74.
10. R. McGhee, *Ancient People of the Arctic* (Univ. of British Columbia Press, Vancouver, 1996).
11. M. Appelt, B. Gulløv, Eds., *Late Dorset in High Arctic Greenland* (Danish Polar Center, Danish National Museum, Copenhagen, 1999).
12. R. W. Park, The Dorset-Thule succession in Arctic North America: Assessing claims for culture contact. *Am. Antiq.* **58**, 203–234 (1993). doi: 10.2307/281966
13. W. W. Fitzhugh, in *Encyclopedia of Archaeology*, D. M. Pearsall, Ed. (Academic Press, New York, 2008), pp. 247–271.
14. M. T. Friesen, C. D. Arnold, The timing of the Thule migration: New dates from the western Canadian Arctic. *Am. Antiq.* **73**, 527–538 (2008).
15. R. E. Hollinger, R. Eric, S. Ousley, C. Utermohle, in *The Northern World AD 900-1400*, H. Maschner, O. Mason, R. McGhee, Eds. (Univ. of Utah Press, Salt Lake City, 2009), pp. 131–154.
16. R. McGhee, in *The Northern World AD 900-1400*, H. Maschner, O. Mason, R. McGhee, Eds. (Univ. of Utah Press, Salt Lake City, 2009), pp. 155–163.
17. D. Morrison, in *The Northern World AD 900-1400*, H. Maschner, O. Mason, R. McGhee, Eds. (Univ. of Utah Press, Salt Lake City, 2009), pp. 164–178.
18. O. K. Mason, in *An Ipiutak Outlier: A 1,500-Year Old Qarigi at Qitchauvik on The Golovin Lagoon*, O. K. Mason, M. A. Sweeney, C. Alix, V. Barber, Eds. (National Park Service, Alaska Region, 2007), pp. 16–22.
19. D. Morrison, The earliest Thule Migration. *Can. J. Archaeol.* **22**, 139–156 (1999).
20. M. Maxwell, *Prehistory of the Eastern Arctic* (Academic Press, Orlando, FL, 1985).
21. R. McGhee, in *Handbook of North American Indians: Vol. 5, Arctic*, W. C. Sturtevant, D. Damas, Eds. (Smithsonian Institution, Washington, DC, 1984), pp. 369–376.
22. W. W. Fitzhugh, E. I. Ward, Eds., *Vikings: The North Atlantic Saga* (Smithsonian Institution Press, Washington, DC, 2000).
23. R. Powers, R. H. Jordan, Human biogeography and climate change in Siberia and Arctic North America in the Fourth and Fifth Millennia B.P. *Philos. Trans. R. Soc. London A* **330**, 665–670 (1990). doi: 10.1098/rsta.1990.0047
24. W. N. Irving, in *Proceedings of the 8th International Congress of Anthropological and Ethnological Sciences* (Science Council of Japan, Tokyo, 1969–1970), vol. 3, pp. 340–342.
25. M. T. Gilbert *et al*., Paleo-Eskimo mtDNA genome reveals matrilineal discontinuity in Greenland. *Science* **320**, 1787–1789 (2008). doi: 10.1126/science.1159750; pmid: 18511654
26. M. Rasmussen *et al*., Ancient human genome sequence of an extinct Palaeo-Eskimo. *Nature* **463**, 757–762 (2010). doi: 10.1038/nature08835; pmid: 20148029
27. W. S. Laughlin, Aleuts: Ecosystem, Holocene history, and Siberian origin: Soviet and U.S. scientists join in a study of the origins of the first Americans. *Science* **189**, 507–515 (1975). doi: 10.1126/science.189.4202.507; pmid: 17798291
28. D. Reich *et al*., Reconstructing Native American population history. *Nature* **488**, 370–374 (2012). doi: 10.1038/nature11258; pmid: 22801491
29. T. L. Black, Aleut Art: *Unangam Aguqaadangin* (Aleutian/Pribilof Islands Association, Anchorage, AK, 2003).
30. J. Meldgaard, in *Selected papers of the 5th International Congress of Anthropological and Ethnological Sciences*, A. F. C. Wallace, Ed. (Univ. of Pennsylvania Press, Philadelphia, 1960), pp. 588–595.
31. F. deLaguna, in *Man in Northeastern North America*. F. Johnson, Ed. (Phillips Academy, Andover, MA, 1946), pp.106–142.
32. W. A. Ritchie, in *Prehistoric Cultural Relations Between the Arctic and Temperate Zones of North America*, J. M. Campbell, Ed. (Arctic Institute of North America, Montreal, 1962), pp. 96–99.
33. H. B. Collins, Archaeological investigations on Southampton and Walrus Islands, N.W. *Natl. Mus. Can. Bull.* **147**, 22–61 (1958).
34. J. M. Savelle, A. S. Dyke, Paleoeskimo occupation history of Foxe Basin, Arctic Canada: Implications for the core area model and Dorset origins. *Am. Antiq.* **79**, 249–276 (2014). doi: 10.7183/0002-7316.79.2.249
35. J. A. Tuck, W. Fitzhugh, in *Palaeo-Eskimo Cultures in Newfoundland, Labrador and Ungava* (Memorial Univ. of Newfoundland, St. John's, 1986), pp. 161–167.
36. J. Meldgaard, in *Prehistoric Cultural Relations Between the Arctic and Temperate Zones of North America*, J. M. Campbell, Ed. (Arctic Institute of North America, Montreal, 1962), pp. 92–95.
37. A. S. Dyke, J. M. Savelle, D. S. Johnson, Paleoeskimo demography and Holocene sea-level history, Gulf of Boothia, Arctic Canada. *Arctic* **64**, 151–168 (2011). doi: 10.14430/arctic4096
38. J. M. Savelle, A. S. Dyke, M. Poupart, in *The Northern World AD 900-1400*, H. Maschner, M. Owen, R. McGhee, Eds. (Univ. of Utah Press, Salt Lake City, 2009), pp. 209–234.
39. E. Harp, *The Cultural Affinities of the Newfoundland Dorset Eskimos* (National Museum of Canada, Ottawa, 1964).
40. M. A. P. Renouf, Ed., *The Cultural Landscapes of Port aux Choix* (Springer, New York, 2011).
41. W. W. Fitzhugh, Biogeographical archeology in the eastern North American Arctic. *Hum. Ecol.* **25**, 385–418 (1997). doi: 10.1023/A:1021819509181
42. J. K. Pickrell, D. Reich, Towards a new history and geography of human genes informed by ancient DNA. *bioRxiv* (2014). doi: 10.1101/003517
43. J. Saillard, P. Forster, N. Lynnerup, H. J. Bandelt, S. Nørby, mtDNA variation among Greenland Eskimos: The edge of the Beringian expansion. *Am. J. Hum. Genet.* **67**, 718–726 (2000). doi: 10.1086/303038; pmid: 10924403
44. A. Helgason *et al*., mtDNA variation in Inuit populations of Greenland and Canada: Migration history and population structure. *Am. J. Phys. Anthropol.* **130**, 123–134 (2006). doi: 10.1002/ajpa.20313; pmid: 16353217
45. J. A. Raff, D. A. Bolnick, J. Tackney, D. H. O'Rourke, Ancient DNA perspectives on American colonization and population history. *Am. J. Phys. Anthropol.* **146**, 503–514 (2011). doi: 10.1002/ajpa.21594; pmid: 21913177
46. M. G. Hayes, J. B. Coltrain, D. H. O'Rourke, in *Contributions to the Study of the Dorset Palaeo-Eskimos*, P. D. Sutherland, Ed. (Canadian Museum of Civilization, Hull, 2005), pp. 11–32.
47. M. T. P. Gilbert *et al*., mtDNA from hair and nail clarifies the genetic relationship of the 15th century Qilakitsoq Inuit mummies. *Am. J. Phys. Anthropol.* **133**, 847–853 (2007). doi: 10.1002/ajpa.20602; pmid: 17427925
48. N. V. Volodko *et al*., Mitochondrial genome diversity in arctic Siberians, with particular reference to the evolutionary history of Beringia and Pleistocenic peopling of the Americas. *Am. J. Hum. Genet.* **82**, 1084–1100 (2008). doi: 10.1016/j.ajhg.2008.03.019; pmid: 18452887
49. M. Meyer *et al*., A high-coverage genome sequence from an archaic Denisovan individual. *Science* **338**, 222–226 (2012). doi: 10.1126/science.1224344; pmid: 22936568
50. M. Rasmussen *et al*., The genome of a Late Pleistocene human from a Clovis burial site in western Montana. *Nature* **506**, 225–229 (2014). doi: 10.1038/nature13025; pmid: 24522598
51. J. K. Pickrell, J. K. Pritchard, Inference of population splits and mixtures from genome-wide allele frequency data. *PLOS Genet.* **8**, e1002967 (2012). doi: 10.1371/journal.pgen.1002967; pmid: 23166502

52. N. Patterson *et al.*, Ancient admixture in human history. *Genetics* **192**, 1065–1093 (2012). doi: 10.1534/genetics.112.145037; pmid: 22960212
53. M. Raghavan *et al.*, Upper Palaeolithic Siberian genome reveals dual ancestry of Native Americans. *Nature* **505**, 87–91 (2014). doi: 10.1038/nature12736; pmid: 24256729
54. R. E. Green *et al.*, A draft sequence of the Neandertal genome. *Science* **328**, 710–722 (2010). doi: 10.1126/science.1188021; pmid: 20448178
55. L. Skotte, T. S. Korneliussen, A. Albrechtsen, Estimating individual admixture proportions from next generation sequencing data. *Genetics* **195**, 693–702 (2013). doi: 10.1534/genetics.113.154138; pmid: 24026093
56. H. B. Collins, Excavations at Thule culture sites near Resolute Bay, Cornwallis Island, N.W.T. *Natl. Mus. Can. Bull.* **123**, 49–63 (1951).
57. R. H. Jordan, in *Handbook of North American Indians: Vol. 5, Arctic*, W. C. Sturtevant, D. Damas, Eds. (Smithsonian Institute, Washington, DC, 1984), pp. 540–548.
58. J. Meldgaard, in *Danish-Netherlands Symposium on Developments in Greenlandic Arctic Culture*, H. P. Kylstra, Ed. (Univ. of Groningen, Groningen, Netherlands, 1976), pp. 19–52.
59. T. Mathiassen, Eskimo migrations in Greenland. *Geogr. Rev.* **25**, 408–422 (1935). doi: 10.2307/209309
60. J. A. Ford, *Eskimo Prehistory in the Vicinity of Point Barrow, Alaska* (American Museum of Natural History, New York, 1959), pp. 19–21.
61. W. E. Taylor, Hypotheses on the origin of Canadian Thule culture. *Am. Antiq.* **28**, 456–464 (1963). doi: 10.2307/278555
62. H. B. Collins, *Vanished Mystery Men of Hudson Bay* (National Geographic Society, Washington, DC, 1956).
63. N. Lynnerup, *The Greenland Norse: A Biological-Anthropology Study*, H. C. Gulløv, Ed. (Commission for Scientific Research in Greenland, Copenhagen, 1998).
64. I. Olalde *et al.*, Derived immune and ancestral pigmentation alleles in a 7,000-year-old Mesolithic European. *Nature* **507**, 225–228 (2014). doi: 10.1038/nature12960 pmid: 24463515
65. P. Skoglund *et al.*, Genomic diversity and admixture differs for Stone-Age Scandinavian foragers and farmers. *Science* **344**, 747–750 (2014). doi: 10.1126/science.1253448; pmid: 24762536
66. E. Tamm *et al.*, Beringian standstill and spread of Native American founders. *PLOS ONE* **2**, e829 (2007). doi: 10.1371/journal.pone.0000829; pmid: 17786201
67. C. J. Mulligan, A. Kitchen, M. M. Miyamoto, Updated three-stage model for the peopling of the Americas. *PLOS ONE* **3**, e3199 (2008). doi: 10.1371/journal.pone.0003199; pmid: 18797500
68. R. McGhee, Speculations on climate change and Thule culture development. *Folk* **11-12**, 173–184 (1969-1970).
69. A. McCartney, *Thule Eskimo Prehistory Along Northwestern Hudson Bay* (National Museum of Man, Ottawa, 1977).
70. R. McGhee, *The Last Imaginary Place: A Human History of the Arctic World.* (Oxford Univ. Press, Oxford, 2005).
71. R. McGhee, in *Identities and Cultural Contacts in the Arctic*, M. Appelt, J. Berglund, H. C. Gulløv, Eds. (The Danish National Museum, Copenhagen, 2000), pp. 181–191.
72. W. W. Fitzhugh, in *Threads of Arctic Prehistory: Papers in Honour of William E. Taylor, Jr.*, D. Morrison, J.-L. Pilon, Eds. (Canadian Museum of Civilization, Gatineau, 1994), pp. 239–268.
73. T. M. Friesen, Contemporaneity of Dorset and Thule cultures in the North American Arctic: New radiocarbon dates from Victoria Island, Nunavut. *Curr. Anthropol.* **45**, 685–691 (2004). doi: 10.1086/425635
74. P. D. Sutherland, in *The Northern World AD 900-1400*, H. Maschner, O. K. Mason, R. McGhee, Eds. (Univ. of Utah Press, Salt Lake City, 2009), pp. 279–299.
75. M. Appelt, H. C. Gulløv, in *The Northern World AD 900-1400*, H. Maschner, O. K. Mason, R. McGhee, Eds. (Univ. of Utah Press, Salt Lake City, 2009), pp. 300–320.
76. R. Park, in *Identities and Cultural Contacts in the Arctic*, M. Appelt, J. Berglund, H. C. Gulløv, Eds. (National Museum of Denmark, Copenhagen, 2000), pp. 192–205.
77. F. de Laguna, *The Prehistory of Northern North America As Seen from the Yukon*. (Society for American Archaeology, Menasha, WI, 1947).
78. J. C. Thomson, Labrador: Archaeological evidence for 8,000 years of human adaptation. *Inuktitut* **69**, 14–34 (1988).
79. S. Rowley, in *Threads of Arctic Prehistory: Papers in Hounour of William E. Taylor, Jr.*, D. Morrison, J.-L. Pilon, Eds. (Canadian Museum of Civilization, Gatineau, 1994), pp. 361–384.
80. H. Malmström *et al.*, Ancient DNA reveals lack of continuity between Neolithic hunter-gatherers and contemporary Scandinavians. *Curr. Biol.* **19**, 1758–1762 (2009). doi: 10.1016/j.cub.2009.09.017; pmid: 19781941
81. W. Haak *et al.*, Ancient DNA from European early Neolithic farmers reveals their near eastern affinities. *PLOS Biol.* **8**, e1000536 (2010). doi: 10.1371/journal.pbio.1000536; pmid: 21085689
82. P. Skoglund *et al.*, Origins and genetic legacy of Neolithic farmers and hunter-gatherers in Europe. *Science* **336**, 466–469 (2012). doi: 10.1126/science.1216304; pmid: 22539720
83. P. Desrosiers, thesis, Université Paris 1 Panthéon-Sorbonne (2009).
84. J. F. Jensen, in *Dynamics of Northern Societies*, J. Arneborg, B. Grønnow, Eds. (National Museum of Denmark, Copenhagen, 2006), pp. 75–86.
85. P. Schledermann, *Crossroads to Greenland: 3000 Years of Prehistory in the Eastern High Arctic* (University of Calgary, Calgary, 1990).

ACKNOWLEDGMENTS

We thank the Danish National Sequencing Centre, T. B. Brand, and P. S. Olsen for technical assistance; anonymous donors for providing DNA samples; A. Helgason and S. Sunna Ebenesersdóttir from deCODE for their input on mtDNA phylogenies; A, Di Rienzo for access to genotyping data from Siberian populations; J. R. Southon (B.T.F.), Kitikmeot Heritage Society (T.M.F.), Polar Continental Shelf Project (T.M.F.), Inuit Heritage Trust (D.H.O'R., Je.C., Jo.C., M.G.H.), Kivalliq Inuit Association (D.H.O'R., Jo.C., M.G.H.), communities of Coral Harbor and Chesterfield Inlet (D.H.O'R., Jo.C., M.G.H.), Canadian Museum of History (D.H.O'R., Je.C., Jo.C., M.G.H.), D. Morrison (D.H.O'R., Je.C., Jo.C., M.G.H.), L. Wood (D.H.O'R., Jo.C., M.G.H.), J. Young (D.H.O'R., Je.C., Jo.C., M.G.H.), D. Stenton (D.H.O'R., Je.C., Jo.C., M.G.H.), S. Girling-Christie (Je.C.), Commission for Scientific Research in Greenland (J.A.), Greenland National Museum and Archives (J.A.), Parks Canada (M.A.P.R., V.G.), Memorial University (V.G., M.A.P.R.), Government of Newfoundland and Labrador (V.G.), The Rooms Inc. (V.G.), Innu Nation (V.G.), Nunatsiavut Government (V.G.), Miawpukek First Nation (V.G.), D. Lavers (V.G.), R. Anstey (V.G.), W. Jones and Qanirtuuq Inc., Quinhagak, Alaska (K.B. and R.K.), the residents of Quinhagak, Alaska (K.B. and R.K.), Nunivak Island Mekoryuk Alaska Corporation, Mekoryuk, Alaska (K.B. and R.K.), and the Carnegie Trust for the Universities of Scotland (K.B. and R.K.). Supported by the Danish National Research Foundation (E.W.) Lundbeck Foundation (E.W., N.L.), Villum Foundation (A.A.), Swiss National Science Foundation Fellowship (A.S.-M, PBSKP3_143259), The Rock Foundation (B.G., M.A.), Social Sciences and Humanities Research Council of Canada (T.M.F.), National Science Foundation Office of Polar Programs (D,H,O'R.: OPP-9974623 and OPP-0327641; Jo.C.: OPP-9726126 and OPP-9977931; M.G.H.: OPP-9813044), Northern Worlds Initiative (H.C.G.), Augustinus Foundation (H.C.G.), the Danish Council for Independent Research (I.M.), National Science Foundation (J.A.: International Polar Year grant 0732327; M.H.C., OPP-9905090 and OPP-0327676), Wenner-Gren Foundation for Anthropological Research (M.G.H.: no. 6364), Natural Sciences and Engineering Research Council of Canada Postgraduate Fellowship (M.G.H.), University of Utah Graduate Research Fellowship (M.G.H.), EU Marie Curie FP7 Initial Training Network Grant (Ma.R.: FP7-ITN-215362-2), Arts and Humanities Research Council (K.B. and R.K.: AH/K006029/1), Memorial University Faculty of Arts Research Initiative (V.G.), Memorial University Office of Research Grant (V.G.), Social Sciences and Humanities Research Council of Canada (M.A.P.R.), EU European Regional Development Fund through the Centre of Excellence in Genomics to Estonian Biocentre (M.M. and R.V.), Estonian Institutional Research (M.M. and R.V.: grant IUT24-1), and Estonian Science Foundation (M.M. and R.V.: grant 8973). Informed consent was obtained for the genome sequencing of the modern individuals, with ethical approval from The National Committee on Health Research Ethics, Denmark (H-3-2012-FSP21). Sequence data for the ancient samples are available for download through European Nucleotide Archive (ENA) accession no. PRJEB6516, and for the Illumina genotype data through Gene Expression Omnibus (GEO) series accession no. GSE59546 and at www.ebc.ee/free_data. Alignment files (BAMs) for the ancient genomes sequenced in this study are available at www.cbs.dtu.dk/suppl/arctic. The data for the modern populations are available for demographic research under data access agreement with E.W. The Thule samples from Silumiut, Kamarvik, and Sadlermiut were made available by D.H.O'R. under agreement with the Canadian Museum of Civilization and local communities who provided research access to the samples. C.B. is on the advisory board of a project at 23andMe and on the scientific advisory boards of Personalis Inc.; InVitae; Etalon Inc.; and Ancestry.com. The authors declare no competing financial interests.

SUPPLEMENTARY MATERIALS

www.sciencemag.org/content/345/6200/1255832/suppl/DC1
Supplementary Text S1 to S5
Figs. S1 to S22
Tables S1 to S13
References (*86–221*)
9 May 2014; accepted 29 July 2014
10.1126/science.1255832

RESEARCH ARTICLE

ION CHANNEL STRUCTURE

X-ray structures of AMPA receptor–cone snail toxin complexes illuminate activation mechanism

Lei Chen,[1] Katharina L. Dürr,[1] Eric Gouaux[1,2]*

AMPA-sensitive glutamate receptors are crucial to the structural and dynamic properties of the brain, to the development and function of the central nervous system, and to the treatment of neurological conditions from depression to cognitive impairment. However, the molecular principles underlying AMPA receptor activation have remained elusive. We determined multiple x-ray crystal structures of the GluA2 AMPA receptor in complex with a *Conus striatus* cone snail toxin, a positive allosteric modulator, and orthosteric agonists, at 3.8 to 4.1 angstrom resolution. We show how the toxin acts like a straightjacket on the ligand-binding domain (LBD) "gating ring," restraining the domains via both intra- and interdimer cross-links such that agonist-induced closure of the LBD "clamshells" is transduced into an irislike expansion of the gating ring. By structural analysis of activation-enhancing mutants, we show how the expansion of the LBD gating ring results in pulling forces on the M3 helices that, in turn, are coupled to ion channel gating.

Fast excitatory signal transduction at the chemical synapses of the brain is largely mediated by the activation of ionotropic glutamate receptors (iGluRs) by glutamate released from presynaptic neurons (*1*). Within the iGluR family of receptors are α-amino-3-hydroxy-5-methyl-4-isoxazolepropionic acid receptor (AMPA), kainate (KA), and *N*-methyl-D-aspartate (NMDA) subtypes, receptors that are all activated by glutamate and related in amino acid sequence, subunit stoichiometry, and domain structure, yet distinct in overall architecture, pharmacology, and biophysical characteristics. AMPA receptors undergo fast, submillisecond activation by glutamate, leading to depolarization of the postsynaptic membrane and relief of magnesium block of NMDA receptors, followed by rapid desensitization and deactivation on a millisecond time scale (*1*). AMPA receptor activity is fundamental to synaptic transmission, synaptic plasticity, and homeostatic scaling (*2*), and allosteric potentiators that slow desensitization and/or deactivation enhance synaptic currents and task-dependent neuron firing and show promise in the treatment of mild cognitive impairment and depression (*3*). By contrast, allosteric antagonists that diminish glutamate-induced AMPA receptor activity reduce glutamate-induced synaptic currents and are promising agents for the treatment of seizure disorders (*4*). Thus, understanding the molecular principles of AMPA receptor activation and action by allosteric modulators is important for continued development of new therapeutic strategies.

AMPA receptors are tetrameric complexes composed of subunits with a modular domain arrangement, beginning with the amino-terminal domain (ATD), the ligand- or agonist-binding domain (LBD), and the pore-forming transmembrane domain (TMD) (*5*). Whereas the ATDs and LBDs are organized as dimers of dimers, the TMD harbors approximate fourfold symmetry, thus yielding a symmetry mismatch between the LBD and TMD layers and giving rise to two nonequivalent subunit pairs, A/C and B/D (*6*). Hence, the mechanism and efficacy of transduction of agonist binding to ion channel gating may differ between the A/C and B/D subunit pairs. Because AMPA receptors undergo rapid and nearly complete desensitization in the continued presence of agonist (*7*), it has proven difficult to elucidate high-resolution structures of agonist-bound, activated states and to define mechanisms by which the chemical potential of agonist binding is transduced into the mechanical force of ion channel gating.

Here, we report x-ray crystal structures of an intact, rat GluA2 AMPA receptor in complex with a homodimeric *Conus striatus* cone snail toxin, con-ikot-ikot (*8*); (R,R)-2b, a high-affinity, twofold symmetric, positive allosteric modulator (*9*); the partial agonist KA (*10*); or the potent partial agonist fluorowillardiine (FW) (*11*). To do this, we expressed, purified, and solved the structure of con-ikot-ikot, a disulfide bond–rich polypeptide previously shown to induce paralysis in fish and potently and selectively block desensitization of AMPA receptors (*8*) (fig. S1). We next screened single–amino acid mutants of the GluA2 receptor for enhanced thermostability in detergent micelles by fluorescence-detection size-exclusion chromatography (FSEC) (*12*) because the native, agonist-bound receptor is unstable in detergent micelles. Substitution of 10 amino acids in the TMD (construct $GluA2_{cryst1}$) gives rise to a receptor with enhanced stability and with retention of agonist-induced ion channel gating activity (fig. S2). By combining con-ikot-ikot toxin with the $GluA2_{cryst1}$ receptor, together with the nanomolar affinity modulator (R,R)-2b and either KA or FW, we were able to grow single crystals of the receptor complex that diffract x-rays to between 3.5 and 4 Å resolution. To further address how agonist binding is coupled to ion channel gating, we resolved the structures of two Lurcher-like mutants (*13*) within the M3 ion channel gate region (*14*).

Architecture of AMPA receptor–toxin complex

The overall shape of the GluA2 receptor complex with con-ikot-ikot, (R,R)-2b, and either KA or FW resembles the letter Y, reminiscent of the preceding GluA2 antagonist complex (Fig. 1, A to D) (*6*). The toxin is entirely enshrouded within a large solvent-filled chamber between the ATD and LBD layers, thus providing molecular explanations for its slow on rate and potent activity (*8*) and requiring movement of the ATDs and/or ATD-LBD portals for binding or unbinding. By wedging between the ATD and LBD layers, the toxin buttresses the receptor complex, extending the height of the ATD to LBD layer by nearly 10 Å, as measured from the centers of masses (COMs) between the ATD and the D1 lobe of the LBD. The boomerang-shaped toxin spans LBD dimers, with interactions both within and between LBD dimers, burying 2128 $Å^2$ of surface area in the interface and aligning its molecular twofold axis with the overall twofold axis of the receptor. Despite proximity to the "overhanging" ATD layer, the toxin participates in few contacts with the ATD, thus explaining why ΔATD AMPA receptor complexes retain toxin sensitivity (*8*).

The 1.6 Å–resolution crystal structure of the isolated toxin unambiguously shows that it is a dimeric complex, in contrast to previous suggestions that it was a dimer of dimers (Fig. 1, E and F) (*8*). The size-exclusion chromatography profile of the toxin confirms that it behaves as a dimer in solution (fig. S1, A and B). Each subunit of the homodimeric toxin harbors a four-helix bundle that is extensively cross-linked by five disulfide bonds and is, in turn, linked to the second subunit by way of three intersubunit disulfide bonds (fig. S1C), yielding a robustly rigidified complex in which the only region of flexibility resides in the subunit-subunit interface. The boomerang-shaped homodimer has a conspicuous pattern of charged residues and nonpolar residues on its surface, with a prominent acidic patch defined by E48 (E, Glu) and the carboxyl terminus of A86 (A, Ala) (Fig. 1F), and hydrophobic regions resulting from exposed nonpolar residues of F34 and I61 (F, Phe; I, Ile).

[1]Vollum Institute, Oregon Health and Science University, 3181 SW Sam Jackson Park Road, Portland, OR 97239, USA. [2]Howard Hughes Medical Institute, Oregon Health and Science University, 3181 SW Sam Jackson Park Road, Portland, OR 97239, USA.
*Corresponding author. E-mail: gouauxe@ohsu.edu

The con-ikot-ikot structure provides a framework to understand the structure and function of other family members.

Complex web of receptor-toxin interactions

Con-ikot-ikot toxin spans the tetrameric LBD "gating ring," participating in extensive interactions with all four subunits such that it simultaneously fortifies intradimer interfaces and spans the interdimer cleft (Fig. 2). The electrostatic surface of the toxin "bottom" (Fig. 1F) shows extensive negative patches, which are complementary to multiple positively charged residues on the receptor surface, suggesting that ionic and polar contacts are crucial for receptor-toxin interaction (Fig. 2A). Furthermore, the convex face of the boomerang-shaped toxin is complementary to the concave receptor binding site, demonstrating that shape is also central to nanomolar toxin binding affinity (*8*).

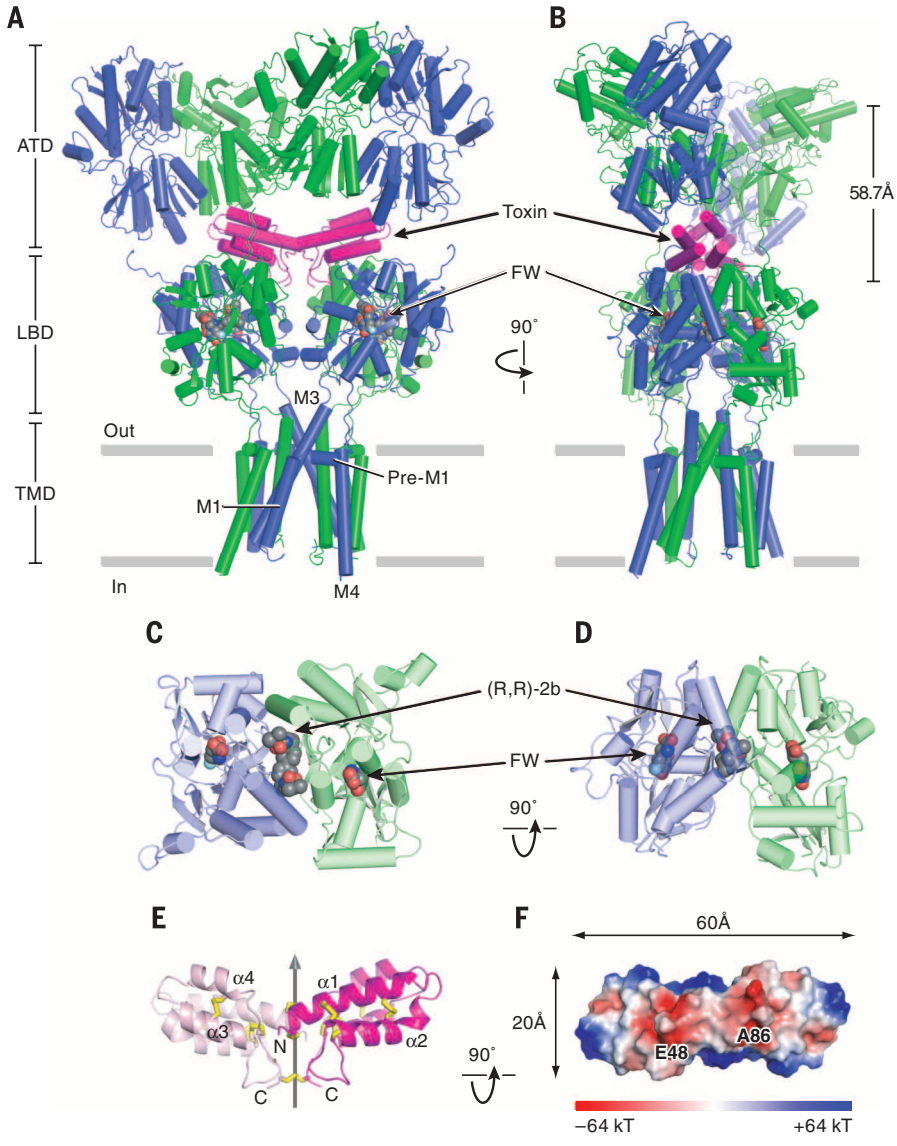

Fig. 1. Architecture of the GluA2-toxin complex. (**A**) View of the GluA2–toxin–(R,R)-2b–FW complex, parallel to the membrane, with the A/C subunits in blue, the B/D subunits in green, and the toxin in magenta. The (R,R)-2b allosteric modulator and the agonist FW are in space-filling representation. (**B**) View of the complex rotated 90° around the overall twofold axis of receptor. The distance between the ATD layer and the LBD layer D1 lobes was defined by measuring the distance between the COM of the ATD layer and the COM of the LBD layer D1 lobes. (**C**) Closeup top view of LBD AD dimer. (**D**) Closeup side view of LBD AD dimer. (**E**) Side view of con-ikot-ikot toxin. Cartoon representation of the dimeric toxin, with one subunit light pink and one magenta, showing how the subunits are related by a noncrystallographic twofold axis of symmetry, shown as a gray vertical arrow. Disulfide bonds are shown as yellow sticks. (**F**) Bottom view of the toxin, looking "up" from the LBD layer, showing the electrostatic surface of the toxin. Negatively charged patches on the LBD-facing surface are implicated in receptor-toxin interactions.

To more precisely understand the mechanism by which the toxin blocks desensitization, we peeled away the toxin from its LBD binding site to give open-book views of the receptor-toxin interface (Fig. 2, A and B). The receptor-toxin interactions can be classified into two types of contacts on the basis of the positions of subunits in the receptor complex (*6*), namely, LBD proximal A/C subunit-toxin interactions and distal B/D subunit-toxin interactions. Crucial contacts are between the extreme C-terminal carboxyl group of the toxin (A86) and the ammonium group of K752 (K, Lys) from the LBD B/D pair D1 lobe (Fig. 2E) and between the side-chain carboxyl group of toxin residue E48 and the side-chain guanidine group of R660 (R, Arg) from the LBD A/C pair D2 lobe (Fig. 2F). Augmenting these interactions is a polar contact between the side-chain carbonyl group of toxin Q37 (Q, Gln) and the side-chain guanidine group of R453 from LBD A/C pair D1 lobe. These residues on the GluA2 receptor are conserved in AMPA-subtype iGluRs but not in KA or NMDA receptors (fig. S3A), which is consistent with previous findings that con-ikot-ikot only potentiates the activity of AMPA receptors (*8*). To validate the interactions we observed in the receptor-toxin crystal structure, we mutated the residues on GluA2 to the corresponding residues on KA receptors and measured the extent to which toxin potentiates the activity of the mutants in comparison with cyclothiazide (CTZ) (*15*). Although all of the mutants respond to CTZ, potentiation by toxin is reduced, and, for the double mutant of R453→Q453 (R453Q)/K752Q, toxin potentiation is ablated (Fig. 2C). Additionally, the R660K mutant desensitizes profoundly, on the basis of the magnitude of CTZ potentiation. This might be because R660 indirectly decreases LBD dimer stability and thus promotes desensitization.

On the basis of extensive structural and functional studies of soluble LBDs (sLBD), the LBD undergoes clamshell-like domain closure upon agonist binding, and the degree of domain closure is correlated with agonist efficacy (*11*, *16*), although partial agonists may nevertheless occupy the fully closed state, albeit with reduced probability (*17*). Because the toxin interacts with both D1 and D2 lobes of the LBD A/C pair of subunits, we compared the KA-bound structure with the FW-bound structure by superposing the toxin domains (fig. S3B). Although the D2 lobes of the two structures are almost superimposable, the D1 lobe shows an outward displacement in the KA-bound structure compared with the FW-bound structure, as evidenced by a 3-Å shift of the marker Cα atom of K458 of the A/C pair, which is on β4 of the D1 lobe and in close proximity to R453. This conformational difference is consistent with the degree of clamshell closure both in full-length structures (fig. S3, E and F) and in sLBDs (*11*, *18*, *19*), which show that the KA clamshells are more open in comparison to the FW subunits. Nevertheless, a change in rotamer conformation of toxin residue Q37 allows it to maintain its interaction

with receptor residue R453 in both complexes (fig. S3C), thus showing how the toxin can interact with the receptor in the presence of KA or FW, despite differences in the degree of LBD clamshell closure. However, if we model a hypothetical complex of the toxin with an apo receptor subunit by superposing the D2 lobe of the apo sLBD (*19*) [Protein Data Bank (PDB) 1FTO chain A] structure onto the KA- and toxin-bound structure, there is a further 7-Å outward shift of the K458 Cα marker atom so that Q37 of the toxin can no longer interact with R453 of the LBD (fig. S3C). Indeed, in a toxin binding assay we show that receptor-toxin complex formation requires the presence of agonist (fig. S3D). Thus, receptor-toxin binding requires ligands that induce clamshell closure. Because the toxin binds to both D1 and D2 lobes of the LBD A/C pair, the LBD is stabilized in a ligand-bound conformation. Consistent with the mechanism, toxin increases apparent agonist affinity in a ^{3}H FW-binding assay (fig. S2F), and previous studies have shown that toxin can modestly retard the rate of receptor deactivation (*8*).

Conformation of the LBD layer in an activated state

The interaxis or "roll" angle (*20*) between the twofold axes of the LBD dimers is smaller in the toxin complex than in the ZK 200775 (ZK) antagonist-bound structure (Fig. 3, A to C), largely because the toxin locks the LBD gating ring in a fixed conformation. Furthermore, the toxin structure with FW bound has a smaller interaxis angle than the KA complex (Fig. 3, B and C) because the D2 lobes, which are coupled to the ion channel, share a common position, but the FW complex has a greater LBD domain closure. Thus, there is a corresponding difference in the position of the D1 lobes (fig. S3, E and F). By binding both subunits within a LBD dimer, the toxin stabilizes the LBD dimer D1-D1 interface in a nondesensitized conformation, yielding a distance between S741 (S, Ser) Cα marker atoms on the D1-D1 interface of 19.3 to 19.7 Å (*21*, *22*). By using the distance between Cα atoms of S741 residues in the D1-D1 interface as a metric, we show that the D1-D1 interfaces adopt nondesensitized conformations in all of the structures (Fig. 3, D, to F). The toxin complexes reported here also have the modulator (R,R)-2b bound because inclusion of modulator improves diffraction quality, presumably by stabilizing the receptor in a conformationally homogeneous population.

In comparison to the GluA2 ZK structure [Protein Data Bank (PDB) code 3KG2] (*6*), the toxin complex structures with either KA or FW bound have much larger degrees of clamshell closure and thus a larger separation of the D2 lobe within dimers. To quantify the separation of the D2 lobes, we compared the distances between S640 Cα marker atoms, which are on helix E of the D2 lobe and directly connected to the D2-M3 linker. There is an 8.4-Å increase in separation between the D2 lobes upon transition from the ZK antagonist state to the FW agonist-bound structure, thus providing structural evidence for the long-standing hypothesis that LBD domain closure is mechanically coupled to ion channel gating (*19*, *21*). Moreover, there is an additional 3.4-Å separation in the proximal A/C pair and a 12.4-Å separation in distal B/D pair distance (Fig. 3, G to I), thus suggesting that there is a nonequivalent "pulling force" of the LBDs onto the LBD-TMD linker (*23*), consistent with the symmetry nonequivalence of the A/C and B/D subunit pairs (*6*).

Toxin stabilization of LBD gating ring

A view of the LBD layer from the ATD shows how the toxin stabilizes the LBD layer in an expanded conformation (Fig. 4). By measuring the distances between Cα marker atoms of R660 on helix F and Q756 on helix J, both of which are close to the central opening of the gating ring, we compared the interdimer distances between selected structures. Beginning with the A665C cross-linked sLBD tetramer (Fig. 4, A and D) (*24*), which is trapped in an inactive state yet has been suggested to represent an activation intermediate, and then to the ZK state (Fig. 4, B and D) and last to the toxin- and FW-bound state (Fig. 4, C and D), we observed an increase of the B/D distance from 16.5 to 23.9 to 27.4 Å, respectively, whereas the A/C distance changed from 19.7 to 24.1 to 22.0 Å, respectively. The overall change in the B/D distances is larger in comparison to the change in the A/C pair, an observation that is correlated with the changes in the S640 Cα distances mentioned previously and consistent with the hypothesis that the B/D pair may play a more important role in ion channel opening. We suggest that, without toxin, the LBD dimers are more conformationally dynamic

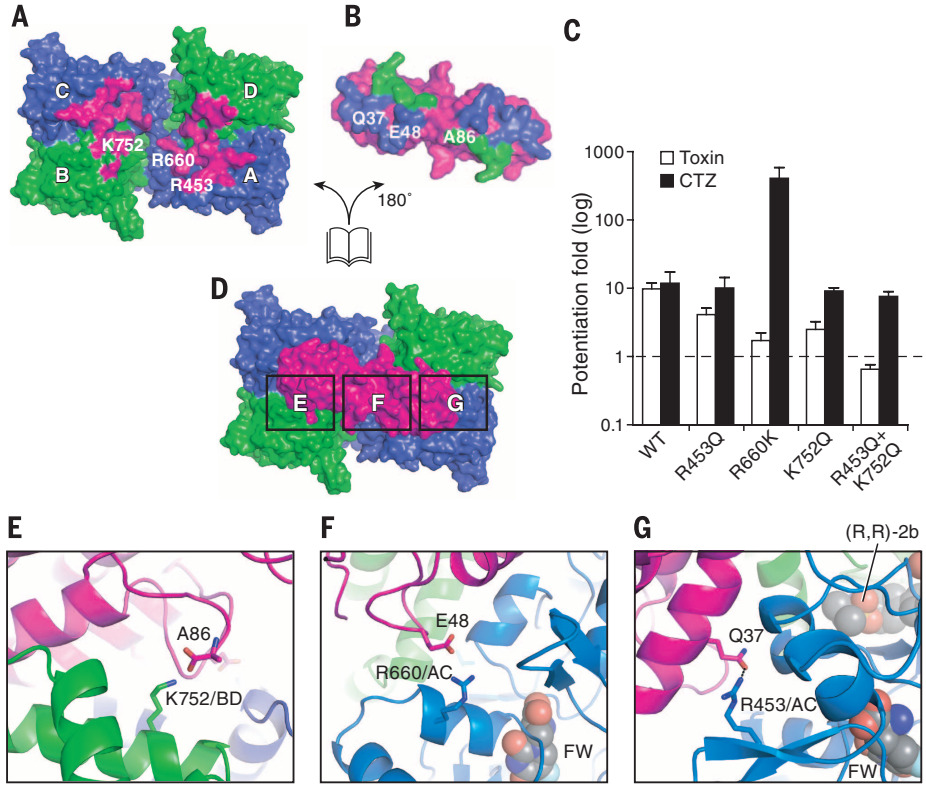

Fig. 2. Complex web of receptor-toxin interactions. (A, B, and D) Open-book views of the GluA2 LBD–toxin interactions shown in surface representation. (**A**) View of the GluA2 LBD layer from the ATD, showing the residues that interact with toxin in magenta. (**B**) View of the toxin residues that interact with the GluA2 A/C subunits in blue and residues that interact with the B/D subunits in green. (**C**) Extents of potentiation by toxin (open bar) and CTZ (black bar) on the steady-state currents of wild-type GluA2 and GluA2 mutants, elicited by application of 10 mM Glu. Data are ±SEM (n = 3). (**D**) Top view onto the LBD layer from the extracellular side, highlighting key regions of toxin-receptor interactions (shown as black rectangles). (**E**) Closeup view of the salt bridge between K752 (GluA2 B/D subunit) and the carboxyl terminus of the toxin (A86) boxed in (D). (**F**) Closeup view of the R660 (GluA2 A/C subunit)–E48 (toxin) interaction boxed in (D). (**G**) Closeup view of the R453 (GluA2 A/C subunit)–Q37 (toxin) interaction boxed in (D).

and can adopt different conformations because of the relatively small interdimer interface (*25*).

Coupling of agonist binding to channel gating via M3-D2 linker

The channel pore of the toxin-GluA2 complex structure with either KA or FW adopts the same closed conformation as the ZK-bound structure (*6*), although there is a small conformational change at the upper region of the crucial M3 helix between residues 623 and 626 (Fig. 5, A and D). In the toxin-complex structures, the LBD dimer interfaces are intact and stabilized by both toxin and modulator. In addition, partial agonists are bound and induce LBD clamshell closure; thus, we propose that these structures represent toxin-bound preopen states. However, the ion channel gate is closed at the M3 bundle crossing, and we speculate that this is because either the crystallization conditions, the absence of lipid bilayer, or the details of the receptor construct favor a closed-gate conformation. It is also possible that the use of partial agonists does not sufficiently populate the open-gate conformation (*11*). To address the issue of the receptor construct, we solved the structure of $GluA2_{cryst2}$ in complex with KA+toxin+(R,R)-2b, where the $GluA2_{cryst2}$ construct only harbors the C815A (C, Cys) mutation, located at the C-terminal end of the M4 helix. The structure of this $GluA2_{cryst2}$ complex is similar to the corresponding $GluA2_{cryst1}$ structure (fig. S5, C and D; overall root mean square deviation of 0.28 Å on main chain atoms), thus demonstrating that other factors are responsible for precluding the crystallization of an open-gate conformation.

To favor the formation of an open state, we generated the Lurcher-like mutants A622T (*26*) and T625G (G, Gly; T, Thr) (*27*) in the context of the $GluA2_{cryst1}$ construct, mutations that are known to greatly facilitate ion channel gating. Structures of these mutants as complexes with KA+toxin+(R,R)-2b showed large conformational changes only within the M3-LBD linkers compared with the structure without the activation mutations (Fig. 5 and fig. S6). Complexes with full agonists or with more-efficacious partial agonists have so far not yielded crystals. Because the structures of the T625G and A622T variants are close to identical, we focused the discussion on the A622T structure unless indicated. In the mutant structures, the side chain of I633 from the B/D subunits binds within a hydrophobic pocket formed by V732, I504, L639, and I645 (L,

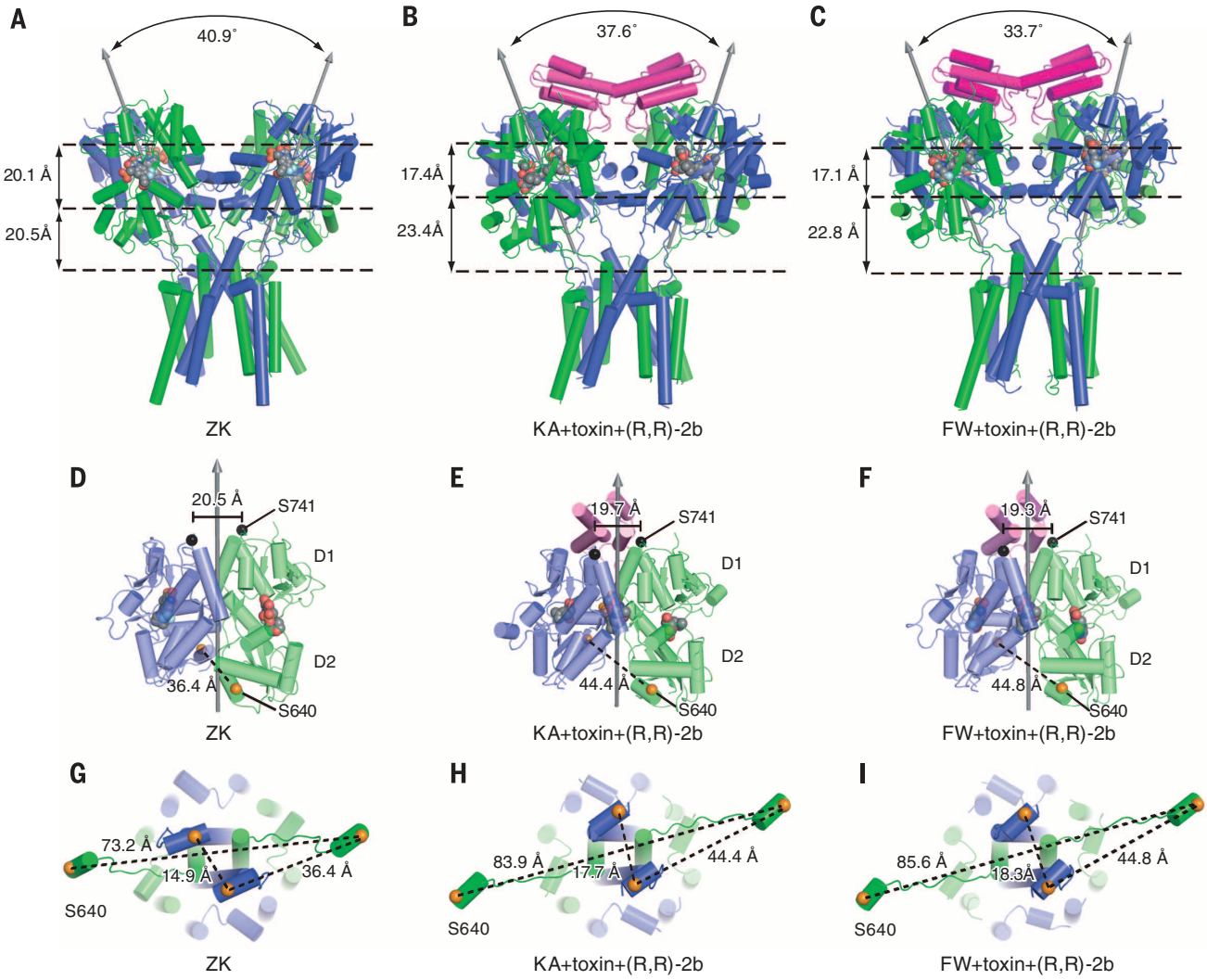

Fig. 3. Conformation of the LBD layer in an activated state. Structures of the GluA2 receptor in the ZK antagonist-bound state (**A**, **D**, and **G**). Structures of the GluA2 receptor in the KA+toxin+(R,R)-2b–bound state (**B**, **E**, and **H**) and in complex with FW+toxin+(R,R)-2b (**C**, **F**, and **I**). (A) to (C) are side views of the LBD-TMD layers showing the angles between the two local twofold rotation axes of the LBD dimers. The distances between the LBD D1 lobes and the D2 lobes and the distances between the D2 lobes and T625 are measured between the COMs of each layer and are shown on the left. (D) to (F) are side views of the A/D LBD dimers. Black arrows depict the local twofold axes of LBD dimers. The Cα atoms of S741 are shown as black spheres, along with the intersubunit distances. The Cα atoms of S640 are shown as orange spheres. (G) to (I) are views of helix E in the LBD layer and the LBD D2-M3 linker, seen from the LBD layer. The Cα atoms of S640 are also shown as orange spheres, together with intersubunit distances.

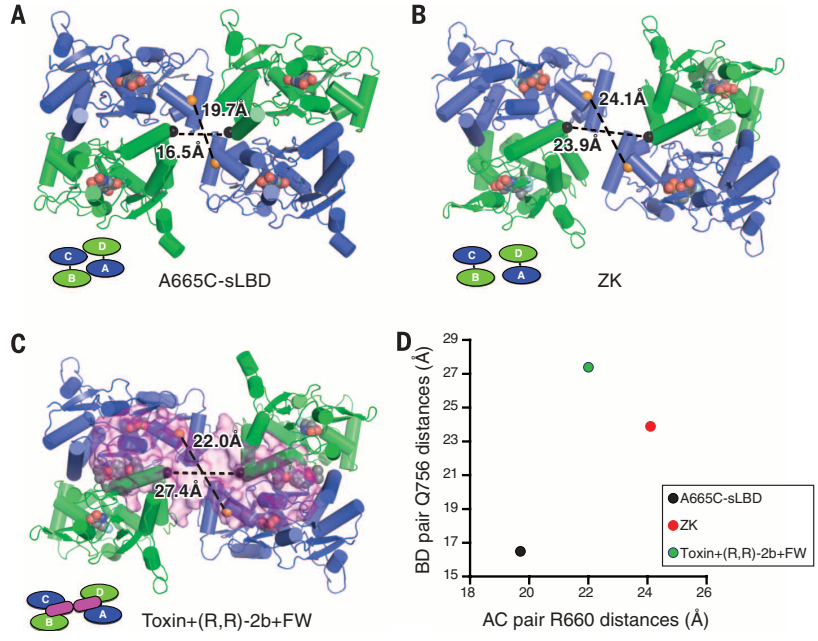

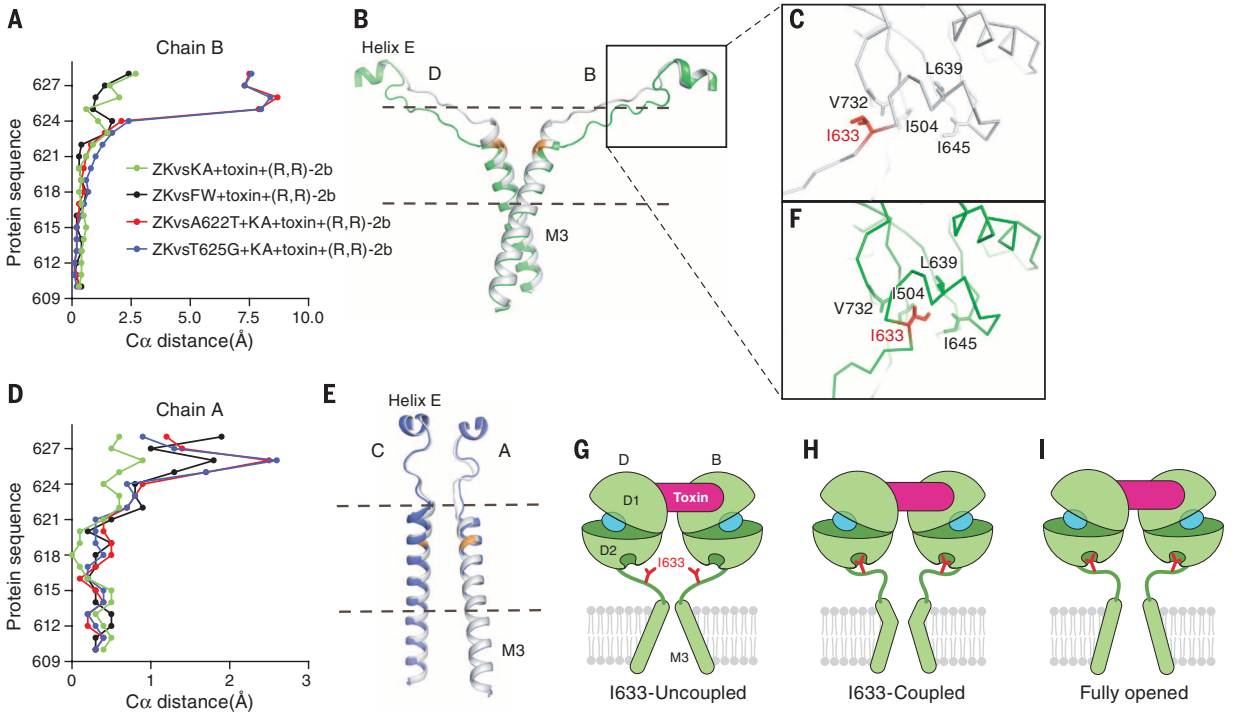

Fig. 4. Toxin stabilizes the LBD gating ring in an expanded conformation. Top view of the LBD layer in the A665C–cross-linked GluA2 sLBD structure (PDB 4L17) (**A**), the GluA2 ZK–bound state (**B**), and the GluA2 FW+toxin+(R,R)-2b–bound state (**C**). The distances between Cα atoms of GluA2 R660 (orange spheres) from the A/C subunits and the distances between the Cα atoms of GluA2 Q756 (black spheres) from the B/D subunit are shown. Distances are plotted in (**D**).

Fig. 5. Coupling of agonist binding to ion channel gating via the M3-D2 linker. (**A**) A plot of the differences in position of Cα atoms from residues in the M3 TMD helixes derived from chain B in the structures reported here after superposition of M1, M3, and M4 helices. (**B**) Cα trace of the LBD D2 to M3 connections in the B/D subunits, where the structure of the GluA2 KA+toxin+(R,R)-2b elements are shown in gray and those derived from the A622T GluA2 mutant KA+toxin+(R,R)-2b complex are shown in green. The main chain atoms of the site of mutation, A622, are illustrated in orange. The region used to generate (A) is shown between dashed lines. (**C**) Closeup view of the uncoupled I633 site in the KA+toxin+(R,R)-2b structure subunit B. I633 is shown in red. The side chains of hydrophobic residues that line the I633-binding pocket are shown in sticks. (**D**) A plot analogous to that shown in (A), using the same structures, of the respective Cα distances from residues in the M3 helix from chain A. (**E**) The LBD D2-to-M3 connections in A/C subunits. The structure of the GluA2 KA+toxin+(R,R)-2b complex is shown in gray, and the structure of the A622T GluA2 KA+toxin+(R,R)-2b complex is shown in blue. At the mutation site, A622, the backbone is colored in orange. The region used to generate (D) is shown between dashed lines. (**F**) Closeup view of the coupled I633 site in the KA+toxin+(R,R)-2b A622T mutant structure subunit B. I633 is in red. The side chains of hydrophobic residues that define the I633-binding pocket are shown in stick representation. (G) to (I) depict schematic illustrations of a mechanism by which the toxin stabilizes an activated conformation of the LBD layer. Only LBD B/D subunits and M3 helices are shown for clarity. I633 residues are shown in red, and agonists are shown in cyan. (**G**) The toxin-bound and I633-uncoupled state, as we observed in the partial agonist, toxin (R,R)-2b structures. (**H**) The toxin-bound and I633-coupled state. The M3 B/D helices expand via a kink in the helices, yet the ion channel gate remains closed, as we observed in the A622T and T625G structures. (**I**) A hypothetical model of the toxin-bound, I633-coupled, and open-channel state. We speculate that even with toxin bound the channel probably flickers between (G) and (I), perhaps via (H) as an intermediate state.

Leu; V, Val) on the D2 lobe of the LBDs, adopting the same binding mode as I633 from the A/C pair or all subunits from the ZK structure (Fig. 5F); we term this the coupled conformation. By contrast, I633 from the B/D pair in the toxin-bound structures without the M3 mutations is pulled out of the hydrophobic D2 pocket and adopts an uncoupled conformation (Fig. 5C).

To better define the register of the region flanking I633, we generated the S635C mutant in a $GluA2_{cryst1}$ background and labeled the resulting protein with mercury. In anomalous difference electron density maps at the LBD-TMD linker region of the S635C mutant, we see density at the A/C subunit positions but no prominent density for the B/D subunits (fig. S5G). Assuming that the sites have similar labeling efficiencies, we can conclude that the S635C sites in the B/D pair are mobile, consistent with a dynamic linker region. However, the electron density is sufficiently strong to unambiguously trace the main chain, which shows that the I633 side chain cannot adopt a coupled conformation in the non-M3 mutant structures. To further probe the role of I633, we generated I633A and I633E mutants in the background of the wild-type receptor, hypothesizing that these mutants would favor an uncoupled conformation and thus diminish agonist-induced gating. Indeed, the I633A mutant shows only very small currents compared with wild-type GluA2 (fig. S4, A, D, and J), whereas the I633E mutant shows even smaller currents (fig. S4, G and J). Both receptor assembly, as assessed by FSEC (fig. S4, B, E, and H), and receptor surface expression are similar to those of the wild-type receptor (fig. S4, C, F, I, K, and L). These results are consistent with the conclusion that the I633 mutant has impaired gating, perhaps similar to the recently reported glycine-insertion mutants of the NMDA receptor LBD-M3 linker (*23*). Indeed, the I633 position is conserved in iGluRs, with the exception that, in the NMDA receptor GluN2 subunit, there is a valine at this site (fig. S4N). Because the uncoupled phenotype of the I633A mutant can be robustly rescued by coexpression with transmembrane AMPA receptor regulatory protein γ2 (TARPγ2) (*28*) (fig. S4M), an AMPA receptor auxiliary subunit that enhances receptor activation, we show that the I633A mutant is properly folded and assembled yet likely has a low open probability in the absence of TARPγ2.

The activation mutant structures show that conformational changes of key gating residues near the M3 helix crossing are more prominent in the B/D subunits than in the A/C subunits (Fig. 5, A and D). As identified in the ZK-bound structure, T617, A621, T625, and M629 (M, Met) form the physically shut gate of the channel (*6*). In the activation mutant structures, the outward movements of the Cα atoms in B/D subunits start at A620, increase in the direction of the extracellular ends of the M3 segments (Fig. 5A), and involve the unwinding of the last turn of the M3 helix. By contrast with the large changes in the upper region of the M3 helix of the B/D subunits, there are only small changes in the lower region of the B/D subunits, N-terminal to T617, and only small changes in the entire M3 segment from the A/C subunits. Together, these results show that the pore is still shut and that the upper M3 helix transforms from fourfold symmetry to twofold symmetry in transitioning from the cytoplasmic to the extracellular side of the membrane (*29*).

The coupled I633 position and the outward movements of the upper regions of the M3 segments in the B/D subunits are consistent with the mutant structures reflecting an activation intermediate state (Fig. 5H) between the toxin-bound structure (Fig. 5G) and a hypothetical fully opened structure (Fig. 5I). Lurcher-like mutants may facilitate current flow by weakening the M3 helix bundle, allowing the ion channel gate to open more easily. In our structures, however, the ion channel has not opened, and instead the mutants have simply facilitated the distortion of the extracellular end of the M3 helix.

We suggest that I633 must be in a coupled position to transmit agonist binding and clamshell closure to gate opening and, secondly, that the unwinding of the M3 helix tip can absorb the pulling force generated by LBD. When we modeled I633 in a coupled state, we found that the linker is not of sufficient length to permit the combination of an activated LBD (closed clamshell) and a closed pore (fig. S6C). Thus, we speculate that, in the fully opened structure, I633 is coupled, the M3 tip preserves its helical structure, and the M3 helix is flexed or kinked outward to allow for an open channel gate.

Conclusion

We show that con-ikot-ikot toxin binds between ATD and LBD layers, forms extensive contacts with all four LBD subunits, and stabilizes the LBD gating ring in an activation-competent conformation. The cross-linking of the LBDs precludes the rupture of the D1-D1 interface, locks the LBD dimers together, and allows for agonist binding to be coupled to ion channel gating. By comparing agonist-bound toxin-receptor structures to the previously determined antagonist-receptor complex (movies S1 and S2), we show how agonist binding is coupled to ion channel gating, thus validating decades of research on the isolated binding domains of iGluRs. We propose that agonist binding generates an asymmetric pulling force on the LBD-TMD linker and that a previously unidentified coupling switch defined by I633 is crucial to convey clamshell closure to channel opening. Taken together, the toxin-bound GluA2 structures provide insight into the gating mechanism of AMPA receptors and shed light on mechanisms of closely related KA and NMDA receptors. Insight into how AMPA receptor activity is modulated may also open new avenues for the development of therapeutic agents.

REFERENCES AND NOTES

1. S. F. Traynelis *et al*., *Pharmacol. Rev.* **62**, 405–496 (2010).
2. R. L. Huganir, R. A. Nicoll, *Neuron* **80**, 704–717 (2013).
3. M. J. O'Neill, D. Bleakman, D. M. Zimmerman, E. S. Nisenbaum, *Curr. Drug Targets CNS Neurol. Disord.* **3**, 181–194 (2004).
4. M. A. Rogawski, *Acta Neurol. Scand. Suppl.* **127** (suppl. 197), 9–18 (2013).
5. J. Kumar, M. L. Mayer, *Annu. Rev. Physiol.* **75**, 313–337 (2013).
6. A. I. Sobolevsky, M. P. Rosconi, E. Gouaux, *Nature* **462**, 745–756 (2009).
7. I. M. Raman, L. O. Trussell, *Neuron* **9**, 173–186 (1992).
8. C. S. Walker *et al*., *Curr. Biol.* **19**, 900–908 (2009).
9. B. H. Kaae *et al*., *Chem. Biol.* **14**, 1294–1303 (2007).
10. D. K. Patneau, L. Vyklicky Jr., M. L. Mayer, *J. Neurosci.* **13**, 3496–3509 (1993).
11. R. Jin, T. G. Banke, M. L. Mayer, S. F. Traynelis, E. Gouaux, *Nat. Neurosci.* **6**, 803–810 (2003).
12. M. Hattori, R. E. Hibbs, E. Gouaux, *Structure* **20**, 1293–1299 (2012).
13. J. Zuo *et al*., *Nature* **388**, 769–773 (1997).
14. T. Kuner, P. H. Seeburg, H. R. Guy, *Trends Neurosci.* **26**, 27–32 (2003).
15. K. M. Partin, D. K. Patneau, C. A. Winters, M. L. Mayer, A. Buonanno, *Neuron* **11**, 1069–1082 (1993).
16. N. Armstrong, M. Mayer, E. Gouaux, *Proc. Natl. Acad. Sci. U.S.A.* **100**, 5736–5741 (2003).
17. A. H. Ahmed, S. Wang, H. H. Chuang, R. E. Oswald, *J. Biol. Chem.* **286**, 35257–35266 (2011).
18. N. Armstrong, Y. Sun, G.-Q. Chen, E. Gouaux, *Nature* **395**, 913–917 (1998).
19. N. Armstrong, E. Gouaux, *Neuron* **28**, 165–181 (2000).
20. C. H. Lee *et al*., *Nature* **511**, 191–197 (2014).
21. Y. Sun *et al*., *Nature* **417**, 245–253 (2002).
22. N. Armstrong, J. Jasti, M. Beich-Frandsen, E. Gouaux, *Cell* **127**, 85–97 (2006).
23. R. Kazi, J. Dai, C. Sweeney, H. X. Zhou, L. P. Wollmuth, *Nat. Neurosci.* **17**, 914–922 (2014).
24. A. Y. Lau *et al*., *Neuron* **79**, 492–503 (2013).
25. M. S. Horning, M. L. Mayer, *Neuron* **41**, 379–388 (2004).
26. L. P. Wollmuth *et al*., *J. Neurosci.* **20**, 5973–5980 (2000).
27. B. S. Moore, U. L. Mirshahi, T. L. Ebersole, T. Mirshahi, *J. Biol. Chem.* **288**, 18842–18852 (2013).
28. A. C. Jackson, R. A. Nicoll, *Neuron* **70**, 178–199 (2011).
29. A. I. Sobolevsky, M. V. Yelshansky, L. P. Wollmuth, *Neuron* **41**, 367–378 (2004).

ACKNOWLEDGMENTS

All members of the Gouaux laboratory and I. Baconguis are gratefully acknowledged for their support and assistance. We thank L. Vaskalis for assistance with figures, the beam line staff at Advanced Light Source—Berkeley Center for Structural Biology and Stanford Synchrotron Radiation Lightsource 12-2 for their support during data collection, B. Olivera for providing crude *Conus striatus* venom, D. King and L. David for mass spectrum analysis, and M. Suga for early work on thermostability mutation screening. L.C. is supported by an American Heart Association postdoctoral fellowship (13POST13960004). K.L.D. was supported by a Long-Term Fellowship of the European Molecular Biology Organization and an institutional National Research Service Award (NRSA) and is currently a recipient of an individual NRSA (F32MH100331). This work is supported by the NIH (E.G.), and E.G. is an investigator with the Howard Hughes Medical Institute. The coordinates have been deposited in the PDB with codes 4U5B, 4U5C, 4U5D, 4U5E, and 4U5F for the GluA2 receptor toxin complex and codes 4U5G and 4U5H for the isolated toxin. L.C. contributed to all aspects of the research; K.L.D. contributed to thermostabilization mutation screening and initial characterization of native snail venom by two-electrode voltage clamp. E.G. directed the research. All authors contributed to the preparation of the manuscript.

SUPPLEMENTARY MATERIALS

www.sciencemag.org/content/345/6200/1021/suppl/DC1
Materials and Methods
Figs. S1 to S6
Tables S1 and S2
References (*30*–*40*)

Movies S1 and S2

7 July 2014; accepted 25 July 2014
Published online 7 August 2014;
10.1126/science.1258409

REPORTS

GLASS STRUCTURE

Observation of the transition state for pressure-induced $BO_3 \rightarrow BO_4$ conversion in glass

Trenton Edwards,[1] Takatsugu Endo,[1] Jeffrey H. Walton,[2] Sabyasachi Sen[1]*

A fundamental mechanistic understanding of the pressure- and/or temperature-induced facile transformation of the coordination environment of boron is important for changing the physical properties of glass. We have used in situ high-pressure (up to 2 gigapascals) boron-11 solid-state nuclear magnetic resonance spectroscopy in combination with ab initio calculations to investigate the nature of the transition state for the pressure-induced $BO_3 \rightarrow BO_4$ conversion in a borosilicate glass at ambient temperature. The results indicate an anisotropic elastic deformation of the BO_3 planar triangle, under isotropic stress, into a trigonal pyramid that likely serves as a precursor for the subsequent formation of a BO_4 tetrahedron.

The importance of the local coordination environments of atoms in the lattice of crystalline matter and their response to pressure and temperature in understanding structure-property relations cannot be overstated (*1*). Coordination changes in glass-forming network liquids are responsible for generation of configurational entropy, controlling viscous flow and structural relaxation (*2*). Therefore, pressure- and/or temperature- (*P-T*) induced coordination changes have been studied fairly extensively in oxide glasses and liquids where the network-forming B, Al, and Si cations display increasing coordination numbers with increasing pressure and temperature (*2*–*12*). One of the most well-studied cases in this regard is the trigonal to tetrahedral $BO_3 \rightarrow BO_4$ conversion in borate and borosilicate glasses and liquids with increasing pressure and/or temperature (*5*–*12*). This B coordination change has pronounced effects on the structure-property relations in these materials relevant for their wide-ranging technological applications in fiber composites, radioactive waste encapsulation, and substrates for display (*9*, *11*). The $BO_3 \rightarrow BO_4$ conversion can be initiated in the supercooled liquid state just above the glass transition temperature T_g, and its magnitude can be strongly enhanced at relatively low pressures of a few hundred megapascals, often achieved in standard processing methods such as injection molding or hot press sintering (*9*).

Typically these structural changes are studied ex situ in glasses quenched from their parent liquids subjected to different *P-T* conditions. Thus, one loses the opportunity of monitoring the mechanism of coordination change in real time or of "seeing" the intermediate or transition state, although in certain favorable cases the transition state can be quenched (*4*). Furthermore, observation of time-dependent changes in the local coordination geometry requires application of an element-specific spectroscopic technique such as nuclear magnetic resonance (NMR) spectroscopy that is sensitive to subtle changes in short-range order. However, the application of solid-state NMR spectroscopy has remained limited largely to ambient pressure owing to the technological challenges associated with designing a high-pressure probe head with suitable nonmagnetic materials that can operate up to a few gigapascals and can allow for sufficient sensitivity and sample volume. Recently, we have designed a high-pressure NMR probe in our laboratory that can maintain hydrostatic pressures of up to 2.5 GPa (*13*). Here, we present the first results of an in situ high-pressure (up to 2.0 GPa) ^{11}B NMR spectroscopic study using this probe, in combination with ab initio calculations that directly demonstrate the nature of the transition state for $BO_3 \rightarrow BO_4$ conversion in a commercial borosilicate glass of Corning code 7059 (*13*) at ambient temperature.

The three NMR parameters that control the ^{11}B NMR line shapes in oxides include the isotropic chemical shift δ_{iso}, the quadrupolar coupling constant C_Q, and the electric field gradient asymmetry parameter η. These parameters are primarily controlled by the nearest-neighbor coordination

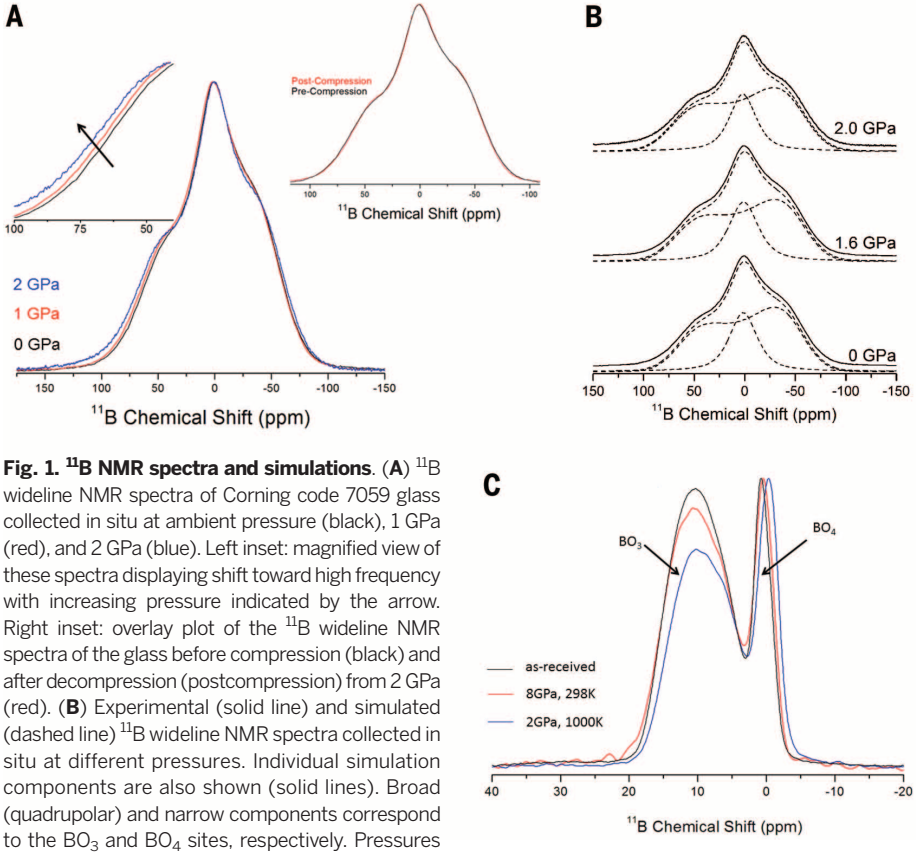

Fig. 1. ^{11}B NMR spectra and simulations. (**A**) ^{11}B wideline NMR spectra of Corning code 7059 glass collected in situ at ambient pressure (black), 1 GPa (red), and 2 GPa (blue). Left inset: magnified view of these spectra displaying shift toward high frequency with increasing pressure indicated by the arrow. Right inset: overlay plot of the ^{11}B wideline NMR spectra of the glass before compression (black) and after decompression (postcompression) from 2 GPa (red). (**B**) Experimental (solid line) and simulated (dashed line) ^{11}B wideline NMR spectra collected in situ at different pressures. Individual simulation components are also shown (solid lines). Broad (quadrupolar) and narrow components correspond to the BO_3 and BO_4 sites, respectively. Pressures are denoted alongside each spectrum. The simulated spectrum and the components are vertically offset with respect to the experimental spectrum for clarity. (**C**) ^{11}B MAS NMR spectra of the as-received glass (black) and of samples of the same glass quenched from 2 GPa and 1000 K (blue) and from 8 GPa and 298 K (red). Broad (quadrupolar) and narrow peaks correspond to the BO_3 and BO_4 sites, respectively, in the glass. All spectra are normalized to the BO_4 peak.

[1]Division of Materials Science and Engineering, University of California at Davis, Davis, CA 95616, USA. [2]Nuclear Magnetic Resonance Facility, University of California at Davis, Davis, CA 95616, USA.
*Corresponding author. E-mail: sbsen@ucdavis.edu

environment of the boron atom and, thus, vary over a relatively narrow range (*14*–*16*). The BO_3 trigonal planar environment with its approximate D_{3h} site symmetry is characterized by a ^{11}B NMR line shape that is controlled by quadrupolar interaction, whereas the BO_4 tetrahedral environment with the locally cubic T_d site symmetry of the central B atom results in a symmetric and relatively narrow Gaussian line shape. The experimental ^{11}B NMR line shape of the 7059 glass at various pressures (Fig. 1A) can be simulated well with two components corresponding to the BO_3 and BO_4 sites in the glass structure (Fig. 1B). The corresponding NMR simulation parameters for the two B sites are listed in table S1 (*13*). The BO_3:BO_4 ratio is ~75:25 at ambient conditions and is consistent with the value obtained from the simulation of the high-resolution ^{11}B magic angle spinning (MAS) NMR spectrum (76:24) of the as-received glass (Fig. 1C and table S2). This ratio at ambient temperature appears to remain unchanged with pressure, at least up to 2 GPa (table S1). This result is consistent with the observation that the BO_3:BO_4 ratio decreases only a small amount (74:26) upon quenching the glass from 8 GPa at ambient temperature, which is not surprising considering that coordination changes in oxide glasses at such low pressures require thermal activation (table S2). The role of thermal activation is evident when we compare the ^{11}B MAS NMR spectrum of the glass quenched from 2 GPa and 1000 K to that of the as-received glass and the glass quenched from 8 GPa at ambient temperature (Fig. 1C). The BO_3:BO_4 ratio of the sample quenched from 2 GPa and 1000 K is substantially lower (70:30) than that of both the as-received, ambient pressure glass (76:24) and the sample quenched from a higher pressure of 8 GPa at ambient temperature (74:26), indicating a pressure-induced $BO_3 \rightarrow BO_4$ conversion that is strongly facilitated by temperature (table S2).

The simulation of the in situ high-pressure ^{11}B NMR line shapes (Fig. 1, A and B) indicates that although the BO_3:BO_4 ratio and the quadrupolar parameters for the BO_3 site do not change significantly in this narrow pressure range (table S1), the ^{11}B isotropic chemical shift δ_{iso} for the BO_3 site shifts monotonically to higher frequency with increasing pressure at a nearly constant rate of ~1.6 parts per million (ppm)/GPa (Fig. 2). On the other hand, the ^{11}B δ_{iso} for the BO_4 sites does not display any significant change with pressure. In contrast, the ^{11}B δ_{iso} values for both BO_3 and BO_4 sites (15.9 and −0.3 ppm, respectively) show a clear shift toward low frequency (increasing shielding) in the case of the sample quenched from 2 GPa and 1000 K (table S2). The structural modification at high pressure corresponding to these changes in the ^{11}B NMR parameters cannot be understood a priori without a systematic understanding of the influence of any change in the BO_3 coordination geometry on the ^{11}B NMR parameters. To understand the evolution of the BO_3 units in the glass, we performed ab initio calculations of ^{11}B NMR parameters using density functional theory (DFT) on a molecule of H_3BO_3 containing a central B atom in triangular planar coordination with three OH groups (*13*). We consider the effects of three types of changes in the B coordination geometry on the ^{11}B NMR parameters.

The first model that we consider is a uniform compression or expansion of the B-O coordination triangle (model 1). This model results in a systematic change in the isotropic chemical shift δ_{iso} while the quadrupolar parameters C_Q and η remain constant (table S3). The ^{11}B δ_{iso} moves to lower frequencies upon shortening of the B-O bond lengths, at a rate of ~76.5 ppm/Å (Fig. 3A). The ^{11}B δ_{iso} of the BO_3 and BO_4 sites in the sample quenched from 2 GPa and 1000 K is shifted to a lower frequency compared to the ambient pressure sample. This shift may be indicative of a compression of the B-O bond length in the sample quenched from high *P-T*. Such a shift can also be attributed to an increased mixing of Si and B, resulting from the increasing concentration of BO_4 units combined with an avoidance in their connectivity via B-O-B linkages (*12*). By contrast, in situ high-pressure ^{11}B NMR experiments show a shift of the ^{11}B δ_{iso} of the BO_3 site to higher frequencies with increasing pressure, which would require a uniform expansion of the BO_3 triangle. Uniform expansion with increasing pressure is clearly unphysical, and thus this model cannot explain the experimental observation made by in situ high-pressure NMR.

The second model that we consider is an anisotropic, in-plane deformation (model 2), where one of the B-O distances is systematically increased while the other atom positions are allowed to relax within the B-O plane to a minimum-energy configuration. This mode of deformation results in a systematic and rapid increase in the quadrupolar asymmetry parameter η (table S4) that is inconsistent with the experimental observations made in this study. The ^{11}B NMR line shapes for the BO_3 site, obtained in situ or ex situ, indicate insignificant changes in η with pressure (tables S1 and S2).

The final model of deformation that we consider is to move the central B atom out of the plane of the oxygen atoms along the threefold symmetry axis while the B-O distances are allowed to relax (*13*). The out-of-plane displacement of the central B atom results in an increase in the B-O bond lengths and a change in the symmetry of the BO_3 environment from trigonal planar (D_{3h}) to trigonal pyramidal (C_{3v}). This mode of deformation affects the ^{11}B δ_{iso} appreciably (Fig. 3B), which moves monotonically to higher frequencies with increasing vertical out-of-plane displacement of the B atom. However, no significant changes in C_Q and η are observed (table S5). These results are consistent with the in situ high-pressure NMR spectra that demonstrate the high-frequency shift of ^{11}B δ_{iso} for the BO_3 site with increasing pressure, without any significant change in C_Q and η. Hence, the experimentally observed shift of 1.6 ppm/GPa for the BO_3 site in in situ high-pressure NMR indicates an average out-of-plane displacement of the B atom by ~0.26 Å/GPa, which would correspond to an increase in the average B-O distance of ~0.007 Å/GPa. This out-of-plane displacement of the central B atom in the BO_3 site is then fully reversible during compression-decompression cycle up to ~2 GPa (Fig. 1A).

Together, the NMR spectroscopy and DFT modeling results indicate that the elastic, out-of-plane

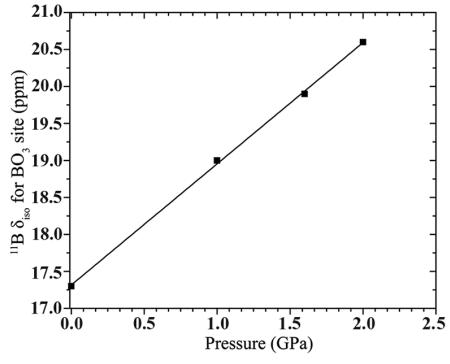

Fig. 2. Pressure change of ^{11}B NMR spectra. Variation of ^{11}B δ_{iso} for the BO_3 sites in Corning code 7059 glass with pressure as obtained from simulation of the ^{11}B wideline NMR spectra collected in situ at various pressures (see Fig. 1, A and B, and table S1). Solid line is a linear least-squares fit to the data points.

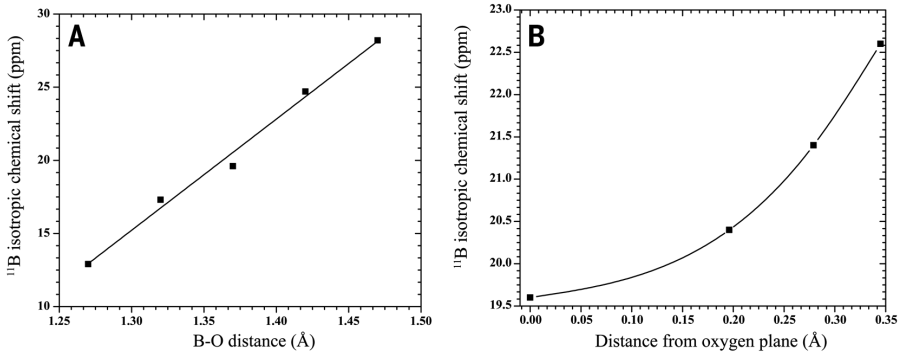

Fig. 3. Calculated change of model ^{11}B NMR parameters. (**A**) Variation of calculated ^{11}B δ_{iso} with B-O bond lengths in the H_3BO_3 molecule in model 1 (see text for details). Solid line is a linear least-squares fit to the data points. (**B**) Monotonic shift of calculated ^{11}B δ_{iso} to higher frequencies with increasing vertical out-of-plane displacement of the B atom in the H_3BO_3 molecule in model 3 (see text for details). Curved line through the data points is a guide to the eye only.

displacement of the central B atom in the BO_3 units best explains the pressure-induced changes observed in the in situ ^{11}B high-pressure NMR spectra. Although it may be counterintuitive at first to expect such anisotropic deformation of the BO_3 coordination environment under hydrostatic stress, an out-of-plane displacement of the B atom in the BO_3 unit is clearly a necessary step in its conversion into a BO_4 tetrahedron under pressure. The ultimate success of the $BO_3 \rightarrow BO_4$ coordination change must depend on the availability of a fourth oxygen atom in the structural neighborhood for bonding to the B atom, but the pressure-induced deformation of a BO_3 triangle into a trigonal pyramid clearly serves as a transition state for this conversion. Such pressure-induced displacement of the central B atom from the plane of the oxygen atoms is also expected to result in electric dipole moments in glass that can interact with light to strongly influence the photoelastic property (e.g., birefringence) of a borate glass (*17*). The application of in situ high-pressure solid-state NMR as a spectroscopic technique presents exciting opportunities in future in developing atomistic understanding of various stress-induced processes in amorphous materials.

REFERENCES AND NOTES

1. S. R. Elliott, *The Physics and Chemistry of Solids* (Wiley, New York, ed. 1, 1998).
2. G. N. Greaves, S. Sen, *Adv. Phys.* **56**, 1–166 (2007).
3. G. H. Wolf, P. F. McMillan, in *Structure, Dynamics and Properties of Silicate Melts*, J. F. Stebbins, P. F. McMillan, D. B. Dingwell, Eds., Reviews in Mineralogy, vol. 32 (Mineralogical Society of America, Washington, DC, 1995).
4. J. F. Stebbins, *Nature* **351**, 638–639 (1991).
5. S. Sen, Z. Xu, J. F. Stebbins, *J. Non-Cryst. Solids* **226**, 29–40 (1998).
6. S. Sen, *J. Non-Cryst. Solids* **253**, 84–94 (1999).
7. S. Sen, T. Topping, P. Yu, R. E. Youngman, Atomic-scale understanding of structural relaxation in simple and complex borosilicate glasses. *Phys. Rev. B* **75**, 094203 (2007).
8. S. S. Uzun, S. Sen, *J. Phys. Chem. B* **111**, 9758–9761 (2007).
9. L. Wondraczek, S. Sen, H. Behrens, R. E. Youngman, *Phys. Rev. B* **76**, 014202 (2007).
10. F. Angeli *et al*., *Phys. Rev. B* **85**, 054110 (2012).
11. F. Michel *et al*., *J. Non-Cryst. Solids* **379**, 169–176 (2013).
12. L.-S. Du, J. R. Allwardt, B. C. Schmidt, J. F. Stebbins, *J. Non-Cryst. Solids* **337**, 196–200 (2004).
13. Materials and methods are available as supplementary materials on *Science* Online.
14. G. L. Turner, K. A. Smith, R. J. Kirkpatrick, E. Oldfield, *J. Magn. Reson.* **67**, 544–550 (1986).
15. S. Kroeker, J. F. Stebbins, *Inorg. Chem.* **40**, 6239–6246 (2001).
16. S. Sen, *Mol. Simul.* **34**, 1115–1120 (2008).
17. M. Guignard, L. Albrecht, J. W. Zwanziger, *Chem. Mater.* **19**, 286–290 (2007).

ACKNOWLEDGMENTS

T. Edwards and S.S. were supported by a grant from the National Science Foundation (NSF-DMR 1104869). T. Endo was supported by a postdoctoral fellowship for research abroad by the Japan Society for Promotion of Science.

SUPPLEMENTARY MATERIALS

www.sciencemag.org/content/345/6200/1027/suppl/DC1
Materials and Methods
Figs. S1 to S5
Tables S1 to S5
References (*18*–*28*)

19 May 2014; accepted 15 July 2014
10.1126/science.1256224

STELLAR DISTANCES

A VLBI resolution of the Pleiades distance controversy

Carl Melis,[1]* Mark J. Reid,[2] Amy J. Mioduszewski,[3] John R. Stauffer,[4] Geoffrey C. Bower[5]

Because of its proximity and its youth, the Pleiades open cluster of stars has been extensively studied and serves as a cornerstone for our understanding of the physical properties of young stars. This role is called into question by the "Pleiades distance controversy," wherein the cluster distance of 120.2 ± 1.5 parsecs (pc) as measured by the optical space astrometry mission *Hipparcos* is significantly different from the distance of 133.5 ± 1.2 pc derived with other techniques. We present an absolute trigonometric parallax distance measurement to the Pleiades cluster that uses very long baseline radio interferometry (VLBI). This distance of 136.2 ± 1.2 pc is the most accurate and precise yet presented for the cluster and is incompatible with the *Hipparcos* distance determination. Our results cement existing astrophysical models for Pleiades-age stars.

Robust physical parameters for stars can only be obtained when an estimate of the distance to the object of interest exists. Trigonometric parallax, which uses the orbit of Earth around the Sun to inform the principle of triangulation, provides the most fundamental distance measurement outside of our solar system. High-precision tests of stellar physical models thus rely heavily on collections of parallax determinations. With reasonable physical models for nearby stars—and some mild assumptions about the homogeneity of classes of astrophysical objects throughout the universe [the Vogt-Russell theorem; see, e.g., (*1*, *2*)]—distance estimates for sources that lie beyond the current limit of trigonometric parallax can be systematically compiled. Such a methodology forms the basis of the cosmic distance ladder that elucidates the structure and evolution of the universe (*3*).

Clusters of coeval stars yield a solid foundation for tests of stellar physical models. Young open clusters are especially important because their stellar constituents define the "zero-age main sequence," the curve along which stable, core-hydrogen–burning stars reside in a color-magnitude diagram. Empirical isochrones developed from these young open clusters can be applied to other vastly more distant groups of stars (when brightness measurements of individual stars in the group can be made) to estimate their distance, thus providing structural information for the galaxies that contain them (*4*, *5*). The Pleiades open cluster of stars is critical for such studies because its relatively young age places many of its stars on the zero-age main sequence. It is the closest cluster to Earth of its age and richness of stars and thus lends itself to highly detailed investigations. One would expect that all astrophysical parameters for such an important sample of stars would be well characterized. However, there still rages an open debate regarding the distance to the Pleiades.

Figure 1 summarizes distances obtained for the Pleiades cluster to date, including the new measurement described here. As can be seen, most measurements are in rough agreement with that produced in this work, with the stark exception of the *Hipparcos* astrometric satellite distances. For a single object near the distance of the Pleiades, *Hipparcos* was not capable of producing a distance measurement with accuracy better than 10%. However, by taking the aggregate of many cluster members, *Hipparcos* was able to achieve a Pleiades parallax with roughly 1% precision (*6*, *7*). In almost any other case, one would simply discard the disagreeable *Hipparcos* cluster distances as bad measurements, but the *Hipparcos* mission represents the most complete astrometric survey of the sky and of the Pleiades cluster to date. It provides a path that is free of stellar physical models to obtaining the cluster distance and combines more than 50 cluster-member distance measurements. Other methods either include at most several cluster members in their distance determination, rely heavily on physical models to obtain a cluster distance (whereas it should be the distance measurement that informs the development of physical models), or result in large uncertainties in the cluster distance.

Although the discrepancy between *Hipparcos* and the average non-*Hipparcos* distance (Fig. 1) amounts to a 10% difference, the resultant changes to physical models needed to obtain agreement with the *Hipparcos* value are quite significant.

[1]University of California, San Diego, Center for Astrophysics and Space Sciences, 9500 Gilman Drive, La Jolla, CA 92093-0424, USA. [2]Harvard-Smithsonian Center for Astrophysics, 60 Garden Street, Cambridge, MA 02138, USA. [3]National Radio Astronomy Observatory, Array Operations Center, 1003 Lopezville Road, Socorro, NM 87801, USA. [4]Spitzer Science Center (SSC), 1200 East California Boulevard, California Institute of Technology, Pasadena, CA 91125, USA. [5]Academia Sinica Institute of Astronomy and Astrophysics (ASIAA), 645 North A'ohoku Place, Hilo, HI 96720, USA.
*Corresponding author. E-mail: cmelis@ucsd.edu

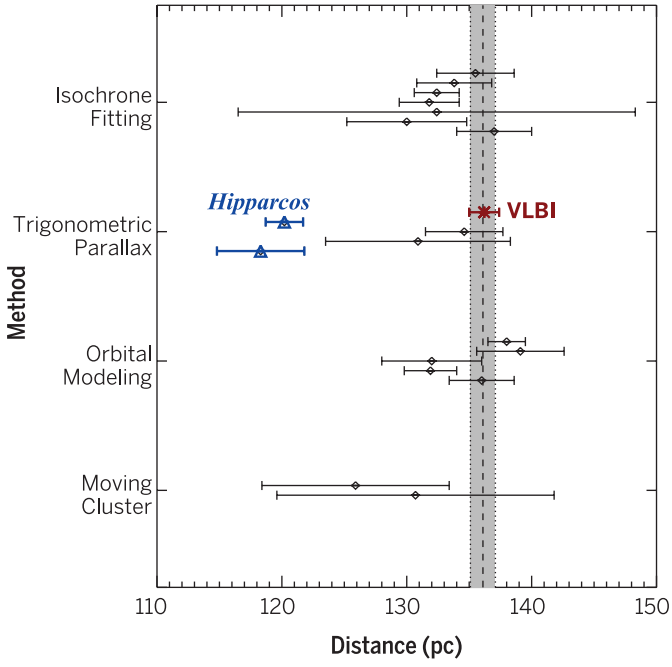

Fig. 1. Pleiades cluster distances. Summary of Pleiades distances obtained through various methods. The red asterisk with a distance of 136.2 ± 1.2 pc is the new VLBI determination. The blue triangles near 120 pc are from two reductions of the *Hipparcos* data (*6*, *7*). The vertical dashed line with uncertainty range shown by dotted lines and filled in with gray is the cluster distance derived from non-*Hipparcos* trigonometric parallaxes and binary orbits. All plotted errors are ±1 SD. References for the distances shown, from top to bottom for each category, are as follows: isochrone fitting—An *et al*. (*4*), Percival *et al*. (*19*), Stello and Nissen (*20*), Pinsonneault *et al*. (*5*), Giannuzzi (*21*), van Leeuwen (*22*), and Nicolet (*23*); trigonometric parallax (excluding *Hipparcos* and VLBI)—Soderblom *et al*. (*8*) and Gatewood *et al*. (*10*); orbital modeling—Groenewegen *et al*. (*11*), Southworth *et al*. (*24*), Zwahlen *et al*. (*12*), Munari *et al*. (*25*), and Pan *et al*. (*26*); moving cluster—Röser and Schilbach (*27*) and Narayanan and Gould (*13*).

One such change requires a 20 to 40% increase in the amount of helium (He) that Pleiades stars are composed of (*5*), a change that throws into question any attempt to systematically apply model isochrones to groups of stars that have not been characterized in great detail, because one typically only has brightness measurements at a few wavelengths. (Making compositional measurements is extremely resource expensive, and He measurements in particular are difficult. He measurements to date suggest that stars formed in the recent Galactic history have similar He abundances.) A more disconcerting explanation invokes different, unknown physics for young stars of roughly Pleiades-age (*6*), thus challenging our general understanding of the star-formation and evolution process. As a result, the controversy surrounding the distance to the Pleiades has not subsided. On the contrary, it has grown as each side of the debate has exchanged their own views and neither side has backed down (*7*, *8*).

Given the disagreement between parallax measurements using a similar methodology (relative astrometry in the optical wavelengths), we pursued a new approach that could provide an independent view on Pleiades cluster distance measurements made to date. Our approach uses radio astrometry (*9*), a technique that provides an absolute distance measurement via referencing to an essentially stationary (to within our measurement capabilities) quasistellar object (an actively accreting supermassive black hole in the distant universe). To achieve sufficient precision (better than 0.0001 seconds of arc) in stellar position measurements, we made observations using an array of widely separated radio antennas that when acting in concert give the resolution of a telescope the size of Earth. The very long baseline interferometry (VLBI) array employed by our study uses the Very Long Baseline Array (VLBA) as its core and additionally incorporates the Robert C. Byrd Green Bank Telescope, the Effelsberg Radio Telescope, and the William E. Gordon Telescope at Arecibo Observatory for enhanced resolution and sensitivity. Four Pleiades star systems were observed with this array over a period of ~1.5 years to completely map their parallax motion (tables S1 to S5 and Fig. 2). Model fits to the motion of each star on the plane of the sky produce the desired parallax measurement (Table 1). The measured distances and ±1 SD errors for the four systems are 134.8 ± 0.5 pc (HII 174), 138.4 ± 1.1 pc (HII 625), 135.5 ± 0.6 pc (HII 1136), and 136.6 ± 0.6 pc (HII 2147 system). Of note is the <1% accuracy for the individual object VLBI distance measurements.

Already evident in each individual stellar distance measurement for our sample is gross disagreement with the *Hipparcos* cluster distance. To derive the cluster absolute parallax, however, one must include with the measurements of the individual stars the additional uncertainty of each star's position with respect to the center of the cluster. We adopt the approach of Soderblom *et al*. (*8*) of using the 1-σ angular dispersion of the cluster as the systematic cluster-depth uncertainty. For an assumed Pleiades distance of 130 pc and cluster dispersion of 1°, we estimate the cluster-depth uncertainty to be 2.3 pc and add this value in quadrature to each object's formal distance uncertainty. This additional error component dominates the final cluster-distance uncertainty. When averaging individual VLBI measured distances to arrive at the final cluster distance, we treat HII 2147 as a single system and use the average of the distance measurements for HII 2147 NE and SW as given above. In this way, we calculate the VLBI-measured Pleiades cluster distance to be 136.2 ± 1.2 pc (±1 SD).

An important aspect of this independent VLBI distance measurement is that it validates previous non-*Hipparcos* parallax and binary orbit distance measurements. As such, we can combine all parallax (including VLBI) and binary orbit distances into a single non-*Hipparcos* cluster distance; this sample includes 17 individual Pleiades star systems. Due to their fitting techniques, which result in coupled individual Pleiades member parallaxes, we treat each of the distance measurements of Soderblom *et al*. (*8*) and Gatewood *et al*. (*10*) as a single system measurement similar to the case of HII 2147 above. Each of the VLBI individual parallaxes, the two binary orbit distances (*11*, *12*), and the distances of Soderblom *et al*. (*8*) and Gatewood *et al*. (*10*) are combined with a weighted mean. In deriving the combined cluster distance and associated uncertainty, cluster-depth uncertainty is added in quadrature to the uncertainty of each system distance measurement. From this, we obtain a non-*Hipparcos* Pleaides cluster distance of 136.1 ± 1.0 pc (the vertical gray band in Fig. 1; this value is nearly identical to the VLBI-measured cluster distance because the VLBI parallaxes have the smallest uncertainty and hence carry the most weight).

Our results conclusively show that the *Hipparcos*-measured distance to the Pleiades cluster is in error. The general agreement of our distance measurement with those distances obtained by isochrone fitting in Fig. 1 suggests that physical models provide an accurate representation of the properties of Pleiades-age stars and that no unusual compositions or unknown physics lurk within this canonical cluster. Although this is likely a great relief for modelers of stars, it raises further questions into what happened with *Hipparcos*. Whatever error that manifested itself as a significantly skewed distance to the Pleiades cluster remains at large [some have suggested possible explanations; see, e.g., (*13*, *14*)]. The unrecognized nature of such an error is especially dangerous when one considers that *Gaia* (*15*), the successor to *Hipparcos* and very similar in design, is just now starting its Galaxy-mapping mission. If the unrecognized *Hipparcos* error has crept into the Gaia pipeline, how would it manifest itself (if it does)? VLBI distance measurements like those presented here will serve as an important cross-check of the *Gaia* output near its predicted precision limits.

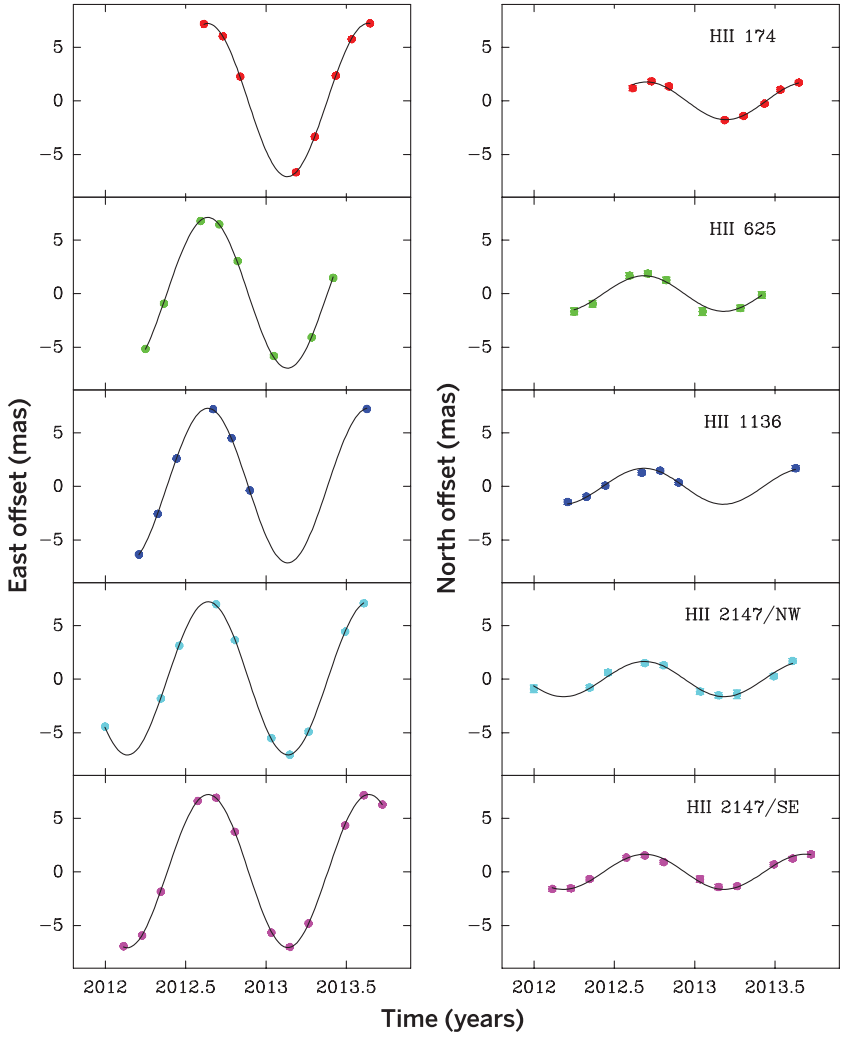

Fig. 2. VLBI Pleiad parallaxes. Parallax fits to VLBI position measurements and associated random errors (±1 SD) for five Pleiades stars, including both components of the HII 2147 binary system. For each object, the solid line is the best-fitting astrometric model that includes proper motion and parallax; the proper motion has been removed in the data points to accentuate the parallax motion. For each component of the HII 2147 binary system and for HII 1136, we additionally include acceleration terms in our fit to model short segments of a binary orbit. (The average angular separation between the two stars of the HII 2147 system over the monitoring period reported in tables S4 and S5 is ≈60 milliarcseconds (mas) or ≈8.2 astronomical units in projection). The left-hand panel curves and data points show east (right ascension times cos(declination)) angular offsets on the sky of the source position relative to a distant quasar. The right-hand panel curves and data points show north (declination) offsets. Each source is color-coded and labeled in the declination panels.

Table 1. Fitted astrometric parameters. For each object in our sample, we conducted astrometric fits to the measured positions to extract stellar parallaxes. Only data taken in 2012–2013 were used for HII 1136 to ensure consistent and readily comparable results. Measured positions are modeled with the sum of a parallax sinusoid (determined by the parallax magnitude, π, and the purely geometrical motion for a given part of the sky induced by Earth's orbit), a reference position at an arbitrarily chosen fixed epoch, and a linear or accelerated proper motion ($\mu_\alpha\cos\delta$, μ_δ, $a_\alpha\cos\delta$, and a_δ). [Acceleration terms account for binary motion when the orbital period is much larger than the time frame over which the system was monitored and have been successfully used in past attempts to measure system parallaxes; see (*16*).] This results in five or seven fitted model parameters. During the fitting process, the data are weighted using the quadrature sum of the formal measured fit uncertainties and an additional component that represents systematic uncertainties. A least-squares fitting routine determines the parameters that minimize the sum of the squares of the residuals. This process allows the systematic error component to be adjusted as necessary to obtain a χ^2 equal to 1 for each of the right ascension and declination data. The fitted proper motions can be compared with the values shown in the second and third columns that were previously determined from optical measurements. All uncertainties are ±1 SD.

Source Name	Optical proper motions (*17*, *18*)		Fitted parameters					
	$\mu_\alpha\cos\delta$ (mas year^{-1})	μ_δ (mas year^{-1})	π (mas)	$\mu_\alpha\cos\delta$ (mas year^{-1})	μ_δ (mas year^{-1})	$a_\alpha\cos\delta$ (mas year^{-2})	a_δ (mas year^{-2})	χ^2
HII 174	22.0 ± 2.0	−45.7 ± 2.1	7.418 ± 0.025	19.86 ± 0.05	−45.41 ± 0.16	–	–	1.018
HII 625	20.0 ± 2.0	−47.9 ± 6.9	7.223 ± 0.057	19.47 ± 0.11	−44.39 ± 0.27	–	–	1.002
HII 1136	17.3 ± 0.7	−44.8 ± 1.8	7.382 ± 0.031	17.18 ± 0.05	−47.39 ± 0.24	−0.43 ± 0.16	0.6 ± 0.8	0.941
HII 2147 NW	17.1 ± 1.0	−45.4 ± 0.7	7.328 ± 0.035	23.22 ± 0.05	−46.76 ± 0.16	1.73 ± 0.19	−3.9 ± 0.7	1.008
HII 2147 SE			7.319 ± 0.027	14.05 ± 0.04	−42.24 ± 0.11	−1.05 ± 0.18	2.0 ± 0.5	0.982

REFERENCES AND NOTES

1. H. L. Johnson, *Astrophys. J.* **126**, 121 (1957).
2. R. J. Trumpler, *Lick Obs. Bull.* **14**, 154–188 (1930).
3. I. N. Reid, *Annu. Rev. Astron. Astrophys.* **37**, 191–237 (1999).
4. D. An *et al.*, *Astrophys. J.* **655**, 233–260 (2007).
5. M. H. Pinsonneault, J. R. Stauffer, D. R. Soderblom, J. R. King, R. B. Hanson, *Astrophys. J.* **504**, 170–191 (1998).
6. F. van Leeuwen, *Astron. Astrophys.* **341**, L71 (1999).
7. F. van Leeuwen, *Astron. Astrophys.* **497**, 209–242 (2009).
8. D. R. Soderblom *et al.*, *Astron. J.* **129**, 1616–1624 (2005).
9. M. J. Reid, M. Honma, *Annu. Rev. Astron. Astrophys* (2014); available at http://arxiv.org/abs/1312.2871.
10. G. Gatewood, J. K. de Jonge, I. Han, *Astrophys. J.* **533**, 938–943 (2000).
11. M. A. T. Groenewegen, L. Decin, M. Salaris, P. De Cat, *Astron. Astrophys.* **463**, 579–587 (2007).

12. N. Zwahlen *et al.*, *Astron. Astrophys.* **425**, L45–L48 (2004).
13. V. K. Narayanan, A. Gould, *Astrophys. J.* **523**, 328–339 (1999).
14. V. V. Makarov, *Astron. J.* **124**, 3299–3304 (2002).
15. M. A. C. Perryman *et al.*, *Astron. Astrophys.* **369**, 339–363 (2001).
16. L. Loinard *et al.*, *Astrophys. J.* **671**, 546–554 (2007).
17. E. Høg *et al.*, *Astron. Astrophys.* **355**, L27–L30 (2000).
18. N. Zacharias *et al.*, *Astron. J.* **145**, 44 (2013).
19. S. M. Percival, M. Salaris, M. A. T. Groenewegen, *Astron. Astrophys.* **429**, 887–894 (2005).
20. D. Stello, P. E. Nissen, *Astron. Astrophys.* **374**, 105–115 (2001).
21. M. A. Giannuzzi, *Astron. Astrophys.* **293**, 360 (1995).
22. F. van Leeuwen, The Pleiades, an astrometric and photometric study of an open cluster. Thesis, Leiden University, Leiden, Netherlands (1983).
23. B. Nicolet, *Astron. Astrophys.* **104**, 185 (1981).
24. J. Southworth, P. F. L. Maxted, B. Smalley, *Astron. Astrophys.* **429**, 645–655 (2005).
25. U. Munari *et al.*, *Astron. Astrophys.* **418**, L31–L34 (2004).
26. X. Pan, M. Shao, S. R. Kulkarni, *Nature* **427**, 326–328 (2004).
27. S. Röser, E. Schilbach, A new assessment of the kinematic distance to the Pleiades: based on radial velocities and proper motions only, *Proc. IAU Symp.* **289**, 66 (2013).

ACKNOWLEDGMENTS

We thank the National Radio Astronomy Observatory, Green Bank Telescope, Arecibo Observatory, and Effelsberg Telescope staff who coordinated, conducted, and correlated observations for this project. All data presented in this paper are maintained in the National Radio Astronomy Observatory archive. The National Radio Astronomy Observatory is a facility of the National Science Foundation operated under cooperative agreement by Associated Universities, Inc. This work made use of the Swinburne University of Technology software correlator, developed as part of the Australian Major National Research Facilities Programme and operated under license. C.M. acknowledges financial support from the U.S. National Science Foundation through awards AST-1313428 and AST-1003318, from a Lawrence Livermore National Laboratory minigrant to the University of California–Los Angeles, and from the Spitzer Science Center Visiting Graduate Student Program. G.C.B. acknowledges support from the Academica Sinica Institute for Astronomy and Astrophysics.

SUPPLEMENTARY MATERIALS

www.sciencemag.org/content/345/6200/1029/suppl/DC1
Supplementary Text
Tables S1 to S5
References (*28*–*33*)

15 May 2014; accepted 23 July 2014
10.1126/science.1256101

CIRCUMSTELLAR DISKS

Large impacts around a solar-analog star in the era of terrestrial planet formation

Huan Y. A. Meng,[1] Kate Y. L. Su,[2] George H. Rieke,[1,2] David J. Stevenson,[3] Peter Plavchan,[4,5] Wiphu Rujopakarn,[2,6,7] Carey M. Lisse,[8] Saran Poshyachinda,[9] Daniel E. Reichart[10]

The final assembly of terrestrial planets occurs via massive collisions, which can launch copious clouds of dust that are warmed by the star and glow in the infrared. We report the real-time detection of a debris-producing impact in the terrestrial planet zone around a 35-million-year-old solar-analog star. We observed a substantial brightening of the debris disk at a wavelength of 3 to 5 micrometers, followed by a decay over a year, with quasi-periodic modulations of the disk flux. The behavior is consistent with the occurrence of a violent impact that produced vapor out of which a thick cloud of silicate spherules condensed that were then ground into dust by collisions. These results demonstrate how the time domain can become a new dimension for the study of terrestrial planet formation.

Circumstellar disks are where planetary systems form and evolve. Gas-rich and optically thick protoplanetary disks are born together with young stars but dissipate within a few million years (My), setting the time scale for gas-giant planet formation (*1*). Dusty, optically thin debris disks then emerge, sustained by the fragmentation of colliding planetesimals (*2*). They are warmed by their stars and light up in the infrared (IR), allowing them to be detected over the entire lifetimes of main-sequence stars. Consequently, debris disks are ideal tools in which to search for phases occurring in other planetary systems that are analogous to major events in the evolution of the solar system, such as the formation of terrestrial planets. Dynamical simulations and meteoritics indicate that the end stage of terrestrial planet formation, from ~30 to ~100 My (*3, 4*), is marked by frequent large impacts, up to the scale of the one leading to the formation of the Moon (*5*–*7*). Such events can produce a huge amount of dust, which may dramatically increase the IR emission from the debris disk (*8*).

ID8 (2MASS J08090250-4858172) is a young solar-analog star, with spectral type G6V and solar metallicity, in the 35-My-old open star cluster NGC 2547 (*9*). It emits strongly in the IR, with a fractional disk luminosity of $L_{disk}/L_* = 3.2 \times 10^{-2}$ (L_*, stellar luminosity) (*10*). The mid-IR spectrum of ID8 (observed in 2007) shows strong crystalline silicate features between 8 and 30 μm, indicative of very fine dust particles (Fig. 1); models of the observed spectral energy distribution (SED) require submicrometer-sized amorphous silicate dust particles as well (*10*). Particles are blown out by radiation pressure and are lost to the system if the ratio of radiation to gravitational forces is larger than 0.5. For ID8, the critical radius (*11*) below which nonporous silicate grains are lost is ~0.5 μm. The tiniest particles in the disk are smaller than this limit, suggesting ongoing dust replenishment in the system.

The disk emission was recently found to vary on a yearly time scale (*8*). Collisional cascades among planetesimals sustain most debris disks. However, variations this rapid cannot be supported by this means, because the cascade time scales for significant variations in dust production are at least a few hundred orbits (*8*). To explore the origin of the variations, we have used the Infrared Array Camera [IRAC (*12*)] onboard the Spitzer Space Telescope to monitor the ID8 system. The observations extended from 25 May 2012 to 23 August 2013, providing a total time baseline of 454 days, with a 157-day gap between visibility windows. At the same time, intensive optical monitoring of ID8 was obtained from the ground in the V and Cousins I bands, where we found that the output of the star is stable within ~1.5% root mean square (supplementary text).

Because the stellar contribution is effectively constant in time, we fitted its spectrum and removed it from the total (star + disk) IR fluxes to obtain the light curves of the debris disk, as shown in Fig. 2. This revealed an average disk color of [3.6] – [4.5] = 1.00, corresponding to a blackbody temperature of 730 K, which is consistent with the temperatures found in previous analyses of the mid-IR spectroscopy (*10*). We calculated the expected color trend of the entire ID8 system for possible causes of the disk variations and compared it with our data. The result is not conclusive within the errors, but suggests that a combination of changing dust temperature and dust-emitting

[1]Lunar and Planetary Laboratory and Department of Planetary Sciences, University of Arizona, 1629 East University Boulevard, Tucson, AZ 85721, USA. [2]Steward Observatory and Department of Astronomy, University of Arizona, 933 North Cherry Avenue, Tucson, AZ 85721, USA. [3]Division of Geological and Planetary Sciences, California Institute of Technology, MC 170-25, 1200 East California Boulevard, Pasadena, CA 91125, USA. [4]NASA Exoplanet Science Institute, California Institute of Technology, MC 100-22, 770 South Wilson Avenue, Pasadena, CA 91125, USA. [5]Missouri State University, 901 South National Avenue, Springfield, MO 65897, USA. [6]Department of Physics, Faculty of Science, Chulalongkorn University, 254 Phayathai Road, Pathumwan, Bangkok 10330, Thailand. [7]Kavli Institute for the Physics and Mathematics of the Universe (WPI), Todai Institute for Advanced Study, University of Tokyo, 5-1-5 Kashiwanoha, Kashiwa, 277-8583, Japan. [8]Space Department, Applied Physics Laboratory, Johns Hopkins University, 11100 Johns Hopkins Road, Laurel, MD 20723, USA. [9]National Astronomical Research Institute of Thailand (Public Organization), Ministry of Science and Technology, 191 Siriphanich Building, Huay Kaew Road, Muang District, Chiang Mai 50200, Thailand. [10]Department of Physics and Astronomy, Campus Box 3255, University of North Carolina at Chapel Hill, Chapel Hill, NC 27599, USA.

area, or in area alone rather than purely in temperature, may be responsible for the disk variations (supplementary text).

In the following analysis, we focus on the 4.5-μm data where we have observations from both years, and the disk is measured at a higher signal-to-noise ratio. The data at 3.6 μm show consistent behavior, although at lower signal-to-noise ratio. In 2012, the disk flux density stayed

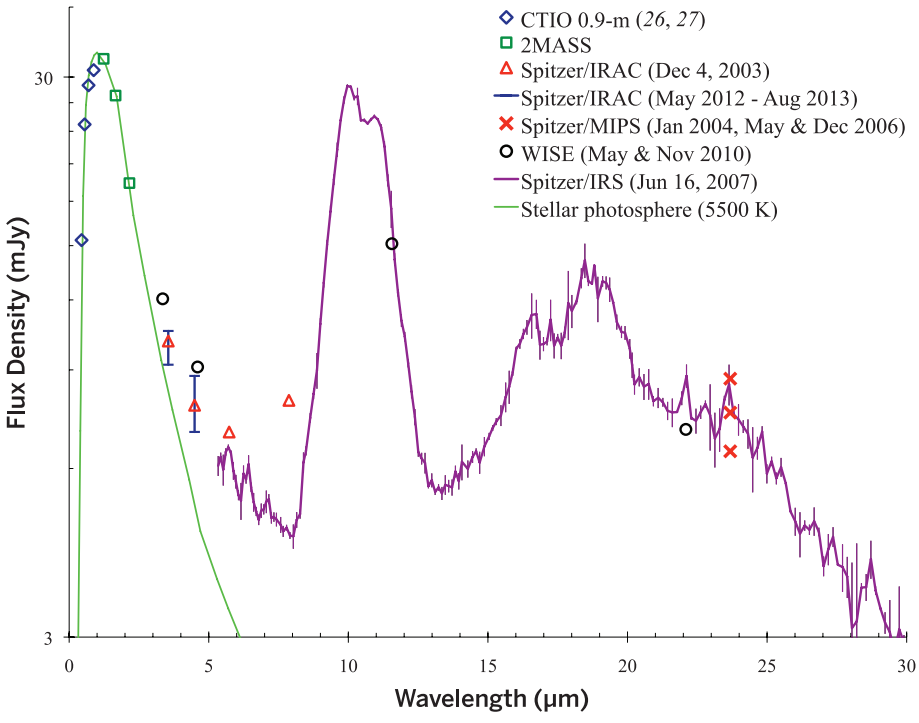

Fig. 1. Spectrum of the ID8 system. The photometric errors are smaller than the symbol size and are not shown; errors of the Spitzer/IRS spectrum are indicated as vertical lines. Red crosses at 24 μm show the three epochs of Spitzer/MIPS observations that led to the discovery of disk variability (*8*). The ranges of the new measurements at 3.6 and 4.5 μm in this work are plotted as blue vertical lines. CTIO, Cerro Tololo Inter-American Observatory; 2MASS, 2 Micron All Sky Survey; MIPS, Multiband Imaging Photometer for Spitzer; IRS, Infrared Spectrograph; WISE, Wide-field Infrared Survey Explorer.

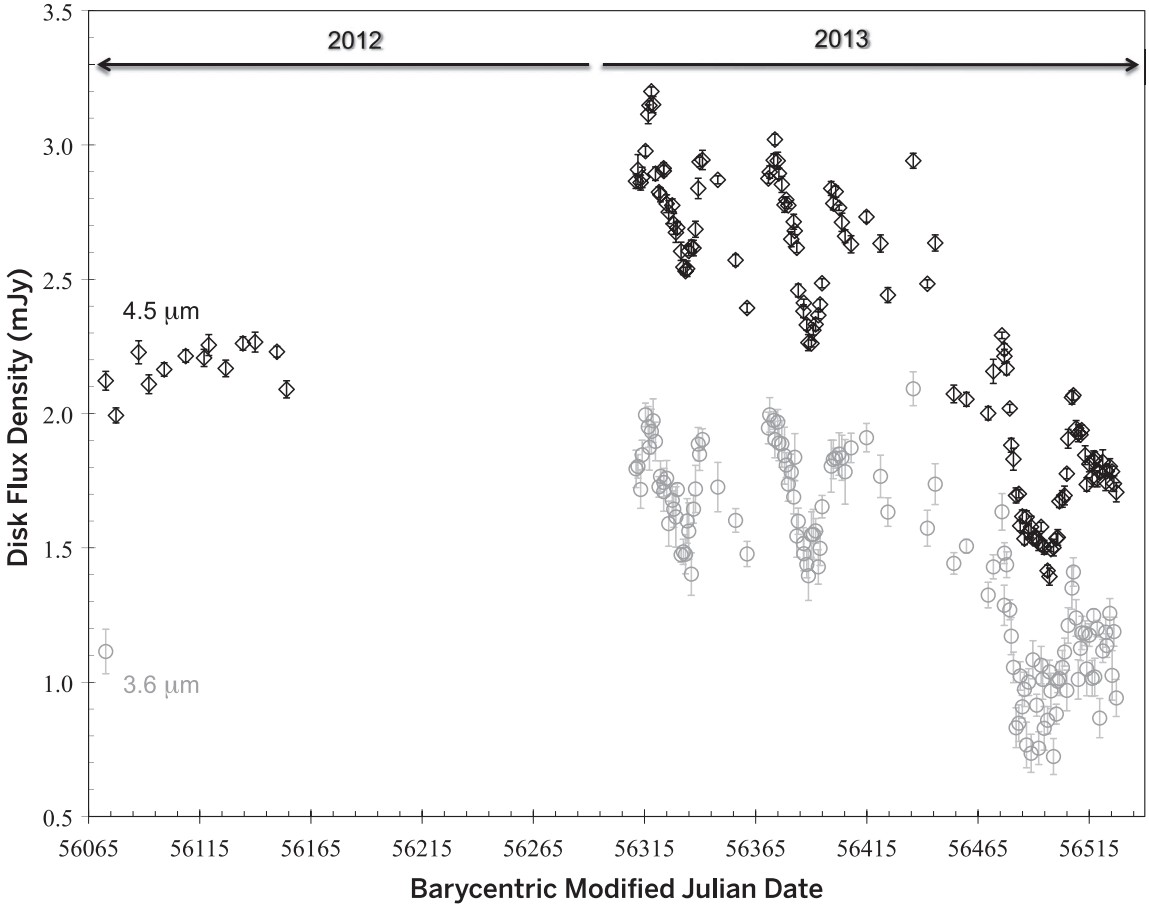

Fig. 2. Light curves of the debris disk of ID8 at 3.6 and 4.5 μm, assuming no error in photosphere subtraction. The gap between Barycentric Modified Julian Date (BMJD) 56155 and 56311 occurred when ID8 was outside of the Spitzer visibility windows.

near 2.2 milli-Jansky (mJy), despite ~10% variations. However, at the start of 2013 it had brightened to above 3.0 mJy, indicating a significant increase in the amount of dust, probably from a new impact before 2013. This elevated level then decayed throughout 2013. An exponential fit suggests a decay time scale of ~370 days at both wavelengths. This is too fast to be reconciled with decades-long collisional cascades (*8*) and is too slow for the direct radiative blowout of tiny particles, which should take <30 days at the orbit derived below for the disk.

To better understand the impact, we estimate the disk mass based on a fit to the entire mid-IR spectrum, which is dominated by small grains. Because the new debris in the disk has not reached equilibrium in a full collisional cascade, we could not make the conventional assumption of a power-law size distribution. For emitting grains of 0.5 μm in radius, we found a disk mass of 1.1×10^{19} kg, which is a lower limit because it ignores larger particles. An independent estimate assuming a power-law grain size distribution up to 1 mm obtains an identical mass estimate (*10*). This mass, if the grains were compacted into a solid body, is equivalent to an ~180-km-diameter asteroid (of density 3700 kg m^{-3}). Given the estimated mass and particle size, the ID8 disk may be optically thick, in which significant mass could be obscured and unseen.

Considering the decay in 2013, and assuming it applies to the full spectrum, we estimated the mass loss rate to be at least 10^{11} kg s^{-1}. The spectrum was obtained in 2007; however, the Spitzer and WISE photometric points (Fig. 1) imply that the mid-IR spectrum had a similar shape at least from January 2004 through November 2010. That is, it appears that the small grains, with a net volume of an ~180-km-diameter asteroid, were lost from the system and would have to be replenished on a decadal (or shorter) time scale to maintain the mid-IR spectrum. Though arising from different physical processes, the mass loss rate is five to seven orders of magnitude greater than the dust mass loss rates of comets Hale-Bopp (*13*) and Halley (*14*), which are among the dustiest comets known in the solar system, and is three orders of magnitude greater than that of the evaporating planet KIC 12557548b (*15*).

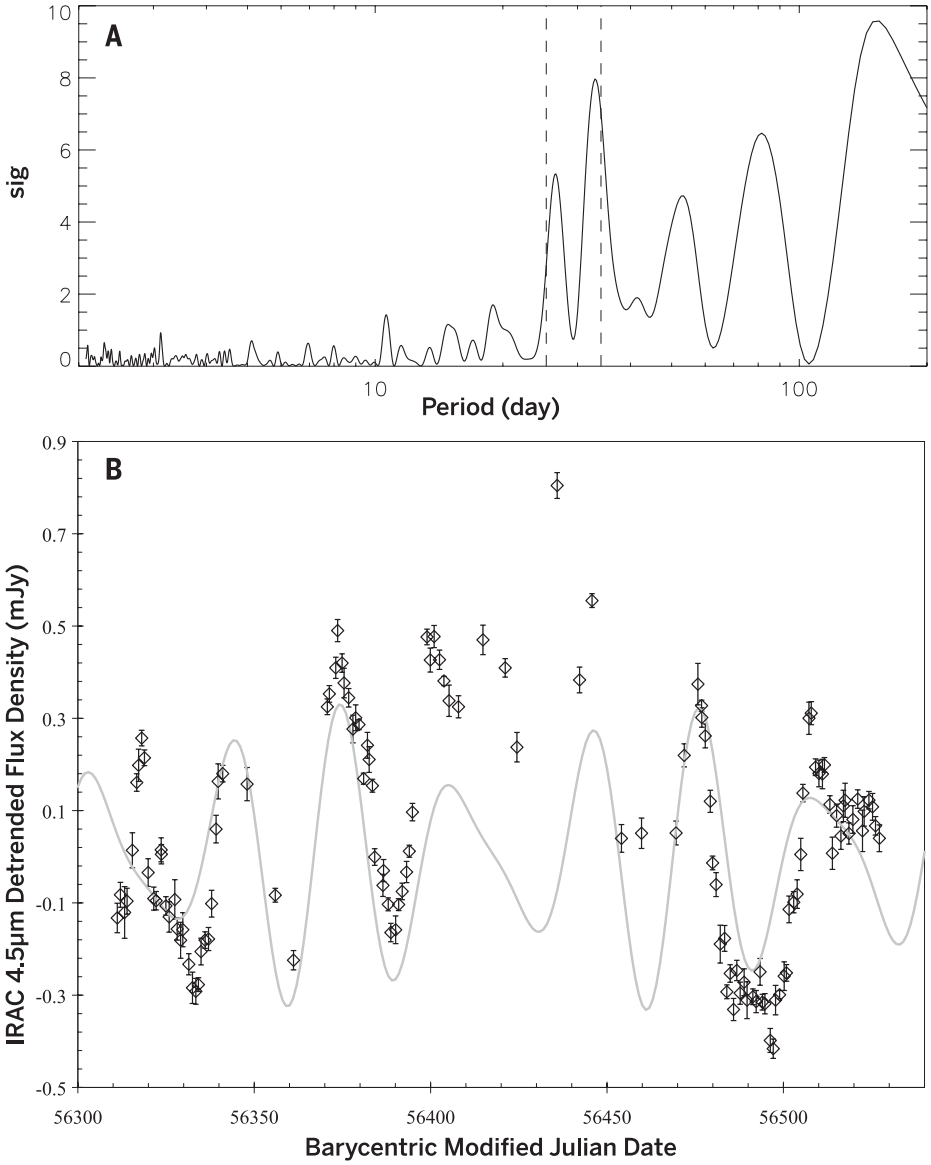

Fig. 3. Analysis of the 4.5-μm time series of the ID8 disk. (**A**) **Periodogram of the detrended 2013 light curve.** The vertical dashed lines represent the identified periods P_1 and P_2, which are determined after removing the strongest frequency in each iteration (*22*) and thus appear slightly offset from the raw peak positions. (**B**) Detrended 4.5-μm data (black diamonds) with the composite of two sine waves of P_1 and P_2 (gray curve). Because their real waveforms are probably nonsinusoidal, the comparison is meaningful only for the general timing of the highs and lows.

The variability of the IR emission of ID8 is much too fast to arise in a conventional debris disk sustained by a collisional cascade (*8*). We hypothesize that the impact responsible for the increased disk emission in 2013 involved two large bodies and was sufficiently violent to yield a silica-rich vapor plume. Glassy silicate spherules will condense from the vapor with diverse forms (*16*), consistent with the presence of amorphous silicates in the SED model (*10*). In this case, there may have been temporal spectral features after the new impact, but they would have been missed because we do not have a new mid-IR spectrum in 2013. The condensation process has been modeled in (*17*), which shows that the typical spherule size depends sensitively on the circumstances of the impact, particularly its velocity, but ranges from about 10 μm to 1 mm. The condensates are produced quickly over several hours. Initially, the cloud of spherules will not radiate efficiently in the mid-IR, because the total surface area of all the spherules is small. However, they will break each other down through collisions, which generate the observed micrometer-sized or smaller particles as daughter products. The IR output will rise as the mass is distributed into many small grains, making the consequences of the initial impact visible as an increase in the IR emission.

Because the size distribution of condensate spherules is strongly peaked around the average (*17*), we treat them as being equal in size. Then a rough estimate of the time scale for destroying them (and hence for the decay of the debris cloud) can be obtained by attributing all the disk mass to them immediately after the impact and assuming that they are removed by breakdown in a collisional cascade with eventual ejection, when their daughter particles are submicrometer in size, by radiation pressure. We found that different models for the destruction rate of such spherules give consistent time scales (*18*, *19*). To order of magnitude, the range of decay time scales as a function of spherule size from 10 to 1000 μm is 100 days to 10 years. The observed decay time of the ID8 disk corresponds to a spherule size of ~100 μm, which corresponds to an impact velocity of 15 to 18 km s^{-1} [for a body with a diameter of 100 to 1000 km impacting on an even larger one (*17*)]. Thus, the 1-year exponential decay time scale is a natural result for a system where seed grains have condensed from a vapor cloud and are destroying themselves through

collisions. An analysis with some similarities to ours for the bright debris disk of HD 172555 (*20*) found that dust created in a hypervelocity impact will have a size slope of ~ −4, in agreement with the fits of (*10*) to the IR spectrum of ID8.

After the exponential decay is removed from the data ("detrending"), the light curves at both wavelengths appear to be quasi-periodic. The regular recovery of the disk flux and lack of extraordinary stellar activity essentially eliminate coronal mass ejection (*21*) as a possible driver of the disk variability. We employed the SigSpec algorithm (*22*) to search for complex patterns in the detrended, post-impact 2013 light curve. The analysis identified two significant frequencies with comparable amplitudes, whose periods are P_1 = 25.4 ± 1.1 days and P_2 = 34.0 ± 1.5 days (Fig. 3A) and are sufficient to qualitatively reproduce most of the observed light curve features (Fig. 3B). The quoted uncertainties (*23*) do not account for systematic effects due to the detrending and thus are lower limits to the real errors. Other peaks with longer periods in the periodogram are aliases or possibly reflect long-term deviation from the exponential decay. These artifacts make it difficult to determine whether there are weak real signals near those frequencies.

We now describe the most plausible interpretation of this light curve that we have found. The two identified periods have a peak-to-peak amplitude of ~6×10^{-3} in fractional luminosity, which provides a critical constraint for models of the ID8 disk. In terms of sky coverage at the disk distance inferred from the IR SED, such an amplitude requires the disappearance and reappearance every ~30 days of the equivalent of an opaque, stellar-facing "dust panel" of radius ~110 Jupiter radii. One possibility is that the disk flux periodicity arises from recurring geometry that changes the amount of dust that we can see. At the time of the impact, fragments get a range of kick velocities when escaping into interplanetary space. This will cause Keplerian shear of the cloud (*24*), leading to an expanding debris concentration along the original orbit (supplementary text). If the ID8 planetary system is roughly edge-on, the longest dimension of the concentration will be parallel to our line of sight at the greatest elongations and orthogonal to the line of sight near conjunctions to the star. This would cause the optical depth of the debris to vary within an orbital period, in a range on the order of 1 to 10 according to the estimated disk mass and particle sizes. Our numerical simulations of such dust concentrations on moderately eccentric orbits are able to produce periodic light curves with strong overtones. P_2 and P_1 should have a 3:2 ratio if they are the first- and second-order overtones of a fundamental, which is consistent with the measurements within the expected larger errors (<2σ or better). In this case, the genuine period should be 70.8 ± 5.2 days (lower-limit errors), a value where it may have been submerged in the periodogram artifacts. This period corresponds to a semimajor axis of ~0.33 astronomical units, which is consistent with the temperature and distance suggested by the spectral models (*10*).

Despite the peculiarities of ID8, it is not a unique system. In 2012 and 2013, we monitored four other "extreme debris disks" (with disk fractional luminosity ≥10^{-2}) around solar-like stars with ages of 10 to 120 My. Various degrees of IR variations were detected in all of them. The specific characteristics of ID8 in the time domain, including the yearly exponential decay, additional more rapid weekly to monthly changes, and color variations, are also seen in other systems. This opens up the time domain as a new dimension for the study of terrestrial planet formation and collisions outside the solar system. The variability of many extreme debris disks in the era of the final buildup of terrestrial planets may provide new possibilities for understanding the early solar system and the formation of habitable planets (*25*).

REFERENCES AND NOTES

1. R. Helled *et al.*, in *Protostars and Planets VI*, H. Beuther, R. Klessen, C. Dullemond, T. Henning, Eds. (Univ. of Arizona Press, Tucson, AZ, 2014), in press; available at http://arxiv.org/abs/1311.1142.
2. M. C. Wyatt, *Annu. Rev. Astron. Astrophys.* **46**, 339–383 (2008).
3. K. Righter, D. P. O'Brien, *Proc. Natl. Acad. Sci. U.S.A.* **108**, 19165–19170 (2011).
4. S. N. Raymond, E. Kokubo, A. Morbidelli, R. Morishima, K. J. Walsh, in *Protostars and Planets VI*, H. Beuther, R. Klessen, C. Dullemond, T. Henning, Eds. (Univ. of Arizona Press, Tucson, AZ, 2014), in press; available at http://arxiv.org/abs/1312.1689.
5. R. M. Canup, *Annu. Rev. Astron. Astrophys.* **42**, 441–475 (2004).
6. M. Ćuk, S. T. Stewart, *Science* **338**, 1047–1052 (2012).
7. R. M. Canup, *Science* **338**, 1052–1055 (2012).
8. H. Y. A. Meng *et al.*, *Astrophys. J.* **751**, L17–L21 (2012).
9. D. R. Soderblom, L. A. Hillenbrand, R. D. Jeffries, E. E. Mamajek, T. Naylor, in *Protostars and Planets VI*, H. Beuther, R. Klessen, C. Dullemond, T. Henning, Eds. (Univ. of Arizona Press, Tucson, AZ, 2014), in press; available at http://arxiv.org/abs/1311.7024.
10. J. Olofsson *et al.*, *Astron. Astrophys.* **542**, 90–115 (2012).
11. P. Artymowicz, *Astrophys. J.* **335**, L79–L82 (1988).
12. G. G. Fazio *et al.*, *Astrophys. J. Suppl. Ser.* **154**, 10–17 (2004).
13. D. Jewitt, H. Matthews, *Astron. J.* **117**, 1056–1062 (1999).
14. J. A. M. McDonnell *et al.*, *Nature* **321**, 338–341 (1986).
15. D. Perez-Becker, E. Chiang, *Mon. Not. R. Astron. Soc.* **433**, 2294–2309 (2013).
16. P. H. Warren, *Geochim. Cosmochim. Acta* **72**, 3562–3585 (2008).
17. B. C. Johnson, H. J. Melosh, *Icarus* **217**, 416–430 (2012).
18. M. C. Wyatt, W. R. F. Dent, *Mon. Not. R. Astron. Soc.* **334**, 589–607 (2002).
19. B. Zuckerman, I. Song, *Astrophys. J.* **758**, 77–86 (2012).
20. B. C. Johnson *et al.*, *Astrophys. J.* **761**, 45–57 (2012).
21. R. Osten *et al.*, *Astrophys. J.* **765**, L44–L46 (2013).
22. P. Reegen, *Astron. Astrophys.* **467**, 1353–1371 (2007).
23. T. Kallinger, P. Reegen, W. W. Weiss, *Astron. Astrophys.* **481**, 571–574 (2008).
24. S. J. Kenyon, B. C. Bromley, *Astron. J.* **130**, 269–279 (2005).
25. S. Elser, B. Moore, J. Stadel, R. Morishima, *Icarus* **214**, 357–365 (2011).
26. T. Naylor *et al.*, *Mon. Not. R. Astron. Soc.* **335**, 291–310 (2002).
27. R. D. Jeffries, T. Naylor, C. R. Devey, E. J. Totten, *Mon. Not. R. Astron. Soc.* **351**, 1401–1422 (2004).

ACKNOWLEDGMENTS

H.Y.A.M, K.Y.L.S., and G.H.R. thank R. Malhotra and A. Gáspár for valuable discussions. This work is based on observations made with the Spitzer Space Telescope, which is operated by the Jet Propulsion Laboratory (JPL), California Institute of Technology, under a contract with NASA. Support for this work was provided by NASA through an award issued by JPL/Caltech and by NASA grant NNX13AE74G. All data are publicly available through the NASA/IPAC Infrared Science Archive.

SUPPLEMENTARY MATERIALS

www.sciencemag.org/content/345/6200/1032/suppl/DC1
Supplementary Text
Figs. S1 to S4
References (*28*–*45*)

23 April 2014; accepted 15 July 2014
10.1126/science.1255153

SUPERFLUIDITY

A mixture of Bose and Fermi superfluids

I. Ferrier-Barbut,* M. Delehaye, S. Laurent, A. T. Grier,† M. Pierce, B. S. Rem,‡ F. Chevy, C. Salomon

Superconductivity and superfluidity of fermionic and bosonic systems are remarkable many-body quantum phenomena. In liquid helium and dilute gases, Bose and Fermi superfluidity has been observed separately, but producing a mixture in which both the fermionic and the bosonic components are superfluid is challenging. Here we report on the observation of such a mixture with dilute gases of two lithium isotopes, lithium-6 and lithium-7. We probe the collective dynamics of this system by exciting center-of-mass oscillations that exhibit extremely low damping below a certain critical velocity. Using high-precision spectroscopy of these modes, we observe coherent energy exchange and measure the coupling between the two superfluids. Our observations can be captured theoretically using a sum-rule approach that we interpret in terms of two coupled oscillators.

In recent years, ultracold atoms have emerged as a unique tool to engineer and study quantum many-body systems. Examples include weakly interacting Bose-Einstein condensates (*1*, *2*), two-dimensional gases (*3*), and the superfluid-Mott insulator transition (*4*) in the case of bosonic atoms, and the crossover between Bose-Einstein condensation (BEC) and fermionic superfluidity described by the the theory of Bardeen, Cooper, and Schrieffer (BCS) for fermionic atoms (*5*). Mixtures of Bose-Einstein condensates were produced shortly after the observation of BEC (*2*), and a BEC mixed with a single-spin state Fermi sea was originally observed in (*6*, *7*). However, realizing a mixture in which both fermionic and bosonic species are superfluid has been experimentally challenging. This has also been a long-sought goal in liquid helium, where superfluidity was achieved separately in both bosonic ^{4}He and fermionic ^{3}He. The double superfluid should undergo a transition

between s-wave and p-wave Cooper pairs as the ^{3}He dilution is varied (*8*). However, because of strong interactions between the two isotopes, ^{3}He-^{4}He mixtures contain only a small fraction of ^{3}He (typically 6%) which, so far, has prevented attainment of simultaneous superfluidity for the two species (*8*, *9*).

Here we report on the production of a Bose-Fermi mixture of quantum gases in which both species are superfluid. Our system is an ultracold gas of fermionic ^{6}Li in two spin states mixed with ^{7}Li bosons and confined in an optical dipole trap. Using radio-frequency pulses, we prepare ^{6}Li atoms in their two lowest hyperfine states $|1_f\rangle$ and $|2_f\rangle$, whereas ^{7}Li is spin polarized in the second-to-lowest state $|2_b\rangle$ (*10*). For this combination of states, in the vicinity of the ^{6}Li Feshbach resonance at a magnetic field of 832 G (*11*), the scattering length of the bosonic isotope $a_b = 70a_0$ (a_0 is the Bohr radius) is positive, preventing collapse of the BEC. The boson-fermion interaction is characterized by a scattering length $a_{bf} = 40.8a_0$ that does not depend on magnetic field in the parameter range studied here. At resonance, the Fermi gas exhibits a unitary limited collision rate, and lowering the optical dipole trap depth leads to extremely efficient evaporation. Owing to a large excess of ^{6}Li atoms with respect to ^{7}Li, the Bose gas is sympathetically driven to quantum degeneracy.

The two clouds reach the superfluid regime after a 4-s evaporation ramp (*10*). As the ^{7}Li Bose gas is weakly interacting, the onset of BEC is detected by the growth of a narrow peak in the density profile of the cloud. From previous studies on atomic Bose-Einstein condensates, we conclude that the ^{7}Li BEC is in a superfluid phase. Superfluidity in a unitary Fermi gas is notoriously more difficult to detect because of the absence of any qualitative modification of the density profile at the phase transition. To demonstrate the superfluidity of the fermionic component of the cloud, we slightly imbalance the two spin populations. In an imbalanced gas, the cloud is organized in concentric layers, with a fully paired superfluid region at its center, where Cooper pairing maintains equal spin populations. This ^{6}Li superfluid core can be detected by the presence of a plateau in the doubly integrated density difference (*12*). Examples of density profiles of the bosonic and fermionic superfluids are shown in Fig. 1, where both the Bose-Einstein condensate (blue circles) and the plateau (black diamonds in the inset) are clearly visible. Our coldest samples contain $N_b = 4 \times 10^4$ ^{7}Li atoms and $N_f = 3.5 \times 10^5$ ^{6}Li atoms. The absence of a thermal fraction in the bosonic cloud indicates a temperature below $0.5T_{c,b}$, where $k_B T_{c,b} = 0.94\hbar\bar{\omega}_b N_b^{1/3}$ is the critical temperature of the ^{7}Li bosons, and $\bar{\omega}_b$ ($\bar{\omega}_f$) is the geometric mean trapping frequency for ^{7}Li (^{6}Li). Combined with the observation of the ^{6}Li plateau, this implies that the Fermi cloud is also superfluid with a temperature below $0.8T_{c,f}$. Here, $T_{c,f}$ is the critical temperature for superfluidity of a spin-balanced, harmonically trapped Fermi gas at unitarity, $T_{c,f} = 0.19T_F$ (*13*), and $k_B T_F = \hbar\bar{\omega}_f(3N_f)^{1/3}$ is the Fermi temperature. The superfluid mixture is very stable, with a lifetime exceeding 7 s for our coldest samples.

As seen in Fig. 1, the Bose-Fermi interaction is too weak to alter significantly the density profiles of the two species (*14*). To probe the interaction between the two superfluids, we study the dynamics of the mass centers of the two isotopes (dipole modes), a scheme used previously for the study of mixtures of Bose-Einstein condensates (*15*, *16*), mixtures of Bose-Einstein condensates and spin-polarized Fermi seas (*17*), spin diffusion in Fermi gases (*18*), or integrability in one-dimensional systems (*19*). In a purely harmonic trap and in the absence of interspecies interactions, the dipole mode of each species is undamped and can therefore be measured over long time spans to achieve a high-frequency resolution and detect small perturbations of the system. We excite the dipole modes by shifting the initial position of the ^{6}Li and ^{7}Li clouds by a displacement d along the weak direction z of the trap (*10*). We then release them and let them evolve during a variable time t, after which we measure their positions. By monitoring the cloud oscillations during up to 4 s, we determine their frequencies with high precision ($\frac{\Delta\omega}{\omega} \lesssim 2 \times 10^{-3}$). In the absence of the other species, the oscillation frequencies of ^{6}Li and ^{7}Li are, respectively, $\omega_f = 2\pi \times 16.80(2)$ Hz and $\omega_b = 2\pi \times 15.27(1)$ Hz. In the axial direction, the confinement is mostly magnetic, and at high magnetic field, both species are in the Paschen-Back regime, where the electronic and nuclear spin degrees of freedom are decoupled. In this regime, the magnetic confinement mostly results from the electronic spin and is therefore almost identical for the two isotopes. The ratio ω_f/ω_b is then very close to the expected value $\sqrt{7/6} \simeq 1.08$ based on the ratio of the atomic masses (*20*).

Contrary to the large damping observed in the Bose-Bose mixtures (*15*), we observe long-lived oscillations of the Bose-Fermi superfluid mixture at frequencies ($\tilde{\omega}_b$, $\tilde{\omega}_f$). These oscillations extend over more than 4 s with undetectable damping (Fig. 2 and fig. S2). This very weak dissipation is only observed when the initial displacement d is below 100 μm, corresponding to a maximum relative velocity $v_{max} = (\tilde{\omega}_b + \tilde{\omega}_f)d$ below 18 mm/s ≃ 0.4 v_F, where $v_F = \sqrt{2k_B T_F/m_f}$. In this situation, the BEC explores only the central part of the much broader Fermi cloud. When $v_{max} > v_c = 0.42^{+0.05}_{-0.11} v_F = 20^{+2}_{-5}$ mm/s, we observe a sharp onset of damping and heating of the BEC compatible with the Landau criterion for breakdown of superfluidity (Fig. 2C) (*10*). For comparison, the sound velocity of an elongated Fermi gas at its center is $v_s' = \xi^{1/4} v_F/\sqrt{5} = 17$ mm/s (*21*), where $\xi = 0.38$ is the Bertsch parameter (*5*, *13*). The measured critical velocity v_c is very close to v_s' and is clearly above the BEC sound velocity of ≃5 mm/s at its center.

Two striking phenomena are furthermore observed. First, whereas the frequency $\tilde{\omega}_f$ of ^{6}Li oscillations is almost unchanged from the value in the absence of ^{7}Li, that of ^{7}Li is downshifted

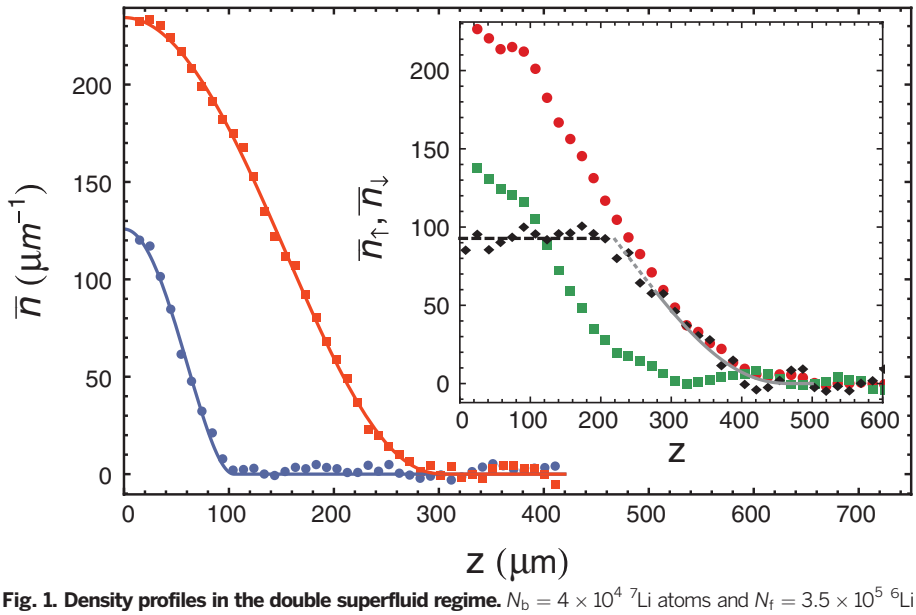

Fig. 1. Density profiles in the double superfluid regime. $N_b = 4 \times 10^4$ ^{7}Li atoms and $N_f = 3.5 \times 10^5$ ^{6}Li atoms are confined in a trap at a temperature below 130 nK. The density profiles $\bar{n}_b$ (blue circles) and $\bar{n}_{f,\uparrow}$ (red squares) are doubly integrated over the two transverse directions. The blue (red) solid line is a fit to the ^{7}Li (^{6}Li) distribution by a mean-field (unitary Fermi gas) EoS in the Thomas-Fermi approximation. Inset: Spin-imbalanced Fermi gas ($N_{f,\uparrow} = 2 \times 10^5$, $N_{f,\downarrow} = 8 \times 10^4$) in thermal equilibrium with a BEC. Red circles: $\bar{n}_{f,\uparrow}$; green squares: $\bar{n}_{f,\downarrow}$; black diamonds: difference $\bar{n}_{f,\uparrow} - \bar{n}_{f,\downarrow}$. The plateau (black dashed line) indicates superfluid pairing (*12*). Gray solid line: Thomas-Fermi profile of a noninteracting Fermi gas for the fully spin-polarized outer shell prolonged by the partially polarized normal phase (gray dashed line).

Laboratoire Kastler-Brossel, École Normale Supérieure, Collège de France, CNRS and UPMC, 24 rue Lhomond, 75005 Paris, France.
***Corresponding author. E-mail: iferrier@lkb.ens.fr** †Present address: Van Swinderen Institute, University of Groningen, Faculty of Mathematics and Natural Sciences, Zernikelaan 25, 9747 AA Groningen, Netherlands. ‡Present address: Institut für Laserphysik, Universität Hamburg, Luruper Chaussee 149, Building 69, D-22761 Hamburg, Germany.

to $\tilde{\omega}_b = 2\pi \times 15.00(2)$ Hz. Second, the amplitude of oscillations of the bosonic species displays a beat at a frequency $\simeq(\tilde{\omega}_f - \tilde{\omega}_b)/(2\pi)$, revealing coherent energy transfer between the two clouds (Fig. 2B). To interpret the frequency shift of the ^{7}Li atoms, we note that $N_b \ll N_f$, which allows us to treat the BEC as a mesoscopic impurity immersed in a Fermi superfluid. Similarly to the Fermi polaron case (*22*), the effective potential seen by the bosons is the sum of the trapping potential $V(r)$ and the mean-field interaction $g_{bf}n_f(r)$, where n_f is the total fermion density, $g_{bf} = 2\pi\hbar^2 a_{bf}/m_{bf}$, and $m_{bf} = \frac{m_b m_f}{m_b+m_f}$ is the ^{6}Li/^{7}Li reduced mass. Neglecting at first the back-action of the bosons on the fermions, we can assume that n_f is given by the local-density-approximation result $n_f(r) = n_f^{(0)}(\mu_f^0 - V(r))$, where $n_f^{(0)}(\mu)$ is the stationary equation of state (EoS) of the Fermi gas. Because the Bose-Einstein condensate is much smaller than the Fermi cloud (Fig. 2A), $V(r)$ is smaller than μ_f^0 over the BEC volume. We can thus expand $n_f^{(0)}$, and we get

$$V_{\mathrm{eff}}(r) = g_{bf}n_f(0) + V(r)\left[1 - g_{bf}\left(\frac{dn_f^{(0)}}{d\mu_f}\right)_{r=0}\right] \quad (1)$$

We observe that the effective potential is still harmonic and the rescaled frequency is given by

$$\tilde{\omega}_b \simeq \omega_b\left(1 - \frac{1}{2}g_{bf}\left(\frac{dn_f^{(0)}}{d\mu_f}\right)_{r=0}\right) \quad (2)$$

For a unitary Fermi gas, the chemical potential is related to the density by $\mu_f = \xi\hbar^2(3\pi^2 n_f)^{2/3}/2m_f$. In the weakly coupled limit, we get $\frac{\delta\omega_b}{\omega_b} = \frac{\omega_b - \tilde{\omega}_b}{\omega_b} = \frac{13k_F a_{bf}}{7\pi\xi^{5/4}}$, where $\hbar k_F = \sqrt{2\hbar m_f \bar{\omega}_f (3N_f)^{1/3}}$ is the Fermi momentum of a noninteracting harmonically trapped Fermi gas. Using our experimental parameters $k_F = 4.6 \times 10^6$ m^{-1}, we predict a value $\tilde{\omega}_b \simeq 2\pi \times 14.97$ Hz, in very good agreement with the observed value 15.00(2)Hz.

To understand the amplitude modulation, we now take into account the back-action on the fermions. A fully quantum formalism using a sum-rule approach (*23*–*25*) leads to a coupled oscillator model in which the positions of the two clouds obey the following equations (*10*)

$$M_f\ddot{z}_f = -K_f z_f - K_{bf}(z_f - z_b) \quad (3)$$

$$M_b\ddot{z}_b = -K_b z_b - K_{bf}(z_b - z_f) \quad (4)$$

where $M_b = N_b m_b$ ($M_f = N_f m_f$) is the total mass of the ^{7}Li (^{6}Li) cloud, $K_b = M_b\omega_b^2$ ($K_f = M_f\omega_f^2$) is the spring constant of the axial magnetic confinement, and K_{bf} is a phenomenological (weak) coupling constant describing the mean-field interaction between the two isotopes. To recover the correct frequency shift (Eq. 2), we take $K_{bf} = 2K_b\frac{\delta\omega_b}{\omega_b}$. Solving these equations with the initial condition $z_f(0) = z_b(0) = d$, and defining $\rho = N_b/N_f$ and $\varepsilon = \frac{2m_b}{m_b - m_f}\left(\frac{\tilde{\omega}_b - \omega_b}{\omega_b}\right)$, in the limit $\rho, \varepsilon \ll 1$ we get

$$z_f = d[(1 - \varepsilon\rho)\cos(\tilde{\omega}_f t) + \varepsilon\rho\cos(\tilde{\omega}_b t)] \quad (5)$$

$$z_b = d[-\varepsilon\cos(\tilde{\omega}_f t) + (1 + \varepsilon)\cos(\tilde{\omega}_b t)] \quad (6)$$

The predictions of Eqs. 5 and 6 agree well with experiment (Fig. 2B). Interestingly, the peak-to-peak modulation of the amplitude of ^{7}Li is much larger than the relative frequency shift, a consequence of the almost exact tuning of the two oscillators (up to a factor $\sqrt{6/7}$). Thus, the mass prefactor in the expression for ε is large (=14) and leads to $\varepsilon \simeq 0.25$ at unitarity. This results in efficient energy transfer between the two modes despite their weak coupling, as observed.

We now extend our study of the Bose-Fermi superfluid mixture to the BEC-BCS crossover by tuning the magnetic field away from the resonance value $B_f = 832$ G. We explore a region from 860 G down to 780 G where $1/k_F a_f$ spans the interval $[-0.4, +0.8]$. In this whole domain, except in a narrow region between 845 and 850 G where the boson-boson scattering length

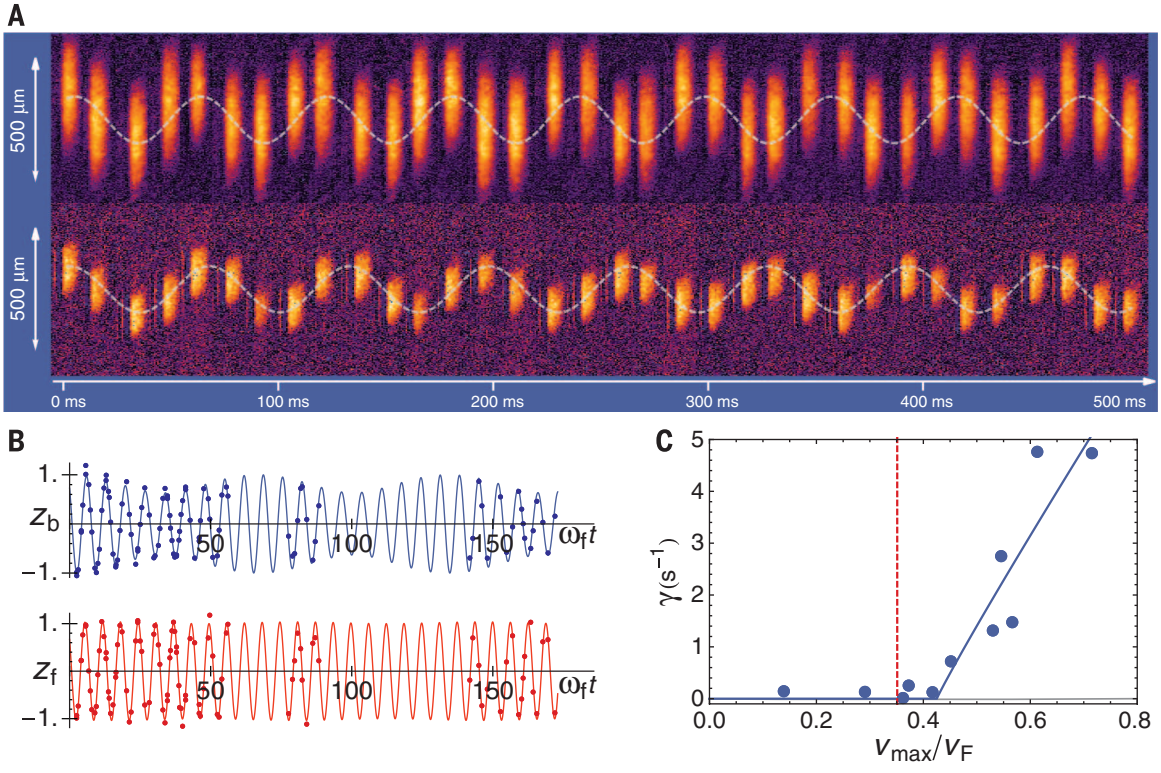

Fig. 2. Coupled oscillations of the superfluid mixture. (**A**) Center-of-mass oscillations. The oscillations are shown over the first 500 ms at a magnetic field of 835 G for a Fermi superfluid (top) and a Bose superfluid (bottom).The oscillation period of ^{6}Li (^{7}Li) is 59.7(1) ms [66.6(1) ms], leading to a dephasing of π near 300 ms. These oscillations persist for more than 4 s with no visible damping. The maximum relative velocity between the two clouds is 1.8 cm/s. (**B**) Coupled oscillations. Symbols: Center-of-mass oscillation of ^{7}Li (top) and ^{6}Li (bottom) displaying coherent energy exchange between both superfluids. Solid lines: Theory for an initial displacement d of 100 μm at a magnetic field of 835 G; see text. (**C**) Critical damping. Symbols: Damping rate (blue circles) of the amplitude of the center-of-mass oscillations of the ^{7}Li BEC as a function of the maximal relative velocity between the two superfluids normalized to the Fermi velocity of the ^{6}Li gas. Data taken at 832 G. From these data and using a fit function given in (*10*) (solid line), we extract $v_c = 0.42^{+0.05}_{-0.11}v_F$. The red dashed line shows the speed of sound of an elongated unitary Fermi superfluid $v_s' = \xi^{1/4}v_F/\sqrt{5} = 0.35v_F$ (*20*).

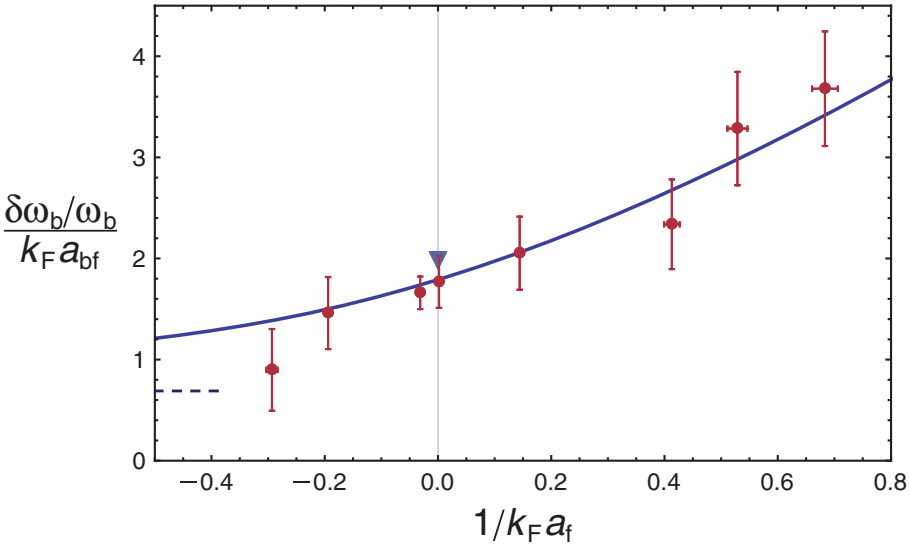

Fig. 3. Dipole mode frequency shift in the BEC-BCS crossover. Red circles: Experiment. Blue line: zero-temperature prediction from the equation of state of (*26*); dashed line: ideal Fermi gas. Blue triangle: prediction from (*13*). Error bars include systematic and statistical errors at 1 SD.

is negative, the mixture is stable and the damping extremely small.

The frequency shift of the BEC (Eq. 2) now probes the derivative of the EoS $n_f(\mu_f)$ in the BEC-BCS crossover. In the zero-temperature limit and under the local density approximation, Eq. 2 obeys the universal scaling $\frac{\delta\omega_b}{\omega_b} = k_F a_{bf} f\left(\frac{1}{k_F a_f}\right)$

In Fig. 3, we compare our measurements to the prediction for the function f obtained from the zero-temperature EoS measured in (*26*). On the BCS side, $(1/k_F a_f < 0)$, the frequency shift is reduced and tends to that of a noninteracting Fermi gas. Far on the BEC side $(1/k_F a_f \gg 1)$, we can compute the frequency shift using the EoS of a weakly interacting gas of dimers. Within the mean-field approximation, we have $\frac{dn_f}{d\mu_f} = \frac{2m_f}{\pi\hbar^2 a_{dd}}$, where $a_{dd} = 0.6a_f$ is the dimer-dimer scattering length. This expression explains the increase in the frequency shift when a_f is reduced, i.e., moving toward the BEC side [see (*10*) for the effect of Lee-Huang-Yang quantum correction].

The excellent agreement between experiment and our model confirms that precision measurements of collective modes are a sensitive dynamical probe of equilibrium properties of many-body quantum systems (*27*). Our approach can be extended to the study of higher-order excitations. In particular, although there are two first sound modes, one for each atomic species, we expect only one second sound for the superfluid mixture (*28*) if cross-thermalization is fast enough. In addition, the origin of the critical velocity for the relative motion of Bose and Fermi superfluids is an intriguing question that can be further explored in our system. Finally, a richer phase diagram may be revealed when N_b/N_f is increased (*29*) or when the superfluid mixture is loaded in an optical lattice (*30*).

REFERENCES AND NOTES

1. W. Ketterle, *Rev. Mod. Phys.* **74**, 1131–1151 (2002).
2. E. A. Cornell, C. E. Wieman, *Rev. Mod. Phys.* **74**, 875–893 (2002).
3. Z. Hadzibabic, P. Krüger, M. Cheneau, B. Battelier, J. Dalibard, *Nature* **441**, 1118–1121 (2006).
4. M. Greiner, O. Mandel, T. Esslinger, T. W. Hänsch, I. Bloch, *Nature* **415**, 39–44 (2002).
5. W. Zwerger, Ed., *The BCS-BEC Crossover and the Unitary Fermi Gas*, vol. 836 of *Lecture Notes in Physics* (Springer, Berlin, 2012).
6. F. Schreck *et al.*, *Phys. Rev. Lett.* **87**, 080403 (2001).
7. A. G. Truscott, K. E. Strecker, W. I. McAlexander, G. B. Partridge, R. G. Hulet, *Science* **291**, 2570–2572 (2001).
8. J. Rysti, J. Tuoriniemi, A. Salmela, *Phys. Rev. B* **85**, 134529 (2012).
9. J. Tuoriniemi *et al.*, *J. Low Temp. Phys.* **129**, 531–545 (2002).
10. See supplementary materials on *Science* Online.
11. G. Zürn *et al.*, *Phys. Rev. Lett.* **110**, 135301 (2013).
12. T. De Silva, E. Mueller, *Phys. Rev. A* **73**, 051602 (2006).
13. M. J. H. Ku, A. T. Sommer, L. W. Cheuk, M. W. Zwierlein, *Science* **335**, 563–567 (2012).
14. K. Mølmer, *Phys. Rev. Lett.* **80**, 1804–1807 (1998).
15. D. S. Hall, M. R. Matthews, J. R. Ensher, C. E. Wieman, E. A. Cornell, *Phys. Rev. Lett.* **81**, 1539–1542 (1998).
16. P. Maddaloni, M. Modugno, C. Fort, F. Minardi, M. Inguscio, *Phys. Rev. Lett.* **85**, 2413–2417 (2000).
17. F. Ferlaino *et al.*, *J. Opt. B Quantum Semiclassical Opt.* **5**, S3–S8 (2003).
18. A. Sommer, M. Ku, G. Roati, M. W. Zwierlein, *Nature* **472**, 201–204 (2011).
19. T. Kinoshita, T. Wenger, D. S. Weiss, *Nature* **440**, 900–903 (2006).
20. Because of a slight deviation from the Paschen-Back regime for ^{7}Li, this ratio is 1.1 instead of 1.08.
21. Y. Hou, L. Pitaevskii, S. Stringari, *Phys. Rev. A* **88**, 043630 (2013).
22. C. Lobo, A. Recati, S. Giorgini, S. Stringari, *Phys. Rev. Lett.* **97**, 200403 (2006).
23. S. Stringari, *J. Phys. IV France* **116**, 47–66 (2004).
24. T. Miyakawa, T. Suzuki, H. Yabu, *Phys. Rev. A* **62**, 063613 (2000).
25. A. Banerjee, *Phys. Rev. A* **76**, 023611 (2007).
26. N. Navon, S. Nascimbène, F. Chevy, C. Salomon, *Science* **328**, 729–732 (2010).
27. M. K. Tey *et al.*, *Phys. Rev. Lett.* **110**, 055303 (2013).
28. G. Volovik, V. Mineev, I. Khalatnikov, *Sov. Phys. JETP* **69**, 675 (1975).
29. T. Ozawa, A. Recati, S. Stringari, http://arxiv.org/abs/1405.7187 (2014).
30. A. B. Kuklov, B. V. Svistunov, *Phys. Rev. Lett.* **90**, 100401 (2003).

ACKNOWLEDGMENTS

We thank S. Stringari and Y. Castin for fruitful discussions and S. Balibar, J. Dalibard, F. Gerbier, S. Nascimbène, C. Cohen-Tannoudji, and M. Schleier-Smith for critical reading of the manuscript. We acknowledge support from the European Research Council Ferlodim and Thermodynamix, the Ile de France Nano-K (contract Atomix), and Institut de France Louis D. Prize.

SUPPLEMENTARY MATERIALS

www.sciencemag.org/content/345/6200/1035/suppl/DC1
Materials and Methods
Figs. S1 to S4
References (*31*–*34*)

29 April 2014; accepted 30 June 2014
Published online 17 July 2014;
10.1126/science.1255380

EARTHQUAKE DYNAMICS

Strength of stick-slip and creeping subduction megathrusts from heat flow observations

Xiang Gao[1] and Kelin Wang[2,3]*

Subduction faults, called megathrusts, can generate large and hazardous earthquakes. The mode of slip and seismicity of a megathrust is controlled by the structural complexity of the fault zone. However, the relative strength of a megathrust based on the mode of slip is far from clear. The fault strength affects surface heat flow by frictional heating during slip. We model heat-flow data for a number of subduction zones to determine the fault strength. We find that smooth megathrusts that produce great earthquakes tend to be weaker and therefore dissipate less heat than geometrically rough megathrusts that slip mainly by creeping.

Subduction megathrusts that primarily exhibit stick-slip behavior can produce great earthquakes, but some megathrusts are observed to creep while producing small and moderate-size earthquakes. The relationship between seismogenesis and strength of subduction megathrust is far from clear. Faults that produce great earthquakes are commonly thought of as being stronger than those that creep (*1*). Megathrusts that are presently locked to build up stress for future great earthquakes are thus described as being "strongly coupled." However, some studies have proposed strong creeping megathrusts because of the geometric irregularities of very rugged subducted sea floor (*2*, *3*).

Contrary to a widely held belief, geodetic and seismic evidence shows that very rough subducting sea floor promotes megathrust creep (*2*). All

the subduction zones that have produced moment magnitude (M_w) 9 or greater earthquakes feature rather smooth subducting sea floor, because the igneous crust is devoid of large seamounts or fracture zones and/or because of large amounts of sediments (*4*, *5*). To know whether the smooth and highly seismogenic megathrusts are stronger or weaker than the rough and creeping megathrusts, we compared the amounts of frictional heat they dissipate. A stronger fault moves against greater resistance and, for the same slip distance, dissipates more heat per unit area.

We first compared two very different subduction zones in terms of seismicity and fault roughness. The Japan Trench (Fig. 1A) is a highly seismogenic subduction zone and has produced many large earthquakes (*6*), including the 2011 M_w 9 Tohoku-oki earthquake that generated a devastating tsunami. The megathrust moves primarily in a stick-slip manner, although various parts of it exhibit creep accompanied with small repeating earthquakes (*7*). The subducting sea floor is smooth, except for the northern and southern ends of the margin beyond the 2011 main rupture area (Fig. 1A). The northern Hikurangi subduction zone (Fig. 1B), however, is in sharp contrast with the Japan Trench. Among all the clearly documented megathrust earthquakes here, the largest is the M_w 5.6 Gisborn earthquake in 1966 (*8*). Most of the megathrust is creeping at the subduction rate (100% creeping ratio), as constrained by Global Positioning System observations from ~350 sites (*9*) (Fig. 1B). The observed creep is probably a persistent instead of transient behavior, given the lack of clear paleoseismic evidence for great megathrust earthquakes. The subducting sea floor is extremely rugged, featuring a number of subducting seamounts (*10*), but becomes smoother to the south owing to large amounts of sediments (Fig. 1B).

To determine frictional heating to infer fault strength, we developed two-dimensional (2D) finite element models. At both the Japan Trench and northern Hikurangi, heat-flow data (Fig. 1) provide adequate model constraints (*11*). The long-term frictional strength of the shallow megathrust is represented by the apparent coefficient of friction $\mu' = \tau^F/\sigma_n$, where τ^F is shear strength and σ_n is normal stress, approximately the weight of the overlying rock column. Parameter μ' includes contributions from both the intrinsic friction and pore-fluid pressure (*11*). It is understood that μ' represents the integrated strength of a shear band that accommodates fault motion. The band can be as thin as millimeters for seismic slip but wider by orders of magnitude for creeping motion (*2*, *12*). The rate of frictional heating per unit area is thus $q = \tau^F V = \mu'\sigma_n V$, where V is the long-term rate of slip of the megathrust. The frictional heating contributes to surface heat flow, so that the value of μ' can be estimated by comparing model predicted q with heat-flow measurements. Because heat is dissipated only when the fault is in motion, for stick-slip faults V is accomplished mainly by repeatedly having large earthquakes, and the μ' value inferred from frictional heating is a representation of the average strength during coseismic slip. The actual stress and strength changes during individual earthquakes are much more complex (*13*), but the frictional heat seen in surface heat-flow measurements is their integrated effect over numerous earthquakes. Unlike with previous thermal models, we invoked a parameterization based on laboratory experiments (*14*) to model the gradual downdip transition along the subduction interface from shallow frictional slip to deeper viscous shearing with increasing temperature (*11*).

The model results show that the thermally defined frictional strength of the subduction faults is low, with $\mu' \approx 0.025$ for the Japan Trench and 0.13 for northern Hikurangi (Fig. 2). In comparison, the effective friction of rocks based on laboratory-derived intrinsic friction (*15*) and at hydrostatic pore-fluid pressure is about 0.4. The low strength is consistent with the long-standing notion that subduction faults are weak, barely transferring enough stress to prevent forearc topography from collapsing under its own weight (*16*, *17*). Of even greater importance to the present study is the difference between the apparent coefficients of friction for the two megathrusts. The difference cannot be reconciled by considering data uncertainties. For example, trading their preferred μ' values fails to fit the heat-flow observations in both places (Fig. 2). Hydrothermal circulation within the subducted oceanic crust can lower the surface heat flow (*11*), but this effect is too small at the Japan Trench to explain the lower observed heat flows (*18*).

One reason for a lower μ' for the Japan Trench is that it primarily represents coseismic fault strength (Fig. 3). In laboratory experiments, faults weaken by a factor of three to five when their slip accelerates to seismic rates of ~1 m/s, independent of their frictional behavior at lower rates (*19*). In real faults, such dynamic weakening may locally cause complete stress drop, but it cannot happen over very large fault areas, as evidenced by the very small average stress drops in great earthquakes (*20*). Even in the 2011 M_w 9.0 Tohoku-oki earthquake, which exhibited a greater stress drop than other great earthquakes, reported average stress drop of the rupture zone is still only about 4 to 7 MPa (*21*, *22*), with peak value in a localized region as high as 40 MPa (*23*). At 20 km depth, roughly in the middle of the depth range of the Tokoku-oki rupture, σ_n is about 500 MPa, so that a 5-MPa static stress drop only requires a 0.01 decrease in μ'. In other words, a factor of 1/3 decrease in μ'—for example, from 0.035 to 0.025—is adequate to explain the Japan Trench results (*24*). The seemingly small decrease in fault stress is sufficient to reverse the stress state of the upper plate in the rupture area from margin-normal compression to tension (*16*), a change that indeed happened as a result of the Tohoku-oki earthquake (*25*).

Therefore, despite the remarkable weakness of subduction faults, the average stress drop in great earthquakes is only a relatively small, although important, fraction of the average fault strength. Large dynamic weakening in parts of the fault must be accompanied by much less weakening or even strengthening in other parts, such that the average stress drop of the entire rupture zone is much less than localized peak values. For example, local strengthening at rupture boundaries is known to trigger well-documented afterslip following subduction earthquakes (*26*). An important implication is that the amount of frictional heat is several times

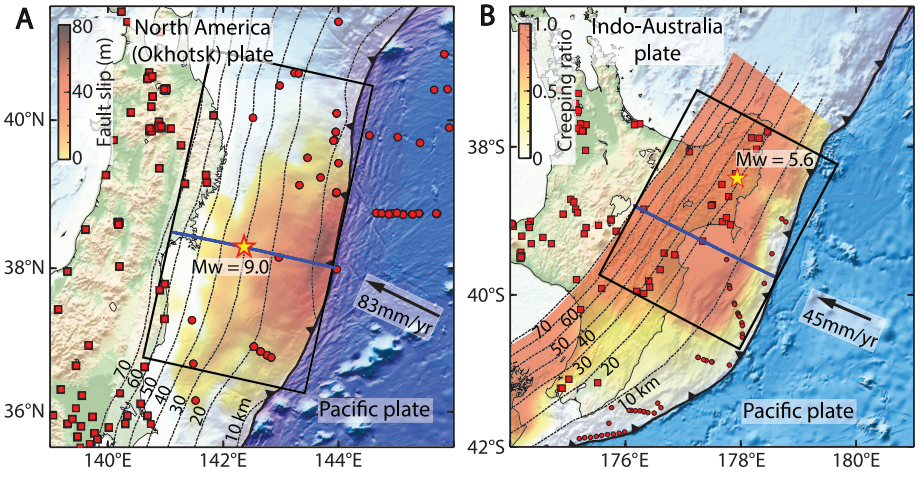

Fig. 1. Tectonic setting of the Japan Trench and northern Hikurangi subduction zones. (**A**) Japan Trench. Coseismic slip distribution of the 2011 M_w 9.0 Tohoku-oki earthquake (table S2) is shown by color shading and epicenter by star. Heat-flow sites are shown by red symbols (circles, marine probe; squares, land borehole) (*11*). (**B**) Northern Hikurangi. Geodetically determined creeping ratio (ratio of creeping rate to subduction rate) is from (*9*). Star shows the location of the largest clearly documented megathrust earthquake (table S2). Heat-flow sites include those of subsea bottom-simulating reflectors (red dots) and bottom-hole temperature measurements (red squares) (*11*). In both (A) and (B), the thick blue line indicates thermal model profile. Heat-flow values in the rectangular area are projected on to the model profile and shown in Fig. 2.

[1]Key Laboratory of Marine Geology and Environment, Institute of Oceanology, Chinese Academy of Sciences, 7 Nanhai Road, Qingdao 266071, China. [2]Pacific Geoscience Centre, Geological Survey of Canada, Natural Resources Canada, 9860 West Saanich Road, Sidney, British Columbia, V8L 4B2, Canada. [3]School of Earth and Ocean Sciences, University of Victoria, Victoria, British Columbia, V8P 5C2, Canada.
*Corresponding author. E-mail: kwang@nrcan.gc.ca

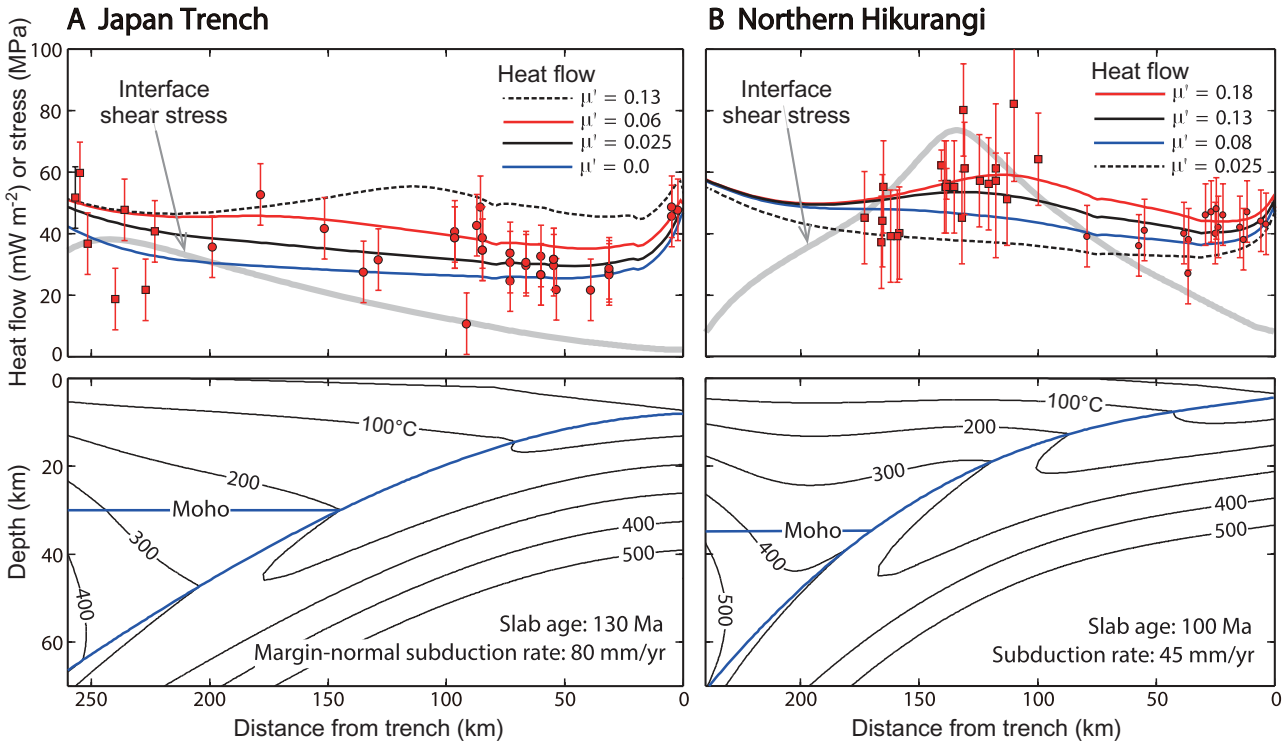

Fig. 2. Heat dissipation models for Japan Trench and northern Hikurangi. (**A** and **B**) For each subduction zone, the top panel shows observed (symbols) and model-predicted (thin lines) surface heat flows and model interface shear stress (thick gray line). Circles and squares indicate marine and land heat-flow measurements, respectively (*11*). Bottom panel shows model subsurface temperatures (contours) and plate interface geometry (blue line) (*11*).

the combination of the energy radiated as seismic waves and consumed in permanently deforming rocks around the rupture (*13*, *27*) (Fig. 3C).

Because the difference in μ′ between the two subduction zones cannot be fully explained by dynamic weakening, it must reflect a difference in static fault strength. From observations (*2*) and theoretical reasoning (*3*), extreme ruggedness of the subducting sea floor such as at northern Hikurangi gives rise to heterogeneous stress and structural environments that promote creep and small earthquakes. But unlike creeping along a smooth fault facilitated by weak gouge [e.g., (*28*)] (shown in Fig. 3 as "weak creep"), rough faults creep by breaking and wearing geometrical irregularities in a broad zone of complex internal structure. The integrated resistance to creep is expected to be relatively high (shown in Fig. 3 as "strong creep"). Our results indicate that the creeping megathrust at northern Hikurangi is indeed stronger than the stick-slip, but much smoother, megathrust at the Japan Trench.

To investigate whether the difference in μ′ for the Japan Trench and northern Hikurangi reflects a systematic correlation between fault strength and predominant mode of fault slip, we analyzed another seven subduction zones where heat flow observations can reasonably constrain frictional heating and allow μ′ to be determined with our modeling (Fig. 4) (*11*). Most good-quality heat-flow data are from highly seismogenic subduction zones, which attract more research efforts. Therefore, northern Hikurangi, Manila Trench, and Kermadec are valuable examples for less seismogenic subduction zones. We also added

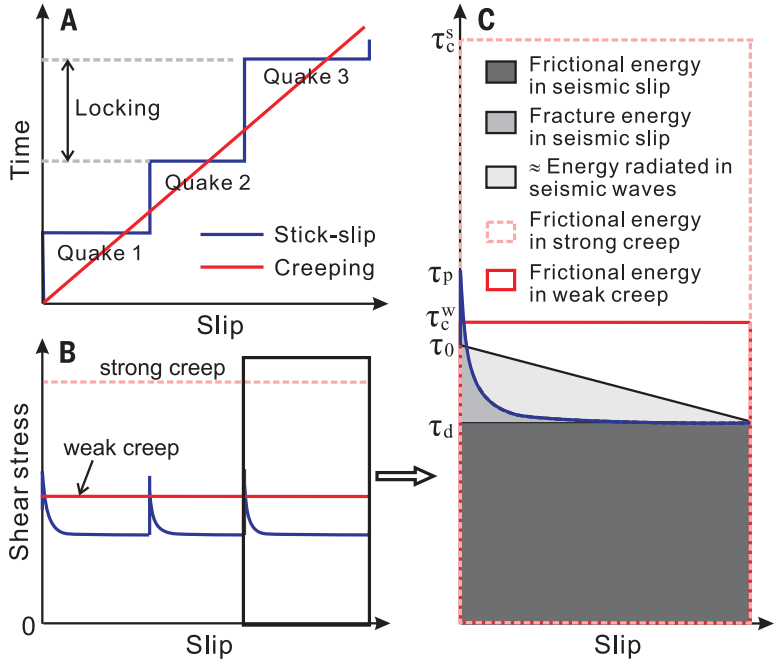

Fig. 3. Schematic illustration of fault stress and frictional heating for stick-slip and creeping faults. (**A**) Fault slip history. (**B**) Fault stress corresponding to slip in (A). (**C**) An enlarged portion of (B) showing partitioning of energy in seismic slip for stick-slip faults, in comparison with energy dissipated by strong and weak creeping faults. For stick-slip fault, τ_0 is pre-earthquake stress, τ_p is peak stress, and τ_d is stress during seismic slip (*13*, *27*). τ_c^w and τ_c^s are yield stresses of smooth/weak and rough/strong creeping faults, respectively.

Costa Rica as an example of intermediate degree of creeping, but its apparent friction is poorly constrained from previous studies (*11*).

The estimated apparent coefficient of friction decreases with increasing M_{max}, the maximum magnitude of clearly documented megathrust earthquake

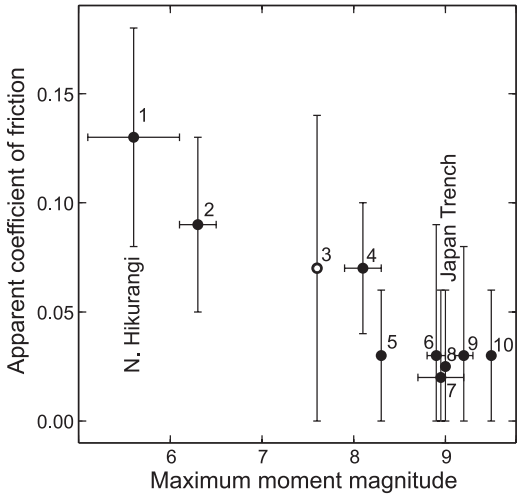

Fig. 4. Apparent friction of megathrust versus maximum size of clearly documented interplate earthquake. 1, northern Hikurangi; 2, Manila Trench; 3, Costa Rica; 4, Kermadec; 5, Nankai; 6, Kamchatka; 7, northern Cascadia; 8, Japan Trench; 9, Sumatra; and 10, south-central Chile (table S2). Except for Costa Rica (*11*), the apparent coefficients of friction are obtained using thermal models developed in this study, with error bars based on numerical testing of model fit to heat-flow data (Fig. 2 and figs. S1 to S7) (*11*). Error bars for M_{max} are based on publications on these earthquakes (table S2).

at each subduction zone (Fig. 4). The M_{max} values provide a proxy of long-term seismic slip. In determining M_{max} for northern Hikurangi, we do not consider two poorly recorded events in 1947 both with M_w ~ 7 (*29*), because they occurred at a very shallow depth of the plate interface and do not represent the general slip mode of the megathrust. For subduction zones with M_{max} 8.3 to 9.5, the fault motion is primarily stick-slip. Coseismic slip in their largest earthquakes is comparable to slip deficits accumulated over typical interseismic intervals of several hundred years, and geodetic observations show a high degree of megathrust locking at present (table S2). For three of the other four subduction zones, the present locking/creeping state of the megathrust is constrained by modern geodetic measurements (table S2). They show large creep, with northern Hikurangi having the most active creep (Fig. 1B). At Kermadec, the present creeping/locking state of the megathrust cannot be adequately determined by geodetic measurements (*30*). All the highly seismogenic subduction zones in this suite feature smooth subducting sea floor, and the faults are weaker than the faults associated with the subduction of rugged sea floor. The general correlation between subducting sea floor ruggedness, creeping, and greater heat dissipation suggests that geomorphological and thermal observations may be useful in assessing earthquake and tsunami hazards for risk mitigation.

REFERENCES AND NOTES

1. C. H. Scholz, J. Campos, *J. Geophys. Res.* **100** (B11), 22,103–22,105 (1995).
2. K. Wang, S. L. Bilek, *Tectonophys.* **610**, 1–24 (2014).
3. K. Wang, S. L. Bilek, *Geology* **39**, 819–822 (2011).
4. A. Heuret, C. P. Conrad, F. Funiciello, S. Lallemand, L. Sandri, *Geophys. Res. Lett.* **39**, L05304 (2012).
5. D. W. Scholl, S. H. Kirby, R. von Huene, American Geophysical Union Fall Meeting, Abstract T14B–01 (2011).
6. Y. Yamanaka, M. Kikuchi, *J. Geophys. Res.* **109**, B07307 (2004).
7. N. Uchida, T. Matsuzawa, *Earth Planets Space* **63**, 675–679 (2011).
8. T. Webb, H. Anderson, *Geophys. J. Int.* **134**, 40–86 (1998).
9. L. M. Wallace *et al.*, *Geochem. Geophys. Geosyst.* **10**, Q10006 (2009).
10. D. H. N. Barker, R. Sutherland, S. Henrys, S. Bannister, *Geochem. Geophys. Geosyst.* **10**, Q02007 (2009).
11. Materials, methods, and other information are available as supplementary material on *Science* Online.
12. C. A. J. Wibberley, G. Yielding, G. Di Toro, in *The Internal Structure of Fault Zones: Implications for Mechanical and Fluid-Flow Properties*, Geol. Soc. Lond. Spec. Pub. 299, C. A. J. Wibberley, W. Kurz, J. Imber, R. E. Holdsworth, C. Collettini, Eds. (Geological Society of London, 2008), pp. 5–33.
13. H. Kanamori, L. Rivera, in *The missing sinks: Slip localization in faults, damage zones, and the seismic energy budget*, Geophys. Monogr. 170, Abercrombie, R., Ed. (America Geophysical Union, Washington DC, 2006), pp. 3–13.
14. H. Noda, T. Shimamoto, *J. Struct. Geol.* **38**, 234–242 (2012).
15. J. Byerlee, *Pure Appl. Geophys.* **116**, 615–626 (1978).
16. K. Wang, K. Suyehiro, *Geophys. Res. Lett.* **26**, 2307–2310 (1999).
17. S. Lamb, *J. Geophys. Res.* **111**, B07401 (2006).
18. Y. Kawada, M. Yamano, N. Seama, *Geochem. Geophys. Geosyst.* **15**, 1580–1599 (2014).
19. G. Di Toro *et al.*, *Nature* **471**, 494–498 (2011).
20. B. P. Allmann, P. M. Shearer, *J. Geophys. Res.* **114** (B1), B01310 (2009).
21. K. Koketsu *et al.*, *Earth Planet. Sci. Lett.* **310**, 480–487 (2011).
22. S. J. Lee, B. S. Huang, M. Ando, H. C. Chiu, J. H. Wang, *Geophys. Res. Lett.* **38**, L19306 (2011).
23. H. Kumagai, N. Pulido, E. Fukuyama, S. Aoi, *Earth Planets Space* **64**, 649–654 (2012).
24. In some earthquakes, the final fault stress at the end of the rupture may be somewhat smaller (overshoot) or larger (undershoot) than the fault strength during slip, but the deviation from the coseismic strength is expected to be a small fraction of the stress drop.
25. A. Hasegawa *et al.*, *Earth Planet. Sci. Lett.* **355-356**, 231–243 (2012).
26. M. E. Pritchard, M. Simons, *J. Geophys. Res.* **111**, B08405 (2006).
27. R. E. Abercrombie, J. R. Rice, *Geophys. J. Int.* **162**, 406–424 (2005).
28. D. A. Lockner, C. Morrow, D. Moore, S. Hickman, *Nature* **472**, 82–85 (2011).
29. D. I. Doser, T. H. Webb, *Geophys. J. Int.* **152**, 795–832 (2003).
30. W. Power, L. Wallace, X. Wang, M. Reyners, *Pure Appl. Geophys.* **169**, 1–36 (2012).

ACKNOWLEDGMENTS

We thank J. He for writing finite element code PGCTherm and implementing the line-element method for fault modeling, W. -C. Chi for making available digital heat-flow data for Manila Trench, and S. Wu and J. Zhang for discussions. X.G. was supported by Chinese Academy of Sciences' Strategic Priority Research Program Grant XDA11030102 and Open Foundation of Key Laboratory of Marine Geology and Environment Grant MGE2012KG04, and K.W. was supported by Geological Survey of Canada core funding and a Natural Sciences and Engineering Research Council of Canada Discovery Grant through the University of Victoria. This is Geological Survey of Canada contribution 2014105. All heat-flow data used are from published sources as listed in the reference list. Modeling parameters and tabulated results are available in the supplementary materials.

SUPPLEMENTARY MATERIALS

www.sciencemag.org/content/345/6200/1038/suppl/DC1
Materials and Methods
Supplementary Text
Figs. S1 to S7
Tables S1 and S2
References (*31*–*109*)

1 May 2014; accepted 18 July 2014
10.1126/science.1255487

CONSERVATION ECONOMICS

Using ecological thresholds to evaluate the costs and benefits of set-asides in a biodiversity hotspot

Cristina Banks-Leite,[1,2]* Renata Pardini,[3] Leandro R. Tambosi,[2] William D. Pearse,[4] Adriana A. Bueno,[5] Roberta T. Bruscagin,[2] Thais H. Condez,[6] Marianna Dixo,[2] Alexandre T. Igari,[7] Alexandre C. Martensen,[8] Jean Paul Metzger[2]

Ecological set-asides are a promising strategy for conserving biodiversity in human-modified landscapes; however, landowner participation is often precluded by financial constraints. We assessed the ecological benefits and economic costs of paying landowners to set aside private land for restoration. Benefits were calculated from data on nearly 25,000 captures of Brazilian Atlantic Forest vertebrates, and economic costs were estimated for several restoration scenarios and values of payment for ecosystem services. We show that an annual investment equivalent to 6.5% of what Brazil spends on agricultural subsidies would revert species composition and ecological functions across farmlands to levels found inside protected areas, thereby benefiting local people. Hence, efforts to secure the future of this and other biodiversity hotspots may be cost-effective.

The combined effects of environmental change are driving species to the brink of extinction across the world's biodiversity hotspots (*1*). If species disappear, the ecological functions they perform will also decline (*2*), with potential consequences including increased pest outbreaks and reduced food security (*3*, *4*). Although the role of large protected areas in preserving species is unquestionable (*5*), people will benefit more widely from

the ecological functions they perform if species occur throughout the biome, not just inside protected areas (*6*). It is in this context that ecological set-asides on private land have emerged as a promising strategy to preserve species and ecological functions across farmlands (*2*, *7*).

Setting aside private land for conservation nonetheless comes with financial costs to the landowner. For instance, in the Atlantic Forest of Brazil, the median yearly gross profit per hectare of agricultural land is $467 (interquartile range $199 to $868; U.S. dollars) (*8*), which is more than the Brazilian minimum wage. Conservation schemes that involve payment for ecosystem services (PES) provide a mechanism to increase landowner participation on set-asides (*9*), and its feasibility is reflected in the ever-increasing number of PES projects across the globe (*7*, *10*). However, most PES projects involving set-asides are relatively local initiatives that do not match the extensive scale of conservation needs and societal issues observed across biodiversity hotspots (*10*). Because large-scale problems require large-scale solutions, we here advocate and provide a realistic plan for a biome-wide set-aside program that concurrently maximizes the provision of habitat to biodiversity, and of ecological functions across rural areas, while minimizing the costs to society. Our aim is to calculate the overall economic costs of a set-aside program tailored to one of the most threatened hotspots of the world (*11*)—the Atlantic Forest of Brazil.

First, we estimated the minimum amount of habitat required to maintain biodiversity. This information is crucial (*12*); if too much area is set aside for conservation, economic costs become an impediment, but if not enough area is set aside, ecological gains are minor. To investigate the relationship between forest cover and species composition, we used data from a large field study conducted in the Atlantic Forest (*13*, *14*). The data set consisted of nearly 25,000 captures of 43 species of mammals, 140 species of birds, and 29 species of amphibians collected in 79 landscapes (200 ha each) varying from 5 to 100% of forest cover (including both old-growth and regrowth) and distributed across a 150-km-wide region (fig. S1) (*8*). For all groups, reduction in forest cover had a similar effect on community integrity, defined here as the similarity in community composition between fragmented and continuously forested landscapes (Fig. 1, I to L). Results indicate that community integrity of all three groups is maintained until 24 to 33% of forest cover, below which integrity declines sharply with further reductions in forest cover. When all three taxa were combined, analyses indicated the existence of a threshold at 28.5% of forest cover [95% confidence interval (CI) 24.0 to 33.1, $N = 56$], hence approximately 30% of native habitat is needed to preserve the integrity of vertebrate communities within each landscape (Fig. 1). Similar results have been observed previously in the northern Atlantic Forest, indicating that the patterns we discern are not exclusive to our sites, to vertebrates, or to a particular landscape scale (*8*, *15*).

Theoretical predictions have suggested that species become more sensitive to habitat alterations below 30% of remaining habitat (*16*). Our results, however, show that community responses are not solely restricted to species loss, as we observed a replacement of forest specialists by species adapted to disturbance (Fig. 1, A to D) (*8*, *17*). Forest specialists make up 75.9% of all species found in areas with 100% forest cover, whereas disturbance-adapted species represent 73% of species in landscapes with ≤10% forest cover (Fig. 1, A to D). Note that the threshold observed for community integrity is caused by a change in dominance; communities above the 30% cover threshold tend to be dominated (i.e., ≥50%) by forest specialists, and communities below the threshold become dominated by disturbance-adapted species (Fig. 1, E to H).

Although the causes and consequences of local species extinction are unknown, we found a strong correlation between species sensitivity and endemism (Pearson's $r = 0.87$, $N = 79$; fig. S2) (*8*), with 70.1% of forest specialists found to be endemic to the Atlantic Forest, whereas 68.5% of disturbance-adapted species occur in other biomes (Fig. 1, A to H). Previous studies have shown that forest specialists present narrow niche breadths and high efficiency in resource exploitation, so the loss of forest specialists potentially affects trophic cascades and ecological functions, such as seed dispersal and pest control (*18*–*20*). Detailed knowledge about the functional role of many Atlantic Forest vertebrates is not available (*8*), but if we assume niche conservatism (*21*), it is possible to infer that changes in lineage composition should broadly correspond to changes across functionally important traits (*22*). Hence, we estimated the phylogenetic integrity of communities, measured as the phylogenetic similarity or fraction of branch length shared between communities present in fragmented and continuously forested landscapes (*8*, *23*). We observed that phylogenetic integrity also decreases below the 30% cover threshold (Fig. 1, M to P), which suggests that the suite of ecological functions performed by these taxa are different above and below the threshold. Our findings highlight the importance of maintaining or restoring forest cover in the Atlantic Forest above the 30% threshold, as extinction of endemic species will lead to the loss of ecological functions that only these species provide.

Upscaling our results to 143 Mha of Atlantic Forest shows that although community integrity is high inside and around protected areas, it is much reduced across the 88.2% of the biome where less than 30% forest cover remains (using 200-ha landscape units; Fig. 2) (*8*). These results reinforce the need to preserve large existing remnants, as they provide a refuge to many species (*5*) (Figs. 1 and 2), and show that the Atlantic Forest is in urgent need of restoration to ensure that biodiversity-derived ecological functions are provided across the biome.

An area of 32.11 Mha would have to be restored to increase every 200-ha landscape of Atlantic Forest to a minimum of 30% forest cover. This is arguably an unfeasible goal, given the livelihoods and needs of 130 million Brazilians living in this biome. However, if we select landscapes with forest cover approaching the threshold, restoration in rural areas becomes better value for money (*8*). This is because highly deforested areas are typically depauperate of forest specialists (*13*, *15*, *24*), and the chances of recolonization after restoration would depend on money- and time-consuming interventions such as translocation. Thus, on the basis of our results and previous prioritization frameworks (*8*, *25*), we selected all landscapes with more than 20% forest cover and calculated how much area would be required to increase these target landscapes to 30% forest cover. Following this framework, we estimate that restoring just 424,000 ha across the biome will push forest cover to 30% in 37,000 landscapes, which together encompass a total area of 7.8 Mha (table S1). Restoring to 30% forest cover will provide benefits to biodiversity but is unlikely to provide a safety net, as it will bring communities just up to the threshold. Preferably, landscapes would be restored to a level of forest cover above the threshold, but this brings additional issues because the amount of area needed for restoration increases at an average rate of 114,000 ha (SE ±2300 ha) for every 1% increase in targeted forest cover (Fig. 3 and table S1) (*8*).

The Brazilian government and local NGOs have been steadily implementing PES schemes for set-asides on private land over the years (*10*). Taking the average PES values across the biome, $132.73 ha^{-1} per year (*10*), it would cost $56.3 million per year (range $25.7 million to $91.6 million; table S1) to target enough set-asides to reach the restoration target of 30% cover in the priority landscapes, and that cost would increase by $15.1 million (SE ±$300,000) per year for every 1% increase in targeted forest cover (table S1) (*8*). Although most areas would follow natural regeneration simply by ceasing the drivers of disturbance (*26*), it has been estimated that 20% of the area considered for restoration would require active reforestation practices, with associated costs of up to $5000/ha during the first 3 years (*26*). Thus, the overall budget to reach 30% forest cover in priority landscapes is $198 million per year, or 6.5% of Brazil's annual expenditure on agricultural subsidies for the first 3 years. This

[1]Grand Challenges in the Ecosystem and Environment, Department of Life Sciences, Imperial College London, Silwood Park Campus, Ascot SL5 7PY, UK. [2]Departamento de Ecologia, Instituto de Biociências, Universidade de São Paulo, 05508-090 São Paulo SP, Brazil. [3]Departamento de Zoologia, Instituto de Biociências, Universidade de São Paulo, 05508-090 São Paulo SP, Brazil. [4]Department of Ecology, Evolution, and Behavior, University of Minnesota, St. Paul, MN 55108, USA. [5]Fundação Florestal, Rua do Horto 931, 02377-000 São Paulo SP, Brazil. [6]Departamento de Zoologia, Instituto de Biociências, Universidade Estadual Paulista, 13506-900 Rio Claro SP, Brazil. [7]Curso de Gestão Ambiental, Escola de Artes, Ciências e Humanidades, Universidade de São Paulo, 03828-000 São Paulo SP, Brazil. [8]Department of Ecology and Evolutionary Biology, University of Toronto, Toronto, Ontario M5S 3B2, Canada.
***Corresponding author. E-mail: c.banks@imperial.ac.uk**

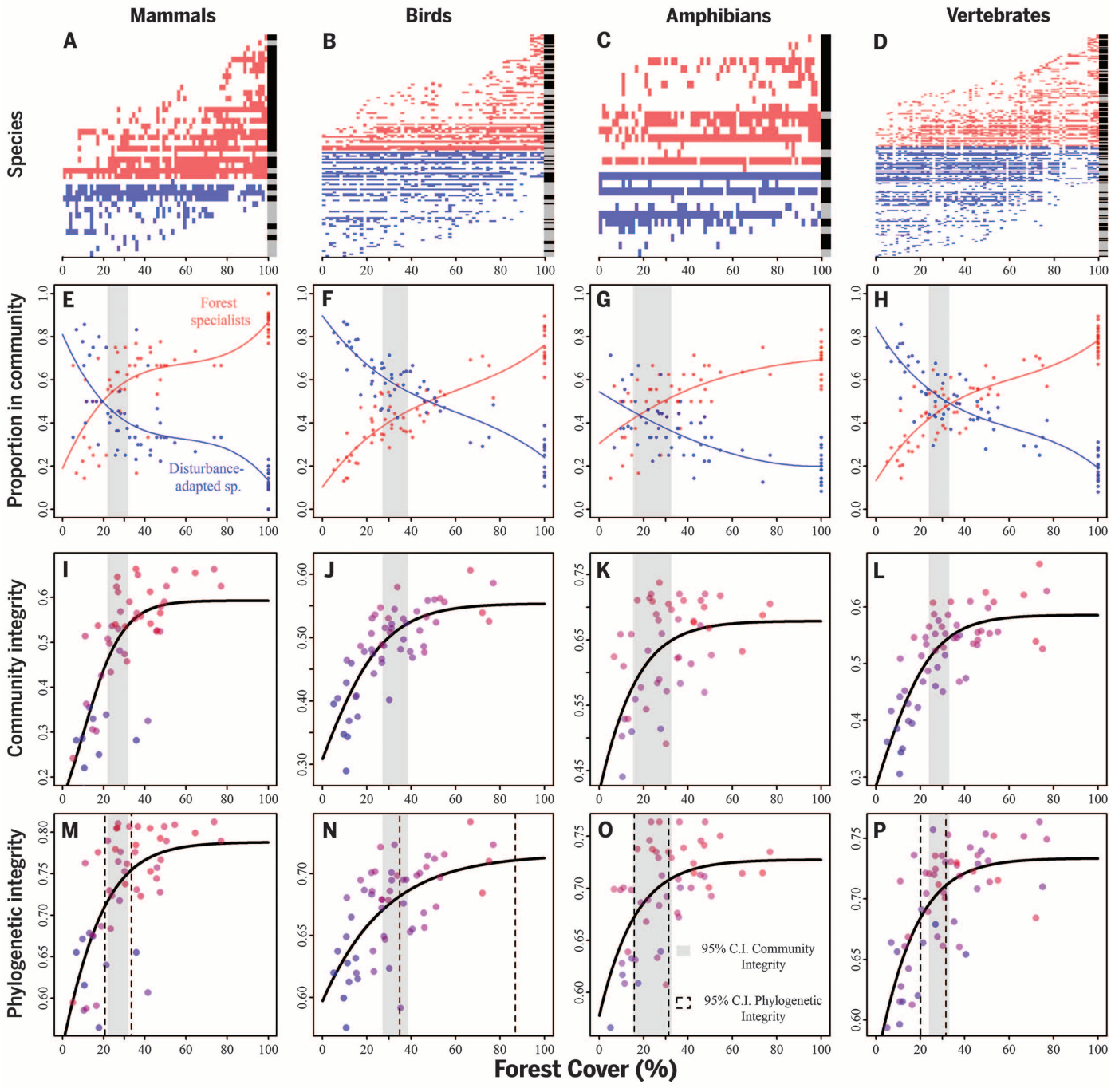

Fig. 1. Community and phylogenetic responses to forest cover in the Atlantic Forest. (**A** to **D**) Species × site matrix of mammals, birds, amphibians, and vertebrates. Sites (columns) are ordered by forest cover, and species (lines) are ordered by their preference to forest cover. Red indicates forest specialists; blue indicates disturbance-adapted species. Columns to the right of each panel represent endemism to the Atlantic Forest, with black cells showing endemic species and gray cells showing nonendemics. (**E** to **H**) Proportional change of forest specialists and disturbance-adapted species in each community. (**I** to **L**) Variation in community integrity. (**M** to **P**) Variation in phylogenetic integrity. Shaded areas in (E) to (P) indicate 95% CIs of threshold estimates obtained from community integrity. In (I) to (P), points are colored to represent the proportion of forest specialists and disturbance-adapted species. Area represented by two dashed lines in (M) to (P) indicates the CI of threshold obtained from phylogenetic integrity.

investment represents 0.0092% of Brazilian annual GDP, and the cost would reduce further to 0.0026% of Brazilian annual GDP once regeneration is under way (Fig. 3).

Creating set-asides to restore priority landscapes back to 30% forest cover may not save the most threatened species from extinction, but it would increase biodiversity and the ecological functions that species provide across rural areas (e.g., pest control and pollination) to a level similar to what is observed in protected areas (Figs. 1 and 3). Set-asides in priority landscapes would incur a loss of only 0.61% of the agricultural GDP produced in these municipalities (*8*), and payments would be targeted directly toward the very same people that would spare their land for conservation (*9*). Only rarely are the trade-offs between ecological gains and economic costs this

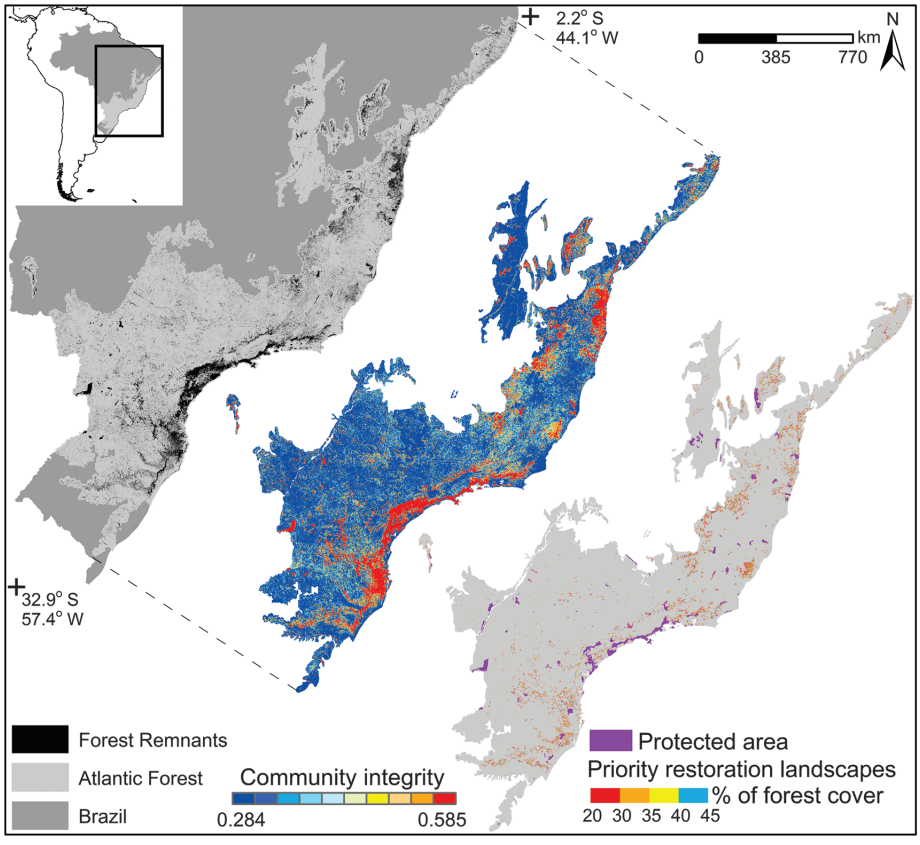

Fig. 2. Upscaling community integrity results for the Atlantic Forest of Brazil. From left to right, map of Atlantic Forest's historic distribution (gray) and current forest remnants (black), map of predicted community integrity of vertebrates across the biome, and map of priority areas for restoration (as well as current network of protected areas in purple). Large values (red) of community integrity indicate where communities have similar species composition relative to protected areas.

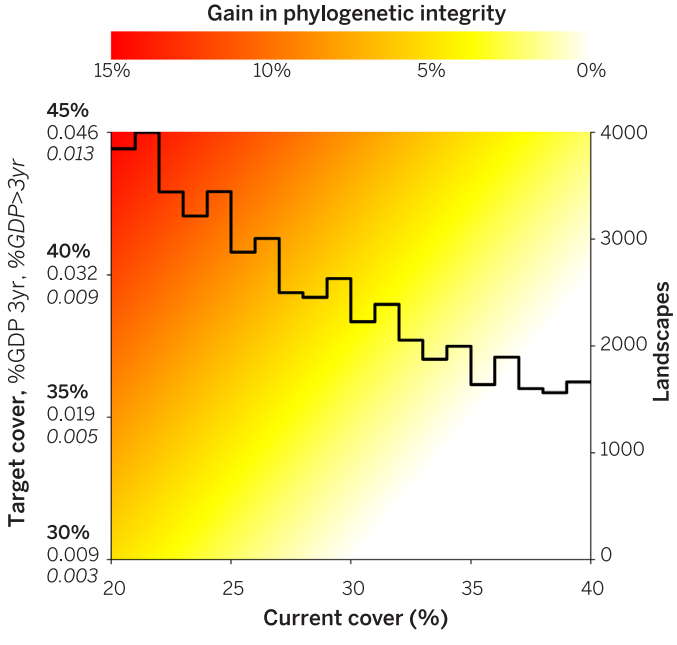

Fig. 3. Trade-offs in economic costs and ecological gains for a biome-wide set-aside program. Gains in phylogenetic integrity (measured as changes in PhyloSor index) are dependent on current percentage of forest cover and on amount of restoration targeted. Dark red indicates gains of up to 15% in phylogenetic integrity; white indicates decrease or no increase in integrity. Left *y* axis indicates target forest cover (in bold), costs relative to Brazil's GDP for the first 3 years (including PES and active restoration costs in priority landscapes), and costs for maintaining set-asides after the first 3 years (in italics). Black line depicts a histogram showing the number of existing priority landscapes in each class of forest cover.

simple; the costs relative to Brazil's GDP are low, those losing productive land are the ones that will directly benefit from PES, ecosystem services (e.g., air and soil quality, carbon storage) would be indirectly enhanced, and the ecosystem itself is one of the most charismatic in the world. At present, the Brazilian Atlantic Forest and other biodiversity hotspots are in serious danger of suffering large losses of endemic species. Our results show that this need not be the case.

REFERENCES AND NOTES

1. T. M. Brooks *et al.*, *Conserv. Biol.* **16**, 909–923 (2002).
2. A. Dobson *et al.*, *Ecology* **87**, 1915–1924 (2006).
3. J. E. Losey, M. Vaughan, *Bioscience* **56**, 311–323 (2006).
4. C. H. Sekercioğlu, G. C. Daily, P. R. Ehrlich, *Proc. Natl. Acad. Sci. U.S.A.* **101**, 18042–18047 (2004).
5. L. Naughton-Treves, M. B. Holland, K. Brandon, *Annu. Rev. Environ. Resour.* **30**, 219–252 (2005).
6. T. A. Gardner *et al.*, *Ecol. Lett.* **12**, 561–582 (2009).
7. J. Van Buskirk, Y. Willi, *Conserv. Biol.* **18**, 987–994 (2004).
8. See supplementary materials on *Science* Online.
9. J. Milder, S. Scherr, C. Bracer, *Ecol. Soc.* **15**, 4 (2010).
10. F. B. Guedes, S. E. Seehusen, *Pagamentos por Serviços Ambientais na Mata Atlântica: Lições aprendidas e desafios* (Ministério do Meio Ambiente, Brazil, 2011).
11. N. Myers, R. A. Mittermeier, C. G. Mittermeier, G. A. da Fonseca, J. Kent, *Nature* **403**, 853–858 (2000).
12. F. P. L. Melo, V. Arroyo-Rodríguez, L. Fahrig, M. Martínez-Ramos, M. Tabarelli, *Trends Ecol. Evol.* **28**, 462–468 (2013).
13. R. Pardini, A. A. Bueno, T. A. Gardner, P. I. Prado, J. P. Metzger, *PLOS ONE* **5**, e13666 (2010).
14. C. Banks-Leite, R. M. Ewers, V. Kapos, A. C. Martensen, J. P. Metzger, *J. Appl. Ecol.* **48**, 706–714 (2011).
15. M. M. Lima, E. Mariano-Neto, *For. Ecol. Manage.* **312**, 260–270 (2014).
16. H. Andren, *Oikos* **71**, 355–366 (1994).
17. C. Banks-Leite, R. M. Ewers, J. P. Metzger, *Ecology* **93**, 2560–2569 (2012).
18. D. L. Finke, W. E. Snyder, *Science* **321**, 1488–1490 (2008).
19. D. P. Edwards *et al.*, *Conserv. Biol.* **27**, 1079–1086 (2013).
20. M. Galetti *et al.*, *Science* **340**, 1086–1090 (2013).
21. J. J. Wiens *et al.*, *Ecol. Lett.* **13**, 1310–1324 (2010).
22. J. Cavender-Bares, K. H. Kozak, P. V. A. Fine, S. W. Kembel, *Ecol. Lett.* **12**, 693–715 (2009).
23. J. A. Bryant *et al.*, *Proc. Natl. Acad. Sci. U.S.A.* **105** (suppl. 1), 11505–11511 (2008).
24. A. C. Martensen, M. C. Ribeiro, C. Banks-Leite, P. I. Prado, J. P. Metzger, *Conserv. Biol.* **26**, 1100–1111 (2012).

25. L. R. Tambosi, A. C. Martensen, M. C. Ribeiro, J. P. Metzger, *Restor. Ecol.* **22**, 169–177 (2014).
26. F. P. L. Melo *et al.*, *Environ. Sci. Policy* **33**, 395–404 (2013).

ACKNOWLEDGMENTS

We thank R. Didham, T. Gardner, R. Gill, and R. Ewers for comments on the manuscript. Supported by NERC grant NE/H016228/1 (C.B.L.), CNPq research fellowship 306715/2011-2 (R.P.), FAPESP grant 05/56555-4, CNPq/BMBF grant 690144/01-6, and a Marie Curie International Incoming Fellowship within the 7th European Community Framework Programme. This article is a contribution to Imperial College's Grand Challenges in Ecosystems and the Environment initiative. The data reported in this paper can be obtained by contacting the corresponding author, and the R code used in analyses is provided in the supplementary materials. C.B.-L., R.P., L.R.T., A.A.B., R.T.B., T.H.C., M.D., A.T.I., and A.C.M. carried out the data collection; C.B.-L., L.R.T., and W.D.P. analyzed the data; C.B.-L., R.P., L.R.T., W.D.P., and J.P.M. wrote the paper.

SUPPLEMENTARY MATERIALS

www.sciencemag.org/content/345/6200/1041/suppl/DC1
Materials and Methods
Figs. S1 to S3
Tables S1 and S2
References (*27*–*40*)
Appendix

7 May 2014; accepted 23 July 2014
10.1126/science.1255768

PALEOCEANOGRAPHY

Holocene history of ENSO variance and asymmetry in the eastern tropical Pacific

Matthieu Carré,[1]* Julian P. Sachs,[2] Sara Purca,[3] Andrew J. Schauer,[4] Pascale Braconnot,[5] Rommel Angeles Falcón,[6] Michèle Julien,[7] Danièle Lavallée[8]

Understanding the response of the El Niño–Southern Oscillation (ENSO) to global warming requires quantitative data on ENSO under different climate regimes. Here, we present a reconstruction of ENSO in the eastern tropical Pacific spanning the past 10,000 years derived from oxygen isotopes in fossil mollusk shells from Peru. We found that ENSO variance was close to the modern level in the early Holocene and severely damped ~4000 to 5000 years ago. In addition, ENSO variability was skewed toward cold events along coastal Peru 6700 to 7500 years ago owing to a shift of warm anomalies toward the Central Pacific. The modern ENSO regime was established ~3000 to 4500 years ago. We conclude that ENSO was sensitive to changes in climate boundary conditions during the Holocene, including but not limited to insolation.

The El Niño–Southern Oscillation (ENSO) represents the largest natural perturbation to the global climate on an interannual time scale, affecting ecosystems and economies globally. Predicting how the amplitude and spatial pattern of ENSO will change in response to evolving radiative forcing from the buildup of greenhouse gases in the atmosphere is a scientific challenge (*1*) that requires knowledge of the character of ENSO under a range of climate boundary conditions as observed during the Holocene epoch.

A central paradigm of ENSO–mean state studies for the past decade has been that changes in insolation resulting from cyclical changes in Earth's orbital geometry exert a strong control on ENSO (*2*–*4*). This hypothesis was recently called into question by a series of coral oxygen isotope ($\delta^{18}O$) records from the Line Islands in the central Pacific showing large variability in the amplitude of ENSO variance over the past 7000 years, but no significant difference between the middle Holocene and the past millennium (*5*). Furthermore, no reconstructions of ENSO have yet been able to document changes in the spatial pattern of ENSO that are now recognized to account for an important component of its global teleconnections (*6*). We used a technique based on $\delta^{18}O$ variations in fossil mollusk shells from the coast of Peru (*7*) to quantify changes in the amplitude and spatial pattern of ENSO through the Holocene.

We reconstructed the distribution of ENSO-related sea surface temperature (SST) anomalies in the eastern tropical Pacific from monthly records of $\delta^{18}O$ values in fossil *Mesodesma donacium* shells on the coast of Peru. *M. donacium* is a fast-growing aragonitic bivalve that inhabits the surf zone of sandy beaches. Well-preserved shells were collected from radiocarbon-dated intervals at seven coastal archaeological sites (*8*) between 11.7 °S and 18.1 °S (Fig. 1, fig. S1, and table S1). *M. donacium* has been gathered and consumed by fishermen for more than 10,000 years (*9*), resulting in anthropogenic shell mounds up to 10 m in height along the Peruvian coastal desert (figs. S2 to S8). Shells were generally perfectly preserved owing to extremely arid conditions, ensuring the fidelity of $\delta^{18}O$ values (figs. S9 and S10) (*8*). Previous calibration work has demonstrated that *M. donacium* shells faithfully record 1 to 4 years of SST variability with ~1 month resolution (Fig. 1C), yielding quantitative estimates of the seasonal SST range (ΔT) in the coastal water (*10*). By analyzing a random sample of shells from a single depth interval that encompasses several decades or centuries of accumulation, the mean, variance, and skewness of coastal ΔT is obtained, as validated with modern specimens (*7*). A rigorous evaluation of the standard error for the mean, variance, and skewness of coastal ΔT was conducted with a series of pseudo-proxy Monte Carlo simulations that took into consideration the uncertainties associated with isotopic analyses, sampling within climate variability, mesoscale spatial variability, and shell growth, enabling the statistical significance of results to be ascertained (*11*).

Peruvian surf clams share similarities with corals as paleoclimate proxies in that the seasonality of SST can be resolved (*5*), and with individual foraminifera (*12*), because a sample of several specimens is required to statistically extract ENSO characteristics. *M. donacium* shells record ENSO variance resulting from La Niña anomalies and moderate El Niño anomalies but do not record extreme El Niño events. When coastal Peru SSTs warm dramatically (maximum anomaly of 7.7°C in January 1998 in Callao), mass mortality of *M. donacium* occurs. Nevertheless, the distribution of ΔT from a sample of modern shells, though truncated, accurately captures the positively skewed distribution of ENSO in the eastern Pacific (*7*). Our composite Holocene record from 180 mollusk shells and seven archaeological sites thus yields a quantitative reconstruction of mean annual SST, mean ΔT, as well as ENSO variance and skewness for coastal Peru. Because the variance of coastal Peruvian ΔT is highly correlated with the variance of SST anomalies in the Niño1+2 region [correlation coefficient (r) = 0.85], var(ΔT) in Peru can be used as a reliable indicator of ENSO variance in the eastern tropical Pacific (*7*).

Mean annual SST was significantly lower 4.5 thousand years ago (ka) to 9.6 ka than today, especially in southern Peru, where SSTs were ~3°C cooler (Fig. 2A). These cooler conditions imply an increase in the intensity of coastal upwelling (*13*, *14*). Although highly variable, the seasonal range of SST (ΔT) was significantly reduced compared with the late 20th century during most of the Holocene, with reductions up to ~30% (equivalent to ~1.1°C) 0.5, 4.7, 8.5, and

[1]UM2-CNRS–Institut pour la Recherche et le Développement (IRD), Institut des Sciences de l'Evolution de Montpellier, UMR 5554, Place Eugène Bataillon, 34095 Montpellier, France. [2]School of Oceanography, University of Washington, Post Office Box 355351, Seattle, WA 98195, USA. [3]Instituto del Mar del Perú (IMARPE), Esquina Gamarra y general Valle S/N, Callao, Perú. [4]Department of Earth and Space Sciences, University of Washington, Post Office Box 351310, Seattle, WA 98195, USA. [5]Institut Pierre-Simon Laplace/Laboratoire des Sciences du Climat et de l'Environnement, unité mixte CEA-CNRS–Université de Versailles Saint-Quentin-en-Yvelines, Orme des merisiers, Bâtiment 712, 91191 Gif sur Yvette, France. [6]Ministerio de Cultura, Museo de sitio de Pachacamac, Lurín, Lima, Perú. [7]Archéologies et Sciences de l'Antiquité, UMR 7041, Maison René Ginouvès, 21 Allée de l'Université, 92023 Nanterre, France. [8]Archéologie des Amériques, UMR 8096, Maison René Ginouvès, 21 Allée de l'Université, 92023 Nanterre, France.
*Corresponding author. E-mail: matthieu.carre@univ-montp2.fr

9.5 ka (Fig. 2B). Furthermore, ENSO variability, as derived from the variance of ΔT, was higher in the late 20th century than at any other sampled interval of the Holocene, even excluding the influence of the 1982–1983 and 1997–1998 extreme El Niño events (Fig. 3A). The lowest ENSO variance in the eastern tropical Pacific occurred at ~4.7 ka (55% reduction, 82% confidence level) (Fig. 3A).

A Holocene minimum in ENSO variance 4 to 5 ka is supported by a sedimentary record of $\delta^{18}O$ values in individual planktonic foraminifera from near the Galápagos that also indicates highly variable conditions throughout the Holocene, interrupted by a period of low foraminiferal $\delta^{18}O$ variance 4 to 5 ka (Fig. 3C) (*12*). In addition to interannual SST variability, however, the variance of foraminiferal $\delta^{18}O$ in marine sediments is influenced by decadal variability and changing precession-driven seasonality. In the central Pacific, coral $\delta^{18}O$ records indicate lower than modern ENSO variance during the Holocene, with large variations before 6 ka and after 3 ka and a minimum in ENSO variance 3 to 5 ka (*5*). Although the latter result is not statistically significant in light of the full data set (*5*), its robustness is now increased by the consistent variance reduction observed in our Peru mollusk record and the foraminiferal record from the Galapagos (*12*). Further support for low ENSO variance in the 4- to 5-ka time period comes from a 175-year coral $\delta^{18}O$ record from Christmas Island, which indicated a 79% reduction of ENSO variance in the central Pacific ~4.3 ka (*15*). A network of evidence thus supports the occurrence of a substantial multicentennial reduction of ENSO variance 4 to 5 ka across the Niño3.4 and Niño1+2 domains.

ENSO variance recorded by Peru mollusks 6 to 10 ka was variable but not statistically different from the Late Holocene. Our reconstruction combined with early Holocene dates of flood deposits in coastal Peru (*16*–*18*) challenge the hypothesis of little or no ENSO variance before ~5 ka (*19*–*21*)—a conclusion based largely on the analysis of clastic sediments in Lake Pallcacocha (*19*, *20*). However, clastic sediments in high Andean Lakes have recently been reinterpreted in terms of soil erosion from mountain glacier activity rather than from rainfall events associated with ENSO (*22*). The only reliable marine evidence for inactive ENSO in the early to middle Holocene is provided by corals from Papua New Guinea (*23*). Apparent disagreements between ENSO records from the Western and Eastern Pacific may in fact be indicative of changes in the spatial pattern of ENSO.

Two spatial modes of ENSO variability have been described, defined by maximum SST anomalies localized in the central Pacific (CP) or eastern Pacific (EP) (*24*, *25*). The EP mode tends to produce strong El Niño warming events in the East and moderate La Niña events. This well-known asymmetry between El Niño and La Niña events results in a positively skewed distribution of SST anomalies (Fig. 1A). The CP mode tends to produce moderate El Niño events centered in

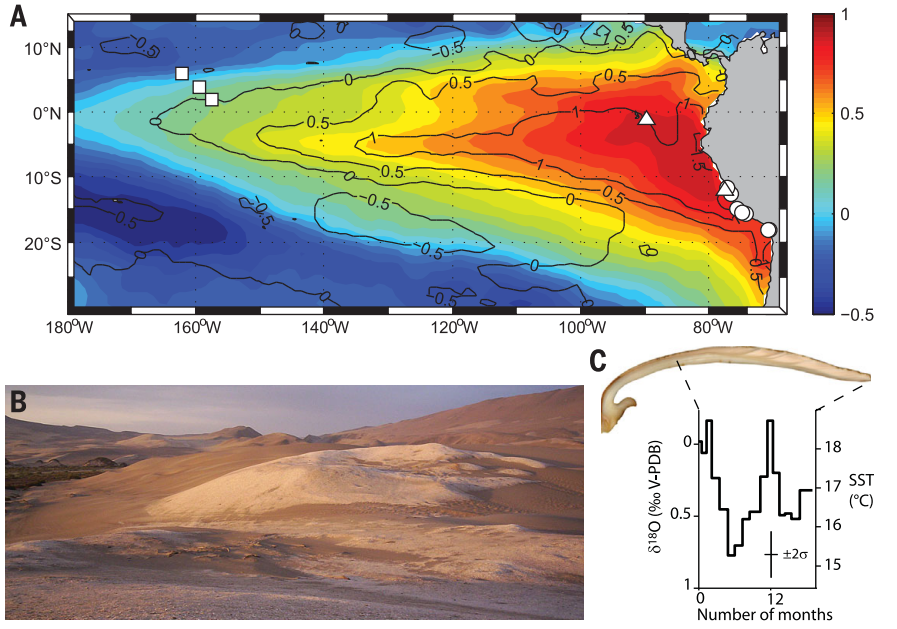

Fig. 1. The Peruvian archaeological shell middens. (**A**) Map of the central and eastern tropical Pacific indicating the location of shell middens (circles), sediment cores (triangles), and coral records (squares) discussed in the text. The skewness of monthly SST anomalies for the 1950–2010 period is represented by isolines, and the EP pattern of ENSO as defined in (*32*) is represented by color shades. For this analysis, the NOAA NCEP Global Reyn_SmithOIv2 product that merges satellite and station data (*33*) was used (NCEP, National Centers for Environmental Prediction). (**B**) Picture of the northern part of the Ica-IS2 archaeological shell midden in the lower Ica valley, Peru (*8*). (**C**) Illustrative example of a *M. donacium* cross section and its associated monthly isotopic record converted to SST (shell ICA-1) (*8*).

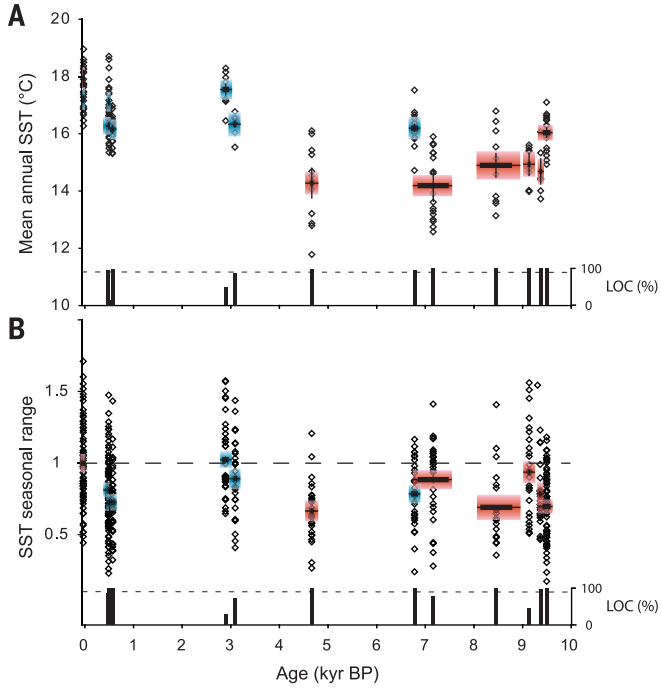

Fig. 2. Holocene reconstruction of mean annual SST and seasonal SST range from fossil mollusk $\delta^{18}O$ values on the Peru coast. (**A**) Mean SST values obtained from individual shells (open diamonds). For each shell midden, the average SST was represented over the occupation time span (thick horizontal line, prolonged by a thin line for the 1σ calibration interval). The standard error (±1σ) of reconstructed SSTs is represented by blue bars for the central coast and red bars for the southern coast of Peru (fig. S1). A second error bar (±1σ) incorporates any potential systematic error introduced by calibration of the mollusk $\delta^{18}O$ SST proxy plus uncertainty in the correction for ice volume effects on ocean $\delta^{18}O$ (*8*, *11*). The level of confidence (LOC) that reconstructed values of mean annual SST are significantly different from modern SSTs (Student's *t* test) is indicated by black bars in the bottom of both (A) and (B), with the dotted line indicating the 90% LOC. (**B**) Seasonal ranges of *M. donacium* shell $\delta^{18}O$ normalized to the modern mean value. Individual shells record one to eight successive ΔT values (open diamonds) (*8*). For each shell midden, average values and standard errors were represented as in (A). The horizontal dashed line represents modern conditions. LOC are indicated as in (A).

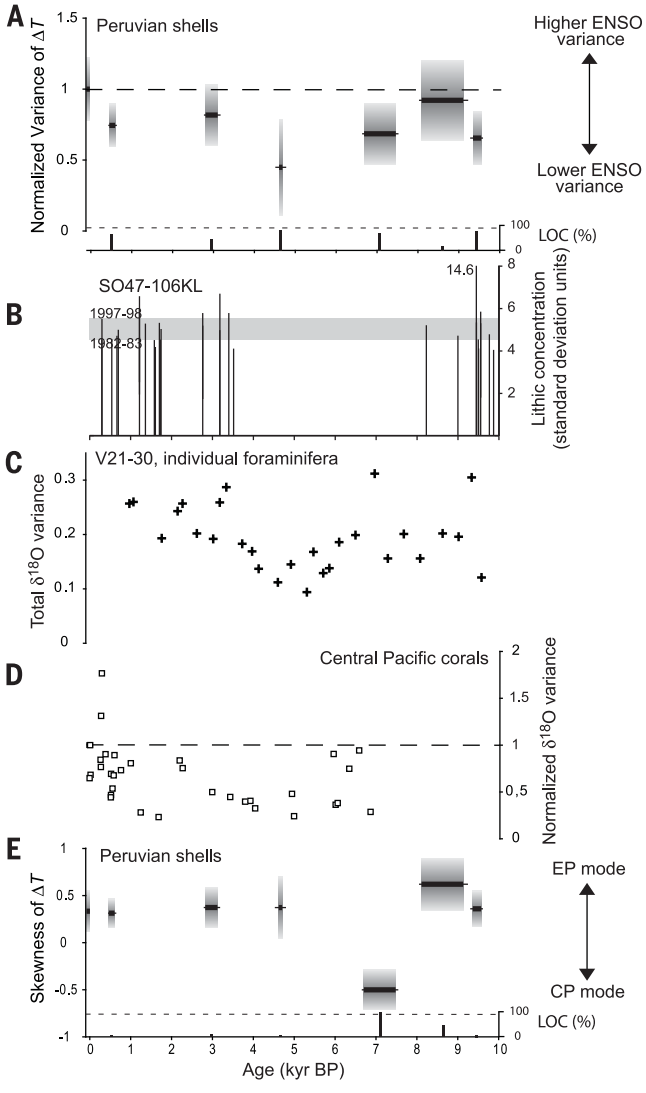

Fig. 3. Holocene records of ENSO from the eastern and central tropical Pacific Ocean. (**A**) Normalized variance of ΔT values in mollusk shell samples (this study) indicating ENSO variance in the Niño1+2 region, with ±1σ standard errors (gray boxes). LOC are indicated as in Fig. 2A. (**B**) Extreme flood events in coastal Peru inferred from lithic concentrations in excess of 4σ of the detrended signal in the SO147-106KL sediment core (*26*) (supplementary text). The level for the very stong El Niño events in 1982–1983 and 1997–1998 is indicated with gray shading for comparison. (**C**) $\delta^{18}O$ variance of individual *Globigerinoides ruber* planktonic foraminifera in core V21-30 from near the Galápagos (*12*). (**D**) ENSO variance inferred from $\delta^{18}O$ values of fossil corals from the Northern Line Islands of Palmyra, Fanning, and Christmas (*5*), normalized by the modern variance at each location (*8*). (**E**) Skewness of ΔT in *M. donacium* shell samples (this study) with standard errors (±1σ), indicating the relative contribution of CP and EP ENSO modes. LOC is shown as in Fig. 2A.

the CP and strong La Niña events, resulting in a negatively skewed distribution of SST anomalies in Peru as shown by instrumental data (*24*–*26*). The skewness of ENSO anomalies in fossil shell samples thus tracks past changes in the dominant spatial pattern of ENSO variability (*8*). Skewness values in the fossil record are positive and similar to modern conditions during most of the Holocene, except for the period 6.7 to 7.5 ka, when a significant shift (95% confidence level) toward negative skewness occurred (Fig. 3E). This result implies that the SST variability in the EP at that time was driven by cold anomalies, and that warm anomalies in the Niño1+2 region were less frequent and/or intense. A possible explanation for this pattern may be a predominantly CP mode of ENSO 6.7 to 7.5 ka.

This hypothesis is supported by a record of flood events from the Peru margin (Fig. 3B) (*27*). High lithic concentrations (exceeding 4σ of the signal) in a sediment core from the continental shelf off central Peru record coastal floods due to extreme El Niño events that are typical of the EP mode (*28*). By indicating extreme El Niño events, this proxy thus fills the gap of ENSO variance that is not recorded by Peruvian mollusk shells (supplementary text). That record clearly shows the occurrence of eight large flood events before 8 ka and 14 after 4 ka (Fig. 3B), which is also consistent with earlier studies of flood-related debris flow deposits in Peru (*16*, *17*, *29*). This is in agreement with the mollusk $\delta^{18}O$ data indicating strong ENSO activity dominated by the EP mode before 8 ka and after 4 ka. From 6.7 to 7.5 ka, on the other hand, the complete absence of flood events contrasts with the substantial though weaker ENSO variance reconstructed from mollusk shells. This apparent disagreement can be most simply explained by a predominance of the CP mode of ENSO at that time, as implied by the negative skewness of the ΔT distribution (Fig. 3E). CP El Niño events have a different teleconnection pattern and do not generate rainfall anomalies on the Peruvian coast.

A central question in climate science is the extent to which changes in the climatic mean state influence ENSO variability. Long unforced climate simulations exhibit multidecadal, internally generated changes in ENSO behavior (*30*). Our data indicate that changes in the character of ENSO during the Holocene persisted for centuries, exceeding the time scale of model-generated internal variability. We therefore surmise that ENSO is sensitive to external forcing. Climate models forced by 6- and 9.5-ka insolation produce a cooling and reduced ΔT in the eastern Pacific, along with reduced ENSO variance (*3*, *4*). The simulated impact of insolation is consistent with the mean annual and seasonal range of SST derived from Peru mollusks, but not for ENSO variance, which the mollusks indicate was high in the early Holocene. Climate simulations have demonstrated that a freshwater flux into the North Atlantic could offset the impact of insolation on ENSO in the early Holocene (*31*). Our data support this scenario and imply that any tendency toward lower ENSO variance during the mid-Holocene insolation regime may have been counteracted 6.7 to 10 ka by the influence of melting ice sheets (*31*). Although the low ENSO activity 4 to 5 ka is consistent with precessional forcing, the shift of ENSO asymmetry 6.7 to 7.5 ka points to factors within the climate system influencing changes in the spatial pattern of ENSO.

REFERENCES AND NOTES

1. A. Santoso *et al.*, *Nature* **504**, 126–130 (2013).
2. A. C. Clement, R. Seager, M. A. Cane, *Paleoceanography* **14**, 441–456 (1999).
3. W. Zheng, P. Braconnot, E. Guilyardi, U. Merkel, Y. Yu, *Clim. Dyn.* **30**, 745–762 (2008).
4. Y. Luan, P. Braconnot, Y. Yu, W. Zheng, O. Marti, *Clim. Past* **8**, 1093–1108 (2012).
5. K. M. Cobb *et al.*, *Science* **339**, 67–70 (2013).
6. T. Lee, M. J. McPhaden, *Geophys. Res. Lett.* **37**, L14603 (2010).
7. M. Carré, J. P. Sachs, A. J. Schauer, W. E. Rodríguez, F. C. Ramos, *Palaeogeogr. Palaeoclimatol. Palaeoecol.* **371**, 45 (2013).
8. Materials and methods are available as supplementary materials on *Science* Online.
9. D. H. Sandweiss *et al.*, *Science* **281**, 1830–1832 (1998).
10. M. Carré *et al.*, *Palaeogeogr. Palaeoclimatol. Palaeoecol.* **228**, 4–25 (2005).
11. M. Carré, J. P. Sachs, J. M. Wallace, C. Favier, *Clim. Past* **8**, 433–450 (2012).
12. A. Koutavas, S. Joanides, *Paleoceanography* **27**, PA4208 (2012).
13. M. Carré *et al.*, *Quat. Int.* **253**, 55–66 (2012).
14. J. Sadler *et al.*, *Geochem. Geophys. Geosyst.* **13**, Q01015 (2012).
15. H. V. McGregor *et al.*, *Nat. Geosci.* **6**, 949–953 (2013).
16. M. Fontugne, P. Usselmann, D. Lavallée, M. Julien, C. Hatté, *Quat. Res.* **52**, 171–179 (1999).
17. D. K. Keefer, M. E. Moseley, S. D. deFrance, *Palaeogeogr. Palaeoclimatol. Palaeoecol.* **194**, 41–77 (2003).
18. D. H. Sandweiss *et al.*, in *Climate Change and Cultural Dynamics: A Global Perspective on Mid-Holocene Transitions*, D. G. Anderson, K. A. Maasch, D. H. Sandweiss, Eds. (Academic Press, New York, 2007) pp. 25–50.
19. D. T. Rodbell *et al.*, *Science* **283**, 516–520 (1999).
20. C. M. Moy, G. O. Seltzer, D. T. Rodbell, D. M. Anderson, *Nature* **420**, 162–165 (2002).
21. J. L. Conroy, J. T. Overpeck, J. E. Cole, T. M. Shanahan, M. Steinitz-Kannan, *Quat. Sci. Rev.* **27**, 1166–1180 (2008).
22. D. T. Rodbell, G. O. Seltzer, B. G. Mark, J. A. Smith, M. B. Abbott, *Quat. Sci. Rev.* **27**, 1612–1626 (2008).
23. A. W. Tudhope *et al.*, *Science* **291**, 1511–1517 (2001).
24. H.-Y. Kao, J.-Y. Yu, *J. Clim.* **22**, 615–632 (2009).
25. S. I. An, F. F. Jin, *J. Clim.* **17**, 2399–2412 (2004).
26. B. Dewitte *et al.*, *Deep Sea Res. Part II Top. Stud. Oceanogr.* **77-80**, 143–156 (2012).
27. B. Rein *et al.*, *Paleoceanography* **20**, n/a (2005).
28. B. Rein, *Quat. Int.* **161**, 56–66 (2007).
29. L. E. Wells, *Geology* **18**, 1134 (1990).

30. A. T. Wittenberg, *Geophys. Res. Lett.* **36**, L12702 (2009).
31. P. Braconnot, Y. Luan, S. Brewer, W. Zheng, *Clim. Dyn.* **38**, 1081–1092 (2012).
32. K. Takahashi, A. Montecinos, K. Goubanova, B. Dewitte, *Geophys. Res. Lett.* **38**, L10704 (2011).
33. R. W. Reynolds, N. A. Rayner, T. M. Smith, D. C. Stokes, W. Wang, *J. Clim.* **15**, 1609–1625 (2002).

ACKNOWLEDGMENTS

This work was supported by the French Pérou-Sud archaeological project (D.L.), by the University of Washington–National Oceanic and Atmospheric Administration (NOAA) Joint Institute for the Study of Atmosphere and Ocean through a postdoctoral fellowship (M.C.), by the U.S. National Science Foundation under grant NSF-ATM-0811382 (J.P.S.), by NOAA under grant NOAANA08OAR4310685 (J.P.S.), by the French National Research Agency under EL PASO grant 10-Blan-608-01 (P.B.), and by the French Institut National des Sciences de l'Univers with accelerator mass spectrometry dating (M.C.). We thank I. Bentaleb and H. Vonhof for their support in the early phase of this work, A. Portal for scanning electron microscopy observations at UM2, and M. Fontugne for his help and for providing the H4 shell sample. We are grateful to N. Mitma García, G. d'Herbes, J. Sadler, and M. Azzoug for technical assistance with sample preparation and to A. Mitma García for his help with fieldwork. The data reported in this paper are tabulated in the supplementary materials.

SUPPLEMENTARY MATERIALS

www.sciencemag.org/content/345/6200/1045/suppl/DC1
Materials and Methods
Figs. S1 to S11
Tables S1 to S3
Supplementary Text
References (*34*–*57*)
Data Tables S1 to S3

13 February 2014; accepted 14 July 2014
Published online 7 August 2014;
10.1126/science.1252220

HUMAN MICROBIOTA

Longitudinal analysis of microbial interaction between humans and the indoor environment

Simon Lax,[1,2]* Daniel P. Smith,[1,2,3]* Jarrad Hampton-Marcell,[1,2] Sarah M. Owens,[2,4] Kim M. Handley,[1,2] Nicole M. Scott,[1,2] Sean M. Gibbons,[2,5] Peter Larsen,[6,7] Benjamin D. Shogan,[8] Sophie Weiss,[9,10] Jessica L. Metcalf,[9] Luke K. Ursell,[9,11] Yoshiki Vázquez-Baeza,[9,11,12] Will Van Treuren,[9] Nur A. Hasan,[13,14] Molly K. Gibson,[15,16,17] Rita Colwell,[13,14] Gautam Dantas,[15,16,17] Rob Knight,[9,11,18] Jack A. Gilbert[1,2,5]†

The bacteria that colonize humans and our built environments have the potential to influence our health. Microbial communities associated with seven families and their homes over 6 weeks were assessed, including three families that moved their home. Microbial communities differed substantially among homes, and the home microbiome was largely sourced from humans. The microbiota in each home were identifiable by family. Network analysis identified humans as the primary bacterial vector, and a Bayesian method significantly matched individuals to their dwellings. Draft genomes of potential human pathogens observed on a kitchen counter could be matched to the hands of occupants. After a house move, the microbial community in the new house rapidly converged on the microbial community of the occupants' former house, suggesting rapid colonization by the family's microbiota.

The global trend toward urbanization has increasingly bound humanity, as a species, to the indoor environment (*1*, *2*). We spend much of our time in our homes but know little about how microbial transmission influences the home and its occupants. Each human maintains a specific microbial "fingerprint" (*3*–*7*), which should transfer to a new indoor space with skin shedding, respiratory activity, and skin-surface contact (*8*), the latter of which can transfer millions of microbial cells per event (*9*). The microbial diversity of the home likely affects immune defense (*10*) and disease transmission (*11*) among its residents, so that tracking how people microbially interact with the indoor environment may provide a "road map" to defining the health in our homes.

In the Home Microbiome Project (www.homemicrobiome.com), we microbially monitored seven ethnically diverse U.S. families and their homes over 6 weeks by sampling their skin- and home-surface bacterial communities. Eighteen participants were trained in the collection of 1625 microbial samples from body and home sites of interest over a 4- to 6-week period from 10 houses (table S1), three dogs, and one cat. For three families, samples were taken immediately before and after moving to a new home. Approximately 15 million high-quality 16*S* rRNA V4 amplicons represented 136,957 distinct operational taxonomic units (OTUs) (97% nucleotide identity). We subsampled this database at 2500 sequences per sample, omitting OTUs represented by <10 reads, which yielded 4 million sequences comprising 21,997 OTUs (97% identity) from 1586 samples.

Samples from different sites within the same home differed less than samples from the same site in different homes [analysis of similarities (ANOSIM) $R = 0.210$, $P < 0.0001$ versus $R = 0.408$, $P < 0.0001$]. A density plot of weighted UniFrac distances between all home and human samples (Fig. 1A) showed that microbial communities of human hands, noses, and bare feet resemble those of home surfaces. However, microbial communities found on home surfaces varied less than those found on humans. In each analyzed home surface, the microbial communities of different houses differed significantly ($P < 0.0001$) (Fig. 1B), but the extent depended on the surface sampled and was highest for floor environments (ANOSIM $R = 0.757$ and 0.716 for kitchen and bedroom floors, respectively), whereas doorknobs were the most similar ($R = 0.379$ for front and 0.402 for bedroom doorknob). ANOSIM tests of the differences between the microbial community structure (weighted UniFrac) of the surfaces of each of the three pre- and postmove house combinations (homes 5, 6, and 7) were insignificant, suggesting rapid colonization of the new home by the microbial signature of the family. Strikingly, one of the premove homes was a hotel room.

Humans sharing a home were more microbially similar than those not sharing a home, with samples taken from the same individual having the greatest similarity (Fig. 1C). Of the three human environments analyzed in this study, foot samples were differentiated most by home ($R = 0.542$) and least by hand samples ($R = 0.261$). Hand samples were also least differentiated by individual ($R = 0.406$), and nose samples differed most between individuals ($R = 0.683$). ANOSIM statistics were robust to sequencing depth, with rarefaction to even 100 reads per

[1]Department of Ecology and Evolution, University of Chicago, 1101 E 57th Street, Chicago, IL 60637, USA. [2]Institute for Genomic and Systems Biology, Argonne National Laboratory, 9700 South Cass Avenue, Argonne, IL 60439, USA. [3]Alkek Center for Metagenomics and Microbiome Research, Department of Molecular Virology and Microbiology, Baylor College of Medicine, Houston, TX 77030, USA. [4]Computation Institute, University of Chicago, Chicago, IL 60637, USA. [5]Graduate Program in Biophysical Sciences, University of Chicago, Chicago, IL 60637, USA. [6]Department of Bioscience, Argonne National Laboratory, 9700 South Cass Avenue, Argonne, IL 60439, USA. [7]Department of Bioengineering, University of Illinois at Chicago, Chicago, IL 60607, USA. [8]Department of Surgery, University of Chicago Medicine, 5841 South Maryland Avenue, Chicago, IL 60637, USA. [9]Biofrontiers Institute, University of Colorado, 3415 Colorado Avenue, Boulder, CO 80304, USA. [10]Department of Chemical and Biological Engineering, University of Colorado at Boulder, Boulder, CO 80304, USA. [11]Department of Chemistry and Biochemistry, University of Colorado at Boulder, Boulder, CO 80304, USA. [12]Department of Computer Science, University of Colorado at Boulder, Boulder, CO 80304, USA. [13]CosmosID, 387 Technology Drive, Suite 3119, College Park, MD 20742, USA. [14]Center for Bioinformatics and Computational Biology, University of Maryland Institute for Advanced Computer Studies, University of Maryland College Park, College Park, MD 20742, USA. [15]Center for Genome Sciences and Systems Biology, Washington University School of Medicine, St. Louis, MO 63108, USA. [16]Department of Pathology and Immunology, Washington University School of Medicine, St. Louis, MO 63110, USA. [17]Department of Biomedical Engineering, Washington University, St. Louis, MO 63130, USA. [18]Howard Hughes Medical Institute, Boulder, CO 80309, USA.
*These authors contributed equally to this work and are listed in alphabetical order. **†Corresponding author. E-mail: gilbertjack@anl.gov**

sample having little effect on the observed strength of differentiation (fig. S1A).

A third of all abundant OTUs (564 OTUs with >500 reads) had relative abundances that did not significantly differ between human and inanimate environments [nonparametric *t* test with false discovery rate (FDR) correction >0.05; ρ = 0.88] (Fig. 2A). Abundant OTUs were less likely to differ significantly in abundance between human and home surfaces when homes were analyzed individually and rarer OTUs (100 reads/OTU) were included (average = 60% undifferentiated OTUs) (fig. S2A). Although relative OTU abundances always correlated tightly between human and home environments, they varied in their correlations with pets (fig. S2B).

Only about one third of OTUs were detected in all three sources, yet these 7200 OTUs composed between 93.6 and 97.8% of sequences in each source (Fig. 2B). OTUs detected exclusively in a single source, although numerous (4137 OTUs), composed <0.6% of sequences in each sample.

Relative abundances of dominant bacterial phyla differed among sources (Fig. 2C, split by sample in fig. S3). Firmicutes and Actinobacteria were enriched in human samples relative to the home, Proteobacteria dominated home and pet samples, whereas Bacteroidetes were abundant in pets. However, the relative abundances of the nine most abundant bacterial classes had no significant relationship with the number of sources that shared them (ANOSIM $P > 0.05$) (Fig. 2D). Pairwise comparison of OTU sharing between surfaces across all homes revealed the greatest phylotype overlap between the two floor environments, with the nose sharing the least OTUs with other surfaces (Fig. 2E). The number of OTUs shared by the surfaces with the greatest overlap and by the surfaces with the least overlap differed only by a factor of two.

We tested whether microbial community profiles could identify the house or surface a sample originated from by using random forest classifiers (table S2). Floor samples were highly diagnostic of the family associated with that sample (ratios of random error to model error of 53.62 and 40.17 for kitchen and bedroom floors, respectively), and even considering all home surface samples together, the family that a sample was taken from was easily predicted (error ratio of 19.91). Models trained to predict the surface type from which a sample was taken were comparatively unsuccessful (error ratio of 3.29), with less predictive accuracy than that of those trained to predict family origin using broader taxonomic groupings. Families 5, 6, and 7 showed no significant difference between pre- and post-move

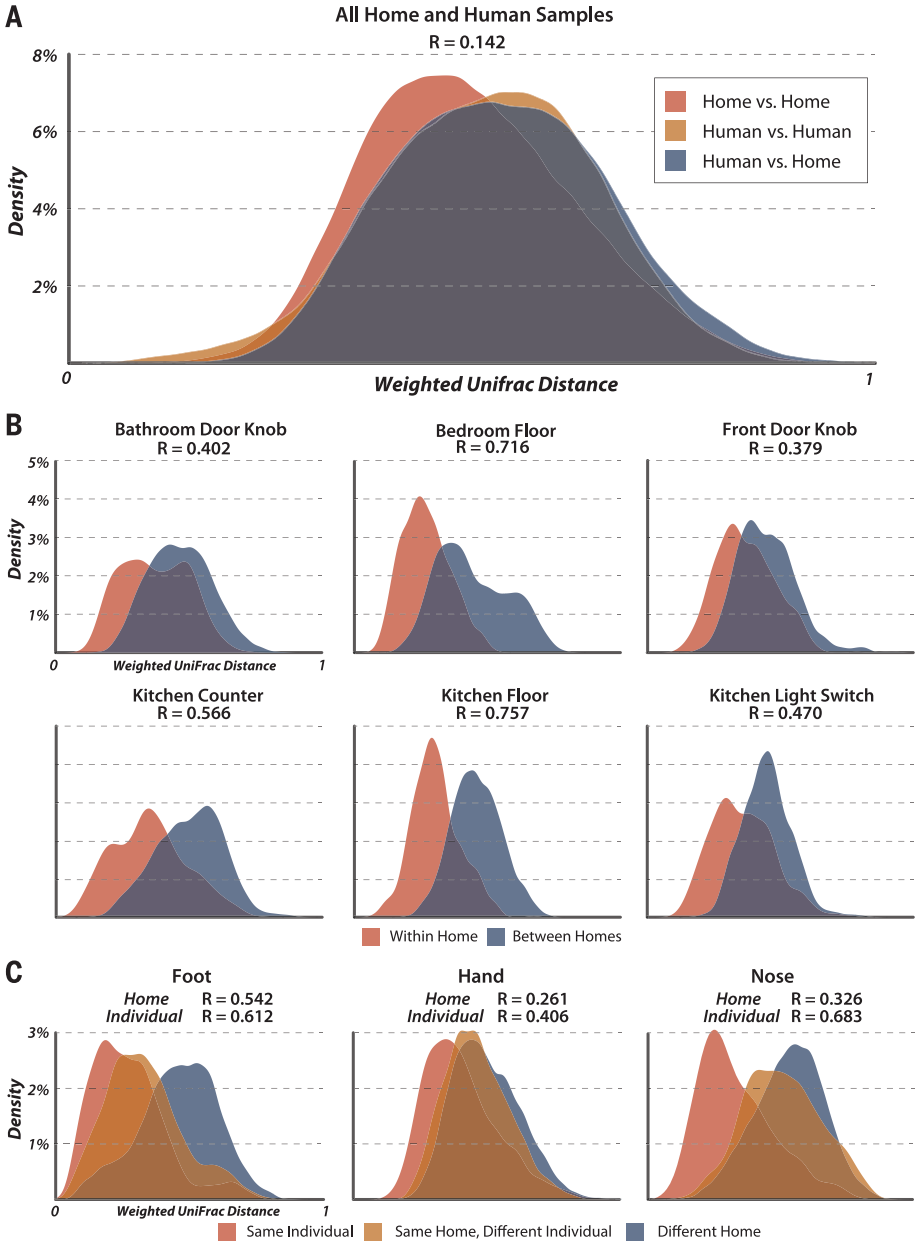

Fig. 1. Differentiation in microbial community structure between homes and individuals. Density plots comparing the distributions of weighted UniFrac distances calculated within and between various criteria with accompanying ANOSIM tests of differentiation (all *P* values are less than 0.0001 based on 10,000 permutations of the randomized data set). (**A**) Distribution of distances calculated between two human samples, between two home samples, and between a human sample and a home sample. An ANOSIM test on the effect of source produced a low *R* value of 0.142, suggesting that home and human surfaces share a large degree of their microbial communities. (**B**) Distribution of distances for within-home and between-home comparisons of all samples taken from individual home surfaces. (**C**) Distribution of distances between human samples for the three sampled surfaces. Comparisons are segregated by whether a sample was compared with another from the same person, a sample taken from an occupant of the same house, or a sample taken from a resident of a different home. ANOSIM results are for tests on the effect of the home the sample was taken from (top) and of the individual the sample was taken from (bottom).

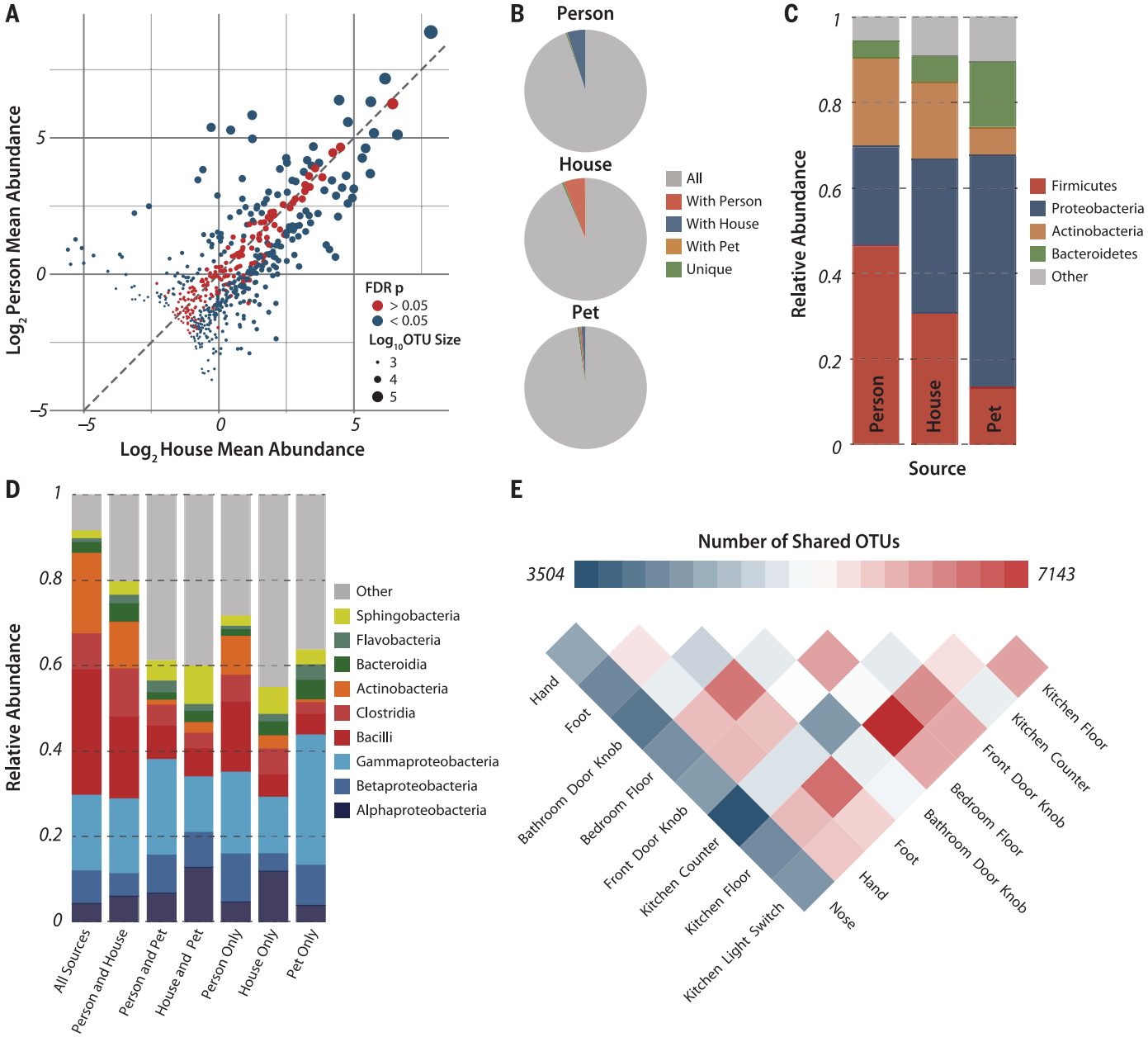

Fig. 2. Widespread sharing of microbial taxa between human and home surfaces. (**A**) Plot of $\log_2$-transformed average relative abundances in the human and home environments for all OTUs in the study with greater than 500 reads. OTUs are colored by whether their average relative abundance is significantly different between the home and person environments based on the FDR-corrected *P* value from a nonparametric *t* test run with 1000 permutations and are sized according to their $\log_{10}$-transformed number of reads. The dashed line is $y = x$, indicating an equal average relative abundance. (**B**) Fraction of all reads from within a source belonging to OTUs shared with other sources, demonstrating the ubiquitous sharing of OTUs between homes and the humans and pets that occupy them. The percent of reads that cluster within source-specific OTUs is less that 0.6% for all three sources. (**C**) Taxonomic summary of observed relative abundance of abundant phyla across all samples divided by source. (**D**) Taxonomic summary of observed relative abundance of taxa at class level for all reads in the study by source-specific OTU overlap. (**E**) Shared phylotypes heatmap for individual surfaces after consolidation of samples taken from the same surface type across temporal sampling series and homes. Pooled samples were rarified to an even depth of 277,500 reads.

homes, with error ratios of <1.75 for each model ($P > 0.05$). The relative success of predicting family of origin, even when models are trained on broader taxonomic levels, suggests that even error-prone reads from degraded DNA might still be a strong signal of an individual family's microbiota. Rarefaction to lower sequencing depth resulted in a steep decline in the models' ability to classify the home a sample was taken from (fig. S1B), suggesting that greater sequencing depth than used in this study might substantially strengthen the models' predictive ability.

We matched human-associated microbial communities to home surfaces using a Bayesian technique known as SourceTracker (Fig. 3) (*12*). Hand samples were pooled by family and considered "vectors" to the bathroom doorknob, front doorknob, and kitchen light switch "recipient" communities. Bare-foot samples were pooled by family and treated as vectors for the bedroom and kitchen floor communities. On average, 76.7% of models successfully attributed the recipient community to the correct vector (68.6% of hand samples were identified as vectors to the correct home's kitchen light switch; 82.9% of pooled family foot samples were identified as vectors to the correct home's bedroom floor). We also estimated the

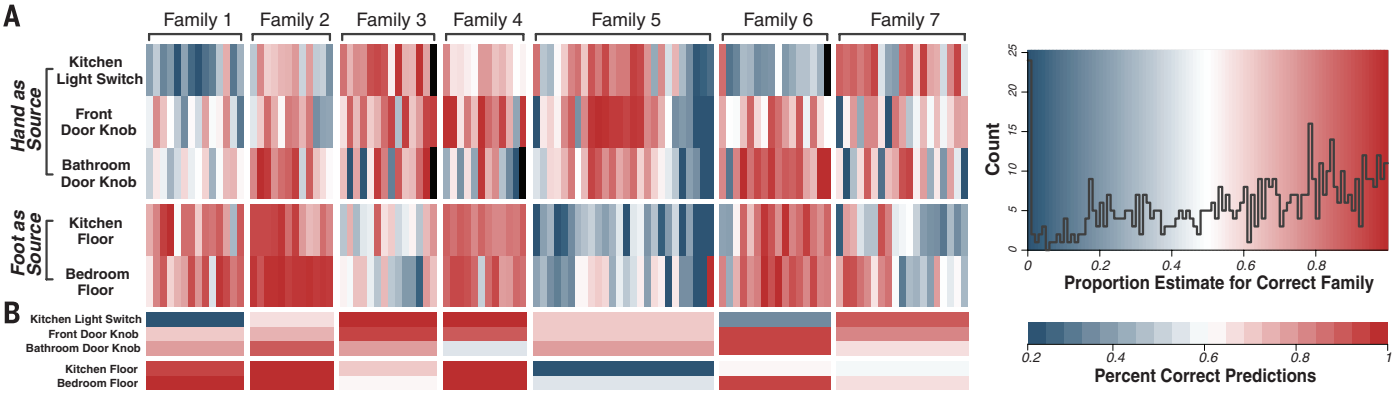

Fig. 3. Summary of predictive accuracy of SourceTracker models. (**A**) Percent composition estimate for the correct source for each home surface sample in the study. Samples within each block are ordered by collection date, and black boxes occur where a sample is missing because it did not pass quality filtering standards. Across all surfaces, the models averaged a 59% prediction for the correct source. (**B**) Heatmap of model success across individual surface time series. The model was considered to be successful when the proportion of the sink community attributed to the correct source was greater than that attributed to any other source.

contribution of individual occupants to their home's surface communities, which appears to be highly variable between surfaces, between homes, and over time. The effect of an individual leaving his or her residence for three sampling days, as occurred in homes 1 and 4, resulted in a decline in that individual's predicted contribution to a number of the home surfaces, which varied between homes, during their absence (fig. S4). This suggests that the human microbiome signature on home surfaces (such as the bathroom, front doorknob, and kitchen counter) decays or is replaced rapidly. Because different surfaces respond differently to a human leaving, careful sampling of each surface could provide a metric for assessing the time course of events related to that house and those persons.

We tested the direction of microbial transfer among surfaces in the four homes where the subjects did not move houses using dynamic Bayesian networks (fig. S5 and table S3). Humans were more likely to be sources of OTUs than were physical surfaces, with an average of 26 taxonomic edges leaving a human skin surface and arriving at a physical surface, versus eight edges in the opposite direction ($P < 0.001$). In contrast, human and home surfaces were equally likely to be recipients (human = 20.6 taxonomic edges; home = 19.3, nonsignificant). OTUs sourced from humans were mainly Actinobacteria and Proteobacteria (table S3), which are major components of the human skin microbial community (*6*).

To assess whether personal relationships affect sharing of microbial taxa, we focused on home 4, where none of the residents were genetically related. The two occupants who were in a relationship shared more of their microbiota with each other than with the third occupant, who resided in a separate part of the house (fig. S6). This differentiation was observed across all surfaces, being greatest in nose samples ($R = 0.690$) and smallest in hand samples ($R = 0.300$) (all $P < 0.0001$). In contrast, only weak or insignificant differentiation was observed between married couples and their young children.

Overall, there were significant differences in the volatility of microbial communities associated with each surface type (Kruskal-Wallis $\chi^2 = 21.6$, $P = 0.0057$) (fig. S7). However, after a pairwise Wilcoxon test and FDR correction, the only significant differences were between hand and bedroom floor, hand and foot, and hand and nose. We can consequently conclude that the hand is especially variable over time relative to other body habitats and surfaces, presumably reflecting high inputs from the various surfaces with which it comes in contact and/or more frequent disruption due to washing.

To determine whether taxa transferred between surfaces and human occupants maintained genes associated with pathogenicity, we selected 56 samples from home 4 for longitudinal analysis via shallow shotgun metagenomic sequencing, including 18 home surface samples, 23 human samples, and 15 dog samples (fig. S8). Genes associated with phage and transposable elements were enriched in human samples. Taxonomic analysis of unassembled metagenomic reads revealed *Corynebacterium* on all human samples; *Enhydrobacter*-, *Corynebacterium*-, and *Streptococcus*-like bacteria on all bathroom doorknob samples; and *Enterobacter*-like bacteria on the kitchen counter. *Enterobacter*-like sequences were also identified on the hands of two occupants on days 2 and 4, further supporting the dynamic Bayesian network analysis above (in addition to genome reconstructions) that indicated a close link between these surfaces (fig. S4). After deeper metagenomic sequencing, multiple draft genomes were assembled from hand and kitchen counter samples, including uncultivated *Enterobacteraceae* and *Acinetobacter* genomes and associated bacteriophage. These latter genomes shared 99.7 and 99.9% reconstructed 16*S* rRNA gene sequence similarity with the respective opportunistic human pathogens *Pantoea agglomerans* and *Acinetobacter baumannii* and maintained genes associated with pathogenicity and antibiotic resistance. Representatives of these genomes sourced from both the kitchen counter and one household occupant's hand on day 2 shared >2400 genes with 100% protein sequence identity. When considering the whole bacterial community, and including phage sequence, a total of 84% (7671) of genes from the hand were shared with the countertop, suggesting a multiorganism transference event between these surfaces. A further 24 to 29% of the community genes (>3100) were also identical between the countertop across days (between days 2 and 4) and between the countertop on day 4 and the hand of one of the other occupants sampled on the same day.

There is strikingly little research into relationships between microbial communities associated with home surfaces and their potential origins. Most studies explore fungal contamination of damp surfaces (*13*–*16*), the role of hygiene in removing microbial communities (*7*, *17*), and the length of time microbes can survive on surfaces (*18*, *19*). Here, we present an intensive longitudinal analysis of the microbial communities associated with the home environment and present evidence for substantial interaction among human, home, and pet microbiota. Such interactions could have considerable human and animal health implications. Further, we suggest that homes harbor a distinct microbial fingerprint that can be predicted by their occupants and that supersedes intersurface differentiation within the home. We further show the rapidity and extent to which a human population can influence the microbial diversity of the space they inhabit.

REFERENCES AND NOTES

1. P. Höppe, I. Martinac, *Int. J. Biometeorol.* **42**, 1–7 (1998).
2. A. Custovic, S. C. O. Taggart, A. Woodcock, *Clin. Exp. Allergy* **24**, 1164–1168 (1994).
3. I. Dekio *et al.*, *J. Med. Microbiol.* **54**, 1231–1238 (2005).
4. Z. Gao, C. H. Tseng, Z. Pei, M. J. Blaser, *Proc. Natl. Acad. Sci. U.S.A.* **104**, 2927–2932 (2007).
5. E. A. Grice *et al.*, *Genome Res.* **18**, 1043–1050 (2008).
6. E. A. Grice *et al.*, *Science* **324**, 1190–1192 (2009).
7. E. A. Grice, *Natl. Rev.* **9**, 244–253 (2011).
8. S. G. Tringe *et al.*, *PLOS One* **3**, e1862 (2008).
9. P. Dawson, I. Han, M. Cox, C. Black, L. Simmons, *J. Appl. Microbiol.* **102**, 945–953 (2007).
10. K. E. Fujimura *et al.*, *Proc. Natl. Acad. Sci. U.S.A.* **111**, 805–810 (2014).

11. S. A. Boone, C. P. Gerba, *Appl. Environ. Microbiol.* **73**, 1687–1696 (2007).
12. D. Knights *et al.*, *Nat. Methods* **8**, 761–763 (2011).
13. A. A. Jaffal *et al.*, *Environ. Int.* **23**, 529–533 (1997).
14. A. Hyvarinen, T. Meklin, A. Vepsalainen, A. Nevalainen, *Int. Biodeterior. Biodegradation* **49**, 27–37 (2002).
15. A. Nevalainen, M. Seuri, *Indoor Air* **15** (suppl. 9), 58–64 (2005).
16. U. Lignell *et al.*, *Lett. Appl. Microbiol.* **47**, 303–308 (2008).
17. K. R. Bright, S. A. Boone, C. P. Gerba, *J. Sch. Nurs.* **26**, 33–41 (2010).
18. A. Kramer, I. Schwebke, G. Kampf, *BMC Infect. Dis.* **6**, 130 (2006).
19. D. J. Moschandreas, K. R. Pagilla, L. V. Storino, *Aerosol Sci. Technol.* **37**, 899–906 (2003).

ACKNOWLEDGMENTS

This work was supported by the Alfred P. Sloan Foundation's Microbiology of the Built Environment Program and a NIH Director's New Innovator Award (DP2-DK-098089) to G.D. S.M.G was supported by a U.S. Environmental Protection Agency STAR Fellowship. M.K.G. is a NSF graduate research fellow (award DGE-11143954). This work was supported in part by the U.S. Department of Energy under contract DE-AC02-06CH11357. We acknowledge the University of Chicago Research Computing Center for support of this work. All sequence data were submitted to the European Bioinformatics Institute's database under accession no. ERP005806.

SUPPLEMENTARY MATERIALS

www.sciencemag.org/content/345/6200/1048/suppl/DC1
Materials and Methods
Supplementary Text
Figs. S1 to S9
Tables S1 to S3
References (*20*–*29*)

8 April 2014; accepted 18 July 2014
10.1126/science.1254529

MICROBIAL METABOLISM

Growth of nitrite-oxidizing bacteria by aerobic hydrogen oxidation

Hanna Koch,[1] Alexander Galushko,[1] Mads Albertsen,[2] Arno Schintlmeister,[1,3] Christiane Gruber-Dorninger,[1] Sebastian Lücker,[1]* Eric Pelletier,[4,5,6] Denis Le Paslier,[4,5,6] Eva Spieck,[7] Andreas Richter,[8] Per H. Nielsen,[2] Michael Wagner,[1] Holger Daims[1]†

The bacterial oxidation of nitrite to nitrate is a key process of the biogeochemical nitrogen cycle. Nitrite-oxidizing bacteria are considered a highly specialized functional group, which depends on the supply of nitrite from other microorganisms and whose distribution strictly correlates with nitrification in the environment and in wastewater treatment plants. On the basis of genomics, physiological experiments, and single-cell analyses, we show that *Nitrospira moscoviensis*, which represents a widely distributed lineage of nitrite-oxidizing bacteria, has the genetic inventory to utilize hydrogen (H_2) as an alternative energy source for aerobic respiration and grows on H_2 without nitrite. CO_2 fixation occurred with H_2 as the sole electron donor. Our results demonstrate a chemolithoautotrophic lifestyle of nitrite-oxidizing bacteria outside the nitrogen cycle, suggesting greater ecological flexibility than previously assumed.

Nitrification, a key nitrogen cycling process, is prevalent in virtually all oxic habitats on Earth (*1*). This two-step process is carried out by chemolithoautotrophic aerobic ammonia-oxidizing bacteria (AOB) and archaea, and nitrite-oxidizing bacteria (NOB). Traditionally, nitrifying microorganisms (nitrifiers) have been regarded as obligate chemolithotrophs that grow only in the presence of ammonia or nitrite. Accordingly, their environmental distribution and population sizes are associated with nitrification, and NOB are thought to depend on ammonia-oxidizing or nitrate-reducing microorganisms as sources of nitrite.

Some nitrifiers, however, are physiologically versatile and can participate in denitrification, even in parallel to aerobic nitrification (*2*), or co-utilize various organic substrates if ammonia or nitrite is available (*3*, *4*). Few *Nitrobacter* isolates (NOB) grow heterotrophically on simple organic compounds (*5*). Moreover, *Nitrosomonas eutropha* (AOB) and *Nitrospira moscoviensis* (NOB) utilize hydrogen (H_2) as electron donor for anoxic respiration with the electron acceptors nitrite or nitrate, respectively [although growth under these conditions was reported only for *N. eutropha* (*6*, *7*)]. Aside from the growth of *Nitrobacter* on organic compounds, these additional metabolic capabilities of nitrifiers are still linked to the nitrogen cycle and actually depend on nitrification as they require ammonia, nitrite, or nitrate as energy source or electron acceptor, respectively.

To understand the metabolic capabilities and flexibility of NOB, we partially sequenced the genome of *Nitrospira moscoviensis*, a member of *Nitrospira* lineage II that grows in pure culture (*7*). *Nitrospira* (*8*) represents the environmentally most widespread group of known NOB found in virtually all environments, including soils, fresh water and the oceans, sediments, subsurface aquifers, volcanic sites, hot springs, caves, iron pipes, drinking water treatment systems, and wastewater treatment plants (*3*). Biological knowledge on the mainly uncultured, slow-growing *Nitrospira* is scarce, and only one genome sequence has been obtained from "*Candidatus* N. defluvii," a *Nitrospira* lineage I member enriched from a wastewater treatment plant (*9*).

The draft genome of *N. moscoviensis* contains a locus with genes coding for the small (HupS) and large (HupL) subunits of a putative group 2a [NiFe] hydrogenase (Hup) and homologs of proteins involved in hydrogenase maturation and transcriptional regulation in other bacteria (Fig. 1, table S1, and supplementary text). The *hup* locus likely explains the weak, anoxic, H_2-oxidizing activity with nitrate of *N. moscoviensis* (*7*). However, in cyanobacteria and terrestrial actinomycetes,

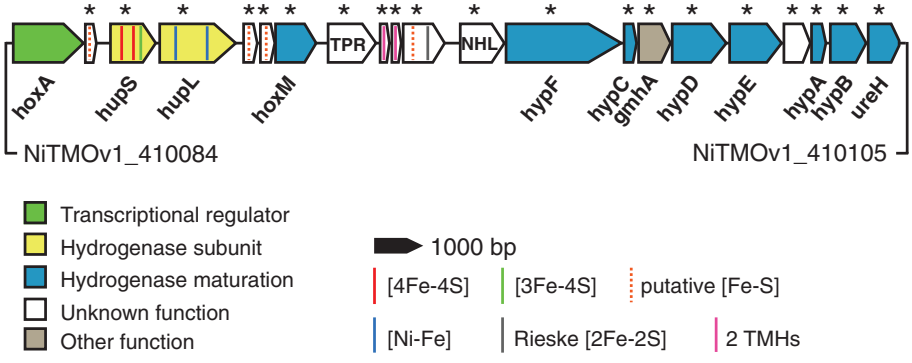

Fig. 1. Schematic illustration of the hydrogenase (*hup*) locus of *N. moscoviensis*. Predicted structural features or domains are marked with colored vertical lines, TPR (tetratricopeptide repeats), or NHL (NHL repeats). Asterisks indicate significant gene up-regulation (DESeq $P_{adj} < 0.05$, fold change ≥2) under H_2-oxidizing conditions, as detected by whole transcriptome shotgun sequencing. Genes are drawn to scale. TMH, transmembrane helix.

[1]Department of Microbiology and Ecosystem Science, Division of Microbial Ecology, University of Vienna, 1090 Vienna, Austria. [2]Center for Microbial Communities, Department of Biotechnology, Chemistry and Environmental Engineering, Aalborg University, 9000 Aalborg, Denmark. [3]Large Instrument Facility for Advanced Isotope Research, University of Vienna, 1090 Vienna, Austria. [4]Commissariat à l'Energie Atomique, Direction des Sciences du Vivant, Institut de génomique, Genoscope, 91057 Evry, France. [5]Centre National de la Recherche Scientifique, UMR8030, 91057 Evry, France. [6]Université d'Evry Val d'Essonne, 91057 Evry, France. [7]Biozentrum Klein Flottbek, Microbiology and Biotechnology, University of Hamburg, 22609 Hamburg, Germany. [8]Department of Microbiology and Ecosystem Science, Division of Terrestrial Ecosystem Research, University of Vienna, 1090 Vienna, Austria.
*Present address: Department of Microbiology, Radboud University Nijmegen, 6525 AJ Nijmegen, Netherlands. †**Corresponding author. E-mail: daims@microbial-ecology.net**

Hup functions as an uptake hydrogenase for the utilization of H_2 as a source of electrons and energy under oxic conditions (*10*, *11*). Consequently, we hypothesized that Hup may enable *N. moscoviensis* to gain energy by oxidizing H_2 with O_2 as the terminal electron acceptor, a Knallgas metabolism described for various non-nitrifying chemolithoautotrophic bacteria (*12*).

To test this hypothesis, we used a pure culture of *N. moscoviensis* that was grown on nitrite, removed all residual nitrite and nitrate, and transferred the cells into nitrite-free mineral medium that contained ammonium as the nitrogen source for assimilation (*13*). Indeed, we observed growth in the presence of H_2 and O_2 as sole electron donor and acceptor, respectively, but not when either H_2 or O_2 was omitted (Fig. 2). Hydrogenotrophic growth continued when a fraction of a H_2-grown batch culture was transferred into fresh mineral medium containing H_2 (fig. S1). H_2-dependent autotrophic carbon fixation of *N. moscoviensis* was confirmed by quantifying the uptake of [^{13}C]HCO_3^- at the single-cell level by nanometer-scale secondary ion mass spectrometry (NanoSIMS) (Fig. 3). The simultaneous specific detection of *N. moscoviensis* by fluorescence in situ hybridization (FISH) in this experiment (Fig. 3A) ensured that the culture was free of contaminants, including other hydrogenotrophic organisms. Comparative transcriptome analyses of *N. moscoviensis* grown on nitrite or H_2 (*13*) revealed that except for the upstream transcriptional regulator *hoxA* and gene NITMOv1_410085, the *hup* locus was upregulated at least twofold and among the 110 most strongly transcribed genes in the presence of H_2 (table S1 and Fig. 1). This up-regulation of Hup and its maturation factors is consistent with a key function in the growth on H_2. Interestingly, the subunit genes *hupL* and *hupS* were also relatively strongly transcribed during growth on nitrite (table S1). A low constitutive level of the hydrogenase might function as a sensory mechanism for H_2. When H_2 becomes available, the resulting increased flux of reductant might trigger the upregulation of the hydrogenase.

N. moscoviensis can oxidize low levels of H_2 injected in the culture headspace. The experiments described above were performed with 50 to 70% (v/v) H_2, which corresponds to initial dissolved H_2 concentrations of 0.37 to 0.52 mM in the medium at the beginning of the incubations (*13*). In additional incubations with only 0.7% (v/v) of H_2 in the headspace (5.2 μM dissolved H_2 in the medium), *N. moscoviensis* partially consumed the H_2 and fixed carbon as shown by addition of [^{13}C]HCO_3^- and isotope ratio mass spectrometry of the biomass (fig. S2, A to C). However, although H_2 was used as an energy source for biosynthesis, net growth of *N. moscoviensis* was not observed (fig. S2D). We assume that only a fraction of the culture was metabolically highly active, whose growth during the incubation period was not detectable by the applied protein quantification assay. This explanation is consistent with the heterogeneous ^{13}C-labeling at the single-cell level observed by NanoSIMS even after incubation under high-H_2 conditions (Fig. 3). As shown by reverse transcription polymerase chain reaction (table S2), the *hupS* and *hupL* genes were also upregulated at 5.2 μM H_2 (fig. S3). Transcription of the only other potentially H_2-oxidizing enzyme identified in the draft genome, a putative formate hydrogenlyase (supplementary text), was very weak at 0.37 to 0.52 mM H_2 (table S1) or not detected at 5.2 μM H_2 (fig. S3), suggesting that Hup catalyzed H_2 oxidation at these H_2 concentrations.

The concentration of 5.2 μM dissolved H_2 is within the range found in gas bubbles in cyanobacterial mats (*14*). In prolonged incubations, *N. moscoviensis* still consumed H_2 at 0.04% (v/v) in the culture headspace (293 nM dissolved H_2) (fig. S4A). Levels of H_2 in this range occur in hot

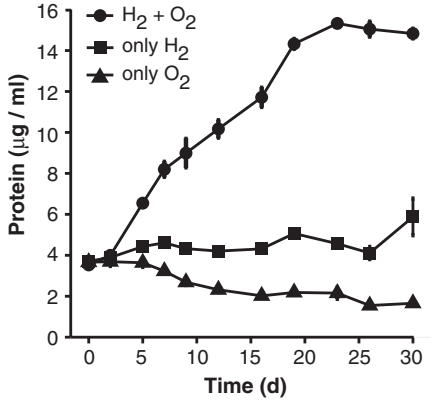

Fig. 2. Hydrogenotrophic growth of *N. moscoviensis* with O_2 as terminal electron acceptor. Data points represent means of three biological replicates for each incubation condition. Error bars represent 1 SD (not shown if smaller than symbols). Growth on H_2 and O_2 was linear, whereas growth of *N. moscoviensis* on nitrite and O_2 is logarithmic (*7*). The slower growth on H_2 indicates a yet unidentified limiting factor. In the incubation with O_2 only, total protein decreased likely because of endogenous respiration in the absence of any external electron donor.

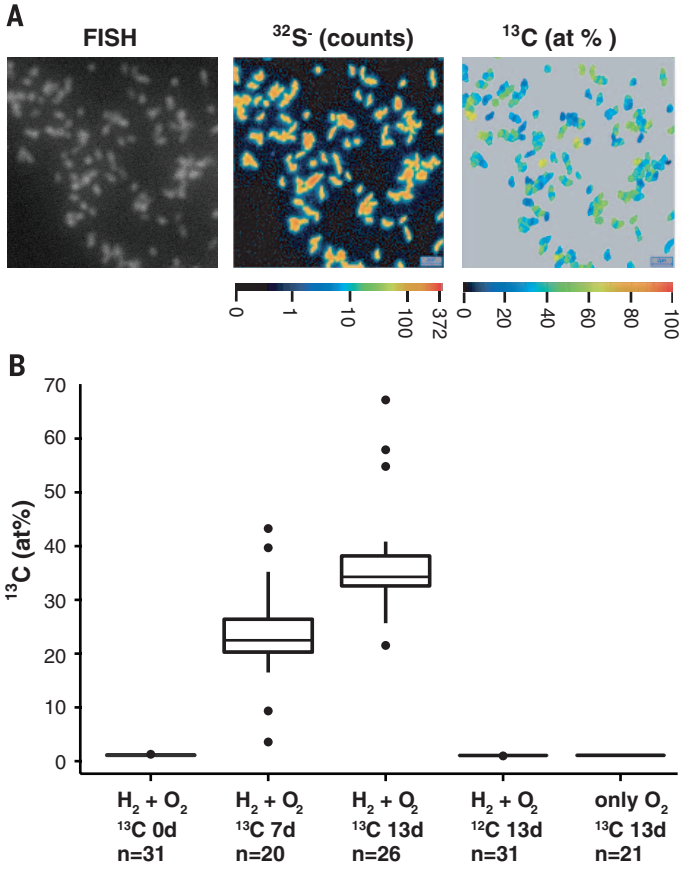

Fig. 3. Chemolithoautotrophic carbon fixation by *N. moscoviensis* with H_2 as sole energy source. (**A**) Representative FISH (left) and NanoSIMS (middle and right) images showing *N. moscoviensis* cells in the same field of view after 13 days of incubation with ^{13}C-labeled bicarbonate, H_2, and O_2. Cells were detected by FISH with the *Nitrospira* lineage II–specific probe Ntspa1151 (control hybridizations with a nonsense probe gave no signals). The $^{32}S^-$ secondary ion signal intensity distribution image is shown to illustrate the distribution of biomass. Carbon fixation is demonstrated by a high ^{13}C content of cells. (**B**) ^{13}C labeling of *N. moscoviensis* quantified by NanoSIMS at the single-cell level at different time points during the same incubation as shown in (A) and control incubations. The label content is presented as the $^{13}C/(^{12}C + {}^{13}C)$ isotope fraction, given in atomic %. The box plots summarize the median and the quartiles of the ^{13}C content of cells. Numbers of measured cells (*n*) are indicated.

springs (*15*) but are higher than steady-state H_2 concentrations in lake and river sediments (*16*). The lowest concentration threshold of H_2 utilization by *N. moscoviensis* was not determined here, but as shown recently, the high substrate affinity of group 2a [NiFe] hydrogenases of terrestrial actinomycetes allows even the scavenging of tropospheric H_2 (*11*).

Phylogenetically, Hup of *N. moscoviensis* clusters with group 2a [NiFe] hydrogenases of *Cyanobacteria* and nonphototrophic *Alpha-* and *Gammaproteobacteria* (fig. S5), although *Nitrospira* belong to a distinct bacterial phylum (*7*). Thus, the *hup* locus was likely acquired by *Nitrospira* through lateral gene transfer. Whether the absence of *hup* in "*Ca.* N. defluvii" results from secondary loss of the hydrogenase locus in this organism, or whether *hup* was laterally acquired only by *Nitrospira* lineage II (including *N. moscoviensis*), will remain unclear until genomic sequences of other *Nitrospira* become available.

Aerobic H_2 oxidation will be ecologically advantageous for NOB, as the amount of energy that can be gained ($\Delta G^{o'}$ = −237 kJ mol^{-1} H_2) is much larger than for nitrite oxidation ($\Delta G^{o'}$ = −74 kJ mol^{-1} NO_2^-). Low-potential electrons from H_2 also reduce the energy requirement for reverse electron transport, which is needed to fix CO_2 with nitrite as the electron donor. Addition of nitrite to H_2-oxidizing cultures, which were incubated with low levels of H_2, revealed that *N. moscoviensis* can oxidize both substrates simultaneously (fig. S4B). A lifestyle in which H_2 and O_2 are used as substrates, exclusively or in addition to aerobic nitrite oxidation, would increase the competitiveness of NOB in habitats where microbial processes provide H_2, such as in cyanobacterial mats, at oxic-anoxic interfaces, and in hypoxic pockets of soils, sediments, or biofilms, or at hydrothermal sites where upwelling fluids contain H_2 (*17*). Indeed, *Nitrospira* have been found in low-oxygen niches such as the basal zones of biofilms (*18*); in marine sediments, subsurface aquifers, and rice paddies; and also in deep-sea hydrothermal field sediment and hot springs (*19*, *20*). In such habitats, aerobic H_2 oxidation may provide extra energy and make (at least some) NOB independent of nitrite supplied by ammonia oxidizers or nitrate reducers.

Loci encoding putative hydrogenases of different types occur also in the genomes of NOB other than *Nitrospira*, indicating that H_2 utilization may be a widespread feature of these organisms. The marine nitrite oxidizer *Nitrospina gracilis* (phylum *Nitrospinae*) possesses the genes of a cytoplasmic group 3b bidirectional [NiFe] hydrogenase (*21*). A group 5 uptake [NiFe] hydrogenase was identified in the genome of *Nitrolancea hollandica* (phylum *Chloroflexi*), a nitrite-oxidizing bacterium isolated from activated sludge (*22*) (fig. S5).

The ability to switch their lifestyle would enable NOB to colonize new ecological niches and may stabilize nitrification by maintaining NOB populations during periods of nitrite depletion. The aerobic growth on H_2 of *N. moscoviensis* suggests that the contribution of NOB to chemolithoautotrophic CO_2 fixation in microbial communities is potentially greater than expected from the low energy yield of nitrite oxidation (*23*). Thus, a reassessment of their functional roles will be essential to more fully understand the ecology of NOB and to determine the impact of these almost ubiquitous microorganisms on the biogeochemical cycles of nitrogen and carbon in natural and engineered ecosystems.

REFERENCES AND NOTES

1. E. Bock, M. Wagner, in *The Prokaryotes: A Handbook on the Biology of Bacteria*, M. Dworkin, S. Falkow, E. Rosenberg, K. H. Schleifer, E. Stackebrandt, Eds. (Springer Science+Business Media, New York, 2001), pp. 457–495.
2. L. Y. Stein, in *Nitrification*, B. B. Ward, D. J. Arp, M. G. Klotz, Eds. (American Society for Microbiology, Washington, DC, 2011), pp. 95–114.
3. H. Daims, J. L. Nielsen, P. H. Nielsen, K. H. Schleifer, M. Wagner, *Appl. Environ. Microbiol.* **67**, 5273–5284 (2001).
4. N. G. Hommes, L. A. Sayavedra-Soto, D. J. Arp, *J. Bacteriol.* **185**, 6809–6814 (2003).
5. E. Bock, *Arch. Microbiol.* **108**, 305–312 (1976).
6. E. Bock, I. Schmidt, R. Stüven, D. Zart, *Arch. Microbiol.* **163**, 16–20 (1995).
7. S. Ehrich, D. Behrens, E. Lebedeva, W. Ludwig, E. Bock, *Arch. Microbiol.* **164**, 16–23 (1995).
8. S. W. Watson, E. Bock, F. W. Valois, J. B. Waterbury, U. Schlosser, *Arch. Microbiol.* **144**, 1–7 (1986).
9. S. Lücker *et al.*, *Proc. Natl. Acad. Sci. U.S.A.* **107**, 13479–13484 (2010).
10. P. Tamagnini *et al.*, *Microbiol. Mol. Biol. Rev.* **66**, 1–20 (2002).
11. C. Greening, M. Berney, K. Hards, G. M. Cook, R. Conrad, *Proc. Natl. Acad. Sci. U.S.A.* **111**, 4257–4261 (2014).
12. J. M. Shively, G. van Keulen, W. G. Meijer, *Annu. Rev. Microbiol.* **52**, 191–230 (1998).
13. Materials and methods are available as supplementary materials on *Science* Online.
14. T. M. Hoehler, B. M. Bebout, D. J. Des Marais, *Nature* **412**, 324–327 (2001).
15. J. R. Spear, J. J. Walker, T. M. McCollom, N. R. Pace, *Proc. Natl. Acad. Sci. U.S.A.* **102**, 2555–2560 (2005).
16. D. R. Lovley, S. Goodwin, *Geochim. Cosmochim. Acta* **52**, 2993–3003 (1988).
17. H. W. Jannasch, M. J. Mottl, *Science* **229**, 717–725 (1985).
18. A. Schramm, D. De Beer, A. Gieseke, R. Amann, *Environ. Microbiol.* **2**, 680–686 (2000).
19. M. Pester *et al.*, *Environ. Microbiol.* (2013).
20. E. V. Lebedeva *et al.*, *FEMS Microbiol. Ecol.* **75**, 195–204 (2011).
21. S. Lücker, B. Nowka, T. Rattei, E. Spieck, H. Daims, *Front. Microbiol.* **4**, 27 (2013).
22. D. Y. Sorokin *et al.*, *ISME J.* **6**, 2245–2256 (2012).
23. B. B. Ward, in *Nitrogen in the Marine Environment*, D. G. Capone, D. A. Bronk, M. R. Mulholland, E. J. Carpenter, Eds. (Academic Press, San Diego, 2008), pp. 199–261.

ACKNOWLEDGMENTS

We thank the anonymous reviewers for their valuable comments and suggestions. The sequences of genes reported in this paper are available at NCBI GenBank under accession nos. KJ920237 to KJ920263. Other supporting data are available in the supplementary materials. This work was supported by the Vienna Science and Technology Fund (WWTF, grant LS09-40), the Austrian Science Fund (FWF, grants P25231-B21 and P24101-B22), the Danish Council for Strategic Research (EcoDesign), the Deutsche Forschungsgemeinschaft (DFG, grant SP667/3-1), and the European Research Council [Advanced Grant Nitrification Reloaded (NITRICARE) 294343].

SUPPLEMENTARY MATERIALS

www.sciencemag.org/content/345/6200/1052/suppl/DC1
Materials and Methods
Supplementary Text
Figs. S1 to S5
Tables S1 and S2
References (*24–50*)

4 June 2014; accepted 21 July 2014
10.1126/science.1256985

MEMORY ENHANCEMENT

Targeted enhancement of cortical-hippocampal brain networks and associative memory

Jane X. Wang,[1] Lynn M. Rogers,[2] Evan Z. Gross,[1] Anthony J. Ryals,[1] Mehmet E. Dokucu,[3] Kelly L. Brandstatt,[1] Molly S. Hermiller,[1] Joel L. Voss[1]*

The influential notion that the hippocampus supports associative memory by interacting with functionally distinct and distributed brain regions has not been directly tested in humans. We therefore used targeted noninvasive electromagnetic stimulation to modulate human cortical-hippocampal networks and tested effects of this manipulation on memory. Multiple-session stimulation increased functional connectivity among distributed cortical-hippocampal network regions and concomitantly improved associative memory performance. These alterations involved localized long-term plasticity because increases were highly selective to the targeted brain regions, and enhancements of connectivity and associative memory persisted for ~24 hours after stimulation. Targeted cortical-hippocampal networks can thus be enhanced noninvasively, demonstrating their role in associative memory.

The hippocampus is necessary for associative (relational/declarative) memory (*1*, *2*). It is a neuroanatomical convergence zone for highly processed sensory information regarding qualities of objects and contexts and therefore could serve as a "hub" to support binding of information from distinct processing modules into associative memories (*1–4*). However, hippocampal interactivity with distributed brain regions has yet to be demonstrated as necessary for associative memory in humans. Few experiments have used functional magnetic

resonance imaging (fMRI) to identify hippocampal interactions with distributed cortical regions that are correlated with associative memory (*5*). Although brain-lesion studies have shown the necessity of an intact hippocampus for associative memory, they cannot readily demonstrate the necessity of hippocampal interactivity with other regions.

We therefore developed methods to modulate cortical-hippocampal brain networks in healthy adults (n = 16 subjects) in order to test their role in associative memory (*6*). We focused modulatory stimulation on the lateral parietal cortex component of a well-characterized cortical-hippocampal network (*4*) on the basis of hypothesized interactions between hippocampus and lateral parietal cortex in memory (*7*) as well as robust functional connectivity between these regions (*8*), which is likely mediated by lateral parietal projections to retrosplenial and parahippocampal cortex (*9*, *10*). We defined a target within the left hippocampus for each subject and used resting-state fMRI to identify a subject-specific left lateral parietal location that demonstrated high functional connectivity with the hippocampal target (Fig. 1A and fig. S1) (*6*). Noninvasive high-frequency repetitive transcranial magnetic stimulation (rTMS) (*6*) was delivered to the parietal location for 5 consecutive days on the basis of evidence that rTMS can induce changes in connectivity within stimulated networks (*11*, *12*) and that such effects can increase over multiple-day stimulation sessions (*13*).

We measured changes in cortical-hippocampal network fMRI connectivity and associative memory using pretreatment (baseline), midtreatment (Mid-Tx), and posttreatment (Post-Tx) assessments (Fig. 1B). Stimulation effects were measured relative to a sham-control condition involving the same parameters, but at subthreshold intensity for neural stimulation (*6*). Compared with sham, Post-Tx resting-state fMRI connectivity was significantly greater than that of the baseline in four regions, including (i) the precuneus/retrosplenial cortex, (ii) the fusiform/parahippocampal cortex, (iii) the superior parietal cortex, and (iv) the left lateral parietal cortex (Fig. 2A and table S1). These stimulation-responsive regions include elements of well-characterized hippocampal intrinsic connectivity networks (*8*) hypothesized to interact with the hippocampus to support associative memory (*4*, *14*, *15*), including the approximate location of lateral parietal cortex that was stimulated.

Increased fMRI connectivity was highly specific to the individual hippocampal target selected for each subject. By assessing Post-Tx versus baseline connectivity changes due to stimulation (relative to sham) along the anterior-posterior axis of the targeted hippocampus (*6*), we noted a rapid decline in stimulation effects on fMRI connectivity with increasing distance from the target (Fig. 2B). At average distances of 1.5 and 3.0 mm from the target in either direction, the T values of the change in whole-brain (global) connectivity from baseline were ~48 and ~17% of the connectivity change for the target, respectively, and were not statistically significant (Fig. 2B). Stimulation-induced changes in connectivity of the hippocampal target with the four stimulation-responsive regions were similarly selective (Fig. 2C). We found no reliable changes for right hippocampal locations that mirrored left hippocampal target locations and no reliable changes for the left hippocampus treated as a unit (*6*).

Stimulation also increased interconnectivity among stimulation-responsive regions. A correlation-weighted fMRI connectivity matrix formed from locations with at least minimal stimulation-related change in connectivity with the hippocampal target (*6*) indicated robust increases in regional interconnectivity (Fig. 3A and fig. S2). To test whether increases in regional interconnectivity were associated with the degree to which an anatomically defined region was part of the hippocampal resting-state network, the matrix was sorted by each region's baseline fMRI connectivity with the hippocampal target. The number of significant interregional links [$P < 0.05$, false discovery rate (FDR)–corrected] was significantly correlated with baseline fMRI connectivity with the hippocampal target [$R^2_{(adj)} = 0.27$, df = 69, $P < 0.0001$] (Fig. 3B). Lateral parietal cortex stimulation thus increased fMRI interconnectivity to a greater extent among regions that were more versus less strongly within baseline cortical-hippocampal networks.

We next tested for corresponding changes in associative memory. Stimulation increased associative memory performance (face-cued word recall) (Fig. 4A) from baseline to Post-Tx [$T_{(15)} = 3.05$, $P = 0.008$], whereas sham treatment caused no significant performance change [$T_{(15)} = 0.82$, $P = 0.425$] (Fig. 4B). The increase in performance for baseline to Post-Tx was greater for stimulation than for sham [$T_{(15)} = 2.21$, $P = 0.043$]. Using regionally constrained correlation analysis (*6*), we found that baseline to Post-Tx changes in performance because of stimulation (relative to sham) correlated significantly with corresponding changes in fMRI connectivity with the hippocampal target for a portion of treatment-responsive brain regions (Fig. 4, C and D). Subjects demonstrating larger stimulation-induced connectivity changes for these regions exhibited greater memory improvements. Targeted analysis of the left lateral parietal cortex identified the same relationship for a portion of this region (*6*), but at subthreshold size for the primary analysis. We administered a battery of additional cognitive tests (*6*) to assess selectivity of stimulation effects for associative memory. No such changes were observed on any of these tests (P = 0.33 to 0.99 for all pairwise Post-Tx versus baseline comparisons performed separately for each test).

A control experiment tested whether aforementioned stimulation effects could have resulted from nonspecific influences of above-threshold brain stimulation rather than targeted stimulation of cortical-hippocampal networks via lateral parietal cortex. Subjects receiving the same stimulation

[1]Department of Medical Social Sciences, Ken and Ruth Davee Department of Neurology, and Interdepartmental Neuroscience Program, Feinberg School of Medicine, Northwestern University, Chicago, IL, USA. [2]The Sensory Motor Performance Program, Rehabilitation Institute of Chicago, Chicago, IL, USA. [3]Department of Psychiatry and Behavioral Sciences, Feinberg School of Medicine, Northwestern University, Chicago, IL, USA.
*To whom correspondence should be addressed. E-mail: joel-voss@northwestern.edu

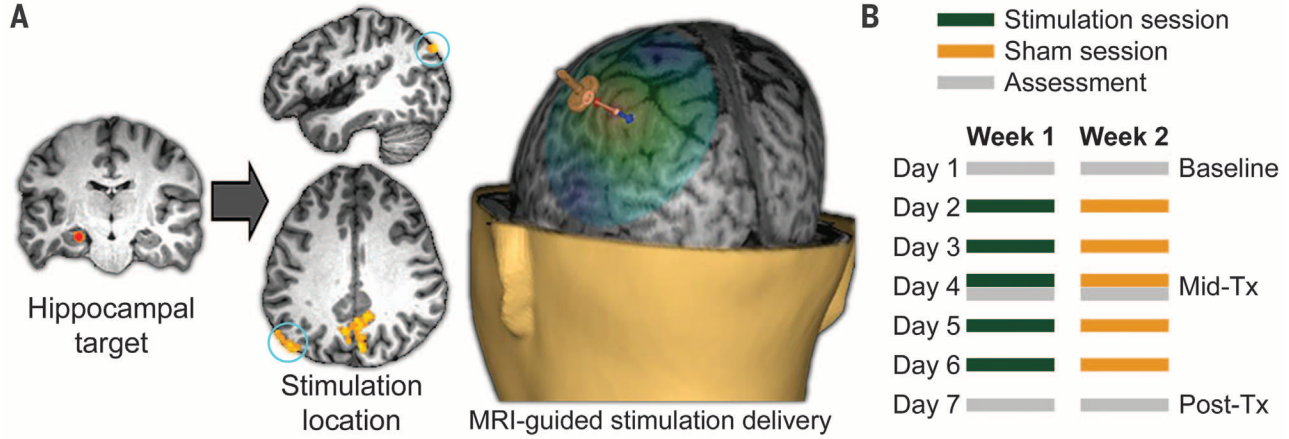

Fig. 1. Targeted cortical-hippocampal network stimulation. (**A**) For each subject, a parietal stimulation location was selected on the basis of maximum local fMRI connectivity with a hippocampal target, and stimulation was applied to this location under MRI guidance (*6*). (**B**) Timing of assessments and stimulation sessions for the stimulation and sham weeks, with week order counterbalanced (*6*). Post-Tx assessment was ~24 hours after the final stimulation session.

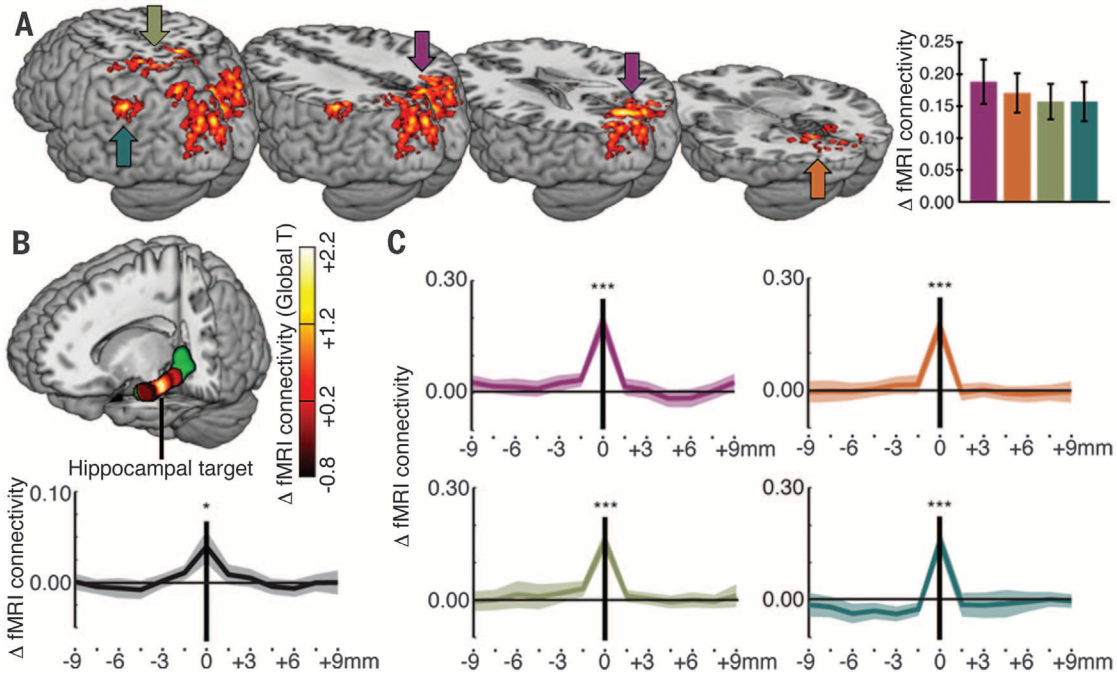

Fig. 2. Stimulation-induced fMRI connectivity increases selectivity to hippocampal targets. (**A**) Regions showing significant change in fMRI connectivity with the hippocampal target (Post-Tx versus baseline for stimulation compared with sham) (*6*) shown on a template brain viewed from the back left. (**B**) Stimulation-induced changes in whole-brain fMRI connectivity (*T* values of differences in global average connectivity) are colorized for the target and other locations along the anterior-posterior axis of the left hippocampus (which is displayed in green on the rendered brain) (*6*). The plot shows changes in fMRI connectivity values for the subject-specific hippocampal target (0 mm) and for 1.5-mm steps along the anterior-posterior hippocampal axis (negative values indicate anterior to the target). (**C**) The same change values are plotted for the four stimulation-responsive regions shown in (A). *$P < 0.05$ versus zero; ***$P < 0.001$ versus zero. Error bars and line shading indicate SEM.

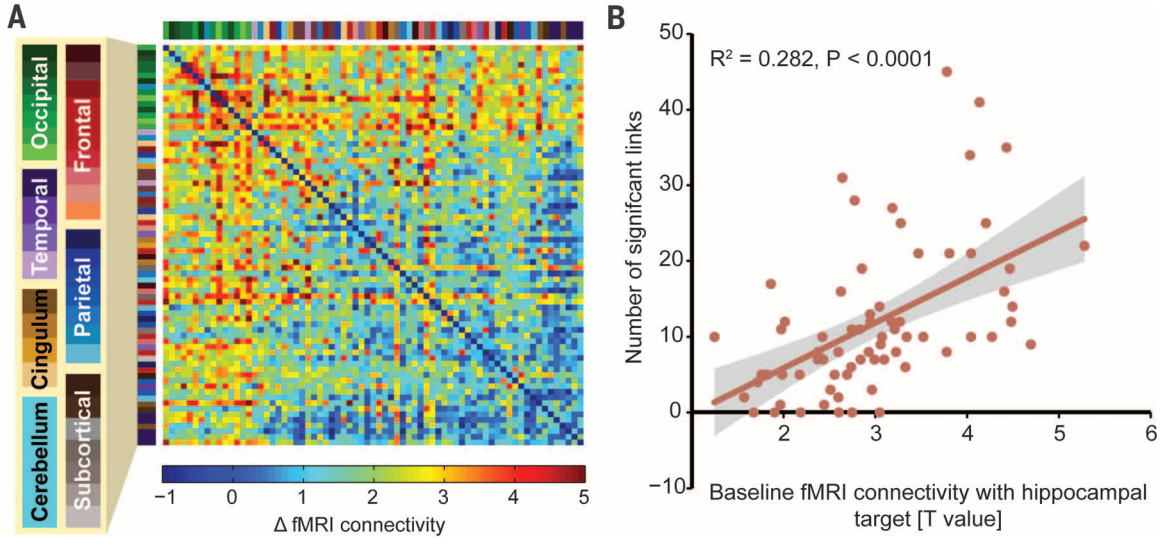

Fig. 3. Stimulation-induced fMRI regional interconnectivity scales with baseline connectivity with hippocampal targets. (**A**) Coloration indicates the effect of stimulation (Post-Tx versus baseline for stimulation relative to sham, *T* value) on fMRI connectivity among stimulation-responsive regions (*6*). Regions are sorted by baseline fMRI connectivity with hippocampal targets (top rows and left columns are highest). Region labels are colorized and expanded in fig. S2. (**B**) The degree of interconnectivity for a region (number of significant links with other regions surviving; $P < 0.05$ with FDR correction) correlated with the strength of baseline connectivity with hippocampal targets for the region. Shading indicates 95% confidence interval.

protocol to a primary motor cortex region that is not reliably included in cortical-hippocampal networks did not exhibit any reliable changes in cortical-hippocampal connectivity or associative memory performance (fig. S4) (*6*).

These findings confirm the proposed role of cortical-hippocampal interactions in associative memory (*1*–*4*). Enhanced memory via neurosurgical (invasive) stimulation of entorhinal cortex (the primary input to hippocampus) has been reported (*16*), although effects were specific to the material studied during stimulation, and network-level function was not tested. Our findings thus demonstrate persistent memory changes and substantiate fMRI correlative evidence for cortical-hippocampal network involvement in associative memory (*5*).

Although effects of noninvasive stimulation on neurophysiology are not fully characterized, findings that resemble *N*-methyl-D-aspartate–receptor–dependent long-term potentiation (LTP) of hippocampal circuits (*17*, *18*) have been observed by using rTMS parameters similar to those reported here (*13*, *19*). fMRI connectivity changes due to stimulation could reflect LTP-like effects throughout cortical-hippocampal networks (*20*). Indeed, changes were evident ~24 hours after stimulation (Post-Tx), indicating long-term plasticity. Alternatively, nonspecific physiological effects [such as neuromodulatory, neurochemical,

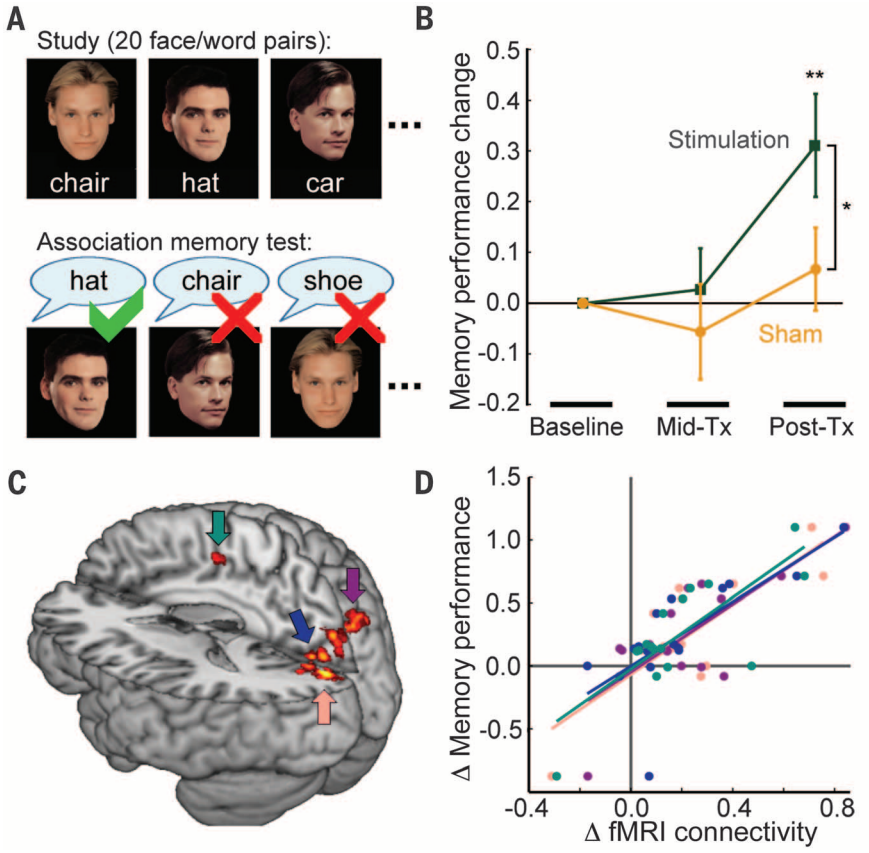

Fig. 4. Stimulation-induced associative memory enhancement. (**A**) Structure of the face-cued word recall test of associative memory, involving recall during test of words arbitrarily paired with faces at study (*6*). Different word-face pairs were used for each assessment. (**B**) Stimulation increased memory, whereas sham did not. Mean performance change for each assessment is expressed as a proportion of baseline. (**C**) Subset of treatment-responsive regions that demonstrate significant correlation between stimulation-induced fMRI connectivity change with hippocampal targets and memory improvement. (**D**) Plot of memory-improvement values (Post-Tx versus baseline for treatment relative to sham) and corresponding values of fMRI connectivity increase with respect to hippocampal targets from each subject for the four areas indicated in (C). *P < 0.05 stimulation versus sham; **P < 0.01 versus zero.

or other more global processes (*13*, *19*)] and/or psychological factors (such as memory recall during fMRI, effort during memory testing, or placebo effects) could have changed connectivity and memory. However, fMRI connectivity changes were remarkably specific for hippocampal targets (Fig. 2, B and C), were significantly correlated with associative memory improvements (Fig. 4, C and D), and did not occur when a motor-cortex region distinct from cortical-hippocampal networks was stimulated in the control experiment, providing strong evidence against these possible nonspecific influences. Additional research is required to determine whether other cortical-hippocampal networks can be modulated with similarly high specificity and to identify neurophysiological mechanisms.

Although memory-related processing by cortical-hippocampal networks is relevant for many cognitive domains (such as attention, language, and executive control) (*21*, *22*), there were no stimulation effects on standardized measures of those domains. However, the instruments were not designed to provide specificity to cortical-hippocampal network influences (*6*). Specialized tests could potentially be used to identify broader effects of stimulation on cognition. Stimulation-responsive regions and the hippocampus are elements of a network that shows high interconnectivity even during periods of quiescence [the "default-mode" network (*23*)], further underscoring the potential broader influences of stimulation-induced changes on cognition.

After hippocampal damage, residual tissue might retain function (*24*) and assume functions previously supported by damaged tissue (*25*). Further, cortical-hippocampal network dysfunction has been implicated in various memory disorders (*26*). The methods reported here potentially could be modified to treat memory disorders by targeting residual hippocampal tissue to improve impaired cortical-hippocampal networks.

REFERENCES AND NOTES

1. H. Eichenbaum, A. P. Yonelinas, C. Ranganath, *Annu. Rev. Neurosci.* **30**, 123–152 (2007).
2. H. Eichenbaum, N. J. Cohen, *From Conditioning to Conscious Recollection: Memory Systems of the Brain* (Oxford Univ. Press, New York, 2001).
3. F. P. Battaglia, K. Benchenane, A. Sirota, C. M. Pennartz, S. I. Wiener, *Trends Cogn. Sci.* **15**, 310–318 (2011).
4. C. Ranganath, M. Ritchey, *Nat. Rev. Neurosci.* **13**, 713–726 (2012).
5. B. P. Staresina, E. Cooper, R. N. Henson, *J. Neurosci.* **33**, 14184–14192 (2013).
6. Materials and methods are available as supplementary materials on *Science* Online.
7. A. D. Wagner, B. J. Shannon, I. Kahn, R. L. Buckner, *Trends Cogn. Sci.* **9**, 445–453 (2005).
8. I. Kahn, J. R. Andrews-Hanna, J. L. Vincent, A. Z. Snyder, R. L. Buckner, *J. Neurophysiol.* **100**, 129–139 (2008).
9. C. Cavada, P. S. Goldman-Rakic, *J. Comp. Neurol.* **287**, 393–421 (1989).
10. M. M. Mesulam, G. W. Van Hoesen, D. N. Pandya, N. Geschwind, *Brain Res.* **136**, 393–414 (1977).
11. M. D. Fox, M. A. Halko, M. C. Eldaief, A. Pascual-Leone, *Neuroimage* **62**, 2232–2243 (2012).
12. T. P. Zanto, M. T. Rubens, A. Thangavel, A. Gazzaley, *Nat. Neurosci.* **14**, 656–661 (2011).
13. E. M. Wassermann, T. Zimmermann, *Pharmacol. Ther.* **133**, 98–107 (2012).
14. J. P. Aggleton, *Neurosci. Biobehav. Rev.* **36**, 1579–1596 (2012).
15. J. R. Andrews-Hanna, J. S. Reidler, J. Sepulcre, R. Poulin, R. L. Buckner, *Neuron* **65**, 550–562 (2010).
16. N. Suthana *et al.*, *N. Engl. J. Med.* **366**, 502–510 (2012).
17. T. V. Bliss, T. Lomo, *J. Physiol.* **232**, 331–356 (1973).
18. T. H. Brown, P. F. Chapman, E. W. Kairiss, C. L. Keenan, *Science* **242**, 724–728 (1988).
19. E. Dayan, N. Censor, E. R. Buch, M. Sandrini, L. G. Cohen, *Nat. Neurosci.* **16**, 838–844 (2013).
20. E. Alvarez-Salvado, V. Pallarés, A. Moreno, S. Canals, *Philos. Trans. R. Soc. London B Biol. Sci.* **369**, 20130–20152 (2014).
21. D. Shohamy, N. B. Turk-Browne, *J. Exp. Psychol. Gen.* **142**, 1159–1170 (2013).
22. R. K. Olsen, S. N. Moses, L. Riggs, J. D. Ryan, *Front. Hum. Neurosci.* **6**, 146 (2012).
23. M. E. Raichle *et al.*, *Proc. Natl. Acad. Sci. U.S.A.* **98**, 676–682 (2001).
24. S. L. Mullally, D. Hassabis, E. A. Maguire, *J. Neurosci.* **32**, 5646–5653 (2012).
25. C. Finke, H. Bruehl, E. Düzel, H. R. Heekeren, C. J. Ploner, *J. Neurosci.* **33**, 11061–11069 (2013).
26. R. La Joie *et al.*, *Neuron* **81**, 1417–1428 (2014).

ACKNOWLEDGMENTS

Research was supported by awards P50-MH094263 from the National Institute of Mental Health and F32-NS083340 from the National Institute of Neurological Disorders and Stroke. The content is solely the responsibility of the authors and does not necessarily represent the official views of the National Institutes of Health. Neuroimaging was performed at the Northwestern University Center for Translational Imaging facility supported by the Northwestern University Department of Radiology. All primary behavioral data are archived in paper and electronic format in the Laboratory for Human Neuroscience of the Northwestern University Feinberg School of Medicine. All primary MRI data are archived in the Northwestern University Neuroimaging Data Archive (https://nunda.northwestern.edu).

SUPPLEMENTARY MATERIALS

www.sciencemag.org/content/345/6200/1054/suppl/DC1
Materials and Methods
Supplementary Text
Figs. S1 to S4
Tables S1 to S2
References (*27*–*38*)

3 March 2014; accepted 23 July 2014
10.1126/science.1252900

GERMINAL CENTERS

Dynamic signaling by T follicular helper cells during germinal center B cell selection

Ziv Shulman,[1] Alexander D. Gitlin,[1] Jason S. Weinstein,[2] Begoña Lainez,[2]* Enric Esplugues,[3]* Richard A. Flavell,[3,4] Joseph E. Craft,[2,3] Michel C. Nussenzweig[1,4]†

T follicular helper (T_{FH}) cells select high-affinity, antibody-producing B cells for clonal expansion in germinal centers (GCs), but the nature of their interaction is not well defined. Using intravital imaging, we found that selection is mediated by large but transient contacts between T_{FH} and GC B cells presenting the highest levels of cognate peptide bound to major histocompatibility complex II. These interactions elicited transient and sustained increases in T_{FH} intracellular free calcium (Ca^{2+}) that were associated with T_{FH} cell coexpression of the cytokines interleukin-4 and -21. However, increased intracellular Ca^{2+} did not arrest T_{FH} cell migration. Instead, T_{FH} cells remained motile and continually scanned the surface of many GC B cells, forming short-lived contacts that induced selection through further repeated transient elevations in intracellular Ca^{2+}.

Germinal centers (GCs) are specialized microanatomical sites where B cells undergo clonal expansion, somatic hypermutation, and affinity maturation (*1*–*3*). Through iterative cycles of diversification and selection, the GC produces high-affinity memory B and plasma cells (*2*–*4*). Selection of high-affinity GC B cells requires their interaction with T follicular helper (T_{FH}) cells, which must discern among B cell clones according to their surface density of peptide–major histocompatibility complex II (pMHCII) (*5*). GC B cells are then programmed by T_{FH} cells to expand and hypermutate in direct proportion to the levels of cognate antigen presented (*6*). These events are controlled by T_{FH} cell–derived signals, including membrane-bound inducible costimulator (ICOS) and CD40L and the cytokines interleukin-4 (IL-4) and IL-21 (*7*, *8*), which are delivered in short-lived intercellular contacts (*9*).

To examine how the interactions between T_{FH} cells and GC B cells control selection, we imaged cells expressing genetically encoded fluorescent proteins in vivo by means of two-photon laser-scanning microscopy (TPLSM). Ovalbumin (OVA)–specific, T cell receptor (TCR) transgenic OT-II T cells expressing DsRed were adoptively transferred into congenic mice before priming with OVA in alum. After 2 to 3 weeks, a 95:5 mixture of nonfluorescent *Ly75*$^{-/-}$ and GFP$^+$ *Ly75*$^{+/+}$ (*Ly75* encodes the cell-surface receptor DEC205) B cells, both specific for NP (4-hydroxy-3-nitrophenylacetyl; B1-8^{hi}) (*10*), was transferred before boosting with soluble OVA conjugated to NP (NP–OVA) (*11*, *12*). To induce selection, we increased the levels of pMHCII on the surface of GC B cells 7 to 8 days later through injection of DEC205 antibody fused to the cognate antigen OVA (αDEC-OVA) (Fig. 1A). This chimeric antibody targets DEC205, an endocytic receptor that carries associated proteins into MHCII-processing compartments of GC B cells (*5*). As a result, targeted GC B cells are initially retained in the GC light zone (LZ) and thereafter proliferate in the dark zone (DZ) (*5*, *6*). As a control, mice were injected with chimeric DEC205 antibody fused to an irrelevant antigen (*Plasmodium falciparum* circumsporozoite protein, αDEC-CS) (*5*). Popliteal lymph nodes were exposed after 4 to 10 hours, GCs were imaged by means of TPLSM (Fig. 1A), and the results were subjected to colocalization analysis (fig. S1).

Consistent with previous observations (*9*, *11*, *13*–*16*), GC lymphocytes were highly motile (T_{FH} cells, 9 μm/min and B cells, 6.6 μm/min) (Fig. 1, B and C, and movie S1). Under steady-state conditions, in which an unknown fraction of B cells are being positively selected, the majority of T-B contacts were short-lived (Fig. 1, B and D, and movie S1). Positive selection through αDEC-OVA injection was associated with a reduction in both GC B and T_{FH} cell velocities, along with an increase in the duration of the T-B contacts ($P < 0.0001$) (Fig. 1, B to D, and movies S2 and S3). In particular, the fraction of conjugates lasting 5 min or longer increased from 2.7 to 20.7% of the total interactions (Fig. 1D), and these occasionally moved at the B cell velocity (4.16 μm/min on average) (Fig. 1E). Although most of the conjugates moved short distances, and it was not possible to determine which one of the partners drags the other (movie S2), in those cases that could be interpreted the conjugates were led by the B cell and rarely, if at all, by the T cell (movie S3). Thus, even under conditions of enforced selection, most T-B interactions resembled those found under physiologic conditions in that they remained transient, with T cells forming and breaking contacts with multiple B cells (Fig. 1D and movie S3). Volume analysis of the T-B colocalized area revealed that the average contact size of the stable T-B conjugates (>5 min) was enlarged threefold during positive selection compared with control (Fig. 1F). As expected, polyclonal follicular B cells within the mantle zone did not slow down or form contacts with T_{FH} cells after αDEC-OVA injection (fig. S2 and movie S4). We conclude that positive selection through increased pMHCII on GC B cells is associated with longer but dynamic T-B contacts involving a larger surface area between the two interacting cells.

To examine whether positive selection interferes with the interactions between T_{FH} cells and GC B cells presenting low levels of pMHCII, we directly imaged selected and nonselected B cells within the same GC. GCs containing OT-II DsRed$^+$ T cells and a mixture of B1-8^{hi} GFP$^+$ *Ly75*$^{-/-}$, CFP$^+$ *Ly75*$^{+/+}$, and nonfluorescent *Ly75*$^{-/-}$ B cells at a ~5:5:90 ratio were generated and imaged as in Fig. 1A. Positive selection of the B1-8^{hi} CFP$^+$ *Ly75*$^{+/+}$ B cells was induced by injecting αDEC-OVA. When compared directly with *Ly75*$^{-/-}$ B cells presenting lower levels of pMHCII in the same GC, positively selected *Ly75*$^{+/+}$ B cells interacted for a longer time with T_{FH} cells ($P < 0.0001$) (Fig. 2, A and B, and movie S5) and formed a greater number of stable contacts (> 5 min) (Fig. 2C). However, selection of *Ly75*$^{+/+}$ GC B cells did not alter the behavior of nonselected *Ly75*$^{-/-}$ cells, which showed no significant change in contact duration or in the total number of interactions (> 0.5 min) with T_{FH} cells (Figs. 1D and 2, B and C, and movie S5). The majority of T_{FH} cells interacting with selected cells concurrently formed transient contacts with nonselected B cells (Fig. 2A and movie S5). We conclude that the increase in contact duration of T_{FH} cells with selected B cells does not substantially affect their interactions with nonselected B cells.

Our experiments indicate that increased contact size and duration correlates with the amount of pMHCII presented by GC B cells and their subsequent clonal expansion in the DZ (*6*), yet how these interactions affect T_{FH} T cell receptor (TCR) signaling is unknown. To examine the relationship between T-B contacts, TCR signaling, and B cell selection in the GC, we sought to measure intracellular Ca^{2+} levels in T_{FH} cells. Traditional Ca^{2+} dyes cannot be used for this purpose because T cells divide extensively and dilute such tracers before reaching the GC (*17*). To circumvent this issue, we used mice expressing a genetically encoded Ca^{2+} indicator (GCaMP3), which changes its fluorescence intensity according to intracellular Ca^{2+} levels (*18*, *19*). Lymphocytes from these mice showed an increase in intracellular fluorescence when stimulated with a Ca^{2+} ionophore or when stimulated through their antigen receptor (fig. S3 and movie S6).

Changes in Ca^{2+} fluorescence are best measured by comparison with a second dye that is insensitive to changes in intracellular Ca^{2+} levels.

[1]Laboratory of Molecular Immunology, The Rockefeller University, New York, NY 10065, USA. [2]Department of Internal Medicine (Rheumatology), School of Medicine, Yale University, New Haven, CT 06520, USA. [3]Department of Immunobiology, School of Medicine, Yale University New Haven, CT 06520, USA. [4]Howard Hughes Medical Institute (HHMI).
*Present address: Immunology Institute, Department of Medicine, Icahn School of Medicine at Mount Sinai, New York, NY 10029, USA.
†Corresponding author. E-mail: nussen@rockefeller.edu

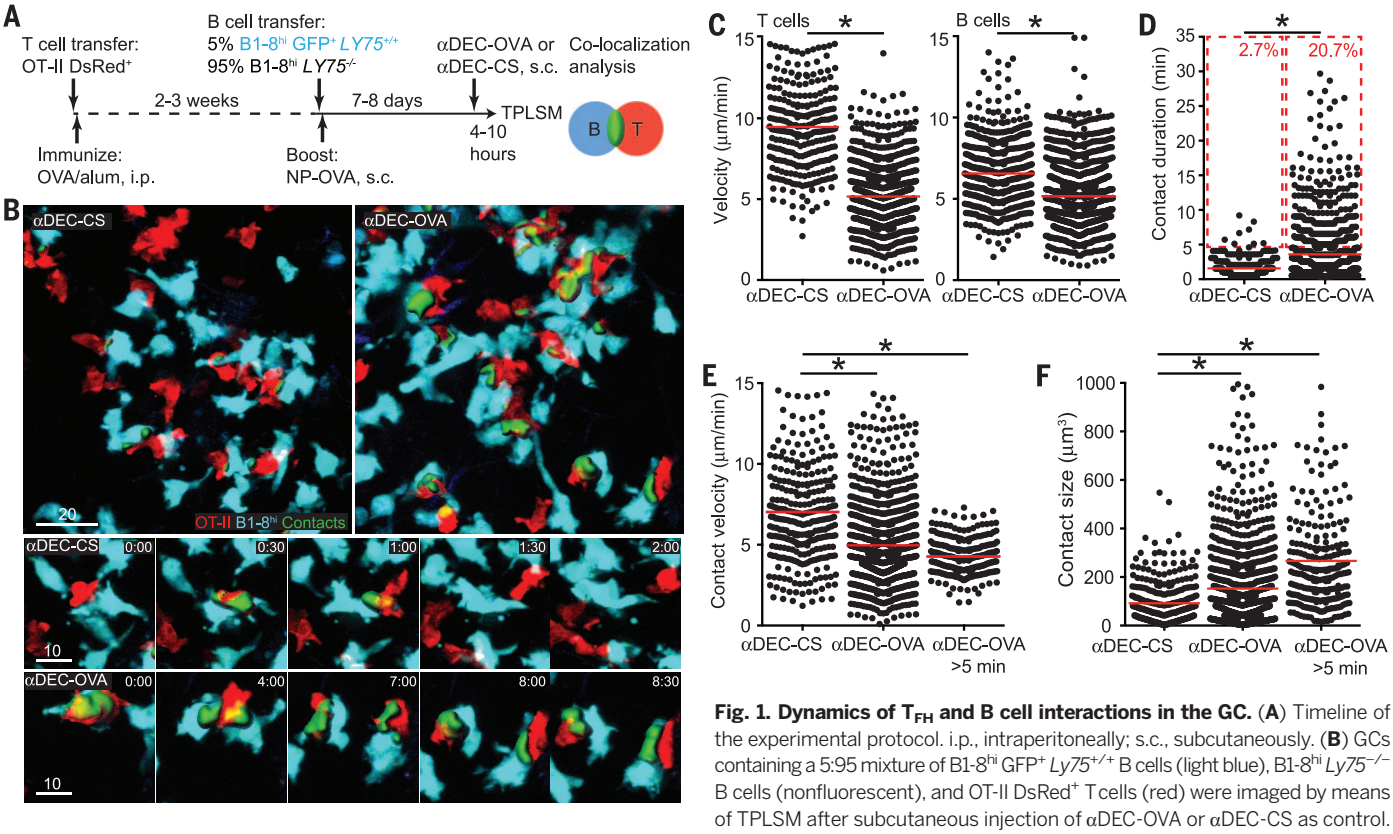

Fig. 1. Dynamics of T_{FH} and B cell interactions in the GC. (**A**) Timeline of the experimental protocol. i.p., intraperitoneally; s.c., subcutaneously. (**B**) GCs containing a 5:95 mixture of B1-8^{hi} GFP$^+$ *Ly75*$^{+/+}$ B cells (light blue), B1-8^{hi} *Ly75*$^{-/-}$ B cells (nonfluorescent), and OT-II DsRed$^+$ T cells (red) were imaged by means of TPLSM after subcutaneous injection of αDEC-OVA or αDEC-CS as control. T-B contacts (green) were detected by means of colocalization. Collapsed z-stacks of 40-μm depth (in 5-μm steps) are shown. (Bottom) T and B cell dynamics over time. Images correspond to movies S1 to S3. (**C**) Velocity analysis of OT-II T cells and B1-8^{hi} B cells in GCs. (**D**) T-B contact duration as measured by the lifetime of the T-B colocalized areas. Percentages indicate events lasting >5 min, marked by a dashed red box. (**E**) T-B conjugate velocity was measured as the velocity of the T-B colocalized area. (**F**) Contact size analysis as measured by T-B colocalized area. Each data point represents a single cell, and red lines represent mean values. Data in (C) to (F) were pooled from two to four mice imaged in two to four independent experiments. *$P < 0.0001$; two-tailed Student's *t* test.

Fig. 2. T_{FH} cell interactions with selected and non-selected GC B cells. (**A**) GCs containing a ~5:5:90 mixture of B1-8^{hi} CFP$^+$ *Ly75*$^{+/+}$ B cells (blue), B1-8^{hi} GFP$^+$ *Ly75*$^{-/-}$ (green), *Ly75*$^{-/-}$ nonfluorescent B cells, and OT-II DsRed$^+$ T cells (red) were imaged by means of TPLSM after subcutaneous injection of αDEC-OVA. Contacts between OT-II T cells and either B1-8^{hi} *Ly75*$^{+/+}$ or *Ly75*$^{-/-}$ B cells are shown in yellow and gray, respectively. 40-μm deep, collapsed z-stacks (5-μm steps) are shown. Arrowheads indicate B1-8^{hi} *Ly75*$^{+/+}$ and *Ly75*$^{-/-}$ GC B cells interacting simultaneously with one OT-II T cell. (**B**) Quantitation of contact duration between OT-II T cells and B1-8^{hi} *Ly75*$^{+/+}$ or *Ly75*$^{-/-}$ B cells. Each data point represents a single cell, and red lines represent mean values. Percentages indicate events >5 min, marked by a dashed red box. (**C**) The number of B cell contacts (>0.5 min, left; >5 min, right) with OT-II T cells was normalized to the number of B cells in each group. Exp., experiment. Data in (B) and (C) were pooled from four independent experiments. *$P < 0.0001$; two-tailed Student's *t* test.

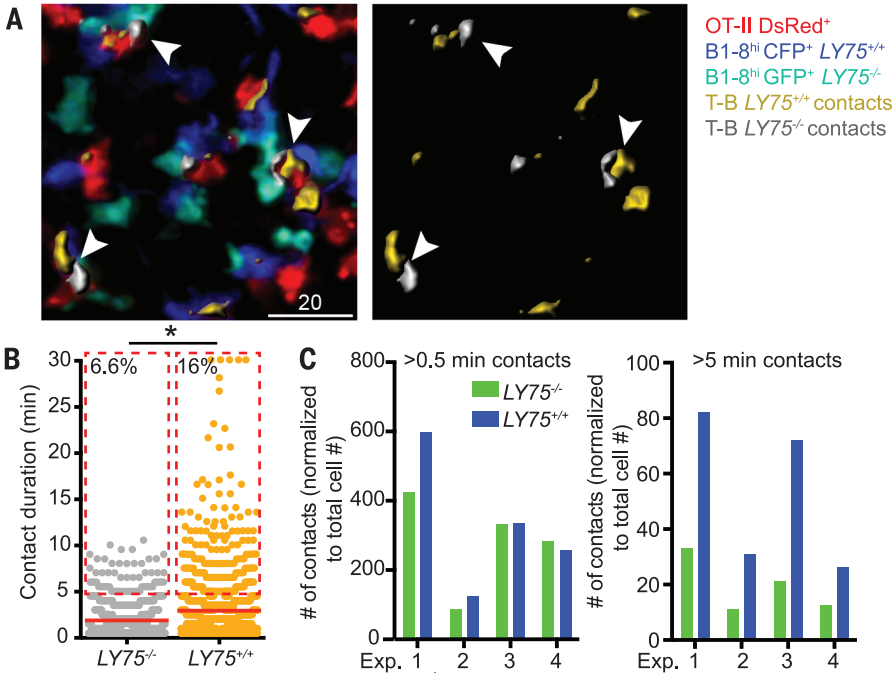

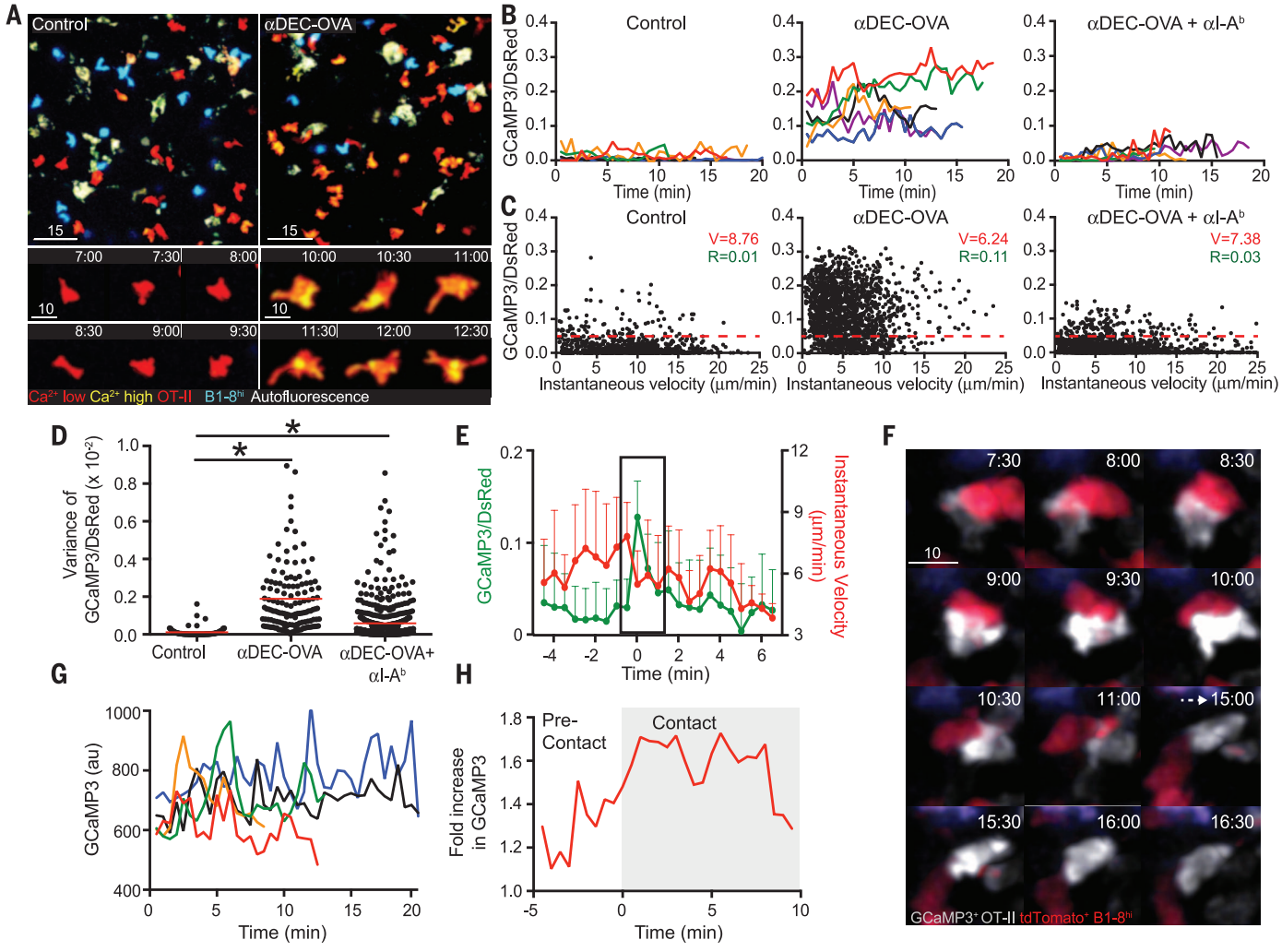

Fig. 3. T_{FH} cell Ca^{2+} signaling during B cell selection. (**A**) GCs containing a 5:95 mixture of B1-8^{hi} CFP^+ *Ly75*$^{+/+}$ B cells (light blue), B1-8^{hi} *Ly75*$^{-/-}$ B cells (nonfluorescent), and OT-II $DsRed^+$ $GCaMP3^+$ T cells (red, Ca^{2+} low; yellow, Ca^{2+} high) were imaged by TPLSM in untreated mice or after subcutaneous injection of αDEC-OVA. (Bottom) Dynamic changes in GCaMP3 fluorescence in individual OT-II T cells over time. (**B**) Traces show changes in the GCaMP3/DsRed ratios over time for six single T cells in each condition. αI-A^b was injected intravenously after αDEC-OVA injection. (**C**) Scatter plots depict the GCaMP3/DsRed ratio versus instantaneous velocity as measured at successive 30-s intervals. Each dot represents a single cell at a single time point. Average velocity (*V*) and GCaMP3/DsRed ratios (*R*) of two to three experiments are indicated in red and green, respectively. (**D**) GCaMP3/DsRed ratio fluctuations in single cells (expressed as variance) under control and αDEC-OVA conditions. (**E**) GCaMP3/DsRed spikes of nine cells were synchronized. Traces of average GCaMP3/DsRed ratios and corresponding instantaneous velocities are shown. The synchronized spikes fall in the black rectangle. Error bars indicate SEM. (**F**) OT-II $GCaMP3^+$ T cells and B1-8^{hi} $tdTomato^+$ *Ly75*$^{+/+}$ B cells were imaged in GCs over time as in (A). Images correspond to movie S11. (**G**) Traces show GCaMP3 mean fluorescence intensities for five OT-II T cells in contact with B1-8^{hi} $tdTomato^+$ *Ly75*$^{+/+}$ GC B cells. (**H**) Initiation of contacts were synchronized in 4 OT-II $GCaMP3^+$ T cells, and the corresponding average of GCaMP3 fluorescence intensity was traced before and during the contact (au, arbitrary units). Data are representative of two or three mice imaged in two or three independent experiments. *$P < 0.0001$; two-tailed Student's *t* test.

We therefore induced and imaged GCs, as described in Fig. 1A, using OT-II $GCaMP3^+$ $DsRed^+$ T cells and measured the ratio of GCaMP3:DsRed fluorescence intensity (fig. S4). To determine whether T_{FH} cell Ca^{2+} content is associated with changes in cellular dynamics, velocities at successive time points were measured (instantaneous velocity) and correlated with intracellular Ca^{2+} content (*17*). Under steady-state conditions, spikes in Ca^{2+} content in GC T_{FH} cells were rare (Fig. 3, A to C; fig. S5A; and movie S7). In contrast, αDEC-OVA injection increased the proportion of GC T_{FH} cells with GCaMP3:DsRed ratios above 0.05 from 9 to 68% (Fig. 3, A to C, and movie S7) and the average ratio by 8.3-fold (fig. S5A). Single T_{FH} cells that were actively engaged in B cell selection showed sustained increases in intracellular Ca^{2+} over time, which did not drop to control levels during the observation period (Fig. 3B). In addition, single T_{FH} cells also displayed frequent Ca^{2+} spike transients (Fig. 3, B and D). Both sustained and transient increases in T_{FH} intracellular Ca^{2+} levels were a result of TCR:pMHCII interactions (Fig. 3, B to D, and fig. S5A). We conclude that selection is associated with TCR:pMHCII–dependent increases in T_{FH} cell Ca^{2+} content that were both transient and long-term.

Increases in intracellular Ca^{2+} content in naïve T cells result in motility arrest and enhanced effector functions (*17*, *20*, *21*). By correlating intracellular Ca^{2+} content and instantaneous velocity in unperturbed GCs, we found that T_{FH} cells moved at an average speed of 8.76 μm/min regardless of their Ca^{2+} content (Fig. 3C and fig. S5B). Consistently, in αDEC-OVA–targeted GCs the velocity of T_{FH} cells with high- and low-Ca^{2+} content was decreased to an average of 6.24 μm/min, and few, if any, of the actively engaged T_{FH} cells stopped moving or lost their morphological polarity while signaling (Fig. 3C, fig. S5B, and movies S7 to S9). However, there was no

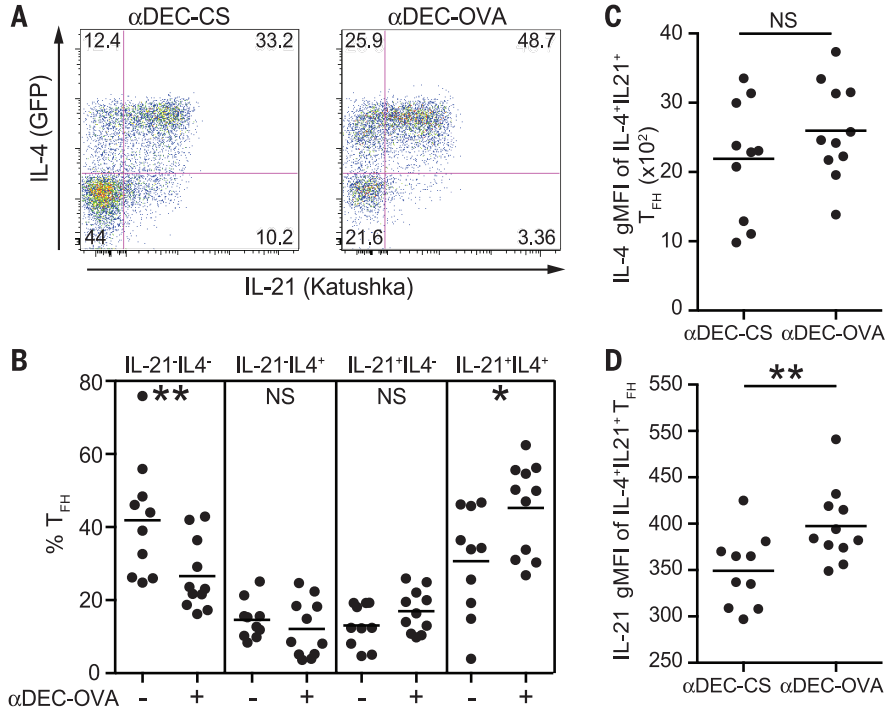

Fig. 4. Multifunctional T_{FH} cells during B cell selection. (**A** and **B**) $CD4^+$ T cells derived from OVA-immunized *Il4-IRES-GFP* and *Il21-IRES-Katushka* double knock-in mice and a 5:95 ratio of B1-8^{hi} *Ly75*$^{+/+}$ and *Ly75*$^{-/-}$ B cells were transferred into TCRβ-deficient mice, before boosting with NP-OVA. After 7 days, mice were injected with αDEC-CS or αDEC-OVA, and lymph nodes were analyzed 9 hours later. The proportions of cytokine-expressing cells among T_{FH} ($CD8^-$, $B220^-$, $CD4^+$, $CD44^+$, $CD62L^-$, $CXCR5^{high}$, and $PD\text{-}1^{high}$) subsets are indicated. (**C** and **D**) gMFI of IL-4 (C) or IL-21 (D) reporter expression. Each data point represents a single mouse, and lines represent mean values. Pooled data from three experiments each with three or four mice per condition. *P = 0.025; **P = 0.014; ***P = 0.02; two-tailed Student's t test. NS, not significant.

clear correlation between the level of Ca^{2+} increase and cell motility because both T_{FH} cells with high- and low-Ca^{2+} content had the same average velocity (Fig. 3C, fig. S5B, and movie S7). Nevertheless, by synchronizing transient small Ca^{2+} peaks of several T_{FH} cells, we found that these were precisely associated with a reduction in instantaneous velocity of ~2.5 μm/min (Fig. 3E, fig. S6, and movie S10).

Given these broad changes in Ca^{2+} content and the regulated T-B interactions, we sought to examine T_{FH} intracellular Ca^{2+} levels during the formation of T-B contacts. To this end, we imaged selection in GCs containing a 95:5 mixture of B1-8^{hi} nonfluorescent *Ly75*$^{-/-}$ B cells, $tdTomato^+$ *Ly75*$^{+/+}$ B cells, and OT-II $GCaMP3^+$ T cells. Injection of αDEC-OVA induced the formation of T cell contacts with *Ly75*$^{+/+}$ B cells that were associated with transient spikes in T_{FH} intracellular Ca^{2+} content (Fig. 3, F and G, and movies S11 and S12). To determine whether these Ca^{2+} transients take place preferentially during T-B conjugate formation, we synchronized clearly isolated contact events and measured the average GCaMP3 fluorescence intensity in T_{FH} cells before and during these interactions. Although the intracellular Ca^{2+} levels in T_{FH} cells were high in αDEC-OVA–targeted GCs (Fig. 3B), an additional small increase at the onset of contact with selected B cells was detected (Fig. 3H and movie S10).

Changes in intracellular Ca^{2+} concentration control T cell effector functions, including the expression of IL-4 and IL-21 (*20*, *22*), both of which are required for effective B cell immune responses (*23*). T effector cells can express either or both of these cytokines, and this multifunctionality is associated with enhanced immunity and vaccine responses (*24*–*28*). To determine whether the long-term increase in T_{FH} intracellular Ca^{2+} levels alters the quality of GC T_{FH} cells, we examined T cells derived from IL4/IL21 double reporter mice expressing *Il4-IRES-GFP* (*29*) and *Il21-IRES-Katushka* (fig. S7). Polyclonal OVA-primed $CD4^+$ T cells isolated from these mice were adoptively transferred into TCRβ-deficient mice along with B1-8^{hi} *Ly75*$^{+/+}$ and *Ly75*$^{-/-}$ B cells at a 5:95 ratio. Recipients were boosted with NP-OVA and injected 7 days later with either αDEC-CS or αDEC-OVA so as to induce selection. T_{FH} cells were examined for cytokine expression 9 hours later by means of flow cytometry. αDEC-OVA injection resulted in a significant decrease in $IL\text{-}4^-IL\text{-}21^-$ T_{FH} cells and a concomitant increase in $IL\text{-}4^+IL\text{-}21^+$ multifunctional T_{FH} cells in the absence of cell division or a significant change in the number of single-cytokine-producing cells (Fig. 4, A and B, and fig. S8). Moreover, there was also a small but significant increase in the amount of IL-21, but not IL-4, produced by the double-positive cells, as measured by an increase in the mean fluorescence intensity of the reporters (Fig. 4, C and D). Thus, increased T_{FH} Ca^{2+} signaling during B cell selection is associated with a rapid change in the quality of the GC T_{FH} response, with increased development of multifunctional T_{FH} cells producing Ca^{2+}–dependent cytokines.

Our results demonstrate that T_{FH} cells respond to pMHCII on GC B cells during selection differently than the prolonged interactions of T cells with dendritic cells (DCs) in the T zone or with B cells at the T-B border (*30*–*36*). The transient interactional dynamics of T_{FH} cells in GCs allow them to continuously seek and find B cells presenting high levels of pMHCII and provide them with preferential help while permitting competitive opportunities for other GC B cells. This mode of B cell scanning allows T_{FH} cells to interact with many cells presenting a range of pMHCII levels, rather than forming a prolonged contact with a single high-affinity B cell.

Our experiments show that the increased size and duration of contacts between GC T_{FH} and selected B cells prolongs Ca^{2+} signaling and modifies the quality of the GC T_{FH} response. These events induce coexpression of the Ca^{2+}-dependent cytokines IL-4 and IL-21, which endow T_{FH} cells with effector capabilities that facilitate high-affinity B cell selection.

REFERENCES AND NOTES

1. C. Berek, A. Berger, M. Apel, *Cell* **67**, 1121–1129 (1991).
2. C. D. Allen, T. Okada, J. G. Cyster, *Immunity* **27**, 190–202 (2007).
3. G. D. Victora, M. C. Nussenzweig, *Annu. Rev. Immunol.* **30**, 429–457 (2012).
4. M. Oprea, A. S. Perelson, *J. Immunol.* **158**, 5155–5162 (1997).
5. G. D. Victora *et al.*, *Cell* **143**, 592–605 (2010).
6. A. D. Gitlin, Z. Shulman, M. C. Nussenzweig, *Nature* **509**, 637–640 (2014).
7. S. Crotty, *Annu. Rev. Immunol.* **29**, 621–663 (2011).
8. C. G. Vinuesa, J. G. Cyster, *Immunity* **35**, 671–680 (2011).
9. C. D. Allen, T. Okada, H. L. Tang, J. G. Cyster, *Science* **315**, 528–531 (2007).
10. T. A. Shih, M. Roederer, M. C. Nussenzweig, *Nat. Immunol.* **3**, 399–406 (2002).
11. T. A. Schwickert *et al.*, *Nature* **446**, 83–87 (2007).
12. Materials and methods are available as supplementary materials on *Science* Online.
13. A. E. Hauser *et al.*, *Immunity* **26**, 655–667 (2007).
14. M. Kitano *et al.*, *Immunity* **34**, 961–972 (2011).
15. S. M. Kerfoot *et al.*, *Immunity* **34**, 947–960 (2011).
16. Z. Shulman *et al.*, *Science* **341**, 673–677 (2013).
17. S. H. Wei *et al.*, *J. Immunol.* **179**, 1586–1594 (2007).
18. J. Nakai, M. Ohkura, K. Imoto, *Nat. Biotechnol.* **19**, 137–141 (2001).
19. H. A. Zariwala *et al.*, *J. Neurosci.* **32**, 3131–3141 (2012).

20. S. Agarwal, O. Avni, A. Rao, *Immunity* **12**, 643–652 (2000).
21. P. A. Negulescu, T. B. Krasieva, A. Khan, H. H. Kerschbaum, M. D. Cahalan, *Immunity* **4**, 421–430 (1996).
22. H. P. Kim, L. L. Korn, A. M. Gamero, W. J. Leonard, *J. Biol. Chem.* **280**, 25291–25297 (2005).
23. K. Ozaki *et al.*, *Science* **298**, 1630–1634 (2002).
24. M. R. Betts *et al.*, *Blood* **107**, 4781–4789 (2006).
25. E. W. Newell, N. Sigal, S. C. Bendall, G. P. Nolan, M. M. Davis, *Immunity* **36**, 142–152 (2012).
26. P. A. Darrah *et al.*, *Nat. Med.* **13**, 843–850 (2007).
27. M. A. Kroenke *et al.*, *J. Immunol.* **188**, 3734–3744 (2012).
28. K. Lüthje *et al.*, *Nat. Immunol.* **13**, 491–498 (2012).
29. M. Mohrs, K. Shinkai, K. Mohrs, R. M. Locksley, *Immunity* **15**, 303–311 (2001).
30. T. R. Mempel, S. E. Henrickson, U. H. Von Andrian, *Nature* **427**, 154–159 (2004).
31. G. Shakhar *et al.*, *Nat. Immunol.* **6**, 707–714 (2005).
32. M. J. Miller, S. H. Wei, I. Parker, M. D. Cahalan, *Science* **296**, 1869–1873 (2002).
33. D. Skokos *et al.*, *Nat. Immunol.* **8**, 835–844 (2007).
34. T. Okada *et al.*, *PLOS Biol.* **3**, e150 (2005).
35. H. Qi, J. L. Cannons, F. Klauschen, P. L. Schwartzberg, R. N. Germain, *Nature* **455**, 764–769 (2008).
36. T. A. Schwickert *et al.*, *J. Exp. Med.* **208**, 1243–1252 (2011).

ACKNOWLEDGMENTS

We thank G. Victora for helpful discussions and suggestions, D. Bosque and T. Eisenreich for help with mouse colony management, A. Abadir for protein production, and K. Yao for technical help. The data reported in this manuscript are tabulated in the main paper and in the supplementary materials. Z.S. is a Human Frontiers of Science Program fellow (reference LT000340/2011-L). A.D.G. is supported by NIH Medical Scientist Training Program grant T32GM07739 to the Weill Cornell/Rockefeller/Sloan-Kettering Tri-Institutional MD-PhD Program. Support for the Rockefeller University multiphoton microscope was granted by the Empire State Stem Cell Fund through New York State Department of Health contract C023046. This work was supported by NIH grants AI037526-19, AI072529-06, and AI100663-02 to M.C.N. and NIH grants AR40072-24 and AR053495-08 (the content is solely the responsibility of the authors and does not necessarily represent the official views of the NIH) and the Alliance for Lupus Research to J.E.C. M.C.N. and R.A.F. are HHMI investigators.

SUPPLEMENTARY MATERIALS

www.sciencemag.org/content/345/6200/1058/suppl/DC1
Materials and Methods
Figs. S1 to S8
References
Movies S1 to S12

24 June 2014; accepted 31 July 2014
10.1126/science.1257861

CELL MIGRATION IN 3D

Generation of compartmentalized pressure by a nuclear piston governs cell motility in a 3D matrix

Ryan J. Petrie,[1]* Hyun Koo,[1,2,3] Kenneth M. Yamada[1]*

Cells use actomyosin contractility to move through three-dimensional (3D) extracellular matrices. Contractility affects the type of protrusions cells use to migrate in 3D, but the mechanisms are unclear. In this work, we found that contractility generated high-pressure lobopodial protrusions in human cells migrating in a 3D matrix. In these cells, the nucleus physically divided the cytoplasm into forward and rear compartments. Actomyosin contractility with the nucleoskeleton-intermediate filament linker protein nesprin-3 pulled the nucleus forward and pressurized the front of the cell. Reducing expression of nesprin-3 decreased and equalized the intracellular pressure. Thus, the nucleus can act as a piston that physically compartmentalizes the cytoplasm and increases the hydrostatic pressure between the nucleus and the leading edge of the cell to drive lamellipodia-independent 3D cell migration.

Cells moving across a flat two-dimensional (2D) surface or inside nonlinearly elastic 3D collagen use polarized signaling to direct the formation of a dendritic actin network and extend flat, lamellipodial protrusions (*1*, *2*). When primary human fibroblasts move within a cross-linked, linearly elastic 3D structure such as dermal or cell-derived matrix, they can switch to a lamellipodia-independent migration mechanism characterized by nonpolarized signaling and blunt, cylindrical protrusions termed "lobopodia" (*1*). Actomyosin contractility via the RhoA–ROCK–myosin II signaling axis is required for cells to form and maintain lobopodia in response to the degree of matrix cross-linking. However, the mechanism by which increased contractility generates lobopodia is unclear.

Lobopodial cells can also be distinguished by rapid membrane blebbing along their sides, oriented perpendicular to the leading edge. Membrane blebs can be generated by elevated intracellular hydrostatic pressure, local weakening of the attachment of the plasma membrane to the underlying cortex, or both (*3*–*5*). We hypothesized that this lateral blebbing could result from elevated intracellular pressure during lobopodial motility. This increased pressure might result from the RhoA, ROCK, and myosin II activities required for the lamellipodia-independent migration of fibroblasts through a physiological linearly elastic 3D matrix (*1*).

We tested the hypothesis by directly determining intracellular pressures in primary human fibroblasts migrating on 2D surfaces compared with a 3D extracellular matrix (ECM). We used a microelectrode coupled to a servo-null micropressure system to penetrate the plasma membrane immediately in front of the nucleus (relative to the leading edge) and to measure the intracellular hydrostatic pressure exerted by the cytoplasm directly (P_{ic}) (Fig. 1) (see supplementary materials and methods). Direct comparisons of pressure in cells migrating on top of a cell-derived matrix (CDM) and embedded within a 3D collagen matrix revealed low hydrostatic pressures in both 2D and 3D lamellipodial cells [~300 and 700 Pa on the linearly elastic 2D surface of the CDM and within nonlinearly elastic 3D collagen, respectively; see (*1*) for characterization of matrix elastic behavior]. In contrast, intracellular pressure was substantially elevated (~2200 Pa) in lobopodial cells migrating inside the 3D CDM. Switching these lobopodial cells to lamellipodial cells by inhibiting RhoA, ROCK, or myosin II (*1*) reduced hydrostatic pressure (to ~400 Pa) in each case. This inhibition distinguished lobopodia from the contractility-independent water permeation mechanism used by certain cancer cells

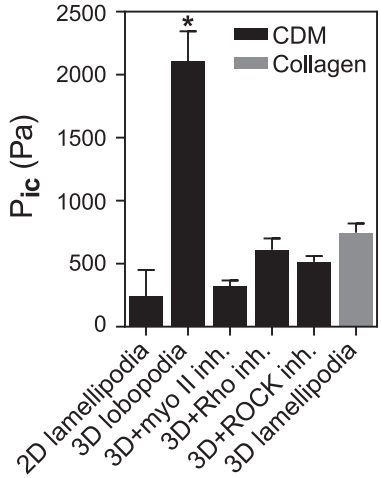

Fig. 1. Actomyosin contractility governs intracellular pressure in a 3D ECM. Comparison of the intracellular pressures ($n \geq 20$ replicates each) of lamellipodial cells on 2D CDM and in 3D collagen, untreated lobopodial cells in 3D CDM, or cells in CDM treated overnight with inhibitors of myosin II (25 μM blebbistatin), ROCK (10 μM Y-27632), or RhoA (10 μg/ml C3 transferase). $N = 3$ independent experiments, $^*P < 0.001$. Error bars indicate SEM.

[1]Laboratory of Cell and Developmental Biology, National Institute of Dental and Craniofacial Research, National Institutes of Health, Bethesda, MD 20892–4370, USA. [2]Center for Oral Biology, Department of Microbiology and Immunology, University of Rochester Medical Center, Rochester, NY 14642, USA. [3]Biofilm Research Labs, Levy Center for Oral Health, Department of Orthodontics, University of Pennsylvania School of Dental Medicine, Philadelphia, PA 19104–6030, USA.
***Corresponding author. E-mail: petrier@mail.nih.gov (R.J.P.); kyamada@mail.nih.gov (K.M.Y.)**

in confined channels (*6*). Control cells using lamellipodia to migrate on 2D glass maintained relatively low intracellular pressure (fig. S1A), with values consistent with indirect pressure estimates for other cell types (*7*, *8*). As expected (*9*), placing cells in a hypotonic medium to trigger an influx of water increased P_{ic}, as did increasing contractility by treating cells with calyculin A. Thus, a linearly elastic, cross-linked 3D ECM activates actomyosin contractility to increase intracellular pressure and maintain the lobopodial mode of 3D cell migration.

To establish whether intracellular pressure is uniformly increased throughout the cytoplasm of lobopodia-bearing cells, we compared hydrostatic pressures immediately in front of and behind the nucleus (Fig. 2, A and B). P_{ic} was significantly elevated and compartmentalized in lobopodia (to ~2400 Pa), with the nucleus separating this anterior high-pressure compartment from a low-pressure zone (~900 Pa) in the cell posterior. In contrast, low pressures were found both in front and back of the nucleus in fibroblasts using lamellipodia to migrate in 2D and 3D environments (~400 and 800 Pa, respectively).

The existence of large differences in hydrostatic pressure in front of versus behind the nucleus suggests that the nucleus physically divides the cytoplasm in lobopodial cells. We tested this prediction by measuring the diffusion and/or convection of cytoplasmic photoactivatable green fluorescent protein (PA-GFP) in live cells (Fig. 2, C and D). After photoactivation near the leading edge (Fig. 2C), fluorescent PA-GFP significantly slowed as it moved past the nucleus in lobopodial cells in 3D CDM compared with lamellipodial cells on 2D glass (Fig. 2D and fig. S2). This matrix-dependent barrier consisted of the nucleus and a dense accumulation of sheets of membranous material, including endoplasmic reticulum (fig. S3).

Given the established links between the nucleus, cytoskeleton, and the ECM (*10*–*13*) and the requirement for actomyosin contractility to generate high-pressure lobopodia (Fig. 1), we hypothesized that the tight-fitting nucleus might be pulled forward like a piston to pressurize the anterior cytoplasmic compartment. Live-cell confocal microscopy showed apparent pulling forward of the nucleus, which periodically accelerated away from the cell's trailing edge in 3D CDM (movie S1). Further, monitoring of nuclear movement and P_{ic} after inhibition of myosin II revealed that the nucleus fell back and pressure equilibrated initially, ultimately becoming low and uniform (Fig. 2, E and F and movie S2), consistent with loss of actomyosin contraction pulling the nuclear piston forward. In direct contrast, the nucleus continued to move forward with no pressure change in 2D lamellipodial cells after myosin II inhibition. Microtubules were not required for nuclear movement in lobopodial cells (fig. S4).

Myosin IIA and vimentin intermediate filaments were polarized anteriorly in lobopodial cells (Fig. 3, A and B). Because nesprin-3, a nucleoskeleton-vimentin linker protein, is a proposed mediator of force transmission through the cytoskeleton to the nucleus and is needed for polarity and migration (*14*), we searched for an actomyosin–vimentin–nesprin-3 complex. Immunoprecipitation revealed a complex of actin, myosin IIA, vimentin, and nesprin-3 in primary cells (Fig. 3C). Actin and myosin II were lost from the complex after inhibiting myosin II [only 18.4 ± 12.8% (SEM) of actin and 26.7 ± 16.3% of myosin IIA remained associated with vimentin after blebbistatin treatment, versus 88.7 ± 14.9%, of the nesprin-3]. Local inhibition of myosin II in front of the nucleus (fig. S1B) blocked forward movement of the nucleus (Fig. 2G), reduced forward pressure, and retracted the leading edge (Fig. 3D), whereas myosin II inhibition behind the nucleus did not. Similarly, local permeabilization of the plasma membrane in front of the nucleus resulted in loss of forward pressure and leading edge retraction (fig. S1C). To test whether nesprin-3 provides a link between myosin contractility and forward movement of the nucleus

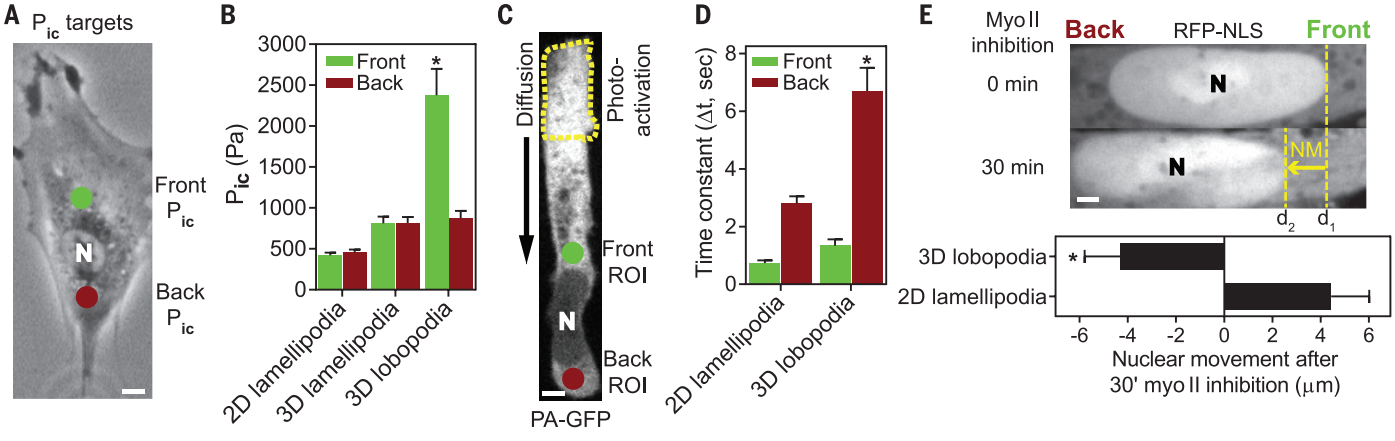

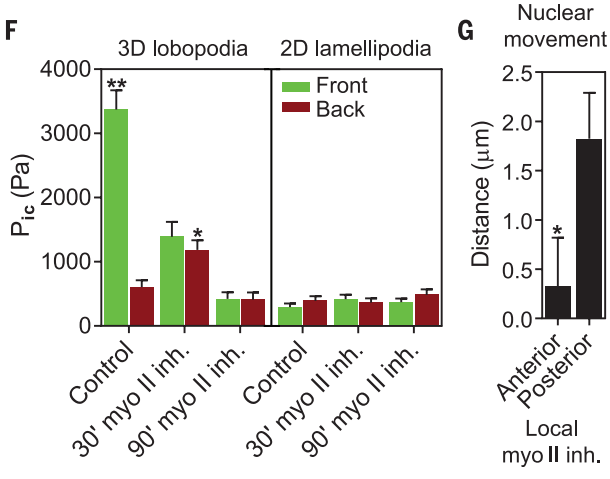

Fig. 2. Lobopodial fibroblasts are compartmentalized into high- and low-pressure zones. (**A**) Intracellular pressures were measured immediately in front of (green dot) and behind (red dot) the nucleus (N). Scale bar, 5 μm. (**B**) Comparison of intracellular pressures in front and behind the nucleus of fibroblasts ($n \geq 25$) migrating on 2D glass (2D lamellipodia), in 3D collagen (3D lamellipodia), or in 3D CDM (3D lobopodia) ($N = 3$). *$P < 0.01$. (**C**) A subpopulation of PA-GFP was activated near the leading edge (dashed box), and the rate of translocation was measured at the indicated regions of interest (ROI) immediately in front of and behind the nucleus in live cells. Scale bar, 5 μm. (**D**) Time constants of PA-GFP accumulation show that the nucleus significantly slows the rate of PA-GFP translocation in 3D lobopodial versus 2D lamellipodial fibroblasts ($n \geq 17$, $N = 3$). *$P < 0.01$. (**E**) Myosin II inhibition results in immediate backward movement of the nucleus in lobopodial but not lamellipodial cells (quantified in the lower panel) ($n = 10$, $N = 3$). *$P < 0.01$. Scale bar, 3 μm. RFP-NLS, red fluorescent protein–nuclear localization signal; NM, nuclear movement. (**F**) Pressure rises transiently behind the nucleus after myosin II inhibition only in lobopodial cells ($n \geq 16$, $N = 3$). **$P < 0.001$ versus front P_{ic}; *$P < 0.01$ versus back P_{ic}. (**G**) Anterior inhibition of myosin II prevents forward movement of the nucleus ($n = 10$, $N = 3$). *$P < 0.01$. Error bars represent SEM.

in lobopodial fibroblasts, we compared instantaneous velocities of the nucleus and the trailing edge in control and nesprin-3 small interfering RNA (siRNA)–treated cells moving through 3D CDM (Fig. 3, E to G, and fig. S5). The nucleus and trailing edge moved independently in control cells, but not in cells with reduced nesprin-3 expression [Pearson's correlation coefficient 0.28 ± 0.01 (SEM) in control versus 0.57 ± 0.07 in nesprin-3 siRNA-treated cells] (Fig. 3G and fig. S6). This loss of independent movement of the nucleus after depleting nesprin-3 was accompanied by a reduction in cell velocity similar to inhibiting global myosin II (Fig. 3H), suggesting that nesprin-3 and the nucleus are connected to a contractile pulling mechanism localized in front of the nucleus required for efficient 3D cell migration.

We tested the hypothesized role of nesprin-3 in piston function of the nucleus by depleting nesprin in cells migrating in 3D CDM. Compartmentalized forward pressure was maintained in cells treated with control siRNA, whereas siRNA knockdown of nesprin-3 reduced and equalized anterior and posterior intracellular pressures (Fig. 4A; verified with independent siRNAs in fig. S5 D and E), even though the diffusion barrier remained intact (fig. S3A). Overall actomyosin contractile function remained unaffected in nesprin-3 knockdown cells, because RhoA

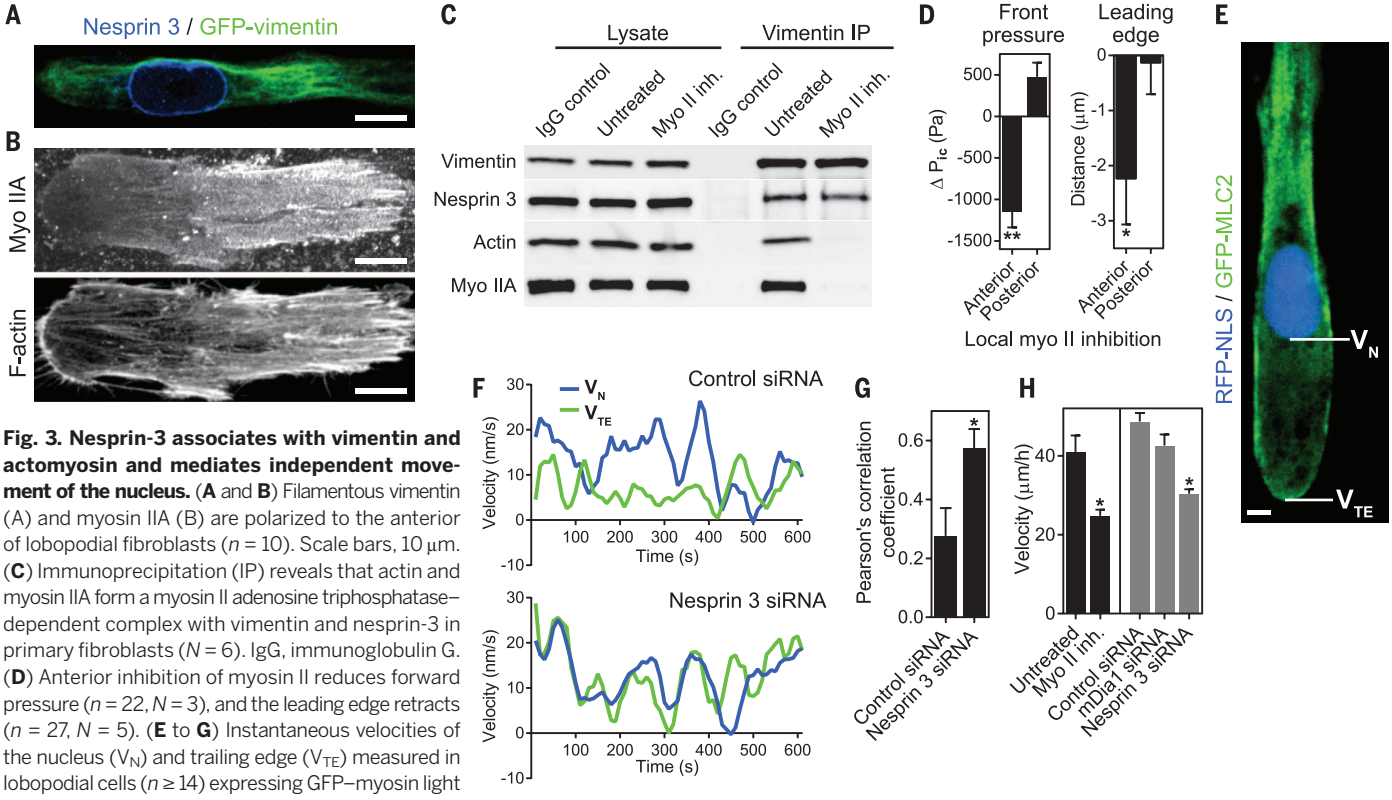

Fig. 3. Nesprin-3 associates with vimentin and actomyosin and mediates independent movement of the nucleus. (**A** and **B**) Filamentous vimentin (A) and myosin IIA (B) are polarized to the anterior of lobopodial fibroblasts ($n = 10$). Scale bars, 10 μm. (**C**) Immunoprecipitation (IP) reveals that actin and myosin IIA form a myosin II adenosine triphosphatase–dependent complex with vimentin and nesprin-3 in primary fibroblasts ($N = 6$). IgG, immunoglobulin G. (**D**) Anterior inhibition of myosin II reduces forward pressure ($n = 22$, $N = 3$), and the leading edge retracts ($n = 27$, $N = 5$). (**E** to **G**) Instantaneous velocities of the nucleus (V_N) and trailing edge (V_{TE}) measured in lobopodial cells ($n \geq 14$) expressing GFP–myosin light chain 2 and RFP-NLS [(E), scale bar, 5 μm] treated with control or nesprin-3 siRNA (F). Nesprin-3 knockdown reduces the independent movement of the nucleus relative to the trailing edge (G) ($N = 3$). (**H**) Myosin II activity and nesprin-3 are each required for efficient 3D migration ($n \geq 45$, $N = 3$). $^{**}P < 0.0001$, $^{*}P < 0.05$. Error bars represent SEM.

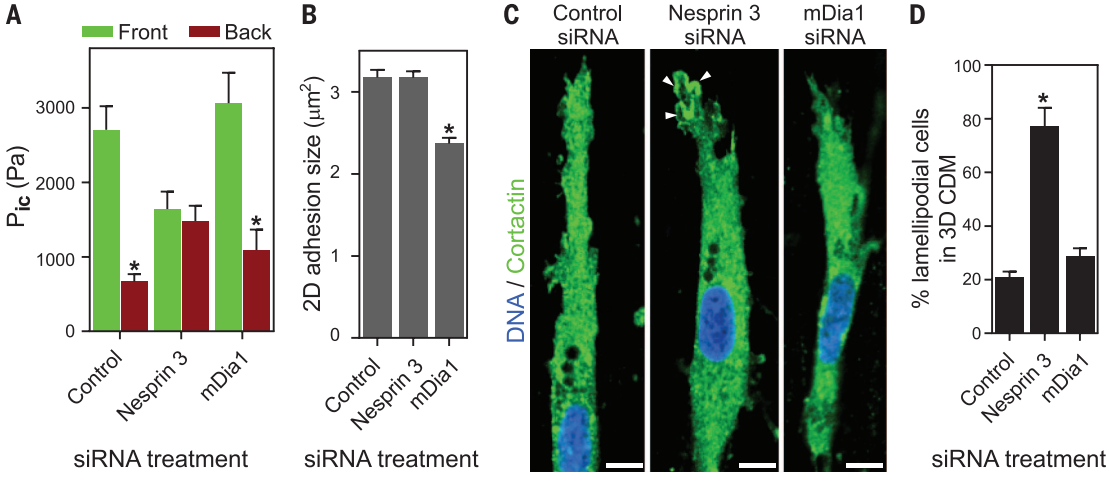

Fig. 4. Nesprin-3 compartmentalizes intracellular pressure to mediate lobopodial 3D migration. (**A**) Comparison of anterior and posterior intracellular pressure in cells treated with the indicated siRNAs ($n \geq 23$, $N = 3$). (**B**) Average size of focal adhesions formed by cells treated with the indicated siRNAs and plated on 2D glass ($n \geq 13$, $N = 3$). (**C**) Cortactin localization in siRNA-treated cells ($n = 17$). Arrowheads indicate local accumulation of the lamellipodial marker cortactin at the leading edge. Scale bars, 10 μm. (**D**) Quantification of lamellipodial cells in 3D CDM after siRNA treatments ($n \geq 33$, $N = 3$). $^{*}P < 0.001$. Error bars indicate SEM.

activation by lysophosphatidic acid still increased 2D focal adhesion size in nesprin-3 siRNA-treated cells on glass (Fig. 4B and fig. S8). Removing the nucleus also reduced and equalized intracellular pressure, in addition to slowing 3D cell movement (fig. S7). Conversely, even though the RhoA effector formin mDia1 was required to increase focal adhesion size on 2D, its depletion did not affect the compartmentalized pressure or velocity of lobopodial cells (Figs. 3H and 4, A and B, and fig. S8). Thus, nesprin-3 is required for pistonlike nuclear movements and pressurizing lobopodial protrusions. This mechanism is distinct from roles of RhoA and contractility controlling focal adhesion size through mDia1.

Finally, we tested whether the loss of nesprin-3 causes a loss of anterior lobopodial protrusions. Whereas control cells continued to use lobopodia to migrate through 3D CDM, the leading edges of nesprin-3 siRNA-treated cells switched to cortactin-positive lamellipodia (Fig. 4, C and D, fig. S9; confirmed with independent siRNAs in fig. S5F). This change mimics the switch from lobopodia to lamellipodia that occurs when RhoA, ROCK, or myosin II are inhibited (*1*), which reduced total intracellular hydrostatic pressure (Fig. 1).

We have shown that when human fibroblasts migrate through a physiological 3D ECM, their intracellular pressure becomes compartmentalized. Furthermore, actomyosin contractility and nesprin-3 act to pull the nuclear piston forward and pressurize the anterior cytoplasmic compartment. The contractility-dependent association of vimentin intermediate filaments with nesprin-3 and actomyosin—along with the known interactions of vimentin filaments, nesprin-3, and the nucleus (*14*–*16*)—supports a model in which actomyosin contractility acts on vimentin filaments to pull the nucleus forward and increase compartmentalized pressure (fig. S10). This polarized intracellular pressure is associated with a nonpolarized distribution of intracellular signaling during 3D migration (*1*) and explains how a nucleoskeleton-cytoskeleton linker protein localized in the nuclear membrane can help to determine the structure and dynamic function of the leading edge of cells migrating in a 3D ECM. This mechanism can operate in a variety of primary human cells (fig. S11) and illustrates how the physical structure of the matrix can influence cellular physical properties to govern biological function.

REFERENCES AND NOTES

1. R. J. Petrie, N. Gavara, R. S. Chadwick, K. M. Yamada, *J. Cell Biol.* **197**, 439–455 (2012).
2. A. J. Ridley *et al.*, *Science* **302**, 1704–1709 (2003).
3. G. T. Charras, J. C. Yarrow, M. A. Horton, L. Mahadevan, T. J. Mitchison, *Nature* **435**, 365–369 (2005).
4. J. Y. Tinevez *et al.*, *Proc. Natl. Acad. Sci. U.S.A.* **106**, 18581–18586 (2009).
5. M. Tozluoğlu *et al.*, *Nat. Cell Biol.* **15**, 751–762 (2013).
6. K. M. Stroka *et al.*, *Cell* **157**, 611–623 (2014).
7. G. T. Charras, M. Coughlin, T. J. Mitchison, L. Mahadevan, *Biophys. J.* **94**, 1836–1853 (2008).
8. J. Dai, M. P. Sheetz, *Biophys. J.* **77**, 3363–3370 (1999).
9. S. M. Kelly, P. T. Macklem, *Am. J. Physiol.* **260**, C652–C657 (1991).
10. A. B. Chambliss *et al.*, *Sci. Rep.* **3**, 1087 (2013).
11. J. Swift *et al.*, *Science* **341**, 1240104 (2013); DOI: 10.1126/science.1240104.
12. K. Wolf *et al.*, *J. Cell Biol.* **201**, 1069–1084 (2013).
13. J. Wu *et al.*, *Biophys. J.* **106**, 7–15 (2014).
14. M. L. Lombardi *et al.*, *J. Biol. Chem.* **286**, 26743–26753 (2011).
15. J. T. Morgan *et al.*, *Mol. Biol. Cell* **22**, 4324–4334 (2011).
16. K. Wilhelmsen *et al.*, *J. Cell Biol.* **171**, 799–810 (2005).

ACKNOWLEDGMENTS

We thank K. Carver for helping to characterize various primary human cells; D. Starr for providing the nesprin-3 antibody; and M. Hoffman, A. Doyle, W. Daley, and K. Holmberg for critical comments on the manuscript. This work was supported by the Intramural Research Program of the National Institute of Dental and Craniofacial Research, NIH. The data presented in this manuscript are found in the main paper and the supplementary materials and methods.

SUPPLEMENTARY MATERIALS

www.sciencemag.org/content/345/6200/1062/suppl/DC1
Materials and Methods
Figs. S1 to S11
References (*17*–*23*)
Movies S1 and S2

4 June 2014; accepted 4 July 2014
10.1126/science.1256965

CHROMATIN REGULATION

Histone H3 lysine-to-methionine mutants as a paradigm to study chromatin signaling

Hans-Martin Herz,[1]* Marc Morgan,[1]* Xin Gao,[1] Jessica Jackson,[2] Ryan Rickels,[1] Selene K. Swanson,[1] Laurence Florens,[1] Michael P. Washburn,[1,3] Joel C. Eissenberg,[2] Ali Shilatifard[1]†

Histone H3 lysine^{27}-to-methionine (H3K27M) gain-of-function mutations occur in highly aggressive pediatric gliomas. We established a *Drosophila* animal model for the pathogenic histone H3K27M mutation and show that its overexpression resembles polycomb repressive complex 2 (PRC2) loss-of-function phenotypes, causing derepression of PRC2 target genes and developmental perturbations. Similarly, an H3K9M mutant depletes H3K9 methylation levels and suppresses position-effect variegation in various *Drosophila* tissues. The histone H3K9 demethylase KDM3B/JHDM2 associates with H3K9M-containing nucleosomes, and its misregulation in *Drosophila* results in changes of H3K9 methylation levels and heterochromatic silencing defects. We have established histone lysine-to-methionine mutants as robust in vivo tools for inhibiting methylation pathways that also function as biochemical reagents for capturing site-specific histone-modifying enzymes, thus providing molecular insight into chromatin signaling pathways.

Histone proteins constitute the core of eukaryotic chromatin (*1*). SET domain–containing histone methyltransferase complexes such as complex of proteins associated with Set1 (COMPASS) and polycomb repressive complex 2 (PRC2) methylate lysine residues within the histone H3 amino-terminal tail and are essential for normal development (*1*). Establishing direct functions for modified lysine residues in histones is difficult because there are multiple histone gene copies in metazoans (*2*). Moreover, histone methyltransferase enzymes occur in multimember families with potential redundant activities and histone methylation–independent functions (*3*). In *Drosophila*, replacing all copies of histone H3 with H3 Lys^{27}-to-Arg^{27} (H3K27R) in a clonal substitution recapitulates the phenotype of mutating *E(z)*, the PRC2 H3 Lys^{27} methyltransferase gene, suggesting this mark is indeed required for PRC2-mediated repression (*4*). Single-allele mutations of histone H3.3 Lys^{27}-to-Met^{27} (H3.3K27M) occur in a subtype of aggressive pediatric brain cancers (*5*, *6*) and act in a dominant manner to deplete H3K27 methylation by inhibiting PRC2 methyltransferase activity (*7*, *8*). Other histone H3 lysine-to-methionine mutants also possess dominant gain-of-function activities (*8*), making them attractive tools for in vivo functional studies of histone lysine modifications. Trimethylation of histone H3 Lys^{27} (H3K27me3) and Lys^{9} (H3K9me3) are associated with distinct forms of transcriptionally silenced chromatin. Histone H3K27me3 catalyzed by PRC2 is enriched at so-called facultative heterochromatin and is implicated in the silencing of key developmental genes, in particular the homoeotic gene clusters (*9*). By contrast, H3K9me3 is associated with "constitutive" heterochromatin at telomeres and centromeres (*10*).

We established wild-type histone H3.3, H3.3K27M, and H3.3K9M constructs with a C-terminal FLAG–hemagglutinin (HA) tag for tissue-specific

[1]Stowers Institute for Medical Research, 1000 East 50th Street, Kansas City, MO 64110, USA. [2]Saint Louis University School of Medicine, Edward A. Doisy Department of Biochemistry and Molecular Biology, St. Louis, MO, USA. [3]Department of Pathology and Laboratory Medicine, University of Kansas Medical Center, Kansas City, KS 66160, USA.
*These authors contributed equally to this manuscript. **†Present address: Department of Biochemistry and Molecular Genetics, School of Medicine, Northwestern University, Chicago, IL, USA. Corresponding author. E-mail: ash@northwestern.edu**

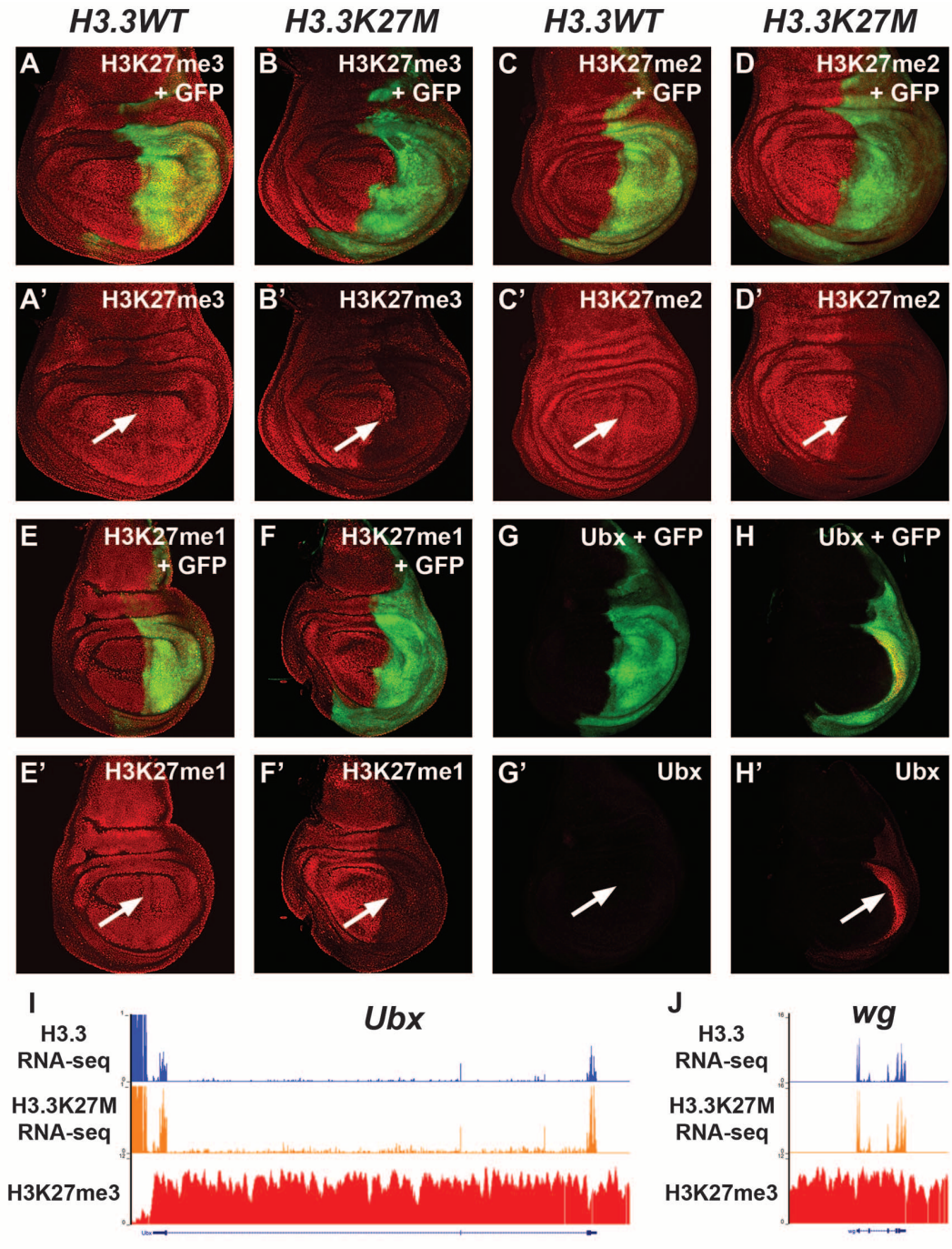

Fig. 1. Overexpression of histoneH3.3K27M results in loss of H3K27 methylation and derepression of polycomb target genes. (**A** to **H**) Overexpression of H3.3WT-FLAG-HA or H3.3K27M-FLAG-HA in the posterior compartment of the wing imaginal disc. *Green fluorescent protein* (*GFP*) expression in green marks the posterior domain where the respective histones are overexpressed. Nonapostrophed panels represent merged images that include the GFP signal in green and the respective antibody signal in red. Apostrophed panels only contain the respective antibody signal in red with a white arrow pointing toward the posterior compartment. Overexpression of H3.3WT-FLAG-HA does not result in bulk changes in H3K27 trimethylation (A and A'), H3K27 dimethylation (C and C'), or H3K27 monomethylation (E and E'). Decreased levels of H3K27 trimethylation (B and B'), H3K27 dimethylation (D and D'), and H3K27 monomethylation (F and F') can be observed when H3.3K27M-FLAG-HA is overexpressed in the posterior compartment of the wing imaginal disc. *Ubx* remains silenced in wing imaginal discs overexpressing H3.3WT-FLAG-HA (G and G'). However, *Ubx* becomes derepressed when H3.3K27M-FLAG-HA is overexpressed (H and H'). RNA-seq analysis of wing imaginal discs expressing either H3.3WT-FLAG-HA or H3.3K27M-FLAG-HA with a *T80-GAL4* driver and ChIP-chip analysis for H3K27 trimethylation of wild-type wing imaginal discs. RNA-seq tracks shown are an average of two biological replicates. Polycomb target genes that are highly enriched for H3K27 trimethylation in wild-type wing imaginal discs, such as *Ubx* (**I**) and *wg* (**J**), are derepressed when H3.3K27M-FLAG-HA is overexpressed in wing imaginal discs.

overexpression in *Drosophila*. Overexpression of H3.3K27M in the posterior compartment of wing imaginal discs driven by *engrailed-GAL4* caused a strong reduction in all three H3K27 methylation states and derepression of the PRC2 target gene *Ultrabithorax* (*Ubx*) (Fig. 1, A to H′, and fig. S1), thus phenocopying knockdown of the catalytic PRC2 subunit E(z) (fig. S2). Also, increased H3K27 acetylation was observed for H3.3K27M overexpression in *Drosophila* and mammalian cells and *E(z)-RNAi* in *Drosophila* (fig. S3). Genome-wide RNA sequencing (RNA-seq) analysis of H3.3K27M-overexpressing wing imaginal discs revealed up-regulated RNA transcripts for known polycomb target genes, including *Ubx*, *wingless* (*wg*), and the PRC1 subunits *Posterior sex combs* (*Psc*) and *Suppressor of zeste 2* [*Su(z)2*] (Fig. 1, I and J; fig. S4, A and B; and table S1). Other *Homeobox* (*Hox*)–containing genes such as *engrailed* (*en*) and *invected* (*in*), and signaling pathway components such as *cubitus interruptus* (*ci*), were down-regulated upon H3.3K27M overexpression (fig. S4, C and D, and table S1). Moreover, flies expressing H3.3K27M under a tissue-specific *Distal-less–GAL4* driver exhibit gross morphological defects—such as severe leg malformations and fusion phenotypes and malformed, reduced, or missing proboscis—and die around eclosion, phenocopying *E(z)-RNAi* under the same conditions (fig. S4, E to G).

Trimethylation of histone H3K9me3 by suppressor of variegation 3-9 [Su(var)3-9] proteins is a hallmark of constitutive heterochromatin (*11*). Histone H3K9me3 serves as a binding substrate for heterochromatin protein 1 α (HP1α, also known as CBX5) (*12*–*15*) and establishes a transcriptionally repressed state (*16*–*18*). Euchromatic genes that become abnormally juxtaposed to heterochromatic regions are subject to transcriptional silencing through position-effect variegation (PEV) (*16*). Less is known about the direct role of H3K9 methylation in the regulation of gene

expression. Indeed, studies in fission yeast point to H3K9 methylation–independent functions for the Su(var)3-9 homolog Clr4 in chromatin silencing (*19*). To test a direct role for H3K9 methylation in the regulation of gene expression in metazoans, we overexpressed H3.3K9M in *Drosophila* wing imaginal discs and mammalian cells and observed a global depletion of H3K9 methylation levels (Fig. 2, A to F, and fig. S5) but no effect on H3K27 methylation (fig. S6, A to C′). In contrast, H3K9 mono- and dimethylation were slightly reduced when H3.3K27M was overexpressed (fig. S6, D to F′). We purified mononucleosomes from wild-type H3.3-, H3.3K9M-, and H3.3K27M-overexpressing human embryonic kidney (HEK) 293 cells and subjected these samples to multidimensional protein identification technology (MudPIT) mass spectrometry (Fig. 2,

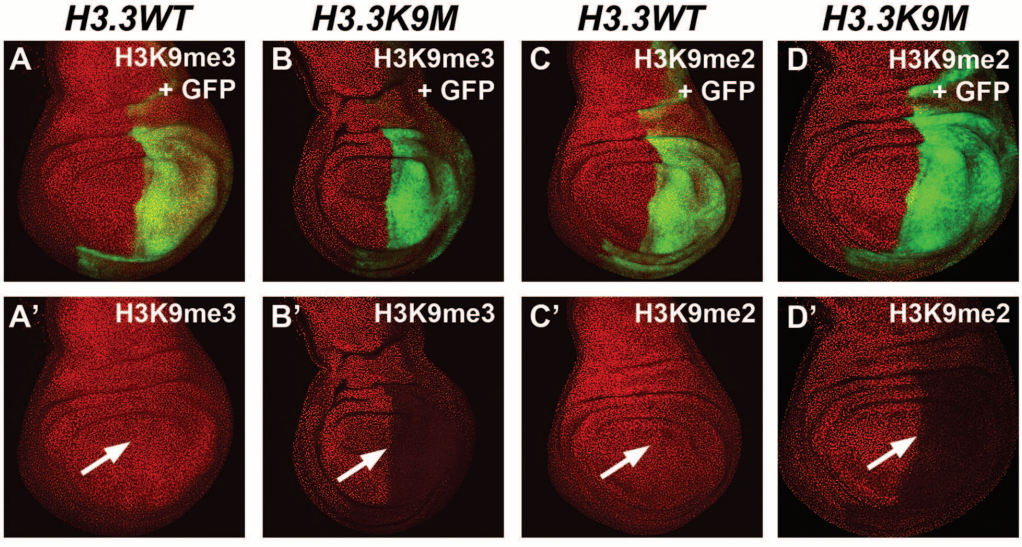

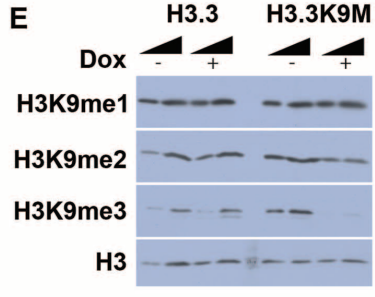

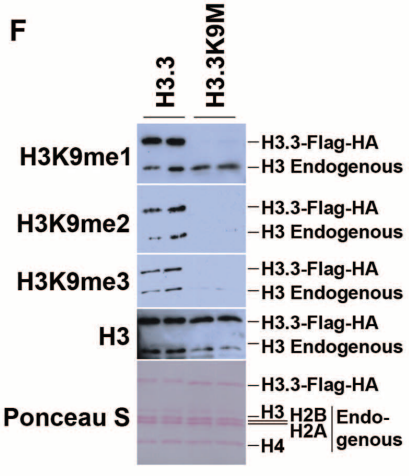

G

	H3.3 dNSAF	H3.3K9M dNSAF	H3.3K9M p-value	H3.3K27M dNSAF	H3.3K27M p-value
SIRT6	0.0003	0.0046	0.0002	0.0003	0.4207
KDM3B	0.0000	0.0003	0.0018	0.0000	0.6004
SUV39H1	0.0000	0.0002	0.0047	0.0001	0.0135
USF1	0.0000	0.0002	0.0037	0.0002	0.0081
CBX1	0.0049	0.0005	0.0002	0.0055	0.3157
CBX3	0.0038	0.0012	0.0054	0.0039	0.5413
CBX5	0.0028	0.0006	0.0019	0.0026	0.3143
CHAF1A	0.0011	0.0001	0.0008	0.0007	0.1045
CHAF1B	0.0013	0.0001	0.0008	0.0010	0.1600
UHRF1	0.0044	0.0012	0.0023	0.0055	0.1782
PCNA	0.0006	0.0001	0.0029	0.0003	0.0668
BRD1	0.000056	0.000062	0.1060	0.00008	0.0346
BRD4	0.000058	0.000016	0.0861	0.000178	0.0441
EZH2	0.00147	0.000558	0.1431	0.00048	0.4646
EED	0.00089	0.00087	0.5619	0.00075	0.3196
SUZ12	0.0014	0.0019	0.2197	0.0016	0.3652

Fig. 2. Histone H3.3K9M overexpression results in depletion of H3K9 methylation levels and alters recruitment of HP1 family members and other H3K9-modifying enzymes. (**A** to **D**) Histone H3.3WT-FLAG-HA and H3.3K9M-FLAG-HA were overexpressed in wing imaginal discs as described in Fig. 1. Overexpression of H3.3WT-FLAG-HA does not result in significant bulk changes of H3K9 trimethylation (A and A'), but leads to a marginal decrease in H3K9 dimethylation (C and C'). A substantial decrease in the levels of H3K9 trimethylation (B and B') and H3K9 dimethylation (D and D') can be observed when H3.3K9M-FLAG-HA is overexpressed. (**E**) Western blotting of whole-cell extracts from human HEK 293 cells expressing H3.3WT-FLAG-HA or H3.3K9M-FLAG-HA. Bulk histone H3K9 trimethylation levels and, to some extent, H3K9 dimethylation levels are reduced in cells expressing H3.3K9M-FLAG-HA. Dox, doxycycline-induced for 9 days. (**F**) Western blot of purified mononucleosomes from human HEK293 cells expressing H3.3WT-FLAG-HA or H3.3K9M-FLAG-HA. Histone H3K9 dimethylation and H3K9 trimethylation are strongly reduced on H3.3K9M-FLAG-HA–containing nucleosomes. (**G**) MudPIT analysis of mononucleosome-interacting proteins. dNSAF, distributed normalized spectral abundance factor; averaged of 9, 5, and 12 replicates for H3.3WT-FLAG-HA, H3.3K9M-FLAG-HA, and H3.3K27M-FLAG-HA, respectively. Green color indicates proteins significantly enriched in lysine-to-methionine mutants containing nucleosomes; red color indicates proteins that are depleted, based on power law global error model signal-to-noise ratios and *P* values; and gray indicates factors that are not significantly changed between wild type (WT) and lysine-to-methionine mutants.

F and G). The bindings of HP1α (CBX5), HP1β (CBX1), and HP1γ (CBX3) were substantially reduced for H3.3K9M-containing mononucleosomes, as were the interactions of the HP1-associated proteins chromatin assembly factor 1a (CHAF1A/p150) (*20*, *21*) and CHAF1B/p60 (Fig. 2G). We also found substantially increased association of the H3K9 demethylase KDM3B and the H3K9/K56 deacetylase SIRT6 with H3K9M-containing mononucleosomes (Fig. 2G).

Reduced dosage of *Drosophila* HP1α [also known as Su(var)205] and Su(var)3-9 results in suppression of PEV (*22*–*24*). By using a heat shock-inducible *lacZ* construct inserted within Y-chromosomal heterochromatin (*25*, *26*), we found that overexpression of H3.3K9M results in suppression of PEV in both *Drosophila* salivary glands and eye-antenna imaginal discs (Fig. 3, A to D). Bulk histone H3K9 methylation levels were decreased in H3.3K9M-overexpressing salivary glands (fig. S7). We also assessed the effects of H3.3K9M overexpression on heterochromatic silencing in *Drosophila* ovaries. The *gypsy-lacZ* construct is normally silenced in almost all follicle cells but is up-regulated upon loss of heterochromatin function (*27*). Overexpression of H3.3K9M results in derepression of *lacZ* (Fig. 3, E to F'). Thus, the H3.3K9M mutation disrupts heterochromatic silencing of retroelements.

KDM3B is a JumonjiC domain-containing histone demethylase that shows specificity toward H3K9 and is involved in gene activation in leukemia cells (*28*, *29*). Because KDM3B specifically interacts with H3.3K9M-containing nucleosomes (Fig. 2, G), we wanted to test whether changes in KDM3B levels would alter H3K9 methylation by knocking down or overexpressing its *Drosophila* homolog, JHDM2, in wing imaginal discs. Depletion of JHDM2 results in increased H3K9 mono- and dimethylation (Fig. 4, A to C'). Conversely, the overexpression of JHDM2 in wing imaginal discs results in depletion in H3K9 dimethylation levels and, to a lesser extent, H3K9 trimethylation (Fig. 4, D to F') and suppresses PEV in both *Drosophila* salivary glands and eye-antenna imaginal discs (Fig. 4, G to L). JHDM2 and SIRT6 also globally affect H3K9 acetylation to a similar degree as H3.3K9M overexpression (figs. S8 and S9). Sirt6 is not a major regulator of PEV in eye-antenna imaginal discs and salivary glands, but *Sirt6-RNAi* results in a somewhat modest derepression of the *gypsy-lacZ* reporter (fig. S10).

We used histone lysine-to-methionine mutants to globally modulate histone methylation in vivo. We established a *Drosophila* animal model of the H3K27M mutation, which may help elucidate the molecular pathogenesis of pediatric gliomas (*5*, *6*). To gain mechanistic insight into the molecular function of these mutants, we used an unbiased proteomic strategy to identify histone lysine-to-methionine-interacting partners. Our biochemical studies do not identify PRC2 components, such as EZH2, SUZ12, and EED, as significantly enriched on H3.3K27M-containing nucleosomes (Fig. 2G) as previously suggested (*8*). However, we detected an increase in H3K27 acetylation levels (fig. S3) and association of bromodomain-containing protein 1 (BRD1) and BRD4 to H3.3K27M-containing nucleosomes (Fig. 2G). These findings suggest that inhibitors of H3K27 acetylation or BRD4 inhibitors, such as JQ1 and iBET, could be useful for the treatment of the H3.3K27M-mutated subtype of aggressive pediatric glioblastomas.

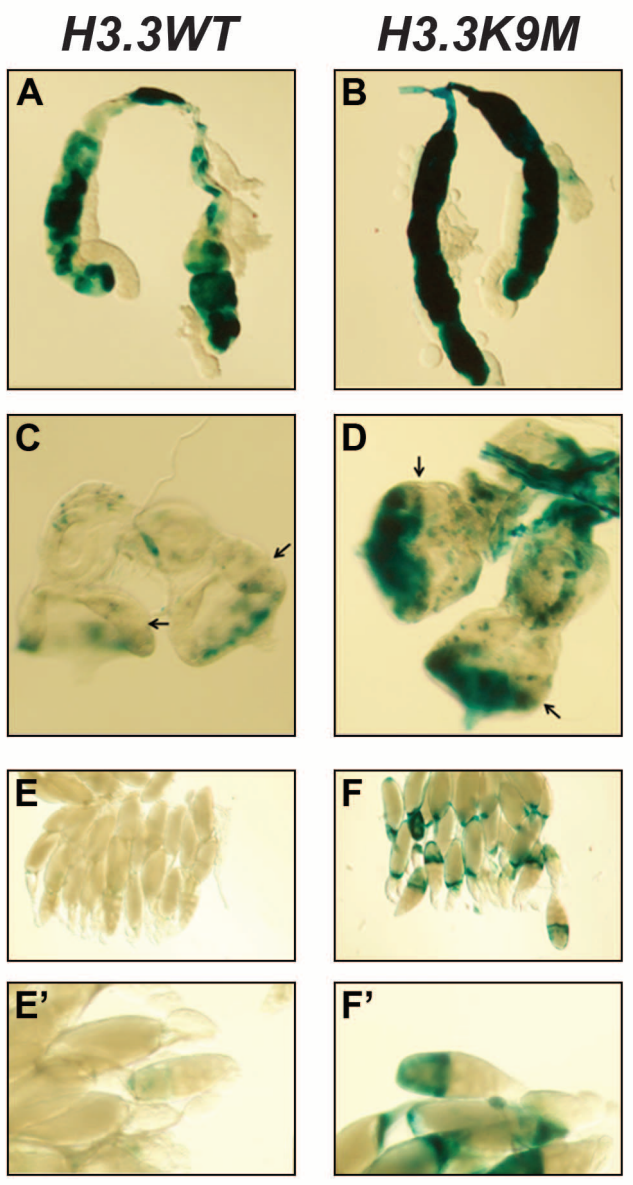

Fig. 3. Overexpression of H3.3K9M suppresses heterochromatic silencing. *Hsp70-lacZ* variegating salivary glands overexpressing H3.3WT-FLAG-HA (**A**) and H3.3K9M-FLAG-HA (**B**), stained for *lacZ* expression by using X-gal. *Hsp70-lacZ* variegating eye-antenna discs overexpressing H3.3WT-FLAG-HA (**C**) and H3.3K9M-FLAG-HA (**D**). Arrows in (C) and (D) indicate the position of the morphogenetic furrow. *gypsy-lacZ* containing ovaries overexpressing H3.3WT-FLAG-HA (**E** and **E'**) and H3.3K9M-FLAG-HA (**F** and **F'**), stained for *lacZ* expression by using X-gal.

We also demonstrated that H3K9M globally depletes H3K9 methylation levels in vivo, disrupts interaction of HP1 proteins, and thus suppresses PEV. Via our unbiased proteomic strategy, we identified KDM3B/JHDM2 and Sirt6 as regulators of H3K9 methylation–dependent heterochromatic silencing (Fig. 4M). Indeed, JHDM2 acts as a suppressor of variegation in multiple tissues in our assays, whereas Sirt6 function seems to be restricted to retroelement silencing. Mutations of histone H3.3K36M were recently discovered in a subtype of bone cancer (*30*). Thus, histone lysine-to-methionine mutations are associated with highly tissue-specific cancer types. Given the importance of heterochromatin in maintaining genomic stability (*17*, *18*), it is plausible that as-yet-uncharacterized H3K9M mutations might occur in some cancers. The system that we established will provide a powerful tool to inhibit histone lysine modifications at specific residues in vivo and allow to biochemically capture the molecular players involved in chromatin signaling pathways.

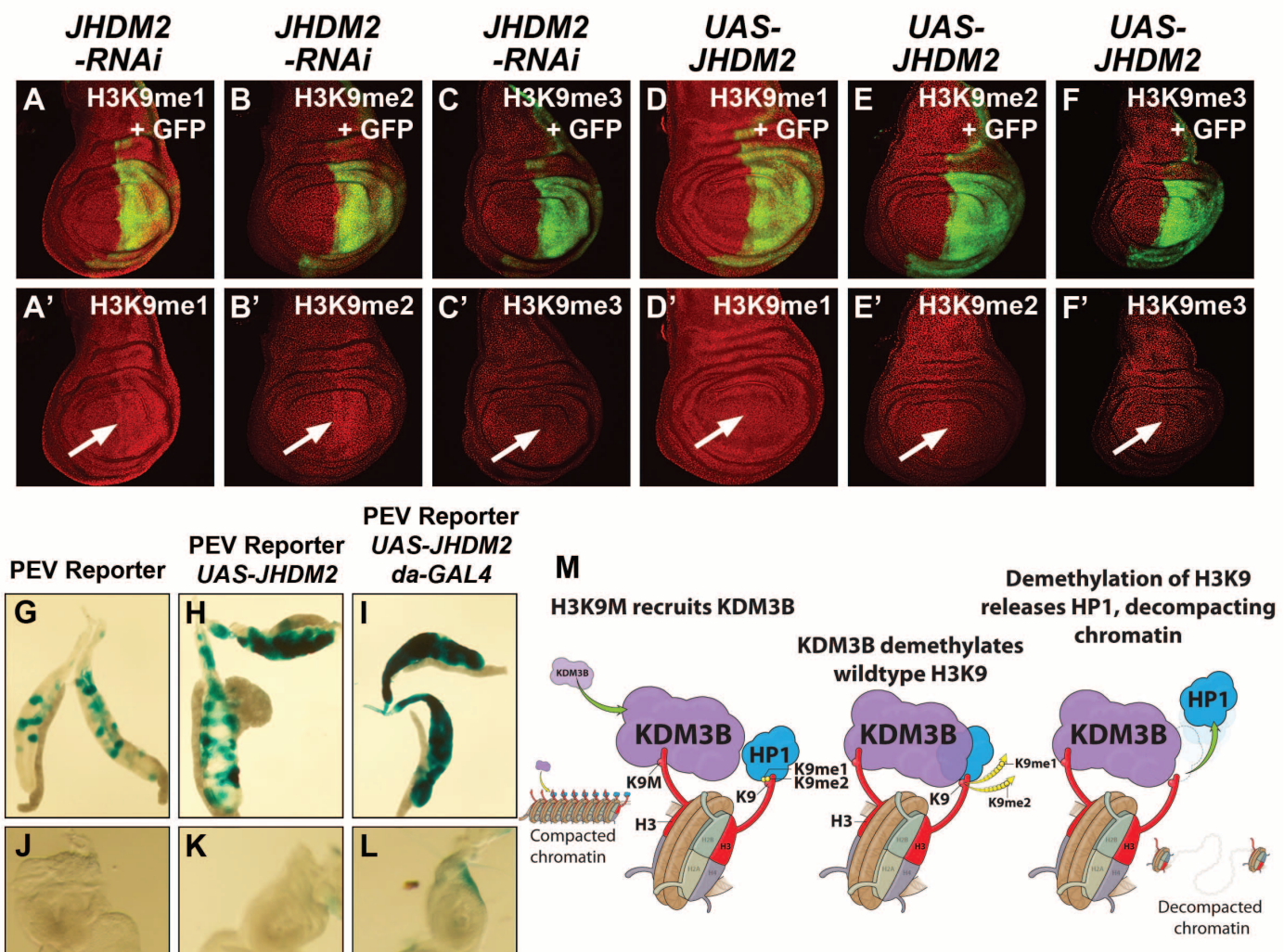

Fig. 4. The histone H3K9 demethylase KDM3B/JHDM2 interacts with H3K9M and regulates H3K9 methylation levels and heterochromatic silencing. (**A** to **F**) RNA interference (RNAi)–mediated knockdown of JHDM2 or JHDM2 overexpression were carried out in wing imaginal discs as described in Fig. 1. RNAi-mediated knockdown of JHDM2 results in increased levels of H3K9 monomethylation (A and A') and H3K9 dimethylation (B and B') but not H3K9 trimethylation (C and C'). JHDM2 overexpression does not affect H3K9 monomethylation (D and D') but leads to decreased H3K9 dimethylation (E and E') and a very weak reduction in H3K9 trimethylation (F and F'). (**G** to **I**) *Hsp70-lacZ* variegating salivary glands with reporter construct (*Hsp70-lacZ*) only (G); reporter construct and *UAS-JHDM2* (H); and reporter construct, *UAS-JHDM2*, and *daughterless-GAL4* driver (I) stained for *lacZ* expression by using X-gal. Compared with salivary glands containing only the reporter construct (G), salivary glands with the reporter construct and *UAS-JHDM2* display a weak enhancement in PEV (H), possibly because of leakiness of the *UAS-JHDM2* construct. PEV is further enhanced when *UAS-JHDM2* is expressed under the control of *daughterless-GAL4* (I). (**J** to **L**) *Hsp70-lacZ* variegating eye-antenna imaginal discs with reporter construct only (J); reporter construct and *UAS-JHDM2* (K); and reporter construct, *UAS-JHDM2*, and *daughterless-GAL4* driver (L) stained for *lacZ* expression by using X-gal. No X-gal staining is observed with the reporter construct only (J). A very weak enhancement is detected with the reporter construct and *UAS-JHDM2* combined (K), possibly because of leakiness of the *UAS-JHDM2* construct. PEV is further enhanced when *UAS-JHDM2* is expressed under the control of *daughterless-GAL4* (L), particularly in differentiating areas posterior to the morphogenetic furrow. (**M**) Model describing the activation of KDM3B/JHDM2 on H3K9M-containing nucleosomes and its possible role in heterochromatic silencing.

REFERENCES AND NOTES

1. A. Shilatifard, *Annu. Rev. Biochem.* **81**, 65–95 (2012).
2. S. Henikoff, A. Shilatifard, *Trends Genet.* **27**, 389–396 (2011).
3. H. M. Herz, A. Garruss, A. Shilatifard, *Trends Biochem. Sci.* **38**, 621–639 (2013).
4. A. R. Pengelly, Ö. Copur, H. Jäckle, A. Herzig, J. Müller, *Science* **339**, 698–699 (2013).
5. J. Schwartzentruber *et al.*, *Nature* **482**, 226–231 (2012).
6. G. Wu *et al.*, *Nat. Genet.* **44**, 251–253 (2012).
7. K. M. Chan *et al.*, *Genes Dev.* **27**, 985–990 (2013).
8. P. W. Lewis *et al.*, *Science* **340**, 857–861 (2013).
9. R. Margueron, D. Reinberg, *Nature* **469**, 343–349 (2011).
10. S. I. Grewal, D. Moazed, *Science* **301**, 798–802 (2003).
11. C. Maison, G. Almouzni, *Nat. Rev. Mol. Cell Biol.* **5**, 296–305 (2004).
12. T. C. James, S. C. Elgin, *Mol. Cell. Biol.* **6**, 3862–3872 (1986).
13. A. J. Bannister *et al.*, *Nature* **410**, 120–124 (2001).
14. J. Nakayama, J. C. Rice, B. D. Strahl, C. D. Allis, S. I. Grewal, *Science* **292**, 110–113 (2001).
15. M. Lachner, D. O'Carroll, S. Rea, K. Mechtler, T. Jenuwein, *Nature* **410**, 116–120 (2001).
16. S. C. Elgin, G. Reuter, *Cold Spring Harb. Perspect. Biol.* **5**, a017780 (2013).
17. A. H. Peters *et al.*, *Cell* **107**, 323–337 (2001).
18. A. Taddei, C. Maison, D. Roche, G. Almouzni, *Nat. Cell Biol.* **3**, 114–120 (2001).
19. E. L. Gerace, M. Halic, D. Moazed, *Mol. Cell* **39**, 360–372 (2010).
20. N. Murzina, A. Verreault, E. Laue, B. Stillman, *Mol. Cell* **4**, 529–540 (1999).
21. J. P. Quivy, A. Gérard, A. J. Cook, D. Roche, G. Almouzni, *Nat. Struct. Mol. Biol.* **15**, 972–979 (2008).
22. J. C. Eissenberg *et al.*, *Proc. Natl. Acad. Sci. U.S.A.* **87**, 9923–9927 (1990).
23. J. C. Eissenberg, G. D. Morris, G. Reuter, T. Hartnett, *Genetics* **131**, 345–352 (1992).
24. G. Schotta *et al.*, *EMBO J.* **21**, 1121–1131 (2002).
25. B. Y. Lu, C. P. Bishop, J. C. Eissenberg, *EMBO J.* **15**, 1323–1332 (1996).
26. B. Y. Lu, J. Ma, J. C. Eissenberg, *Development* **125**, 2223–2234 (1998).
27. E. Sarot, G. Payen-Groschêne, A. Bucheton, A. Pélisson, *Genetics* **166**, 1313–1321 (2004).
28. M. Brauchle *et al.*, *PLOS ONE* **8**, e60549 (2013).
29. J. Y. Kim *et al.*, *Mol. Cell. Biol.* **32**, 2917–2933 (2012).
30. S. Behjati *et al.*, *Nat. Genet.* **45**, 1479–1482 (2013).

ACKNOWLEDGMENTS

We thank T. Jenuwein, J. Müller, R. White, and the Bloomington Stock Center for providing antibodies and fly stocks; the Stowers Molecular Biology core for generating histone point mutants; the Stowers Tissue Culture Core for generating histone mutant cell lines; and S. Marshall and W. Hodges for technical assistance. Histone lysine-to-methionine studies in the Shilatifard laboratory were supported in part by NIH grant CA R01CA089455. Data generated for this study are deposited under Gene Expression Omnibus (GEO) accession number GSE59891. Chromatin immunoprecipitation (ChIP)–chip data of H3K27me3 are from GEO accession number GSE42106. Antibodies toward H3K27M were provided by Cell Signaling Technology. A.S. is a paid member of the scientific advisory board of Cell Signaling Technology.

SUPPLEMENTARY MATERIALS

www.sciencemag.org/content/345/6200/1065/suppl/DC1
Materials and Methods
Figs. S1 to S10
References (*31*–*37*)

22 April 2014; accepted 30 July 2014
10.1126/science.1255104

ION CHANNEL STRUCTURE

Structure of an agonist-bound ionotropic glutamate receptor

Maria V. Yelshanskaya, Minfen Li, Alexander I. Sobolevsky*

Ionotropic glutamate receptors (iGluRs) mediate most excitatory neurotransmission in the central nervous system and function by opening their ion channel in response to binding of agonist glutamate. Here, we report a structure of a homotetrameric rat GluA2 receptor in complex with partial agonist (*S*)-5-nitrowillardiine. Comparison of this structure with the closed-state structure in complex with competitive antagonist ZK 200775 suggests conformational changes that occur during iGluR gating. Guided by the structures, we engineered disulfide cross-links to probe domain interactions that are important for iGluR gating events. The combination of structural information, kinetic modeling, and biochemical and electrophysiological experiments provides insight into the mechanism of iGluR gating.

Ionotropic glutamate receptors (iGluRs) are ligand-gated ion channels that mediate most excitatory neurotransmission in the central nervous system (*1*). iGluRs are implicated in nearly all aspects of nervous system development and function, and their dysfunction is associated with devastating chronic neurodegenerative conditions, such as Alzheimer's and Parkinson's diseases; psychiatric disorders, such as schizophrenia and depression; and acute disorders, such as brain trauma and stroke (*1*–*3*). The iGluR family includes three major subtypes: AMPA, kainate (KA), and *N*-methyl-D-aspartate (NMDA) receptors, which have diverse kinetic and pharmacological properties and play disparate roles in cognition but share common structural features (*1*).

iGluRs function as assemblies of four subunits. Whereas the majority of iGluRs in the nervous system are heterotetramers composed of at least two types of subunits, AMPA and select KA subunits can form functional homotetramers. Each iGluR subunit has a modular design (*4*) and includes an extracellular amino-terminal domain (ATD) that controls subunit assembly, receptor trafficking, channel gating, agonist potency, and allosteric modulation; a clamshell-shaped ligand-binding domain (LBD or S1S2) composed of two stretches of polypeptide, S1 and S2, and responsible for agonist and antagonist recognition; a transmembrane domain (TMD) that forms a cation-conducting channel and contributes to iGluR tetrameric stability; and a cytoplasmic C-terminal domain involved in synaptic localization, trafficking, mobility, and receptor regulation (*1*). Currently, structural information on iGluRs is limited to high-resolution crystal structures of genetically excised, water-soluble ATDs and LBDs and 3.6 to 4.0 Å resolution structures of an intact AMPA receptor in the antagonist-bound closed state (*5*) and NMDA receptors in the allosterically inhibited agonist-bound closed state (*6*, *7*).

iGluRs function by opening their ion channel in response to binding of agonist glutamate (Glu) (*1*). This process of activation gating is accompanied by the typically slower process of desensitization, which leads to closure of the ion channel and causes a reduction of iGluR-mediated currents in the continuous presence of Glu. Desensitization represents a versatile mechanism for shaping synaptic transmission (*8*), and controlling it could be an effective way of regulating synaptic integration, modulating circuit function, and altering iGluR activity in pathological conditions (*1*, *9*). Here, we used a combination of biochemical and biophysical approaches to study iGluR gating. We focused on AMPA subtype rat GluA2 receptors, for which a modified construct, $GluA2_{cryst}$, had previously yielded the structure in the closed antagonist-bound state (*5*). We used a construct, GluA2*, that is similar to $GluA2_{cryst}$ but has several mutations reversed back toward the wild-type GluA2 background (see supplementary materials).

For functional characterization, we expressed GluA2* in human embryonic kidney (HEK) 293 cells and used patch clamp with fast solution exchange to record GluA2*-mediated currents. As is typical for AMPA subtype iGluRs at near-physiological membrane potentials, Glu application elicited an inward current that quickly decayed in the continuous presence of Glu as a result of desensitization (Fig. 1A). Desensitization in GluA2* receptors had a similar rate and extent as in wild-type receptors (fig. S1, A and D) and was blocked by the positive allosteric modulator cyclothiazide (CTZ) (*10*).

AMPA receptors can also be activated by partial agonists, which elicit smaller maximal whole-cell currents than the full agonist Glu but have similar single-channel conductance (*11*–*13*). In our studies, we used a partial agonist, (*S*)-5-nitrowillardiine (NOW). In crystal structures of isolated LBD, NOW demonstrated the ability to keep the LBD clamshell completely closed (*13*), just like full agonists. NOW elicited currents with ~four times smaller maximal amplitude than Glu and had similar potency for GluA2* and wild-type GluA2 receptors (fig. S1, B and C). The rates of desensitization and, to a greater extent, recovery from it for NOW were apparently slower than those for Glu (fig. S1, D to G). Kinetic modeling of the effects of full and partial agonists on AMPA receptors (*14*) (fig. S2) closely reproduced our experimental data and predicted that, in the presence of saturating concentrations of either, nearly all receptors accumulate in the agonist-bound desensitized states (D_A, Fig. 1B).

We purified GluA2* and crystallized it in the presence of NOW. The best crystals belonged to the $C222_1$ space group and diffracted to 4.8 Å resolution (table S1). We solved the structure ($GluA2_{NOW}$) by molecular replacement, using the high-resolution structure of the isolated ATD dimer [Protein Data Bank (PDB) identification code (ID) 3H5V] (*15*) and the ion channel domain from $GluA2_{cryst}$ (PDB ID 3KG2) (*5*) as search models. The NOW-bound structure of the isolated LBD (PDB ID 3RTW) (*13*) did not work as a molecular replacement search model for LBD, suggesting that the LBD conformation is different in the context of $GluA2_{NOW}$. We solved the structure by separately using the D1 and D2 lobes of LBD as molecular replacement search models. The conformation of LBD in the $GluA2_{NOW}$ structure most closely resembles the 6-cyano-7-nitroquinoxaline-2,3-dione–bound conformation of the isolated LBD (PDB ID 3B7D) (*16*), and their superposition yields a root mean square deviation (RMSD) of 0.31 Å. Phases were improved by multidomain noncrystallographic symmetry averaging, solvent flattening, and histogram matching. The electron density maps were of sufficient clarity to build the majority of linkers connecting the LBD to the ion channel and the ATD to the LBD (fig. S3). The resulting model was refined to good crystallographic statistics and stereochemistry (R_{work}/R_{free} = 0.228/0.262, table S1).

The $GluA2_{NOW}$ structure (Fig. 1C) is shaped like the letter Y and has a domain arrangement similar to the antagonist ZK 200775 (ZK)–bound closed-state $GluA2_{cryst}$ structure (*5*). For better comparison with $GluA2_{NOW}$, we cocrystallized GluA2* with ZK (table S1). The resulting structure ($GluA2_{ZK}$) closely resembles the original $GluA2_{cryst}$ structure (superposition of individual domains of $GluA2_{ZK}$ and $GluA2_{cryst}$ yields RMSD of 0.3 to 1 Å).

Department of Biochemistry and Molecular Biophysics, Columbia University, 650 West 168th Street, New York, NY 10032, USA.
*Corresponding author. E-mail: as4005@columbia.edu

Grossly, $GluA2_{NOW}$ and $GluA2_{ZK}$ have similar architectures (Fig. 2A). The conformations of ATD are very similar (fig. S4A). The ion channel of $GluA2_{NOW}$ adopts a closed-pore conformation that is also similar to $GluA2_{ZK}$ (figs. S4, B and C, and S5). Nevertheless, small differences in the cross-pore dimensions between two pairs of diagonal subunits A/C and B/D (fig. S4, D to G) suggest deeper expansion of the twofold rotational symmetry of extracellular domains into the extracellular half of the $GluA2_{NOW}$ ion channel. The strongest difference in domain conformation was observed for the LBD: Each clamshell is ~11° more closed in $GluA2_{NOW}$ compared with $GluA2_{ZK}$ (Fig. 2B). The closure of individual clamshells results in wider and shorter conformations of the back-to-back LBD dimers in $GluA2_{NOW}$ (Fig. 2, C and D).

The altered conformation of LBD dimers in $GluA2_{NOW}$ results in increased tension in linkers connecting LBD to ATD and TMD. Because ATD and the ion channel maintain their closed-state–like conformations, the additional tension forces pull ATD dimers down, tilting them ~1.2° away from the overall twofold axis of symmetry (Fig. 2A). The ~2.4° splaying of the ATD dimers away from each other occurs around a hinge point at the ATD dimer-dimer interface. This interface maintains nearly identical conformations in $GluA2_{NOW}$ and $GluA2_{ZK}$, strongly supporting a critical role of ATD in iGluR tetramerization (*1*). Simultaneously, the tension forces pull the ion channel up by making the whole structure ~2 Å shorter and push the two LBD dimers toward each other. As a result, the interface between the two LBD dimers in $GluA2_{NOW}$ becomes tighter and covers a surface area three times larger than that in $GluA2_{ZK}$ (fig. S4, H and I). Accordingly, the $GluA2_{NOW}$ structure becomes ~2 Å narrower at the level of the LBD.

We tested the functional importance of agonist-induced tightening of the interface between two LBD dimers predicted by the $GluA2_{NOW}$ structure in experiments with GluA2-I664C (Ile^{664}→Cys^{664}) receptors activated by Glu. I664 residues are located in the middle of the dimer-dimer interface; the Cα's are 13.5 Å apart in $GluA2_{ZK}$ and 11.3 Å apart in $GluA2_{NOW}$ (fig. S6A). Cross-linking of I664C has been shown in experiments with purified receptors (*5*). We compared the rates of GluA2-I664C receptor recovery from desensitization in reducing and nonreducing conditions. In nonreducing conditions, the recovery was incomplete (fig. S6, B to D), apparently because of slow peak current reduction. The reduction was faster with longer exposures to Glu, accompanied by a decrease in the steady-state current amplitude without substantial changes in the fast rate of desensitization, and completely reversed by dithiothreitol (DTT) (fig. S6, E and F). The majority of receptors quickly become nonconducting in the presence of agonist; thus, slow inactivation of GluA2-I664C receptors under nonreducing conditions is consistent with agonist-induced tightening of LBD dimer-dimer interface.

Compared with $GluA2_{ZK}$, the LBD clamshells in $GluA2_{NOW}$ are ~11° more closed (Fig. 2B), presenting structural evidence of clamshell motion in the context of the intact, multidomain iGluR, consistent with studies of isolated LBDs (*17*). The conformational change is smaller than in agonist- or partial agonist–bound structures of isolated LBD, where clamshells are up to ~14° more closed than in $GluA2_{NOW}$ (fig. S7). Despite different extents of clamshell closure between the isolated LBD and $GluA2_{NOW}$, the orientation of the NOW molecule in the binding pocket is similar (fig. S8). However, increased distances between atoms of NOW and the binding pocket residues (table S2) suggest weakened interactions. Perhaps the most unexpected feature of the $GluA2_{NOW}$ structure is the conformation of the LBD dimer interface. Although the $GluA2_{NOW}$ structure was crystallized at conditions apparently favoring desensitization (Fig. 1B), the D1-D1 interface appears nearly intact rather than ruptured (*18*). Indeed, the difference in distance between upper lobes D1 in $GluA2_{NOW}$ and $GluA2_{ZK}$ does not exceed ~1 Å, whereas the distance between lower lobes D2 is ~6 Å larger in $GluA2_{NOW}$ (Fig. 2, C and D).

To probe the LBD dimer–interface conformation at conditions favoring different gating states in solution, we substituted individual residues at this interface with cysteines (Fig. 3, A and B) and purified wild-type and cysteine-substituted GluA2* receptors in their tetrameric forms (fig. S9). Cysteine cross-linking was tested in the presence or absence of reducing agent (2 mM DTT) and in the presence of different ligands. The $GluA2_{NOW}$ and $GluA2_{ZK}$ structures predicted position-specific differences in

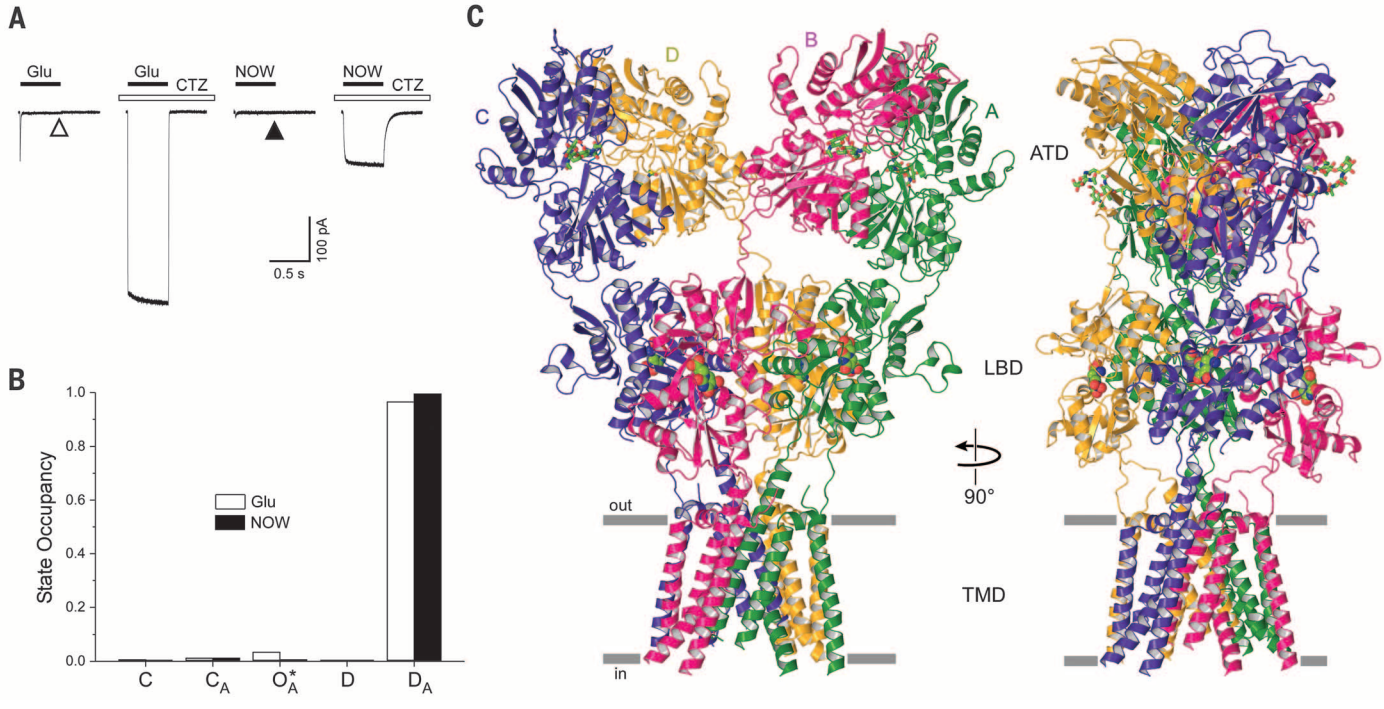

Fig. 1. Functional characterization and structure of NOW-bound GluA2*. (**A**) Representative whole-cell currents recorded at −60-mV membrane potential from HEK 293 cells expressing GluA2* in response to 500-ms application of 1 mM Glu alone, application of Glu in the continuous presence of 30 μM of the positive allosteric modulator CTZ, application of 100 μM NOW alone, and application of NOW in the continuous presence of CTZ. Solid and open triangles indicate steady-state currents at the end of NOW and Glu applications, respectively. (**B**) Occupancies of the closed (C), open (O), and desensitized (D) states of the receptor at the time points indicated by the triangles in (A). Subscript "A" and * indicate agonist-bound and ion-conducting states, respectively. The occupancies were predicted by using kinetic modeling (fig. S2). (**C**) The broad (left) and narrow (right) faces of the $GluA2_{NOW}$ structure viewed parallel to the membrane and perpendicular to the overall twofold axis of molecular symmetry. Inner and outer sides of the membrane are indicated by parallel gray bars. Each of four subunits is in a different color.

cross-interface distances between substituted cysteines (Fig. 3C), but nearly all of them were capable of forming cross-links in nonreducing conditions favoring all gating states: closed, open, and desensitized (Fig. 3D). We obtained similar results for the wild-type and K493C full-length GluA2 receptors (fig. S10). Such high reactivity of cysteines at the dimer interface indicates that LBD is highly dynamic (*13*, *19*–*27*) and that its conformation fluctuates during gating. Because the cross-dimer disulfide bonds are unstable and reversible (*20*), they cannot abolish these fluctuations (Fig. 3D), but they can favor certain gating states.

To study the effect of LBD interface cross-linking on iGluR gating, we recorded Glu-activated currents from HEK 293 cells expressing wild-type or cysteine-substituted receptors (Fig. 4A and fig. S11). To separate effects on receptor activation and desensitization, we measured two parameters. The first parameter gives an estimate for the effect of cross-link on AMPA receptor activation (Fig. 4B). No difference in activation between reducing and nonreducing conditions was observed for wild-type and K493C receptors. Cross-linking of cysteines in the lower D1-D1 interface (P494C and S497C; P, Pro; S, Ser) had a positive effect on activation. In a reducing environment, cysteine substitution of P494 almost entirely abolished iGluR function, whereas cross-linking recovered small currents, consistent with the very low probability of disulfide bond formation (Fig. 3D). The S497C receptors demonstrated robust Glu-activated currents that had larger amplitudes under cross-linking conditions. Overall, strengthening of the D1-D1 interface seemed to promote channel ability to open, which was most obvious when cysteine substitutions themselves inhibited this ability. In contrast, cross-linking of cysteines substituted in the D2 lobe produced negative effects on iGluR activation that were stronger for positions located closer to the ion channel. Hence, the LBD D2 lobes interlocking appears to prevent their separation, which is necessary for channel opening.

The second parameter reflects apparent changes in AMPA receptor desensitization, particularly its inhibition (Fig. 4C). No strong inhibition of desensitization was observed for wild type, K493C, or any receptors with cysteine substitutions in D2. Some of these mutant receptors had rates and extents of desensitization that were somewhat different from those of wild type (table S3), but those effects were due to mutations themselves and did not depend on the redox condition. Moreover, it is possible that the D2 cysteine cross-links can promote desensitization by locking receptors in the nonconducting state, unable to activate (Fig. 4B). Only P494C and S497C substitutions in the lower D1-D1 interface showed strongly reduced desensitization (Fig. 4C). Whereas for P494C, inhibition of desensitization was apparently independent of redox condition, it was greatly enhanced by cysteine cross-linking in S497C receptors. The inhibition of desensitization observed in P494C and S497C receptors is reminiscent of the effect of the L483Y (L, Leu; Y, Tyr) mutation (*28*) and of CTZ binding (*10*, *29*), both of which take place at the D1-D1 interface.

On the basis of our mutational, structural, and functional experiments in combination with previous work, we present two possible gating models (fig. S12); both assume that LBDs are highly mobile (Fig. 3); agonist binding causes LBD clamshell

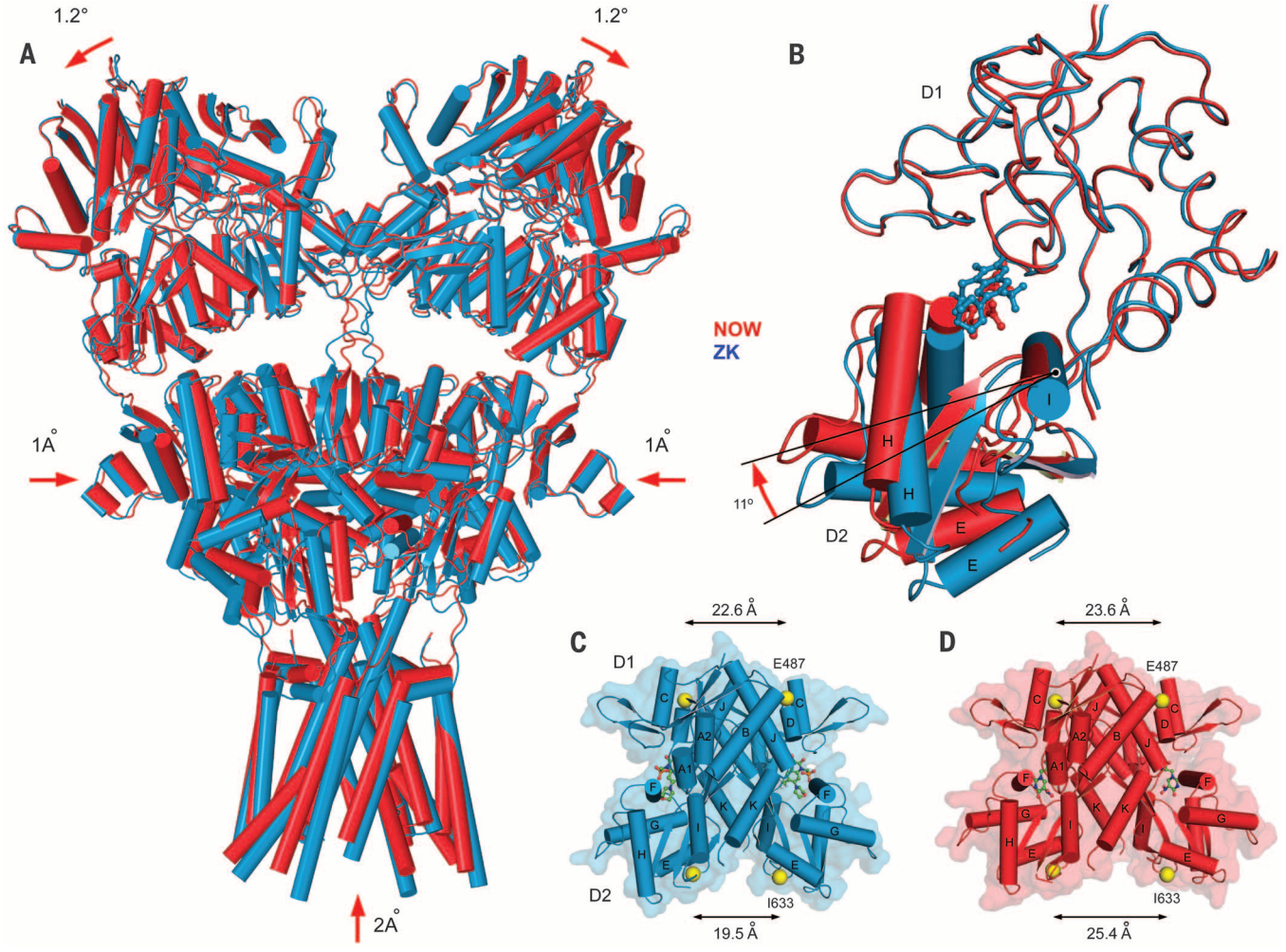

Fig. 2. Comparison of NOW-bound and ZK-bound GluA2*. (**A**) Superposition of the full-length $GluA2_{NOW}$ (red) and $GluA2_{ZK}$ (blue). Red arrows show changes in the $GluA2_{NOW}$ structure compared with $GluA2_{ZK}$. (**B**) Superposition of individual LBDs from $GluA2_{NOW}$ and $GluA2_{ZK}$ structures based on the upper lobe D1 and viewed along the axis of 11° rotation that brings the lower lobe D2 of $GluA2_{ZK}$ into $GluA2_{NOW}$. Helices E, H, and I are labeled. (**C** and **D**) LBD dimers from the $GluA2_{ZK}$ (C) and $GluA2_{NOW}$ (D) structures. Shown are Cα's (yellow spheres) and distances between them for E487 and I633 as well as ZK and NOW molecules as stick models.

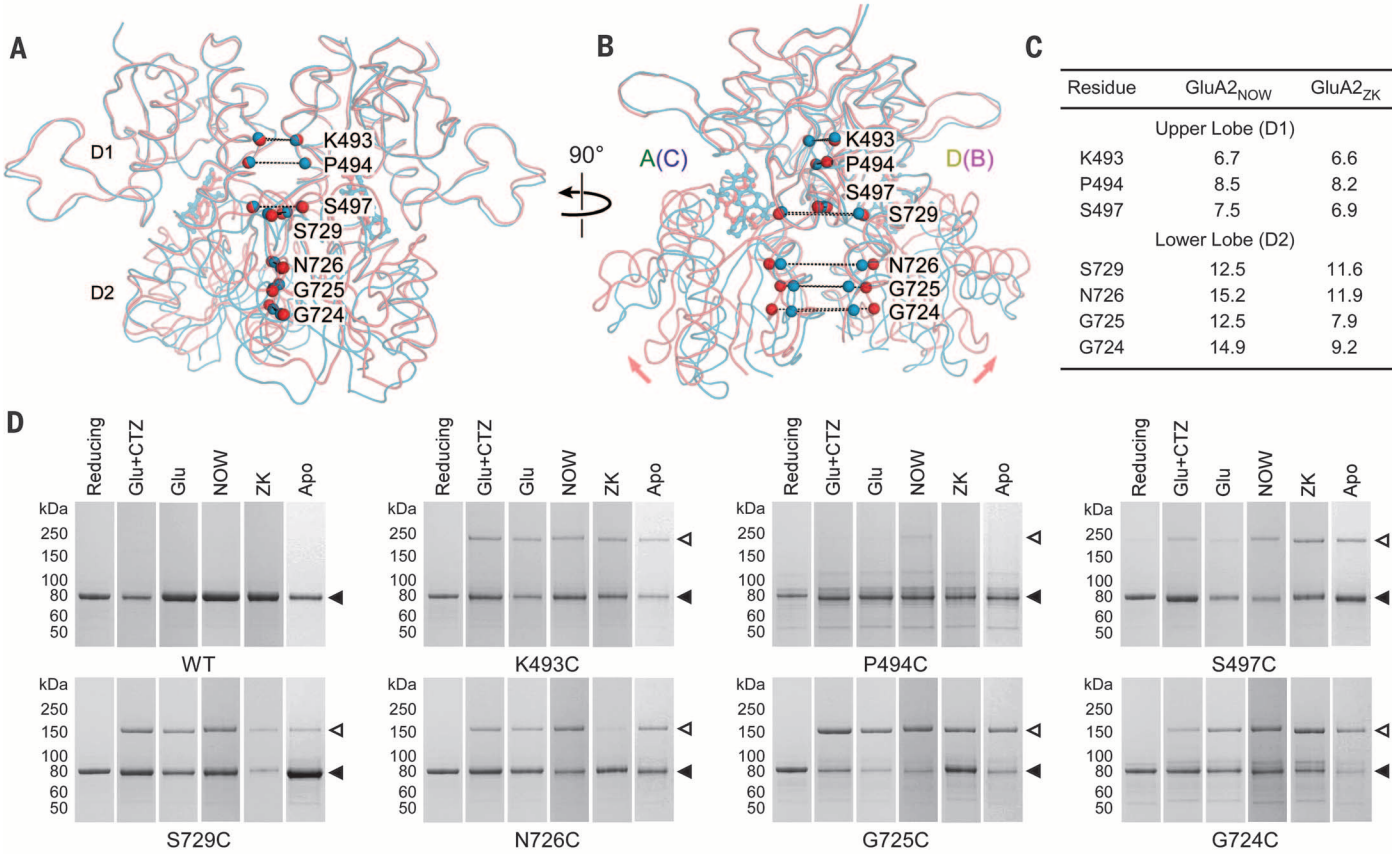

Fig. 3. LBD dimer-interface cross-linking and high mobility of LBD. (**A** and **B**) Superposition of LBD dimers from $GluA2_{NOW}$ (red) and $GluA2_{ZK}$ (blue) structures based on the upper lobes D1 and viewed perpendicular to (A) or along (B) the axes of rotation that brings the lower lobes D2 of $GluA2_{ZK}$ into $GluA2_{NOW}$. Spheres show Cα's for residues at the LBD interface substituted with cysteines. D, Asp; G, Gly; K, Lys; N, Asn. (**C**) Table showing LBD cross-interface distances between Cα's of the cysteine-substituted residues. Each number is the average of distances for the AD and BC dimers in angstroms. (**D**) SDS–polyacrylamide gel electrophoresis analysis of spontaneous cross-linking of cysteines introduced at the LBD interface. The experiments were carried out with GluA2* receptors in reducing conditions (2 mM DTT, left lanes); in nonreducing conditions but in the presence of 3 mM Glu and 50 μM CTZ (Glu+CTZ, favoring the open state), 3 mM Glu (Glu, favoring the desensitized state), 500 μM NOW (NOW, favoring the desensitized state), or 100 μM ZK (ZK, favoring the antagonist-bound closed state); or in the absence of ligands (Apo, favoring the unliganded closed state). Solid and open triangles indicate positions of monomeric and dimeric bands, respectively. In the absence of reducing agent, substituted cysteines can cross-link in conditions that favor different gating states, indicating high mobility of GluA2* LBDs in solution. WT, wild type.

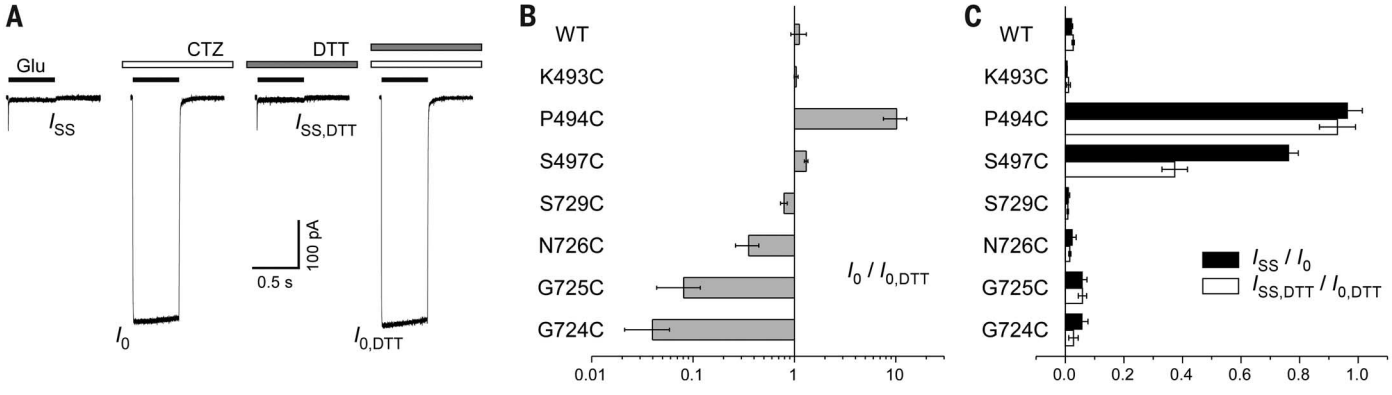

Fig. 4. Effects of LBD dimer interface cross-linking on gating. (**A**) Representative whole-cell currents recorded at −60-mV membrane potential from a HEK 293 cell expressing GluA2-K493C in response to a 500-ms application of 1 mM Glu alone and applications of Glu in the continuous presence of 30 μM CTZ or 2 mM DTT or CTZ and DTT. Subscripts 0, SS, and DTT label initial, steady-state, and measured in reducing conditions current amplitudes, respectively. (**B**) Effects of cysteine cross-linking on activation. Shown is the ratio of initial currents recorded in the continuous presence of CTZ in the absence and presence of DTT. (**C**) Effects of cysteine cross-linking on GluA2 desensitization. Shown is the extent of current reduction resulting from desensitization measured in absence (solid bars) or presence (open bars) of DTT. Error bars indicate SE.

closure (*17*); and channel opening occurs when LBD clamshells adopt their maximally closed conformation (*22*, *23*, *30*–*32*), represented by agonist-bound structures of isolated LBD (*13*, *17*) with the D1-D1 interface intact (fig. S7). The first model represents a traditional view (*18*) where the final desensitized state has the D1-D1 interface modified (fig. S12A). In this model, the $GluA2_{NOW}$ structure represents the agonist-bound closed state, which is predicted to be a transient state with negligible occupancy (Fig. 1B and fig. S2F) insufficient to produce protein crystals. Nevertheless, such a scenario is plausible if only a limited range of conformations of the protein is accessible in the solubilized receptor or the crystal lattice contacts substantially affect protein conformation.

The second model (fig. S12B) assumes two-step desensitization with $GluA2_{NOW}$ representing a deep desensitized state. This model is consistent with the predictions of kinetic modeling that, at high NOW concentrations, the majority of receptors accumulate in the deep desensitized state (D_24 in fig. S2). It also predicts that the same tension forces, applied from ATD and the ion channel through the connecting linkers that open LBD clamshells during deactivation, help transition the receptor from the deep desensitized state back to the desensitized state. Therefore, the second model explains why mutations that change the rate of deactivation often produce similar effects on the rate of recovery from desensitization (*14*, *33*, *34*).

Independent of gating model, the entry into desensitization is associated with modification of the D1-D1 interface (fig. S12) (*18*, *20*, *35*–*37*). One possible modification is represented by structures of the S729C and G725C cross-linked isolated LBDs (*18*) where the D1-D1 interface is ruptured. However, K493C cross-linking does not affect desensitization (Fig. 4C) and argues against these structures representing the desensitized state of the intact receptor. Alternatively, the D1-D1 interface modification might be a rotation of the D1 lobes relative to each other that does not change the distance between K493 lysines but introduces relative displacement of pairs of other residues at the D1-D1 interface. Correspondingly, mutations like L483Y (*28*) or S497C (Fig. 4C and fig. S11) or positive allosteric modulators like CTZ (*10*, *29*) would block desensitization by imposing constraints on the D1-D1 interface rearrangement.

REFERENCES AND NOTES

1. S. F. Traynelis *et al.*, *Pharmacol. Rev.* **62**, 405–496 (2010).
2. D. Bowie, *CNS Neurol. Disord. Drug Targets* **7**, 129–143 (2008).
3. P. Paoletti, C. Bellone, Q. Zhou, *Nat. Rev. Neurosci.* **14**, 383–400 (2013).
4. Z. Galen Wo, R. E. Oswald, *Trends Neurosci.* **18**, 161–168 (1995).
5. A. I. Sobolevsky, M. P. Rosconi, E. Gouaux, *Nature* **462**, 745–756 (2009).
6. C. H. Lee *et al.*, *Nature* **511**, 191–197 (2014).
7. E. Karakas, H. Furukawa, *Science* **344**, 992–997 (2014).
8. M. V. Jones, G. L. Westbrook, *Trends Neurosci.* **19**, 96–101 (1996).
9. M. D. Black, *Psychopharmacology (Berl.)* **179**, 154–163 (2005).
10. D. K. Patneau, L. Vyklicky Jr., M. L. Mayer, *J. Neurosci.* **13**, 3496–3509 (1993).
11. R. Jin, T. G. Banke, M. L. Mayer, S. F. Traynelis, E. Gouaux, *Nat. Neurosci.* **6**, 803–810 (2003).
12. K. Poon, L. M. Nowak, R. E. Oswald, *Biophys. J.* **99**, 1437–1446 (2010).
13. K. Poon, A. H. Ahmed, L. M. Nowak, R. E. Oswald, *Mol. Pharmacol.* **80**, 49–59 (2011).
14. A. Robert, N. Armstrong, J. E. Gouaux, J. R. Howe, *J. Neurosci.* **25**, 3752–3762 (2005).
15. R. Jin *et al.*, *EMBO J.* **28**, 1812–1823 (2009).
16. K. Menuz, R. M. Stroud, R. A. Nicoll, F. A. Hays, *Science* **318**, 815–817 (2007).
17. N. Armstrong, E. Gouaux, *Neuron* **28**, 165–181 (2000).
18. N. Armstrong, J. Jasti, M. Beich-Frandsen, E. Gouaux, *Cell* **127**, 85–97 (2006).
19. A. S. Maltsev, A. H. Ahmed, M. K. Fenwick, D. E. Jane, R. E. Oswald, *Biochemistry* **47**, 10600–10610 (2008).
20. A. J. Plested, M. L. Mayer, *J. Neurosci.* **29**, 11912–11923 (2009).
21. M. K. Fenwick, R. E. Oswald, *J. Biol. Chem.* **285**, 12334–12343 (2010).
22. C. F. Landes, A. Rambhadran, J. N. Taylor, F. Salatan, V. Jayaraman, *Nat. Chem. Biol.* **7**, 168–173 (2011).
23. A. Y. Lau, B. Roux, *Nat. Struct. Mol. Biol.* **18**, 283–287 (2011).
24. P. A. Postila, M. Ylilauri, O. T. Pentikäinen, *J. Chem. Inf. Model.* **51**, 1037–1047 (2011).
25. S. Ramaswamy *et al.*, *J. Biol. Chem.* **287**, 43557–43564 (2012).
26. A. H. Ahmed *et al.*, *J. Biol. Chem.* **288**, 27658–27666 (2013).
27. Y. Yao, J. Belcher, A. J. Berger, M. L. Mayer, A. Y. Lau, *Structure* **21**, 1788–1799 (2013).
28. Y. Stern-Bach, S. Russo, M. Neuman, C. Rosenmund, *Neuron* **21**, 907–918 (1998).
29. Y. Sun *et al.*, *Nature* **417**, 245–253 (2002).
30. W. Zhang, Y. Cho, E. Lolis, J. R. Howe, *J. Neurosci.* **28**, 932–943 (2008).
31. A. H. Ahmed, S. Wang, H. H. Chuang, R. E. Oswald, *J. Biol. Chem.* **286**, 35257–35266 (2011).
32. D. M. MacLean, A. Y. Wong, A. M. Fay, D. Bowie, *J. Neurosci.* **31**, 2136–2144 (2011).
33. M. C. Weston, C. Gertler, M. L. Mayer, C. Rosenmund, *J. Neurosci.* **26**, 7650–7658 (2006).
34. A. L. Carbone, A. J. Plested, *Neuron* **74**, 845–857 (2012).
35. C. R. Midgett, A. Gill, D. R. Madden, *Front. Mol. Neurosci.* **4**, 56 (2012).
36. A. Y. Lau *et al.*, *Neuron* **79**, 492–503 (2013).
37. D. M. Schauder *et al.*, *Proc. Natl. Acad. Sci. U.S.A.* **101**, 5921–5926 (2013).

ACKNOWLEDGMENTS

We thank the personnel at beamlines X4A, X4C, X25, and X29 of the National Synchrotron Light Source and at beamlines 24-ID-C and 24-ID-E of the Advanced Photon Source. 24-ID-C and 24-ID-E are the Northeastern Collaborative Access Team beamlines, which are supported by a grant from the National Institute of General Medical Sciences (P41 GM103403) from the NIH. This research used resources of the Advanced Photon Source, a U.S. Department of Energy (DOE) Office of Science User Facility operated for the DOE Office of Science by Argonne National Laboratory under contract no. DE-AC02-06CH11357. We thank L. Wollmuth and R. Kazi for help in setting up electrophysiological experiments and K. Saotome for comments on the manuscript. This work was supported by the NIH (NS083660) and the Klingenstein Foundation (A.I.S.). Coordinates and structure factors have been deposited in the Protein Data Bank with accession numbers 4U4F for $GluA2_{NOW}$ and 4U4G for $GluA2_{ZK}$.

SUPPLEMENTARY MATERIALS

www.sciencemag.org/content/345/6200/1070/suppl/DC1
Materials and Methods
Figs. S1 to S12
Tables S1 to S3
References (*38*–*50*)

27 May 2014; accepted 25 July 2014
Published online 7 August 2014;
10.1126/science.1256508

EVOLUTIONARY GENOMICS

Rabbit genome analysis reveals a polygenic basis for phenotypic change during domestication

Miguel Carneiro,[1]* Carl-Johan Rubin,[2]* Federica Di Palma,[3,4]* Frank W. Albert,[5]† Jessica Alföldi,[3] Alvaro Martinez Barrio,[2] Gerli Pielberg,[2] Nima Rafati,[2] Shumaila Sayyab,[6] Jason Turner-Maier,[3] Shady Younis,[2,7] Sandra Afonso,[1] Bronwen Aken,[8,9] Joel M. Alves,[1,10] Daniel Barrell,[8,9] Gerard Bolet,[11] Samuel Boucher,[12] Hernán A. Burbano,[5]‡ Rita Campos,[1] Jean L. Chang,[3] Veronique Duranthon,[13] Luca Fontanesi,[14] Hervé Garreau,[11] David Heiman,[3] Jeremy Johnson,[3] Rose G. Mage,[15] Ze Peng,[16] Guillaume Queney,[17] Claire Rogel-Gaillard,[18] Magali Ruffier,[8,9] Steve Searle,[8] Rafael Villafuerte,[19] Anqi Xiong,[20] Sarah Young,[3] Karin Forsberg-Nilsson,[20] Jeffrey M. Good,[5,21] Eric S. Lander,[3] Nuno Ferrand,[1,22]* Kerstin Lindblad-Toh,[2,3]*§ Leif Andersson[2,6,23]*§

The genetic changes underlying the initial steps of animal domestication are still poorly understood. We generated a high-quality reference genome for the rabbit and compared it to resequencing data from populations of wild and domestic rabbits. We identified more than 100 selective sweeps specific to domestic rabbits but only a relatively small number of fixed (or nearly fixed) single-nucleotide polymorphisms (SNPs) for derived alleles. SNPs with marked allele frequency differences between wild and domestic rabbits were enriched for conserved noncoding sites. Enrichment analyses suggest that genes affecting brain and neuronal development have often been targeted during domestication. We propose that because of a truly complex genetic background, tame behavior in rabbits and other domestic animals evolved by shifts in allele frequencies at many loci, rather than by critical changes at only a few domestication loci.

Domestication of animals (that is, the evolution of wild species into tame forms) has resulted in notable changes in behavior, morphology, physiology, and reproduction (*1*). The genetic underpinnings of the initial steps of animal domestication are poorly understood but probably involved changes in behavior that allowed the animals to survive and reproduce under conditions that might be too stressful for wild animals. Given the differences

in behavior between wild and domesticated animals, we investigated to what extent this process involved fixation of new mutations with large phenotypic effects, as opposed to selection on standing variation. Such studies are hampered in most domestic animals due to ancient domestication events, extinct wild ancestors, or geographically widespread wild ancestors.

Rabbit domestication was initiated in monasteries in southern France as recently as ~1400 years ago (*2*). At this time, wild rabbits were mostly restricted to the Iberian Peninsula, where two subspecies occurred (*Oryctolagus cuniculus cuniculus* and *O. c. algirus*), and to France, colonized by *O. c. cuniculus* (Fig. 1B). Additionally, the area of origin of domestic rabbits is still populated with wild rabbits related to the ancestors of the domestic rabbit (*3*). This recent and well-defined origin provides a major advantage for inferring genetic changes underlying domestication.

We performed Sanger sequencing and assembly of a female rabbit genome (*4*). The draft OryCun2.0 assembly size is 2.66 Gb, with a contig N50 size of 64.7 kb and a scaffold N50 size of 35.9 Mb (tables S1 and S2). The genome assembly was annotated using the Ensembl gene annotation pipeline (Ensembl release 73, September 2013) and with both rabbit RNA sequencing data and the annotation of human orthologs (*4*) (table S3). Our analysis of rabbit domestication used Ensembl annotations as well as a custom pipeline for annotation of untranslated regions (UTRs) (168,286 distinct features), noncoding RNA (n = 9666), and noncoding conserved elements (2,518,476 distinct features).

To identify genomic regions under selection during domestication, we performed whole-genome resequencing (10× coverage) of pooled samples (table S4) of six different breeds of domestic rabbits (Fig. 1A), 3 pools of wild rabbits from southern France, and 11 pools of wild rabbits from the Iberian Peninsula, representing both subspecies (Fig. 1B). We also sequenced a close relative, the snowshoe hare (*Lepus americanus*), to deduce the ancestral state at polymorphic sites. Short sequence reads were aligned to our assembly; single-nucleotide polymorphism (SNP) calling resulted in the identification of 50 million high-quality SNPs and 5.6 million insertion/deletion polymorphisms after filtering (table S5). The numbers of SNPs at noncoding conserved sites and in coding sequences were 719,911 and 154,489, respectively. The per-site nucleotide diversity (π) within populations of wild rabbits was in the range of 0.6 to 0.9% (Fig. 1C). Thus, the rabbit is one of the most polymorphic mammals sequenced so far, presumably due to a larger long-term effective population size relative to other sequenced mammals (*5*). Identity scores confirm that the domestic rabbit is most closely related to wild rabbits from southern France (fig. S1A), and we inferred a strong correlation (r = 0.94) in allele frequencies at most loci between these groups (fig. S1B). The average nucleotide diversity of each sequenced population is consistent with a bottleneck and reduction in genetic diversity when rabbits from the Iberian Peninsula colonized southern France and a second bottleneck during domestication (*3*) (Fig. 1, B and C).

Selective sweeps occur when beneficial genetic variants increase in frequency due to positive selection together with linked neutral sequence variants (*6*). This results in genomic islands of reduced heterozygosity and increased differentiation between populations around the selected site. We compared genetic diversity between domestic rabbits as one group to wild rabbits representing 14 different locations in France and the Iberian Peninsula. We calculated fixation index (F_{ST}) values between wild and domestic rabbits and average pooled heterozygosity (H) in domestic rabbits in 50-kb sliding windows across the genome (hereafter referred to as the F_{ST}-H outlier approach). We identified 78 outliers with $F_{ST} > 0.35$ and $H < 0.05$ (Fig. 2A, fig. S2, database S1). We also used SweepFinder (*7*), which calculates maximum composite likelihoods for the presence of a selective sweep, taking into account the background pattern of genetic variation in the data and with a significance threshold set by coalescent simulations incorporating the recent demographic history of domestic and wild rabbits (figs. S3 and S4 and databases S1 and S2) (*4*). This analysis resulted in the identification of 78 significant sweeps (false discovery rate = 5%) (Fig. 2A, database S1). Thirty-one (40%) of these were also detected with the F_{ST}-H approach (Fig. 2A). This incomplete overlap is probably explained by the fact that SweepFinder primarily assesses the distribution of genetic diversity within the selected population, whereas the F_{ST}-H analysis identifies the most differentiated regions of the genome between wild and domestic rabbits. We carried out an additional screen using targeted sequence capture on an independent sample of individual French wild and domestic rabbits. We targeted more than 6 Mb of DNA sequence split into 5000 1.2-kb intronic fragments that were distributed across the genome and selected independently of the genome resequencing results above. Coalescent simulations, using the targeted resequencing data set and incorporating the recent demographic history of domestic rabbit as a null model (figs. S3 and S4 and databases S1 and S2) (*4*), revealed that the majority of the sweep regions detected by whole-genome resequencing showed levels and patterns of genetic variation that were observed less than 5% of the time in the simulated data set (76.0% with SweepFinder and 73.7% with F_{ST}-H outlier regions, excluding regions without targeted fragments), a highly significant overlap (Fisher's exact test, $P < 1 \times 10^{-5}$ for both tests). Furthermore, 26 of the 31 sweep regions detected with both SweepFinder and the F_{ST}-H approach were targeted in the capture experiment, and an even greater proportion (88.5%) showed levels and patterns of genetic variation unlikely to be generated under the specified demographic model.

An example of a selective sweep overlapping the 3′-part of *GRIK2* (glutamate receptor, ionotropic, kainate 2) is shown in Fig. 2B. Parts of this region have low heterozygosity in domestic rabbits, and at position chr12:90,153,383 base pairs, domestic rabbits carry a nearly fixed derived allele at a site with 100% sequence conservation among 29 mammals except for the allele present in domestic rabbits (*8*), suggesting functional importance. *GRIK2* encodes a subunit of a glutamate receptor that is highly expressed in the brain and has been associated with recessive mental retardation in humans (*9*). Both SweepFinder and the F_{ST}-H outlier analysis identified two sweeps near *SOX2* (SRY-BOX 2), separated by a region of high heterozygosity (Fig. 2C). *SOX2* encodes a transcription factor that is required for stem cell maintenance (*10*).

Given the comprehensive sampling in our study and the correlation in allele frequencies between domestic and French wild rabbits (fig. S1B), highly differentiated individual SNPs are likely either to have been directly targeted by selection or to occur in the vicinity of loci under selection. For each SNP, we calculated the absolute allele frequency difference between wild and domestic rabbits (ΔAF) and sorted these into 5% bins (ΔAF = 0 to 0.05, etc.). The majority of SNPs showed low ΔAF between wild and domestic

[1]CIBIO/InBIO, Centro de Investigação em Biodiversidade e Recursos Genéticos, Campus Agrário de Vairão, Universidade do Porto, 4485-661, Vairão, Portugal. [2]Science for Life Laboratory Uppsala, Department of Medical Biochemistry and Microbiology, Uppsala University, Uppsala, Sweden. [3]Broad Institute of Harvard and Massachusetts Institute of Technology, 7 Cambridge Center, Cambridge, MA 02142, USA. [4]Vertebrate and Health Genomics, The Genome Analysis Centre, Norwich, UK. [5]Department of Evolutionary Genetics, Max Planck Institute for Evolutionary Anthropology, Leipzig, Germany. [6]Department of Animal Breeding and Genetics, Swedish University of Agricultural Sciences, Uppsala, Sweden. [7]Department of Animal Production, Ain Shams University, Shoubra El-Kheima, Cairo, Egypt. [8]Wellcome Trust Sanger Institute, Hinxton, UK. [9]European Molecular Biology Laboratory, European Bioinformatics Institute, Wellcome Trust Genome Campus, Hinxton, Cambridge CB10 1SD, UK. [10]Department of Genetics, University of Cambridge, Cambridge CB2 3EH, UK. [11]Institut National de la Recherche Agronomique (INRA), UMR1388 Génétique, Physiologie et Systèmes d'Elevage, F-31326 Castanet-Tolosan, France. [12]Labovet Conseil, BP539, 85505 Les Herbiers Cedex, France. [13]INRA, UMR1198 Biologie du Développement et Reproduction, F-78350 Jouy-en-Josas, France. [14]Department of Agricultural and Food Sciences, Division of Animal Sciences, University of Bologna, 40127 Bologna, Italy. [15]Laboratory of Immunology, National Institute of Allergy and Infectious Diseases (NIAID), National Institutes of Health, Bethesda, MD 20892, USA. [16]U.S. Department of Energy Joint Genome Institute, Lawrence Berkeley National Laboratory, 2800 Mitchell Drive, Walnut Creek, CA 94598, USA. [17]ANTAGENE, Animal Genomics Laboratory, Lyon, France. [18]INRA, UMR1313 Génétique Animale et Biologie Intégrative, F- 78350, Jouy-en-Josas, France. [19]Instituto de Estudios Sociales Avanzados, (IESA-CSIC) Campo Santo de los Mártires 7, Córdoba, Spain. [20]Science for Life Laboratory, Department of Immunology, Genetics and Pathology, Uppsala University, Uppsala, Sweden. [21]Division of Biological Sciences, The University of Montana, Missoula, MT 59812, USA. [22]Departamento de Biologia, Faculdade de Ciências, Universidade do Porto, Rua do Campo Alegre s/n. 4169-007 Porto, Portugal. [23]Department of Veterinary Integrative Biosciences, College of Veterinary Medicine and Biomedical Sciences, Texas A&M University, College Station, TX 77843-4458, USA.

*These authors contributed equally to this work. †Present address: Department of Human Genetics, University of California, Los Angeles, Gonda Center, 695 Charles E. Young Drive South, Los Angeles, CA 90095, USA. ‡Present address: Department of Molecular Biology, Max Planck Institute for Developmental Biology, Tübingen, Germany. **§Corresponding author. E-mail: kersli@broadinstitute.org (K.L.-T.); leif.andersson@imbim.uu.se (L.A.)**

rabbits (Fig. 2D). We examined exons, introns, UTRs, and evolutionarily conserved sites for enrichment of SNPs with high ΔAF, as would be expected under directional selection on many independent mutations (Fig. 2D and table S6). We observed no consistent enrichment for high ΔAF SNPs in introns, but we found significant enrichments in exons, UTRs, and conserved noncoding sites (χ^2 test, $P < 0.05$). We detected a significant excess of SNPs at conserved noncoding sites for each bin $\Delta AF > 0.45$ (χ^2 test, $P = 1.8 \times 10^{-3}$ to 7.3×10^{-17}), whereas in coding sequence, a significant excess was found only at $\Delta AF > 0.80$ (χ^2 test, $P = 3.0 \times 10^{-2}$ to 1.0×10^{-3}). Compared to the relative proportions in the entire data set, there was an excess of 3000 SNPs at conserved noncoding sites with $\Delta AF > 0.45$, whereas for exonic SNPs with $\Delta AF > 0.80$, the excess was only 83 SNPs (table S6). Thus, changes at regulatory sites have played a much more prominent role in rabbit domestication, at least numerically, than changes in coding sequences.

We selected the 1635 SNPs at conserved noncoding sites with $\Delta AF > 0.80$, which represent 681 nonoverlapping 1-Mb blocks of the rabbit genome. So as not to inflate significances due to inclusion of SNPs in strong linkage disequilibrium, we selected only one SNP per 50 kb, leaving 1071 SNPs. More than 60% of the SNPs were located 50 kb or more from the closest transcriptional start site (TSS) (Fig. 2E), suggesting that many differentiated SNPs are located in long-range regulatory elements. A gene ontology (GO) overrepresentation analysis (*11*) examining all genes located within 1 Mb from high-ΔAF SNPs showed that the most enriched categories of biological processes involved "cell fate commitment" (Bonferroni $P = 3.1 \times 10^{-3}$ to 5.4×10^{-5}) (Table 1 and database S3), whereas the statistically most significant categories involved brain and nervous system cell development (Bonferroni $P = 2.9 \times 10^{-3}$ to 3.7×10^{-10}). Many of the mouse orthologs of genes associated with noncoding high-ΔAF SNPs were expressed in the brain or sensory organs, and this enrichment was highly significant (Table 1). We also examined phenotypes observed in mouse mutants (www.informatics.jax.org) for these genes, revealing a significant (Bonferroni $P = 3.7 \times 10^{-2}$ to 7.5×10^{-17}) enrichment of genes associated with defects in brain and neuronal development, development of sensory organs (hearing and vision), ectoderm development, and respiratory system phenotypes (fig. S5). These highly significant overrepresentations were obtained because there were many genes in the overrepresented categories (Table 1). For example, we observed high-ΔAF SNPs associated with 191 genes (113 expected by chance) from the nervous system–development GO category (Bonferroni $P = 3.7 \times 10^{-10}$). Thus, rabbit domestication must have a highly polygenic basis with many loci responding to selection and where genes affecting brain and neuronal development have been particularly targeted.

None of the coding SNPs that differed between wild and domestic rabbits was a nonsense or frame-shift mutation, consistent with data from chicken (*12*) and pigs (*13*), suggesting that gene loss has not played a major role during animal domestication. This is an important finding, as it has been suggested that gene inactivation could be an important mechanism for rapid evolutionary change, for instance, during domestication (*14*). Of 69,985 autosomal missense mutations, there were no fixed differences, and only 14 showed a ΔAF above 90%. On the basis of poor sequence conservation, similar chemical properties of the substituted amino acids, and/or the derived state of the domestic allele, we assume that most of these result from hitchhiking rather than being functionally important (database S4). However, two missense mutations stand out; these may be direct targets of selection because at these two positions the domestic rabbit differs from all other sequenced mammals (>40 species). The first is a $Gln^{813} \rightarrow Arg^{813}$ substitution in *TTC21B* (tetratricopeptide repeat domain 21B protein), which is part of the ciliome and modulates sonic hedgehog signaling during embryonic development (*15*). The other is an $Arg^{1627} \rightarrow Trp^{1627}$ substitution in *KDM6B* (lysine-specific demethylase 6B), which encodes a histone H3K27 demethylase involved in *HOX* gene regulation during development (*16*).

Deletions distinct to domestic rabbits were difficult to identify because the genome assembly is based on a domestic rabbit, but some convincing duplications were detected with marked frequency differences between wild and domestic rabbits (database S5). We observed a

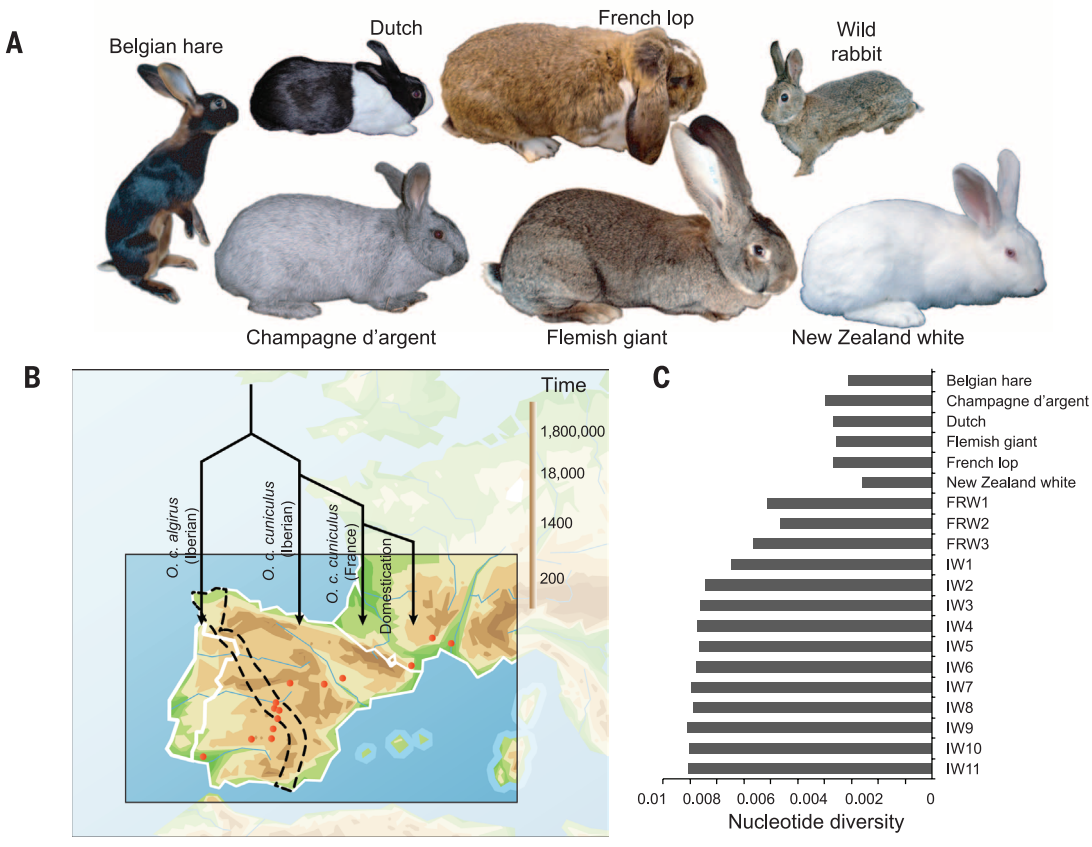

Fig. 1. Experimental design and population data. (**A**) Images of the six rabbit breeds included in the study (sized to reflect differences in body weight) and of a wild rabbit. (**B**) Map of the Iberian Peninsula and southern France with sample locations marked (orange dots). Demographic history of this species is indicated, and a logarithmic time scale is shown at right. The hybrid zone between the two subspecies is marked with dashes. (**C**) Nucleotide diversities in domestic and wild populations. The French (FRW1 to FRW3) and Iberian (IW1 to IW11) wild rabbit populations are ordered according to a northeast-to-southwest transection. Sample locations are provided in table S4.

one–base pair insertion/deletion polymorphism located within an intron of *IMMP2L* (inner mitochondrial membrane peptidase-2 like protein), where domestic and wild rabbits were fixed for different alleles. The polymorphism occurs in a sweep region and is the sequence polymorphism with highest ΔAF in the region (fig. S6). Mutations in *IMMP2L* have been associated with Tourette syndrome and autism in humans (*17*).

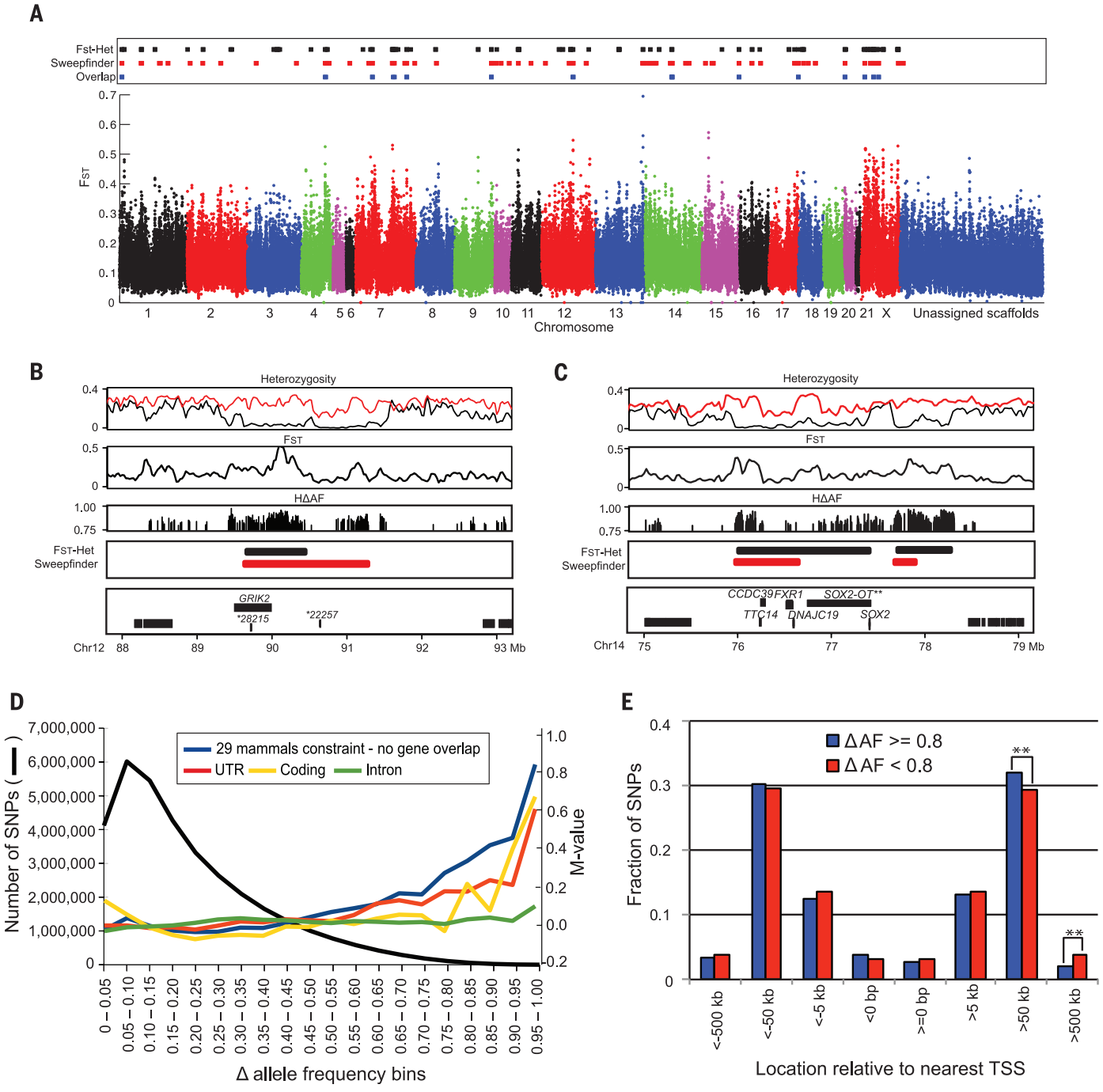

Fig. 2. Selective sweep and Δ allele frequency analyses. (**A**) Plot of F_{ST} values between wild and domestic rabbits. Sweeps detected with the F_{ST}-*H* outlier approach, SweepFinder, and their overlaps are marked on top. Unassigned scaffolds were not included in the analysis. (**B** and **C**) Selective sweeps at *GRIK2* (B) and *SOX2* (C). Heterozygosity plots for wild (red) and domestic (black) rabbits together with plots of F_{ST} values and SNPs with $\Delta AF > 0.75$ (HΔAF). The bottom panels show putative sweep regions, detected with the F_{ST}-*H* outlier approach and SweepFinder, marked with horizontal bars. Gene annotations in sweep regions are indicated: * represents ENSOCUT000000; ***SOX2-OT* represents the manually annotated SOX2 overlapping transcript (*4*). (**D**) The majority of SNPs showed low ΔAF between wild and domestic rabbits. The black line indicates the number of SNPs in nonoverlapping ΔAF bins (left *y* axis). Colored lines denote M values (log2-fold changes) of the relative frequencies of SNPs at noncoding evolutionary conserved sites (blue), in UTRs (red), exons (yellow), and introns (green), according to ΔAF bins (right *y* axis). M values were calculated by comparing the frequency of SNPs in a given annotation category in a specific bin with the corresponding frequency across all bins. (**E**) Location of SNPs at conserved noncoding sites with $\Delta AF \geq 0.8$ SNPs ($n = 1635$) and $\Delta AF < 0.8$ SNPs ($n = 502{,}343$) in relation to the TSS of the most closely linked gene. **$P < 0.01$.

Table 1. Summary of results from enrichment analysis of $\Delta AF > 0.8$ SNPs located in conserved noncoding elements. One significantly enriched term was chosen from each group of significantly enriched intercorrelated terms. Full lists of enriched terms and intercorrelations are presented in database S3, and the most enriched intercorrelated terms are presented in fig. S5. *P* values are Bonferroni-corrected. O/R, number of distinct nonoverlapping 1-Mb windows observed (O) and the average number of 1-Mb windows observed in 1000 random (R) samplings of the same number of genes (rounded to the nearest integer). TS, Thieler stage.

Database entry	Enriched term	Number of genes	*P*	Enrichment	Distinct loci (O/R)
		Gene Ontology biological process			
GO:0007399	Nervous system development	191	3.7×10^{-10}	1.7	154/155
GO:0045595	Regulation of cell differentiation	107	4.5×10^{-6}	1.8	94/91
GO:0045935	Positive regulation of nucleobase-containing compound metabolic process	122	2.0×10^{-5}	1.7	101/100
GO:0045165	Cell fate commitment	36	5.5×10^{-5}	2.9	31/32
GO:0007389	Pattern specification process	57	1.4×10^{-4}	2.2	43/44
GO:0009887	Organ morphogenesis	85	2.0×10^{-3}	1.8	72/73
GO:0048646	Anatomical structure formation involved in morphogenesis	75	2.8×10^{-3}	1.8	65/64
GO:0045892	Negative regulation of transcription, DNA-dependent	82	1.4×10^{-2}	1.7	62/62
GO:0034332	Adherens junction organization	13	1.5×10^{-2}	4.7	11/11
		Mouse Genome Informatics gene expression			
11853	TS23 diencephalon, lateral wall, mantle layer	109	3.9×10^{-25}	3.3	86/85
12449	TS23 medulla oblongata, lateral wall, basal plate, mantle layer	115	2.6×10^{-13}	2.3	90/89
2257	TS17 sensory organ	113	3.4×10^{-13}	2.3	98/99
1324	TS15 future brain	72	8.5×10^{-9}	2.4	61/61
		Mouse Genome Informatics phenotype			
MP:0010832	Lethality during fetal growth through weaning	240	7.5×10^{-17}	1.8	197/189
MP:0003632	Abnormal nervous system morphology	237	1.2×10^{-13}	1.7	191/193
MP:0005388	Respiratory system phenotype	127	1.7×10^{-7}	1.8	101/102
MP:0000428	Abnormal craniofacial morphology	109	1.4×10^{-6}	1.9	93/92
MP:0002925	Abnormal cardiovascular development	88	3.3×10^{-5}	1.9	73/73
MP:0005377	Hearing/vestibular/ear phenotype	73	1.8×10^{-4}	2.0	61/62

Cell fate determination was a strongly enriched GO category (enrichment factor = 4.9) (database S3) for genes near variants with high ΔAF. We examined the functional importance of 12 *SOX2*, 4 *KLF4*, and 1 *PAX2* high ΔAF SNPs associated with this GO category and where all 17 SNPs were distinct to domestic rabbits compared with other sequenced mammals. Electrophoretic mobility shift assay (EMSA) with nuclear extracts from mouse embryonic stem cell–derived neural stem cells revealed specific DNA-protein interactions (Fig. 3, fig. S7, table S7). Four probes, all from the *SOX2* region, showed a gel shift difference between wild and domestic alleles. Nuclear extracts from a mouse P19 embryonic carcinoma cell line before and after neuronal differentiation recapitulated these four gel shifts and revealed three additional probes, one in *PAX2* and two more in *SOX2*, that showed gel shift differences between wild-type and mutant probes only after neuronal differentiation. Thus, altered DNA-protein interactions were identified for 7 of the 17 high ΔAF SNPs that we tested, qualifying them as candidate causal SNPs that may have contributed to rabbit domestication.

Our results show that very few loci have gone to complete fixation in domestic rabbits and none at coding sites or at noncoding conserved sites. However, allele frequency shifts were detected at many loci spread across the genome, and the

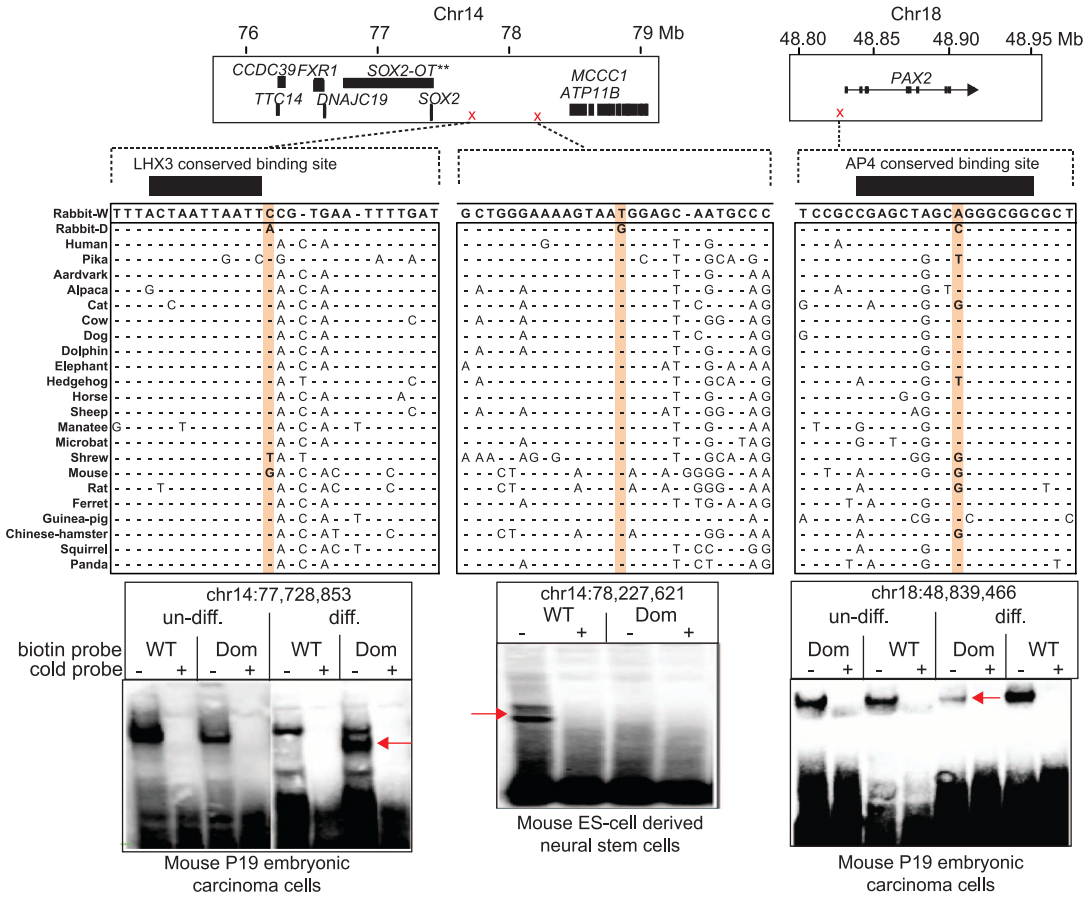

Fig. 3. Bioinformatic and functional analysis of candidate causal mutations. Three examples of SNPs near *SOX2* and *PAX2* where the domestic allele differs from other mammals. The locations of these three SNPs assessed with EMSA are indicated by red crosses on top. EMSA with nuclear extracts from embryonic stem cell–derived neural stem cells or from mouse P19 embryonic carcinoma cells before (un-diff) or after neuronal differentiation (diff) are shown for three SNPs. Exact nucleotide positions of polymorphic sites are indicated. Allele-specific gel shifts are indicated by arrows. WT, wild-type allele; Dom, domestic, the most common allele in domestic rabbits. Cold probes at 100-fold excess were used to verify specific DNA-protein interactions.

great majority of domestic alleles were also found in wild rabbits, implying that directional selection events associated with rabbit domestication are consistent with polygenic and soft sweep modes of selection (*18*) that primarily acted on standing genetic variation in regulatory regions of the genome. This stands in contrast with breed-specific traits in many domesticated animals that often show a simple genetic basis with complete fixation of causative alleles (*19*). Our finding that many genes affecting brain and neuronal development have been targeted during rabbit domestication is fully consistent with the view that the most critical phenotypic changes during the initial steps of animal domestication probably involved behavioral traits that allowed animals to tolerate humans and the environment humans offered. On the basis of these observations, we propose that the reason for the paucity of specific fixed domestication genes in animals is that no single genetic change is either necessary or sufficient for domestication. Because of the complex genetic background for tame behavior, we propose that domestic animals evolved by means of many mutations of small effect, rather than by critical changes at only a few domestication loci.

REFERENCES AND NOTES

1. C. Darwin, *On the Origins of Species by Means of Natural Selection or the Preservation of Favoured Races in the Struggle for Life* (John Murray, London, 1859).
2. J. A. Clutton-Brock, *Natural History of Domesticated Mammals* (Cambridge Univ. Press, Cambridge, 1999).
3. M. Carneiro *et al.*, *Mol. Biol. Evol.* **28**, 1801–1816 (2011).
4. Materials and methods are available as supplementary materials on *Science* Online.
5. M. Carneiro *et al.*, *Mol. Biol. Evol.* **29**, 1837–1849 (2012).
6. J. M. Smith, J. Haigh, *Genet. Res.* **23**, 23–35 (1974).
7. R. Nielsen *et al.*, *Genome Res.* **15**, 1566–1575 (2005).
8. K. Lindblad-Toh *et al.*, *Nature* **478**, 476–482 (2011).
9. M. M. Motazacker *et al.*, *Am. J. Hum. Genet.* **81**, 792–798 (2007).
10. K. Takahashi, S. Yamanaka, *Cell* **126**, 663–676 (2006).
11. C. Y. McLean *et al.*, *Nat. Biotechnol.* **28**, 495–501 (2010).
12. C.-J. Rubin *et al.*, *Nature* **464**, 587–591 (2010).
13. C.-J. Rubin *et al.*, *Proc. Natl. Acad. Sci. U.S.A.* **109**, 19529–19536 (2012).
14. M. V. Olson, *Am. J. Hum. Genet.* **64**, 18–23 (1999).
15. P. V. Tran *et al.*, *Nat. Genet.* **40**, 403–410 (2008).
16. K. Agger *et al.*, *Nature* **449**, 731–734 (2007).
17. H. Deng, K. Gao, J. Jankovic, *Nat. Rev. Neurol.* **8**, 203–213 (2012).
18. J. K. Pritchard, J. K. Pickrell, G. Coop, *Curr. Biol.* **20**, R208–R215 (2010).
19. L. Andersson, *Curr. Opin. Genet. Dev.* **23**, 295–301 (2013).

ACKNOWLEDGMENTS

This work was supported by grants from the National Human Genome Research Institute (U54 HG003067 to E.S.L.), European Research Council project BATESON to L.A., the Wellcome Trust (grants WT095908 and WT098051), the intramural research program of the NIH, NIAID (R.G.M.), the European Molecular Biology Laboratory, Programa Operacional Potencial Humano–Quadro de Referência Estratégica Nacional funds from the European Social Fund and Portuguese Ministério da Ciência, Tecnologia e Ensino Superior [postdoc grants to M.C. (SFRH/BPD/72343/2010) and R.C. (SFRH/BPD/64365/2009) and Ph.D. grant to J.M.A. (SFRH/BD/72381/2010)], a NSF international postdoctoral fellowship to J.M.G. (OISE-0754461), FEDER funds through the COMPETE program and Portuguese national funds through the Fundação para a Ciência e a Tecnologia (PTDC/CVT/122943/2010, PTDC/BIA-EVF/115069/2009, PTDC/BIA-BDE/72304/2006, and PTDC/BIA-BDE/72277/2006), the projects "Genomics and Evolutionary Biology" and "Genomics Applied to Genetic Resources" cofinanced by North Portugal Regional Operational Programme 2007/2013 (ON.2 – O Novo Norte) under the National Strategic Reference Framework and the European Regional Development Fund, travel grants to M.C. (COST Action TD1101), and Higher Education Commission in Pakistan (support for Sh.S.). We are grateful to L. Gaffney for assistance with figure preparation, P. C. Alves and S. Mills for providing the snowshoe hare sample, and S. Pääbo for hosting M.C., S.A., and R.C. Sequencing was performed by the Broad Institute Genomics Platform. Computer resources were supplied by BITS and UPPNEX at Science for Life Laboratory. The *O. cuniculus* genome assembly has been deposited in GenBank under the accession number AAGW02000000. The RNA sequencing data have been deposited in GenBank under the bioproject PRJNA78323, the rabbit genome resequencing data under the bioproject PRJNA242290, and the sequence capture data under the bioproject PRJNA221358. **Author contributions:** K.L.-T., F.D.P., and E.S.L. oversaw genome sequencing, assembly, and annotation performed by J.A., J.T.-M., J.J., D.H., J.L.C., and Sa.Y. B.A., D.B., M.R., and St.S. did Ensembl annotations. C.R.-G., V.D., L.F., R.G.M., and Z.P. contributed to the genome project. L.A., M.C., C.-J.R., N.F., and K.L.-T. led the domestication study, and A.M.B., N.R., and Sh.S. contributed with bioinformatic analyses. Sh.Y. and G.P. performed EMSA, and A.X. and K.F.-N. developed neural stem cells for EMSA. M.C., F.W.A., J.M.G., S.A., J.M.A., G.B., S.B., H.A.B., R.C., H.G., G.Q., and R.V. designed, performed, and analyzed the sequence capture experiment. L.A., M.C., C.-J.R., K.L.-T., N.F., and F.D.P. wrote the paper with input from other authors.

SUPPLEMENTARY MATERIALS

www.sciencemag.org/content/345/6200/1074/suppl/DC1
Materials and Methods
Figs. S1 to S7
Tables S1 to S7
References (*20*–*61*)
Databases S1 to S5

21 March 2014; accepted 11 July 2014
10.1126/science.1253714

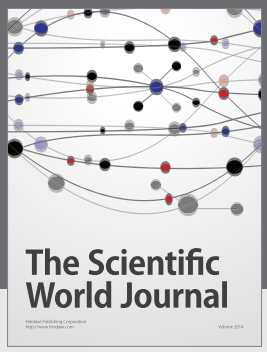

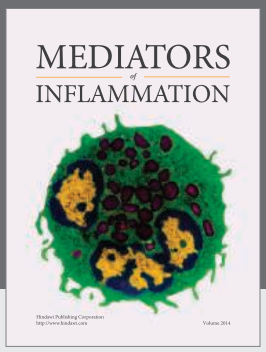

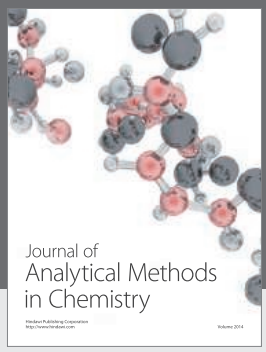

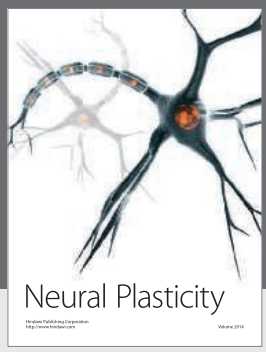

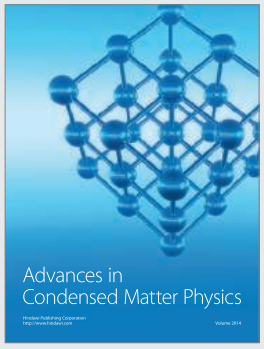

Hindawi

Submit your manuscripts at
http://www.hindawi.com

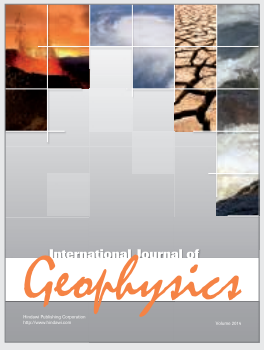

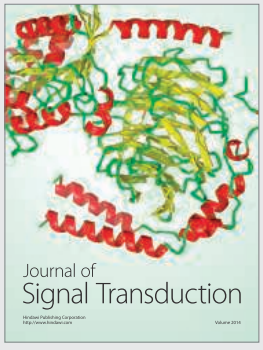

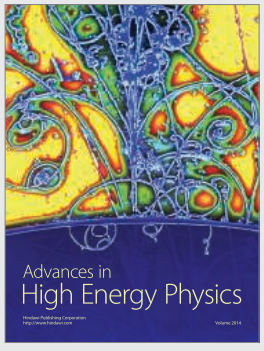

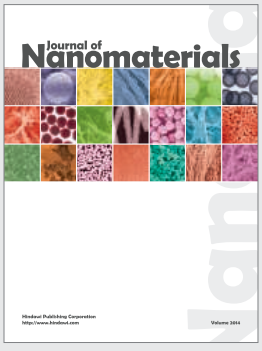

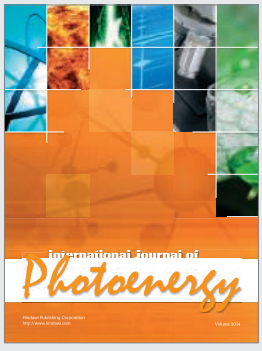

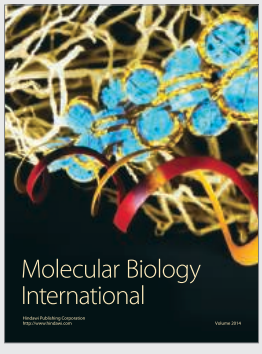

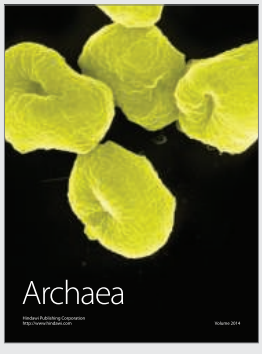

100 YEARS
OF EXPERT-CURATED CONTENT FOR 50 YEARS.

WE'RE THE STEWARDS OF THE INFORMATION THAT MATTERS MOST TO YOU.

CARING

FOR THE RESEARCH COMMUNITY'S MOST IMPACTFUL CONTENT

Web of Science™ connects scholarly content and researchers through citations and controlled indexing. For the past 50 years, we've curated databases spanning every discipline, so you know you're getting the most critical and regionally relevant information driving research around the world.

The global standard for finding and connecting scholarly content across disciplines and the globe, Web of Science is the only database that effectively translates the collective wisdom of the best researchers in each field into a dataset that makes that knowledge available to all.

Web of Science allows you to:

- **Benefit from cover-to-cover indexing** with an objective evaluation process to meet the highest standards
- **Use citation connections** to draw the full picture of the most reputable and impactful research in the scholarly community
- **Identify hidden patterns,** gaining insight into emerging research trends

Visit us at **go.thomsonreuters.com/quality** to learn about all of our offerings.

THOMSON REUTERS™

©2014 Thomson Reuters. All rights reserved. Thomson Reuters and the Kinesis logo are trademarks of Thomson Reuters.

Webinar

A Systems Approach to the Modern Microbiome World: Investigating Host-Microbiota Symbiosis

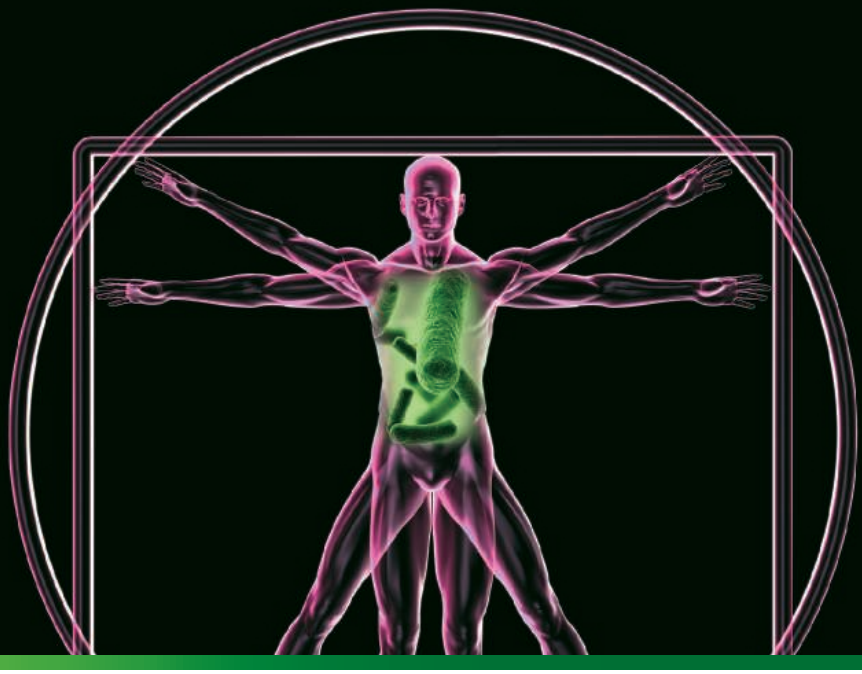

Wednesday, September 24, 2014

12 noon Eastern, 9 a.m. Pacific,
5 p.m. UK, 6 p.m. Central Europe

During this webinar, viewers will:

- Learn about important ways in which the host and microbiome interact
- Hear how the human skin microbiota influences host physiology and immunity
- Be introduced to the complex interactions between gut microbes and human health
- Have an opportunity to put questions to the panel, live!

Register Now!

webinar.sciencemag.org

Microorganisms living in or on the body of a healthy human adult outnumber human cells by 10 to one. A large number of the 100 trillion microbes that compose the majority of life on Earth have coevolved a close relationship with the mammalian immune system. Therefore, by solely limiting research to either the host or bacteria, only half of the information required in microbiome studies is being seen. The symbiotic relationship of the host and resident microbiota must remain in delicate harmony to maintain a healthy body. Disruption of the microbial community can lead to an imbalance in homeostasis of the immune cells including Th17, T regulatory, and innate lymphoid cells, which can influence susceptibility of the host to a variety of health disorders including rheumatoid arthritis, obesity, inflammatory bowel disease, Crohn's disease, diabetes, and ulcerative colitis, among others. As the number of microbiome studies grow, it is becoming increasingly clear that the host and microbiota do not operate alone. To understand the complete story, the interaction between the host and bacterial systems needs to be considered through a more holistic, systematic approach. This webinar will discuss just such an approach, examining the problem from the perspective of both the host and microbiome.

Speakers

Oleg Paliy, Ph.D.
Wright State University
Dayton, OH

Yasmine Belkaid, Ph.D.
National Institutes of Health
Bethesda, MD

Webinar sponsored by

affymetrix
Biology for a better world

Brought to you by the *Science*/AAAS Custom Publishing Office

Science
AAAS

@SciMagWebinars

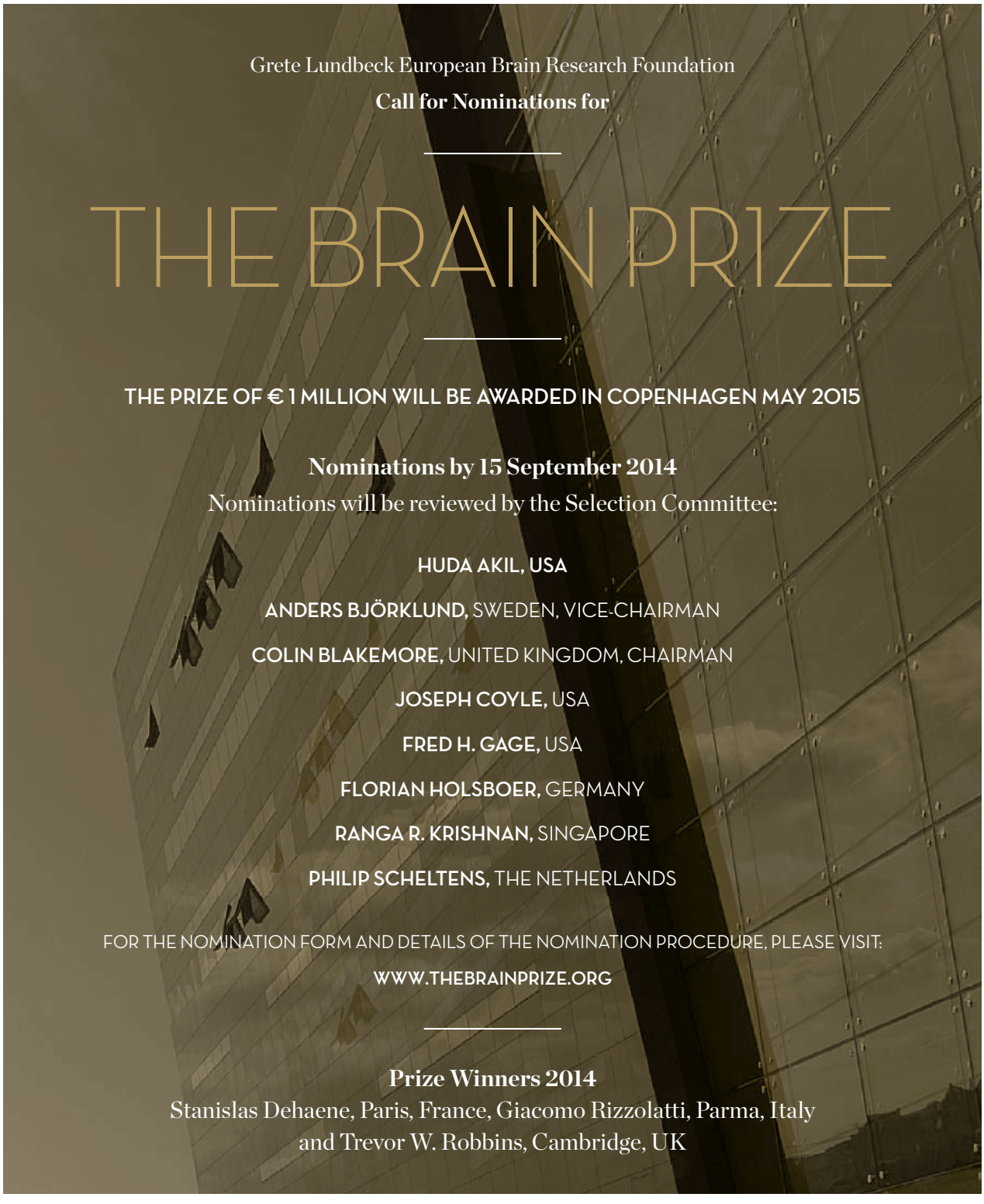

Grete Lundbeck European Brain Research Foundation

Call for Nominations for

THE BRAIN PRIZE

THE PRIZE OF € 1 MILLION WILL BE AWARDED IN COPENHAGEN MAY 2015

Nominations by 15 September 2014

Nominations will be reviewed by the Selection Committee:

HUDA AKIL, USA

ANDERS BJÖRKLUND, SWEDEN, VICE-CHAIRMAN

COLIN BLAKEMORE, UNITED KINGDOM, CHAIRMAN

JOSEPH COYLE, USA

FRED H. GAGE, USA

FLORIAN HOLSBOER, GERMANY

RANGA R. KRISHNAN, SINGAPORE

PHILIP SCHELTENS, THE NETHERLANDS

FOR THE NOMINATION FORM AND DETAILS OF THE NOMINATION PROCEDURE, PLEASE VISIT:

WWW.THEBRAINPRIZE.ORG

Prize Winners 2014

Stanislas Dehaene, Paris, France, Giacomo Rizzolatti, Parma, Italy
and Trevor W. Robbins, Cambridge, UK

GRETE LUNDBECK EUROPEAN BRAIN RESEARCH FOUNDATION

THE BRAIN PRIZE

The Brain Prize recognizes and rewards outstanding contributions to European neuroscience, from basic to clinical

immunogenomics 2014

September 29 - October 1, 2014

HudsonAlpha Biotechnology Campus
Huntsville, Alabama, USA

Join us at the intersection of Immunology and Genomics!

Keynote Speakers

Christophe Benoist, Harvard Medical School
Mary Ellen Conley, University of Tennessee, College of Medicine, Memphis
Mark Davis, Howard Hughes Medical Institute; Stanford University School of Medicine

Session Chairs

Lou Bridges, University of Alabama at Birmingham, AL, USA • **Jean-Laurent Casanova**, Howard Hughes Medical Institute, Rockefeller • **Alain Fischer**, Imagine Institute, Necker Hospital, Paris, France • **Dan Littman**, New York University, NY, USA • **Sara Marsal**, University of Barcelona, Spain • **Kristen Mueller**, *Science* • **Harlan Robins**, University of Washington/Fred Hutchinson Cancer Research Center

Session Speakers

Scott Boyd, Stanford University School of Medicine, CA • **Zhijian James Chen**, UT Southwestern, TX • **Yanick Crow**, University of Manchester, UK • **Malek Faham**, Sequenta, CA • **Wendy Garrett**, Harvard University School of Public Health, MA • **Peter Gregersen**, Feinstein Institute for Medical Research, NY • **Jian Han**, HudsonAlpha Institute for Biotechnology, AL • **Lionel Ivashkiv**, Hospital for Special Surgery, NY • **Thirumala-Devi Kanneganti**, St. Jude Children's Research Hosp. • **Julian Knight**, Merton College , University of Oxford, UK • **Mike Lenardo**, National Institutes of Health, Washington D.C. • **Xochitl Morgan**, Harvard University School of Public Health, MA • **Barbara Methe**, J. Craig Venter Institute, MD • **Kees Murre**, University of California, San Diego, CA • **Richard M. Myers**, HudsonAlpha Institute for Biotechnology, AL • **Soumya Raychaudhuri**, Broad Institute, MA • **Lars Steinmetz**, European Molecular Biology Laboratory, Germany • **Barbara Stranger**, University of Chicago, IL USA

Platinum Sponsors

BAY CITY CAPITAL

iRepertoire, Inc.

Gold Sponsors

UAB COMPREHENSIVE ARTHRITIS, MUSCULOSKELETAL, AND AUTOIMMUNITY CENTER

Silver Sponsors

Genapsys

illumina®

Bronze Sponsors

SEQUENTA

follow @immunogenomics on twitter

Register today at immunogenomics.com

presented by

HUDSONALPHA INSTITUTE FOR BIOTECHNOLOGY

Science AAAS

Microarray Screening Device

The b-screen label-free microarray screening device is an analysis tool for microarrays in the standard microscope format allowing the detailed studies of biomolecular interactions. Kinetic data can be obtained for almost any kind of biomolecular interaction such as for protein/protein, peptide/protein, and small molecules/protein. b-screen provides a label-free readout of up to 10,000 spots per square centimeter. It utilizes a precise and automated microfluidics system for incubation of the microarray with the sample of interest. The device can be used with multiple array layouts (highly scalable), uses glass or plastic type substrates, and is compatible with almost any common microarray printer. The high throughput analysis is characterized by a high time resolution (no scanning) at low noise of the optical readout. No fluorescence labels are needed, which leads to assay conditions as close as possible to the in vivo situation combined with minimal sample pretreatment and minimized reagent consumption.

Biametrics
For info: +49-7071-2973048
www.biametrics.com

Mass Spectrometer Control Module

A new control module for the expression compact mass spectrometers (CMS) includes both digital control of the detector and digital data acquisition of the detector signal. It also allows performing all service operation necessary for the detector from the Device Monitor software window. Clarity Chromatography Software provides seamless integration of expression CMS with a wide range of high-performance liquid chromatography (HPLC) systems that are already controlled by Clarity. Clarity MS Extension greatly extends Clarity capabilities. Clarity is able to evaluate spectral data from MS detectors together with data from conventional HPLC detectors (including quantification) and add the third dimension for data analysis. Clarity Chromatography software can provide interactive spectral analysis, peak purity analysis and compound identification that is based on a spectral library search. The extension is prepared to function with single quadrupole mass spectrometer (MS) and time-of-flight MS detectors. Clarity is highly regarded for its intuitive approach, excellent performance, cost-effectiveness and proficient technical support.

DataApex
For info: +420-251-013-400
www.dataapex.com

Biochemistry Analyzers

The YSI brand 2900 Series Biochemistry Analyzers constitute an essential part of many stages of bioprocessing and life sciences applications due to their ability to accurately and rapidly monitor and control fermentations and cell cultures. YSI biochemistry analyzers offer both offline and online analysis of critical samples for companies that manufacture vaccines, small molecules, alcoholic beverages, chemicals, and biofuels. The YSI 2900 Series includes the 2900, the 2950, and the recently launched 2900M biochemistry analyzers. YSI biochemistry analyzers are able to measure, monitor, and control processes accurately, easily, and quickly (under one minute) due to their innovative biosensor technology. To obtain high product yields in biotech or pharmaceutical applications, the metabolism and health of the cell cultures have to be assessed regularly. And there's a crucial need to monitor key nutrients and byproducts levels, and to adjust feed rates on the bioreactor accordingly. The YSI 2900 Series biochemistry analyzers offer accurate, rapid, and reproducible methods to measure and monitor the process.

Xylem Analytics
For info: 978-778-1010
www.xylemanalytics.com

Metabolic Microplate Assay

The XF^{e}96 Spheroid Microplate is a unique 96-well plate featuring geometry that enables functional, metabolic measurements of individual spheroids for the study of three-dimensional cell culture, which more closely mimics in vivo conditions. Of particular importance for tumor studies, the real-time metabolism of multicellular spheroids can now be analyzed and used for evaluating the metabolic response to therapeutic agents. Using the XF^{e}96 Spheroid Microplate and the XF^{e}96 Extracellular Flux Analyzer, scientists can obtain sensitive and reproducible data from individual spheroids with high specificity. The XF^{e}96 Extracellular Flux Analyzer simultaneously measures the two major energy-producing pathways within the cell—mitochondrial respiration and glycolysis—in a microplate, in real time. The XF^{e}96 Analyzer and Stress Test Kits standardize the measurement of mitochondrial function and glycolysis. The addition of the XF^{e}96 Spheroid Microplate further advances the study of cell metabolism. The XF^{e}96 Spheroid FluxPak contains six cartridges, six microplates, and calibrant.

Seahorse Bioscience
For info: 978-671-1600
www.seahorsebio.com

Cell Sorting and Sub-Micron Particle Detection

The MoFlo Astrios EQ is a six-way jet-in-air sorter, which delivers patent pending enhanced dual forward scatter (eFSC) technology for simultaneous sorting and detection of particles from 200 nm to 30 µm in diameter. The instrument sets a new standard for flow cytometry core facilities, delivering high-speed cell sorting and microparticle detection in a single package. Featuring detailed and precise forward scatter resolution, beadless drop sample handling and increased biosafety, Astrios EQ meets a range of analysis needs. Intellisort II, the world's first and only beadless drop-delay technology, eliminates the need for bead-based drop-delay routines. This alleviates the requirement to remove sterile samples during drop-delay recalculation due to nozzle blockages and ensures uninterrupted sort sterility. Intellisort II's ability to maintain droplet breakoff for uninterrupted aseptic sorting helps to preserve sort integrity. A broad standard laser palette provides more wavelength choices than is found in most standard cuvette-based systems.

Beckman Coulter Life Sciences
For info: 800-526-3821
www.astrioseq.com

Electronically submit your new product description or product literature information! Go to www.sciencemag.org/products/newproducts.dtl for more information.

Newly offered instrumentation, apparatus, and laboratory materials of interest to researchers in all disciplines in academic, industrial, and governmental organizations are featured in this space. Emphasis is given to purpose, chief characteristics, and availability of products and materials. Endorsement by *Science* or AAAS of any products or materials mentioned is not implied. Additional information may be obtained from the manufacturer or supplier.

Science Signaling

The Leading Journal for Cell Signaling

Publishing key findings of broad relevance in the multidisciplinary field of cell signaling

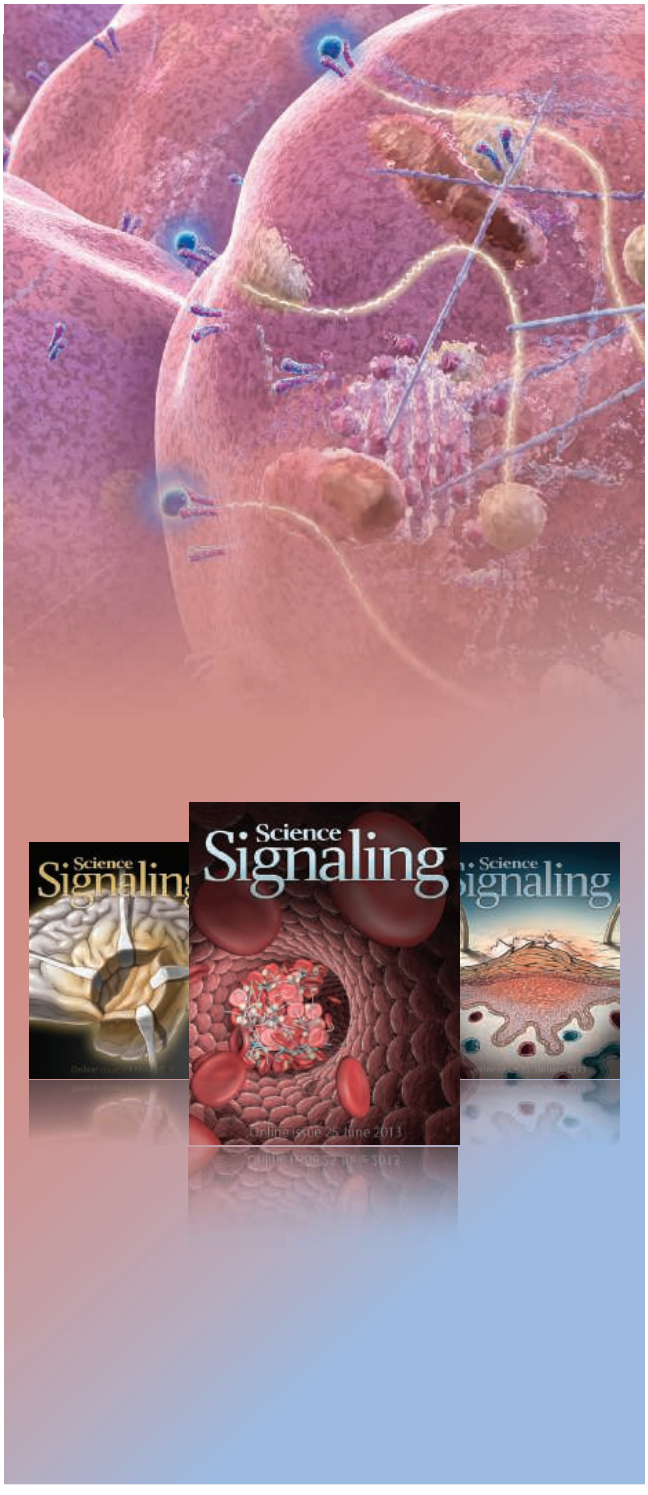

Submit your research

ScienceSignaling.org

Recommend to your library

ScienceOnline.org/recommend

Join the ranks of high-profile papers published in *Science Signaling*:

Cancer Biology

Vemurafenib Potently Induces Endoplasmic Reticulum Stress–Mediated Apoptosis in BRAFV600E Melanoma Cells

D. Beck *et al.* (F. Meier), *Sci. Signal.* **6**, ra7 (2013)

Neuroscience

Requirement for Nuclear Calcium Signaling in *Drosophila* Long-Term Memory

J.-M. Weislogel *et al.* (H. Bading), *Sci. Signal.* **6**, ra33 (2013)

Cell and Molecular Biology

A Nontranscriptional Role for HIF-1α as a Direct Inhibitor of DNA Replication

M. E. Hubbi *et al.* (G. L. Semenza), *Sci. Signal.* **6**, ra10 (2013)

Immunology

Monovalent and Multivalent Ligation of the B Cell Receptor Exhibit Differential Dependence upon Syk and Src Family Kinases

S. Mukherjee *et al.* (A. Weiss), *Sci. Signal.* **6**, ra1 (2013)

Computational and Systems Biology

Cross-Species Protein Interactome Mapping Reveals Species-Specific Wiring of Stress Response Pathways

J. Das *et al.* (H. Yu), *Sci. Signal.* **6**, ra38 (2013)

Chief Scientific Editor

Michael B. Yaffe, M.D., Ph.D.
Massachusetts Institute of Technology

Editor

Nancy R. Gough, Ph.D.
AAAS, Washington, DC

Science Signaling
AAAS

sciencesignalingeditors@aaas.org

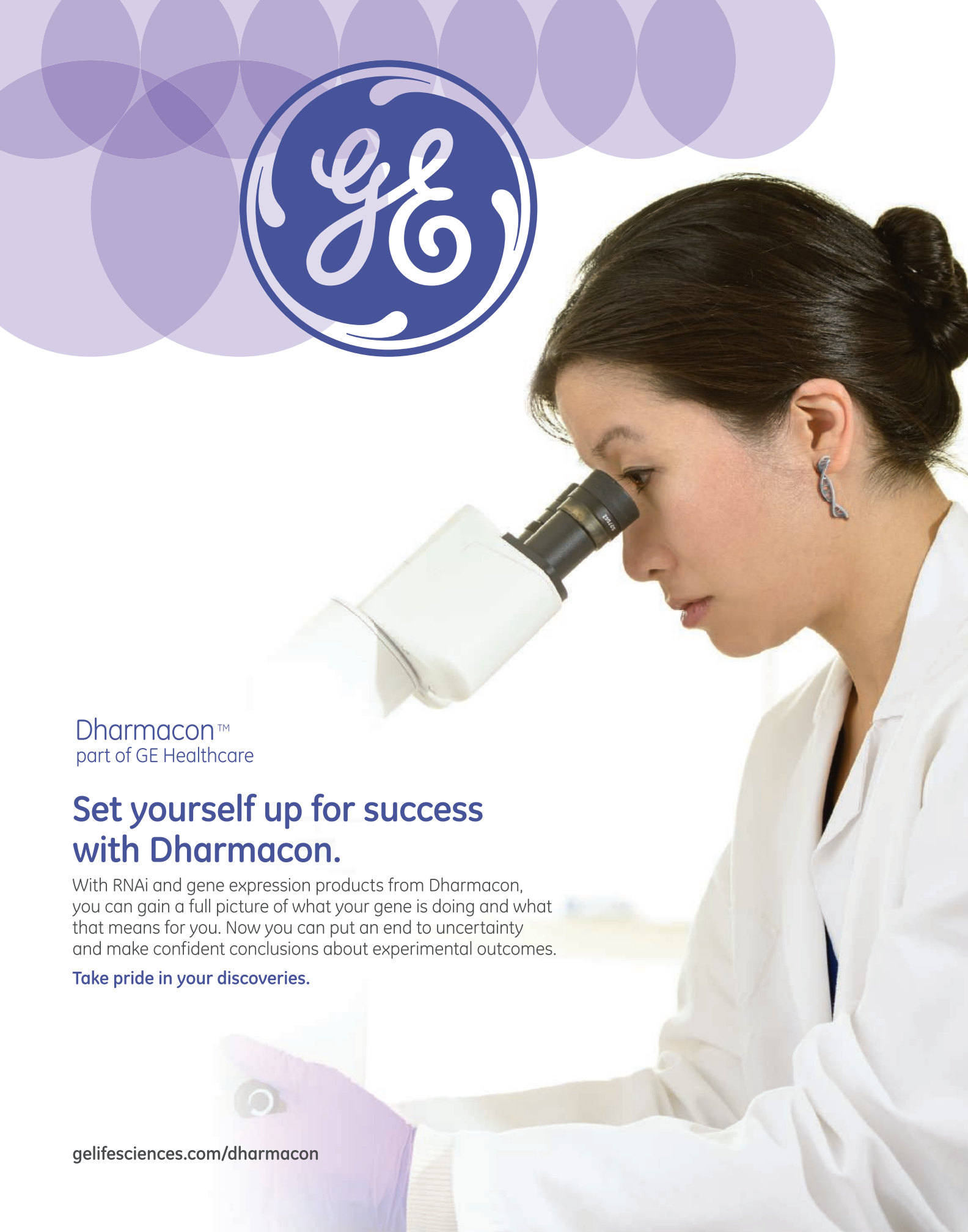

Dharmacon™
part of GE Healthcare

Set yourself up for success with Dharmacon.

With RNAi and gene expression products from Dharmacon, you can gain a full picture of what your gene is doing and what that means for you. Now you can put an end to uncertainty and make confident conclusions about experimental outcomes.

Take pride in your discoveries.

gelifesciences.com/dharmacon

Science Careers Advertising

For full advertising details, go to ScienceCareers.org and click For Employers, or call one of our representatives.

Tracy Holmes
Worldwide Associate Director
Science Careers
Phone: +44 (0) 1223 326525

THE AMERICAS

E-mail: advertise@sciencecareers.org
Fax: 202 289 6742

Tina Burks
Phone: 202 326 6577

Nancy Toema
Phone: 202 326 6578

Marci Gallun
Sales Administrator
Phone: 202 326 6582

Online Job Posting Questions
Phone: 202 312 6375

EUROPE / INDIA / AUSTRALIA / NEW ZEALAND / REST OF WORLD

E-mail: ads@science-int.co.uk
Fax: +44 (0) 1223 326532

Axel Gesatzki
Phone: +44 (0) 1223 326529

Sarah Lelarge
Phone: +44 (0) 1223 326527

Kelly Grace
Phone: +44 (0) 1223 326528

JAPAN

Katsuyoshi Fukamizu (Tokyo)
E-mail: kfukamizu@aaas.org
Phone: +81 3 3219 5777

Hiroyuki Mashiki (Kyoto)
E-mail: hmashiki@aaas.org
Phone: +81 75 823 1109

CHINA / KOREA / SINGAPORE / TAIWAN / THAILAND

Ruolei Wu
Phone: +86 186 0082 9345
E-mail: rwu@aaas.org

All ads submitted for publication must comply with applicable U.S. and non-U.S. laws. *Science* reserves the right to refuse any advertisement at its sole discretion for any reason, including without limitation for offensive language or inappropriate content, and all advertising is subject to publisher approval. *Science* encourages our readers to alert us to any ads that they feel may be discriminatory or offensive.

Science Careers
From the journal *Science* AAAS

ScienceCareers.org

UNIVERSITÄT HEIDELBERG
ZUKUNFT SEIT 1386

The Department of Physics and Astronomy at Heidelberg University invites applications for a

FULL PROFESSORSHIP (W3) IN EXPERIMENTAL PHYSICS (ENVIRONMENTAL PHYSICS)

The position will be hosted at the Institute for Environmental Physics.

Candidates are expected to conduct atmospheric research and should have an internationally recognized track record in the field of environmental studies of the atmosphere. Possible subject areas include the physical basis of climate dynamics, remote sensing of the atmosphere or the study of trace gases, but are not limited to those topics.

Requirements for an application include a degree and doctorate in physics and/or closely related fields as well as a research and training track record similar to the requirements needed for a habilitation in physics, or the successful accomplishment and evaluation of a junior professorship position or similar qualification.

The successful candidate is expected to participate in the bachelor and master lecture and teaching programs of the Department of Physics and Astronomy in accordance with the usual University obligations.

Heidelberg University seeks to increase the percentage of female researchers in domains where women are underrepresented; hence qualified female researchers are particularly encouraged to apply. Preference will be given to disabled applicants with equal qualifications for the position.

Applications must be addressed to the Dean of the Department of Physics and Astronomy (Address: Im Neuenheimer Feld 226, 69120 Heidelberg, Germany, or electronically to dekanat@physik.uni-heidelberg.de) including a curriculum vitae, a list of publications and lectures, copies of diploma and degrees and a maximum 5 page long exposé on future research and training activities. The deadline for applications is the **15th October 2014.**

LEHIGH UNIVERSITY

Presidential Endowed Chair in Health and Biomedicine

Lehigh University invites applications and nominations for a **Presidential Endowed Chair in Health and Biomedicine**. Applicants must hold a Ph.D. or M.D. degree and should be qualified for an appointment in the Department of Biological Sciences at the rank of Full Professor with tenure. The successful candidate will have a distinguished record in biomedical research, including significant external support, demonstrated leadership skills, and a strong commitment to graduate and undergraduate training and education. The position carries an expectation of scholarly and administrative leadership. As part of these responsibilities, the successful applicant will be expected to assume the Department Chair's position two years following the appointment. The Department Chair's position is a 3-year term that can be renewed. The Department is highly interdisciplinary and welcomes applicants with research interests from any area of bioscience, broadly defined. A strong interest in building collaborations among bioscience-related fields is expected.

Lehigh's Biological Sciences Department includes 21 faculty with additional growth anticipated. Current faculty research interests span molecular, cellular, and developmental biology, neuroscience, evolution, and animal behavior. The department has Ph.D. programs in Integrative Biology, Neuroscience, Biochemistry and Cell/Molecular Biology, a Distance Education M.S. program in Molecular Biology, and is home to the largest undergraduate major constituency in the College of Arts and Sciences.

Applications, including a C.V., letter of intent, description of administrative experience and philosophy, and the names of three potential references should be submitted to **https://academicjobsonline.org/ajo/jobs/4159**. For additional information contact **Dr. Neal Simon, Search Committee Chair, Biological Sciences, 111 Research Dr., Bethlehem, PA 18015; inbios@lehigh.edu**. For more information about the department: **www.lehigh.edu/~inbios**. The deadline for submission is **October 10, 2014**.

The College of Arts and Sciences at Lehigh is especially interested in qualified candidates who can contribute, through their research, teaching, and/or service, to the diversity and excellence of the academic community. Lehigh University is a recipient of an NSF ADVANCE Institutional Transformation award for promoting the careers of women in academic sciences and engineering.

Lehigh University is an Equal Opportunity Affirmative Action Employer.
The University provides comprehensive benefits including partner benefits.
(http://www.lehigh.edu/~inprv/work_life_balance.html)

Dartmouth

Faculty Position in Quantitative/Computational Cellular and Molecular Biology

The Department of Biological Sciences at **Dartmouth** seeks applicants for a tenure-track Assistant Professorship in the area of **Quantitative/Computational Cellular and Molecular Biology**. We seek candidates who combine experimental with quantitative, computational, and /or modeling approaches to address foundational questions in cell and molecular biology. Areas of research interest include but are not limited to cell biology, biochemistry, microbiology, biophysics, and neuroscience. The successful candidate will be expected to direct an independent research program that will attract extramural funding, provide research training for graduate and undergraduate students, and teach at the undergraduate and graduate levels. This is a period of expansion and investment in interdisciplinary computational science at Dartmouth. The candidate will join a vibrant community of quantitative scientists including faculty in the departments of Biochemistry, Genetics, Microbiology and Immunology as well as the Institute for Quantitative Biomedical Science and the Neukom Institute for computational science. The department is affiliated with the Molecular and Cellular Biology graduate program and has strong collaborations with the Geisel School of Medicine at Dartmouth. Application materials should include a cover letter, curriculum vitae, five representative publications, statements of research and teaching interests, and at least three confidential letters of reference. Please upload application materials electronically to: **https://apply.interfolio.com/25563**.

Application review will begin on **October 1, 2014** and continue until the position is filled. For further information about the department and graduate programs, see **http://biology.dartmouth.edu** as well as **http://www.dartmouth.edu/~mcb/**

One of the most diverse institutions of higher education in New England, Dartmouth is an equal opportunity/ affirmative action employer with a strong commitment to diversity. In that spirit, we are particularly interested in receiving applications from a broad spectrum of people, including women, persons of color, persons with disabilities, veterans or any other legally protected group.

AAAS is here –
helping scientists achieve career sucess.

Every month, over 400,000 students and scientists visit ScienceCareers.org in search of the information, advice, and opportunities they need to take the next step in their careers.

A complete career resource, free to the public, *Science* Careers offers hundreds of career development articles, webinars and downloadable booklets filled with practical advice, a community forum providing answers to career questions, and thousands of job listings in academia, government, and industry. As a AAAS member, your dues help AAAS make this service available to the scientific community. If you're not a member, join us. Together we can make a difference.

To learn more, visit
aaas.org/plusyou/sciencecareers

AAAS + U = Δ

UNIVERSITY OF CAMBRIDGE

www.jobs.cam.ac.uk

Two Tenure-Track Faculty Positions University Lecturer

Department of Physiology, Development and Neuroscience
Salary: £38,511-£48,743

Applications are invited for two research-oriented, tenure-track University Lectureships. The posts are available from 1 April 2015 or as soon as possible thereafter. We are searching for outstanding scientists, with excellent publication records, undertaking cutting edge and fundable work in fields which complement our broad, existing programme of research in the Department of Physiology, Development and Neuroscience (http://www.pdn.cam.ac.uk/research/). Applicants should also have an aptitude and enthusiasm for teaching and be willing to contribute effectively to our undergraduate programme (http://www.pdn.cam.ac.uk/teaching).

Appointment will be for a probationary period of five years with appointment to the retiring age thereafter, subject to satisfactory performance.

The pensionable salary scale starts at £38,511 to £48,743 per annum.

Further particulars are available from http://www.pdn.cam.ac.uk/jobs Applications, including a curriculum vitae and a completed CHRIS/6 form (Parts 1 and 3 only, available at http://www.admin.cam.ac.uk/offices/hr/forms/chris6) should be emailed to hodsec@pdn.cam.ac.uk

Informal enquiries may be made to Professor Bill Harris, Head of Department wah20@cam.ac.uk; 01223 766137/333772.

Closing Date: 10 October 2014

Please quote reference PM03960 on your application and in any correspondence about this vacancy.

The University values diversity and is committed to equality of opportunity.

The University has a responsibility to ensure that all employees are eligible to live and work in the UK.

OPEN FACULTY POSITIONS INSTITUTE OF MOLECULAR BIOLOGY ACADEMIA SINICA, TAIWAN, ROC

One tenure-track faculty position is open for a highly qualified individual to establish independent research programs in **all disciplines of molecular and cellular biology**. Applicants should hold a Ph.D. degree or its equivalent, with appropriate postdoctoral research experience. The successful recruit will be appointed at the levels of **Assistant, Associate,** or **Full Research Fellows** (equivalent to academic ranks of Assistant, Associate and Full Professors at universities), and receive a generous multi-year start-up package, followed by annual intramural support.

The Institute of Molecular Biology at Academia Sinica (**http://www.imb.sinica.edu.tw/en**) provides an active and stimulating research environment, is well supported by both extramural and long-term intramural funding, and features several core facilities (imaging, microarray, Next Generation Sequencing, RNAi, electrophysiology, FACS, bioinformatics and mouse facilities) that provide state-of-the-art resources and key technical expertise to the Institute's research community. Recent research works were published in top journals such as Science, Nature, and Cell. Currently three Ph.D. programs, with one recruiting international students, are formally affiliated with the Institute. English is the official language for regular seminars and most of the lectures at the Institute, and proficiency in Chinese language is not a prerequisite for application.

Applicants should send their Curriculum Vitae, a description of past research accomplishments and future research plans, and arrange for three letters of recommendation to be sent directly to:

Dr. Soo-Chen Cheng, Director
c/o Ms. Vivi Chiang
Institute of Molecular Biology, Academia Sinica
Taipei, Taiwan 11529, ROC

The selection process will start on **December 15, 2014** until the positions are filled. Further information can be obtained from **Ms. Vivi Chiang at vivi@imb.sinica.edu.tw**

Queensland University of Technology
BRISBANE AUSTRALIA

Outstanding opportunities for tomorrow's research and academic leaders

Fast track your academic career

Join our highly regarded **Early Career Academic Recruitment and Development Program** which has already put more than 325 early-career academics on the path to success.

Eight ongoing (tenure-track) positions are available at Level B in the following disciplines:

- Biomedical Engineering and Medical Physics
- Business Process Management
- Information Ecology
- Vision and Signal Processing
- Power Engineering
- Earth Sciences
- Environmental Systems

Build a research career with impact

QUT is offering up to **15 Vice-Chancellor's Research Fellowships** for leading postdoctoral researchers at Levels B and C on a three-year, fixed-term basis. These prestigious fellowships are available in the following target areas:

- Digital Media • Machine Learning
- Robotics and Computer Vision
- Biofabrication and Biomaterials
- Plant Biotechnology
- Environmental Health / Air Quality
- Children and Youth Intervention
- Intellectual Property
- Healthy Ageing • Systems Biology
- Health Economics • Business Innovation

More information visit www.qut.edu.au/jobs Applications close on 16 September 2014.

CRICOS No. 00213J QUT-14-256

fnrs
FREEDOM TO RESEARCH

"GAGNA A. & CH. VAN HECK PRIZE - 2015"

Application field:

The "Fonds de la Recherche Scientifique – FNRS" will grant, in 2015, the "Gagna A. & Ch. Van Heck Prize" to a scientist or a medical doctor, in recognition of a research work which has contributed to the treatment of a disease currently incurable, or which has raised hopes for curing a disease.

Amount:

The Prize amounts to **75.000 €.**

Nominations:

This triennial and international Prize is intended to reward a work done by one or max. two researcher(s).

Application files must be submitted electronically to **prix@frs-fnrs.be** no later than **October 1st, 2014**.

The personality proposing the nomination must provide:

- A memorandum of 5 to 10 pages (written in English) on the candidates merits,
- The CV of the candidate(s), including a list of received Prizes,
- The complete list of publications of the candidate(s).

Regulations:

The complete regulations are available online at the address **www.frs-fnrs.be** (section « Mécénat & Prix ») or can be obtained on demand at **prix@frs-fnrs.be**

UCLA

Plant Ecologist, Evolutionary Biologist or Systematist

The University of California, Los Angeles (UCLA) Department of Ecology and Evolutionary Biology seeks to fill an open-rank (tenure track or tenured) faculty position in Plant Sciences. Qualified candidates will have a Ph.D. in a related field of biological sciences. We are interested in all subfields within organismal plant biology but especially in candidates with experimental or comparative approaches in plant evolution, systematics, ecology, conservation biology, and/or biogeography. The successful candidate is expected to establish an internationally recognized and externally funded research program. Although not required, we encourage applicants with interest in the Mildred E. Mathias Botanical Garden, a seven-acre garden on the UCLA campus, through teaching, research, and/or public outreach/education to indicate so in their cover letter. As a campus with a diverse student body, individuals with a history of mentoring under-represented minorities in the sciences are encouraged to apply and include details in cover letter. Applicants should submit materials online to **https://recruit.apo.ucla.edu/apply/JPF00342** including detailed cover letter; curriculum vitae; statements of research and teaching; and names and contact information of four references. Review of candidates will begin on **October 3, 2014** and continue until the position is filled. Please use job number **JPF00342** in all correspondence.

Additional information about the Department and the Botanical Garden and may be found at http://www.eeb.ucla.edu and http://www.botgard.ucla.edu/ respectively. Inquiries regarding the position should be directed to **Grace Angus** (**gracea@lifesci.ucla.edu**) or **Search Chair, Professor Lawren Sack** (**lawrensack@ucla.edu**). Women and minority applicants are encouraged to apply.

The University of California is an Equal Opportunity/Affirmative Action Employer. All qualified applicants will receive consideration for employment without regard to race, color, religion, sex, national origin, disability, age or protected veteran status. For the complete University of California nondiscrimination and affirmative action policy see: UC Nondiscrimination & Affirmative Action Policy

CIC nanoGUNE

Nanotechnology-applications Group Leader

The nanoscience Cooperative Research Center CIC nanoGUNE invites applications and nominations for the position of Group Leader to lead a nanotechnology-applications laboratory.

NanoGUNE (**www.nanogune.eu**), located in San Sebastian, Basque Country (Spain), is a R&D center that has the mission of conducting basic and applied world-class research in nanoscience and nanotechnology, fostering training and education excellence, and supporting the growth of a nanotechnology-based industry.

We look for a high-caliber researcher with substantial experience and a strong track record of world-class research on subjects of direct industrial relevance and verifiable industry/product impact. The candidate should have extensive experience of work in an industrial environment, preferably in (or with) the Basque industry. His/her research activity should be developed in the framework of research projects that are designed for or initiated by industrial collaborators and, consequently, sponsored by these industrial partners. Relevant research fields include areas of nanotechnology with an impact in advanced manufacturing, energy applications, and/or biosciences. A substantial thematic overlap with at least some of nanoGUNE's already existing research groups is expected and desired.

Candidates should have an outstanding track record of applied research and technological achievements. Proficiency in spoken and written English is compulsory.

Applicants should forward their CV, a summary of research interests, and a list of at least three references to **director@nanogune.eu**.

Closing date: 30 September 2014

www.nanogune.eu
CIC nanoGUNE
Tolosa Hiribidea, 76
E-20018 Donostia, Spain
+34 943 574 000 nano@nanogune.eu

MICHIGAN STATE UNIVERSITY

Computational Genomics Faculty Positions

Michigan State University invites applications for tenure track faculty positions at the Assistant, Associate or Full Professor level focused on computational and data analysis issues related to genomics, genetics and personalized medicine. This cluster of positions will be associated with a new Quantitative Health Science and Engineering Institute, and departments across the Colleges of Engineering, Human Medicine and Natural Science. This program will focus on the development of computational tools necessary for large-scale application of genomics. We are particularly interested in scalable pipelines for processing and analyzing genomic data related to disease and wellbeing.

Applications are invited in areas such as computational and statistical genomics, bioinformatics, epidemiology and cancer genomics. This search seeks to build significant research expertise in these areas and will be followed by additional hires over multiple years. The candidate should have a Ph.D. with strong evidence of research accomplishments, teaching skills, and an ability to work effectively with other researchers and campus programs. Candidates are expected to develop a research program of international visibility.

Applications for this position should be submitted through: **https://jobs.msu.edu/** (Faculty/Academic Staff, posting **9832**). Review of applications will begin October 1, 2014 and will continue until the positions are filled. Questions can be directed to **Dr. Doug Gage** (**gage@msu.edu**).

MSU is an Affirmative Action, Equal Opportunity Employer, and is committed to achieving excellence through a diverse workforce. The university actively encourages applications and/or nominations of women, persons of color, veterans and persons with disabilities.

ASSISTANT/ASSOCIATE PROFESSOR

Department of Molecular Medicine - College of Medicine

We are seeking candidates for a tenure-track position at the rank of Assistant or Associate Professor, who study the molecular basis of metabolic disorders such as obesity, metabolic syndrome, and type II diabetes, which complement existing strengths in the Department and College. The Department of Molecular Medicine is located on the energetic and expanding USF Health campus that includes the Colleges of Medicine, Nursing, Pharmacy, and Public Health, the H. Lee Moffitt NCI-designated Comprehensive Cancer Center and the Byrd Alzheimer's Institute. USF is ranked 34rd in total research expenditures and 27th in federal research expenditures for public universities by the National Science Foundation for 2013 with extramural grants and contract activity in excess of $412 million annually. Integration with clinical providers is through the Bariatric Center (**https://www.tgh.org/weight.htm**), a joint partnership by USF and Tampa General Hospital; the center follows more than 3,500 patients who underwent bariatric surgery using a patient-centered, hypothesis-driven, evidence-based interdisciplinary approach. Research opportunities include access to longitudinal outcomes data, a tissue repository and small animal models of obesity and bariatric surgery.

Successful candidates for this position are expected to develop and maintain a competitively funded research program, participate in interdisciplinary research addressing metabolic disease, and educate medical and graduate students. The Department offers institutional salary support commensurate with experience, competitive start-up packages, dry and wet laboratory space, excellent core facilities, and a collegial atmosphere to create an environment that promotes success. Minimum requirements for an Assistant Professor position include a MD, PhD, or MD/PhD with at least two years postdoctoral experience and current grant funding support. Appointment at the Associate Professor level requires a minimum of five years experience as an Assistant Professor or equivalent, a nationally-recognized and federally funded research program and experience mentoring graduate students.

All applications must be submitted on line by going to: USF Careers (**http://www.usf.edu/about-usf/work-at-usf.aspx**) and uploading a PDF that includes a cover letter, curriculum vitae, research plan, and statement of teaching philosophy. Separately, request three letters of reference to be sent by mail or e-mail to Dana Pettaway at **dpettawa@health.usf.edu**. Review of applicants will begin immediately and will continue until the position is filled. **Chair Search Committee, Department of Molecular Medicine, University of South Florida-Health, 12901 Bruce B. Downs Blvd. MDC7, Tampa, Florida 33612-4799, http://health.usf.edu/nocms/research/molecular_medicine/**

The University of South Florida is an Equal Opportunity / Affirmative Action / Equal Access Institution.

For disability accommodations, contact Dana Pettaway at (813) 974-8320- a minimum of 5 working days in advance. According to Florida law, search records, including applications and search committee meetings, are open to the public.

USF HEALTH MORSANI COLLEGE OF MEDICINE UNIVERSITY OF SOUTH FLORIDA

• Tampa • St. Petersburg • Sarasota - Manatee

Open Senior Faculty Positions
Beijing Institute of Technology

Beijing Institute of Technology (BIT) is a prestigious national key university in China and enjoys a high reputation in research and education in science, technology and other areas of scholarship. The institute was founded in 1940, which is one of the first Chinese universities to run a graduate school, and one of the national "Project 211" and "Project 985" universities which are given priority for development by the Chinese government.
The University is currently in the midst of an ambitious recruitment plan that will expand our faculty numbers at high ranks and make significant investments in areas of research initiatives. We warmly welcome you to join the ranks of the renowned scholars and researchers who work hard to make BIT a world class engineering and technology university.

I. Major open faculty positions

Equipment Science • • Technology Engineering	Mechanical Engineering	Optical Engineering	Information and Communication Engineering
Mechanics	Control Science and Engineering	Materials Science and Engineering	Management Science and Engineering
Chemical Engineering and Technology	Power Engineering and Engineering Thermo Physics	Electronic Science and Technology	Computer Science and Technology
Software Engineering	Biomedical Engineering	Aeronautic and Astronautic Science and Technology	Mathematics
Physics	Chemistry		

II. Talent programs

The University is especially interested in candidates who can contribute, through their research, teaching, and/or service, to the diversity and excellence of the academic community, and is actively seeking to hire outstanding faculty members according to the following recruitment programs: the Recruitment Program of Global Experts (Its subprograms include Long-term Program for Innovative Talents, Short-term Program for Innovative Talents, Young Scholars Program, Global Experts Program, and Top Talents and Innovation Team Program.)supported by the Chinese government, the Chang Jiang Scholars Program, the Program supported by the China National Science Foundation for Distinguished Young Scholars, the Program supported by the China National Foundation for Excellent Young Scholars, the New Century Excellent Talents in University Program supported by the Ministry of Education (MOE), and the recruitment programs supported by the University.

III. Pay and benefits

Those who are interested to work in BIT (Upon being recruited by the above national recruitment programs) will receive from the University a competitive pay and benefits package including start-up research funds and work assistants in addition to the pay and benefits offered by the Chinese government.
For application requirements and specifics of pay and benefits, please visit http://renshichu.bit.edu.cn/ .

IV. Contact us

Applicants should send a curriculum vitae, 2-3 publications in full, and certificates including a degree certificate, employment documents, and certificates of research funds, grants and awards via email to: sscsr@bit.edu.cn, or shizike@bit.edu.cn.
Contacts: Mr. Shi Rui, Mr. He Xiaowei
Tel.: +8610-68918577/68912338
Add.: Human Resources Department, Beijing Institute of Technology, 5 South Zhongguancun Street, Haidian District, Beijing, China
Postcode:100081

For more faculty positions, please visit our website http://renshichu.bit.edu.cn/ .

大连理工大学
DALIAN UNIVERSITY OF TECHNOLOGY

Faculty Positions in DUT

Dalian University of Technology (DUT) is located in the beautiful coastal city of Dalian, in northeastern China's Liaoning Province. It is a national key university of the "211" and "985" project directly under the Ministry of Education.
DUT is seeking to recruit excellent expert, scholars (i.e. The Recruitment Program of Global Experts, The Plan for Recruiting 1,000 Professorship for Young Talent, Changjiang Scholar Distinguished Professors and Changjiang Scholar Guest Professors) and faculties from both home and abroad. Qualified applicants of professors, associate professors and lecturers are required to be under the age of 45,40,35 separately, and have obtained a PhD degree in a nation(world)-renowned university or academy of Chinese Academy of Sciences. DUT will provide a good academic environment, competitive salaries at international levels. Potential candidates are encouraged to send your application latter enclosing a current CV to Jiailing or ZhangYan(zhaopin@dlut.edu.cn), indicating in the email subject with "academy + position + applicant`s name".

For more details, please visit the website: http://rc.dlut.edu.

Job Vacancies in China's Universities

赛尔互联 CERNET

Science Careers
From the journal *Science* AAAS

赛尔互联：《科学》在中国大陆高校人才引进服务独家合作伙伴
CER is Science' s exclusive agent for recruitment advertisement service in mainland China universities and colleges

China's Rapid Development
—— More Opportunities

❖ **Xi' an Jiaotong University (Shanxi, China)**

Position Offered: Dean, Fuli School of Food Scienceand Engineering (FSFSE) of Xi'an Jiaotong University (XJTU)

❖ **Xi' an Jiaotong University (Shanxi, China)**

Faculty positions offered in the Joint School of Sustainable Development (JSSD) of Sustainable Energy, Sustainable Materials and Sustainable Systems.

❖ **Nanchang University (Jiangxi, China)**

Zhejiang University of Technology provides positions for global experts on multiple disciplines.

❖ **Peking University (Beijing, China)**

The School of Life Sciences (SLS) at Peking University invites applications for multiple faculty positions at tenure-track assistant professor, associate professor and full professor levels.

For more details, visit http://www.eol.cn/

广告联系：赵佳 zhaojia@cernet.com +86 10 62603373

eol 中国教育在线 www.eol.cn 是赛尔互联旗下品牌

南京工業大學
NANJING TECH UNIVERSITY

海外领军人才招聘

Overseas Talents Recruitment

Nanjing Tech University, with a history of more than one hundred years, is a multidisciplinary university with a particular strength in engineering.

Aiming at excellence and innovation, Nanjing Tech University is set to become a first-class research university with a global vision. We are now seeking outstanding academic and research leaders in the following and related fields: Basic disciplines from within the Physical Sciences; Cutting edge disciplines from within the Life Sciences; Applied disciplines from within the Information Sciences; Humanities represented by Management Science.

Applicants should have a Ph.D. with at least 3-years research experience from leading universities or institutes. Candidates should demonstrate an internationally recognized research record and outstanding achievements. Successful candidates are expected to develop vigorous research programs and lead an independent research team. Successful candidates will be provided with a competitive relocation fee and salary package, generous start-up funds and spacious laboratories.

Interested candidates should visit **http://rczyb.njtech.edu.cn** for application details.
Phone: **Ms. Wang +86-25-58139148.**
E-mail: **job@njtech.edu.cn**

Science Careers

CER

“《科学》职业” 已经与赛尔互联(CER)开展合作。中国大陆的高校可以直接联系CER进行国际人才招聘。

请访问 Sciencecareers.org/CER 点得联系信息。

招募学术精英，《科学》是您的不二之选 **Science**

AAAS is here –
promoting universal science literacy.

In 1985, AAAS founded Project 2061 with the goal of helping all Americans become literate in science, matematics, and technology. With its landmark publications *Science for All Americans* and *Benchmarks for Science Literacy*, Project 2061 set out recommendations for what all students should know and be able to do in science, mathematics, and technology by the time they graduate from high school.

As a AAAS member, your dues help support Project 2061. If you are not yet a member, join us. Together we can make a difference.

To learn more, visit
aaas.org/plusyou/project2061

AAAS + U = Δ

THE UNIVERSITY OF ARIZONA

Director for the Center for Innovation in Brain Science

The University of Arizona seeks an accomplished scientist and leader in translational neuroscience to direct a new Center for Innovation in Brain Science. We seek an established neuroscientist with a strong record of extramural funding and research productivity who embraces a collaborative and inclusive approach to clinical and basic neuroscience research and education, and who has had experience building successful multidisciplinary programs. **Interested candidates should visit** http://ahsc.arizona.edu/news/director-center-innovation-brain-science for details and application instructions.

As an equal opportunity and affirmative action employer, the University of Arizona recognizes the power of a diverse community and encourages applications from individuals with varied experiences and backgrounds.

The University of Arizona is a committed Equal Opportunity/ Affirmative Action Institution. Women, minorities, veterans and individuals with disabilities are encouraged to apply.

Two Faculty Career Features

September 12, 2014	October 3, 2014
Reserve ads by August 26 to guarantee space *	Reserve ads by September 16 to guarantee space**

There's only one **Science**

Hiring Faculty? The Sept. 12 feature offers advice for faculty who are working with professionals in different industries/government/ academic cultures. **The Oct. 3 feature** explores how faculty can best collaborate with professionals in different cultures and countries.

Why you should advertise in these issues of *Science*:

Reach: Your job ad is seen by 570,400 readers around the globe

- The Sept. 12 issue includes a special bonus distribution to 100,000 scientists beyond our regular circulation

To book your ad:

advertise@sciencecareers.org

THE AMERICAS
202-326-6582

EUROPE/ROW
+44 (0) 1223 326500

JAPAN
+81 3 3219 5777

CHINA / KOREA / SINGAPORE / TAIWAN
+86 186 0082 9345

Science Careers
From the journal *Science* AAAS
ScienceCareers.org

*Ads accepted until September 5 if space is still available. **Ads accepted until September 26 if space is still available. Produced by the *Science*/AAAS Custom Publishing Office.

Assistant/Associate Vice President for Research and Director of Sponsored Programs

The Pennsylvania State University, a major public research university with $848 million in research expenditures last year, invites applications and nominations for the position of Assistant/Associate Vice President for Research (AVPR) and Director of Sponsored Programs. The successful candidate will serve as the focal point and principal coordinator for the University`s sponsored research programs and as such will be responsible for establishing and maintaining effective partnerships and linkages between university administration, faculty, government funding agencies, foundations, and the business and industrial communities within Pennsylvania and the nation.

The AVPR and Director of Sponsored Programs reports directly to the Vice President for Research and is an integral member of the university's leadership team for research administration. The AVPR-Director provides strategic vision and oversight to the University's Office of Sponsored Programs, is an ex-officio member of the University Research Council, and Co-Chairs the Administrative Committee on Research. The AVP-Director is expected to represent the interests of the University on key national research administration policy advisory groups and participates in national professional organizations that deal with the administration of research.

QUALIFICATIONS:

The successful candidate will possess extensive knowledge of sponsored programs administration in a research 1 institution and have broad working knowledge of federal funding agencies (e.g., DoD, NSF, NIH, and DOE), with cumulative experience of at least ten years of leadership responsibility in research administration, grants and contracts administration, or equivalent experience. Experience and familiarity with industrial sponsors and related contracting practices and procedures are also essential. A Master`s Degree or equivalent is required; a PhD or CRA is desirable.

Please submit letters of application, resumes, and contact information for three references. Review of resumes will begin immediately. Applications will continue to be received until an appointment is made.

Apply to job 52026 at http://apptrkr.com/504048

CAMPUS SECURITY CRIME STATISTICS:

For more about safety at Penn State, and to review the Annual Security Report which contains information about crime statistics and other safety and security matters, please go to http://www.police.psu.edu/clery/ , which will also provide you with detail on how to request a hard copy of the Annual Security Report.

PENNSTATE
1855

Penn State is an equal opportunity, affirmative action employer, and is committed to providing employment opportunities to minorities, women, veterans, disabled individuals, and other protected groups.

Science Careers online @sciencecareers.org

POSITIONS OPEN

POSTDOCTORAL FELLOWSHIPS AVAILABLE

To pursue research on (1) computational modeling by performing in-silico docking prediction analysis of receptor-ligand interactions and high throughput target screening of small-molecule library of compounds as anti-inflammatory agents and (2) microbiome analysis of datasets using publicly available analysis tools. The candidate should have expertise in bioinformatics technology for 'omic data analysis to assess microbiota in colitis, obesity, M.S., and other autoimmune and inflammatory diseases.

A Ph.D. in any discipline of Biomedical Sciences/Biology/Bioinformatics/Computational Biology or other related fields with experience to perform the research independently required. Send curriculum vitae and three references to: **Dr. Mitzi Nagarkatti, Carolina Distinguished Professor and Chair, Department of Pathology, Microbiology and Immunology, University of South Carolina School of Medicine, Columbia, SC29229** or **e-mail: pdbioinformatics@uscmed.sc.edu.** *University of South Carolina, Columbia is an Equal Opportunity/Affirmative Action Employer and encourages applications from women and minorities.*

MICROBIOLOGIST

The Department of Biological Sciences, California State University, East Bay, seeks a Microbiologist for appointment to a tenure-track position at the level of **ASSISTANT PROFESSOR** beginning fall 2015. First consideration will be given to individuals with a background in molecular mechanisms of gene expression and/or pathogenesis but other areas of study and expertise will be considered. We seek applicants who are committed to excellence in teaching and the development of a student-centered research program in a culturally diverse intellectual community. The primary teaching responsibility will include undergraduate and Master's level courses in microbiology. A Ph.D. and postdoctoral experience are required. Submit curriculum vitae, research and teaching plans, selected reprints, and three letters of recommendation as hard copy to: **Microbiologist Search Committee OAA 15-16 BIOL-MICRO-TT, Department of Biological Sciences, California State University, East Bay, Hayward CA 94542.** Review of applications will begin on October 15, 2014, and will continue until the position is filled. Direct inquiries to the chair of the search committee **e-mail: carol.lauzon@csueastbay.edu.** *Equal Opportunity Employer.*

Help employers find you. Post your resume/cv.

Science Careers
From the journal *Science* AAAS

www.ScienceCareers.org

POSITIONS OPEN

TENURE-TRACK FACULTY POSITION in Neuroscience

Saint Louis University, a Catholic, Jesuit institution dedicated to student learning, research, health care, and service is seeking applicants for a tenure-track **ASSISTANT PROFESSOR** position in Neuroscience in the Department of Biology. This position will support a new interdisciplinary undergraduate major in Neuroscience that is being jointly administered by the Departments of Biology and Psychology. Applicants should have a Ph.D., postdoctoral experience, a record of research productivity, and a commitment to undergraduate and graduate student mentoring in Neuroscience. The successful candidate is expected to establish an independent, extramurally funded research program addressing fundamental questions in areas including, but not limited to, molecular, cellular, and/or comparative neuroscience, potentially incorporating use of model organisms. She or he will develop and teach a new undergraduate neuroscience lecture and laboratory course and an advanced/graduate course in the candidate's area of expertise. Excellent facilities and a competitive startup package are provided, and opportunities are available to collaborate with researchers in the Psychology Department, at the nearby Health Science Center, and other local universities. Candidates whose research interests complement those of existing faculty in the Biology Department are encouraged to apply.

All applications must be made online at **website: http://jobs.slu.edu** (**Req ID 20140606**) and include a cover letter, curriculum vitae, a research statement, and a statement of teaching experience and philosophy. In addition, please have three letters of reference sent to: **Dr. Robert Wood, Department of Biology, Saint Louis University, 3507 Laclede Avenue, St. Louis, MO, 63103-2010.** Review of applications will begin October 27, 2014 and will continue until suitable candidates are identified. Additional information on the Department of Biology can be found at **website: http://bio.slu.edu.** Additional information about the Neuroscience program can be found at **website: http://www.slu.edu/department-of-biology-home/interdisciplinary-programs/neuroscience-at-slu.**

Saint Louis University is an Affirmative Action/Equal Opportunity Employer, and encourages nominations of and applications from women and minorities.

THREE OPEN FACULTY POSITIONS
Boston College
Chemistry Department

The Chemistry Department of Boston College invites applications for three tenure-track positions to be effective in the fall of 2015. Applicants will be evaluated based on their potential to establish a prominent and well-funded research program and to excel in teaching at the graduate and undergraduate levels. Successful applicants will join a department of approximately 120 doctoral students, 30 postdoctoral fellows, 200 undergraduate majors, and an internationally recognized faculty.

ASSISTANT PROFESSORS in the areas of Chemical Biology, Organic Chemistry, and Physical/Materials Chemistry: requires a Ph.D. in Chemistry or related areas; postdoctoral experience is desirable but not required. The candidate is expected to have published in top-refereed journals and demonstrated the ability to perform outstanding independent research.

Interested applicants must submit a cover letter (which includes the names of three references), a graphical executive summary of research plans (one page), curriculum vitae, a summary of research plans (eight pages maximum), a statement of teaching philosophy and arrange to have three letters of reference submitted via the online faculty application at: **website: http://apply.interfolio.com/25361** for physical/materials chemistry, **website: http://apply.interfolio.com/25362** for chemical biology, **website: http://apply.interfolio.com/25357** for organic chemistry.

All application materials must be submitted electronically on or prior to 15 October 2014.

Boston College, a university of eight schools and colleges, is an Equal Opportunity Employer and supports Affirmative Action.

Nontraditional Careers: Opportunities Away From the Bench Webinar

Want to learn more about exciting and rewarding careers outside of academic/industrial research? View a roundtable discussion that looks at the various career options open to scientists and strategies you can use to pursue a nonresearch career.

Now Available On Demand
www.sciencecareers.org/webinar

Produced by the *Science*/AAAS Business Office.

Science Careers
From the journal *Science* AAAS

For your career in science, there's only one Science

A career plan customized *for* you, *by* you.

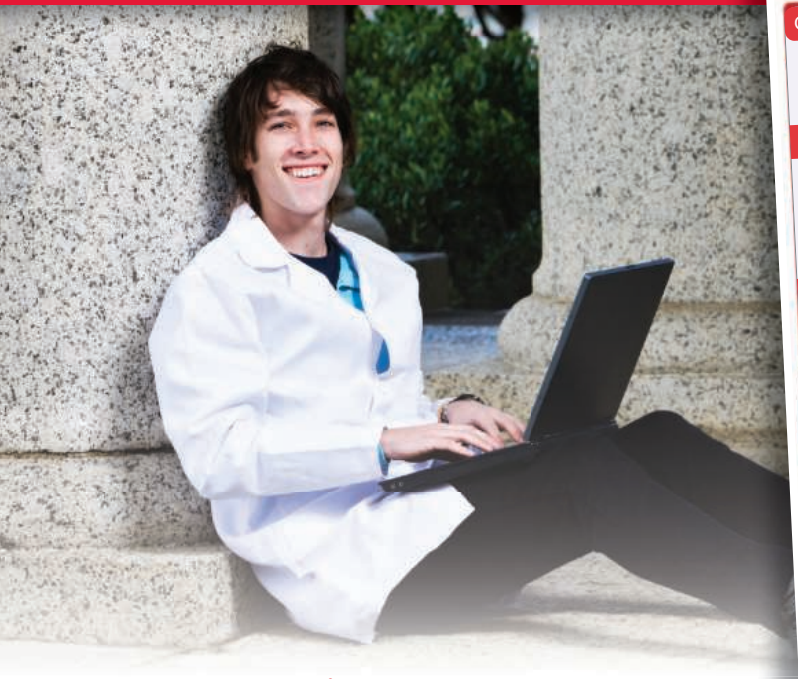

myIDP.sciencecareers.org

Recommended by leading professional societies and endorsed by the National Institutes of Health, an individual development plan will help you prepare for a successful and satisfying scientific career.

my IDP Science Careers

In collaboration with FASEB, UCSF, and the Medical College of Wisconsin and with support from the Burroughs Wellcome Fund, AAAS and *Science* Careers present the first and only online app that helps scientists prepare their very own individual development plan.

Visit the website and start planning today!
myIDP.sciencecareers.org

In partnership with:

advancing the life sciences 1912-2012 FASEB Federation of American Societies for Experimental Biology

UCSF University of California San Francisco

Medical College of Wisconsin

Burroughs Wellcome Fund

By **Jyoti Mishra**

Having it all

I grew up in urban India in a middle-class family, the daughter of two hard-working professionals. They always encouraged me. They never objected when I did mostly what boys did, like be the only girl in astronomy camp. My closest friends were boys, and we formed study groups and competed for the best grades. When I pursued graduate school in the United States for computational neurobiology, I was the only woman in my international class. A decade later, I'm a happy academic at a time when many leave this field.

Can women have it all? I'm a scientist and university faculty member. I aspire for more, yet I don't feel I've made any sacrifices in my career or family life to get here. In that sense, I *do* have it all. This is my perspective.

My *all* is different from your *all*. Genetic and life histories have shaped our brains to be unique, so why should our objectives be the same? Identify *your* all and work hard to achieve it. Follow *your* dream.

***All* changes over time.** I am in my vigorous 30s, and I perceive life as long. Yes, the career clock and biological clock clash now, but there is time to achieve what I want in both my work and family. At my university, there are impressive women leaders who are older, with fewer family responsibilities. They illustrate that women lead ambitious lives after the children are grown. I expect a time to come when I immerse myself in my career even more deeply than I do now. For now, I am content with no internal dilemmas and no mental resources wasted on guilt, yet I am also eager to surge ahead.

"Lean in" to every moment. I interpret Sheryl Sandberg's message to apply to every demand of daily life, at work and at home. Be attentive in the present and make sound decisions on the issue at hand. Don't let yourself be distracted by the day's other tasks. When parenting, parent. When working, work.

Climbing small mountains makes big ones easier. Challenging research projects can take 5 years or more to complete. Raising a child takes far longer. Our brains generate the same reward signals when we conquer any challenge, big or small, so I take on smaller challenges outside work. My daily physical workouts are diverse—running, yoga, Pilates, strength training—and I progress by focusing on today's form and peak performance. Time spent on small challenges builds precious mental metal that makes big challenges seem easier.

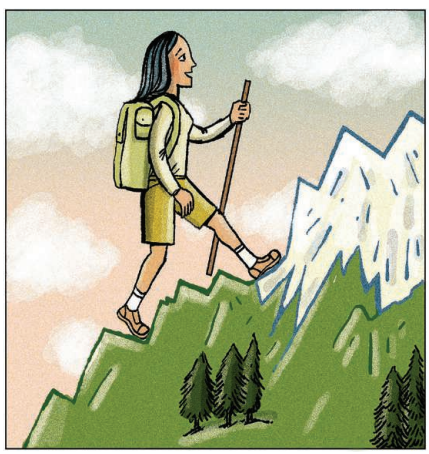

"Climbing small mountains makes big ones easier."

It takes a village. I am reaping the benefits of being raised in a family that inculcated self-belief. My mother is a role model, balancing career and family superbly and loving it. After the kids left home, she became the dean of a reputed medical university. During crises in my life, I ask, "WWMD? What would Mamma do?" When there is no role model close to home, I look for one in the community or at work because role models are vital for success.

My professional husband is the pillar of my village. He encourages me to excel in my career, as I support his, and together we encourage each other's joy in equal parenting. My in-laws cheer my successes. Bosses and mentors express confidence in me. I love to see my son look forward to day care, which is right next to my work. We hire help for mundane house chores, liberating time to focus on what really matters. It takes a village!

It makes a village. Enabled by their villages, women and men of my generation are finding success and contentment, reaping the benefits of hard work sown by previous generations of village makers. Now it is our time to sprout new villages—to become confident role models for junior colleagues and students, the best parents we can be to our children, and supportive members of our broader families. Women need women to show how it can be done—how not to succumb to multitasking demands or be overcome by guilt, how to instead take delight in the diverse experiences and challenges life brings and feel that we do have it all. ■

Jyoti Mishra is an assistant professor of neurology at the University of California, San Francisco. For more on life and careers, visit www.sciencecareers.org.

ILLUSTRATION: ROBERT NEUBECKER

Downloaded from www.sciencemag.org on August 29, 2014

Published by AAAS